

Materials Forming, Machining and Tribology

J. Paulo Davim *Editor*

# Traditional Machining Processes

Research Advances

 Springer

# **Materials Forming, Machining and Tribology**

**Series editor**

J. Paulo Davim, Aveiro, Portugal

More information about this series at <http://www.springer.com/series/11181>

J. Paulo Davim  
Editor

# Traditional Machining Processes

Research Advances

 Springer

*Editor*  
J. Paulo Davim  
Department of Mechanical Engineering  
University of Aveiro  
Aveiro  
Portugal

ISSN 2195-0911                      ISSN 2195-092X (electronic)  
ISBN 978-3-662-45087-1          ISBN 978-3-662-45088-8 (eBook)  
DOI 10.1007/978-3-662-45088-8

Library of Congress Control Number: 2014953896

Springer Heidelberg New York Dordrecht London

© Springer-Verlag Berlin Heidelberg 2015

This work is subject to copyright. All rights are reserved by the Publisher, whether the whole or part of the material is concerned, specifically the rights of translation, reprinting, reuse of illustrations, recitation, broadcasting, reproduction on microfilms or in any other physical way, and transmission or information storage and retrieval, electronic adaptation, computer software, or by similar or dissimilar methodology now known or hereafter developed. Exempted from this legal reservation are brief excerpts in connection with reviews or scholarly analysis or material supplied specifically for the purpose of being entered and executed on a computer system, for exclusive use by the purchaser of the work. Duplication of this publication or parts thereof is permitted only under the provisions of the Copyright Law of the Publisher's location, in its current version, and permission for use must always be obtained from Springer. Permissions for use may be obtained through RightsLink at the Copyright Clearance Center. Violations are liable to prosecution under the respective Copyright Law.

The use of general descriptive names, registered names, trademarks, service marks, etc. in this publication does not imply, even in the absence of a specific statement, that such names are exempt from the relevant protective laws and regulations and therefore free for general use.

While the advice and information in this book are believed to be true and accurate at the date of publication, neither the authors nor the editors nor the publisher can accept any legal responsibility for any errors or omissions that may be made. The publisher makes no warranty, express or implied, with respect to the material contained herein.

Printed on acid-free paper

Springer is part of Springer Science+Business Media ([www.springer.com](http://www.springer.com))

# Preface

The term *machining* refers a group of processes that remove gradually material from a workpiece by various methods involving single-point or multipoint cutting tools, each with a clearly defined geometry as well as abrasive wheels which consist of a large number of micro-cutting edges with geometrically undefined. Machining processes can be applied to work metallic and non-metallic materials such as polymers, wood, composites and special materials. Typical applications of machining processes include complex geometry, high accuracy and good surface finish. Today, machining processes present great importance to automotive, aircraft, moulds and dies and other advanced industries placed in all industrialized or emerging countries.

The purpose of this book is to present a collection of examples illustrating research in machining processes. Chapter 1 of the book provides information on polycrystalline diamond (PCD) tool material (emerging applications, problems and possible solutions). Chapter 2 is dedicated to analysis of orthogonal cutting experiments using diamond-coated tools with force and temperature measurements. Chapter 3 describes estimation of cutting forces and tool wear using modified mechanistic models in high performance turning. Chapter 4 contains information on cutting under gas shields (phenomenological concepts versus industrial applications). Chapter 5 is dedicated to machinability of magnesium and its alloys (a review). Chapter 6 provides information on grinding science. Finally, Chap. 7 is dedicated to flexible integration of shape and functional modelling of machine tool spindles in a design/optimisation framework.

The present book can be used as a research book for final undergraduate engineering course or as a topic on manufacturing engineering at the postgraduate level. Also, this book can serve as a useful reference for academics, researchers, mechanical, manufacturing, industrial and materials engineers, professionals in machining processes and related industries. The scientific interest in this book is evident from many important centers of the research, laboratories and universities as well as industry. Therefore, it is hoped this book will inspire and enthuse others to undertake research in machining processes.

The Editor acknowledges Springer for this opportunity and for their enthusiastic and professional support. Finally, I would like to thank all the chapter authors for their availability for this work.

Aveiro, Portugal, September 2014

J. Paulo Davim

# Contents

<b>1 Polycrystalline Diamond (PCD) Tool Material: Emerging Applications, Problems, and Possible Solutions. . . . .</b>	<b>1</b>
Viktor P. Astakhov and Andrew Stanley	
<b>2 Analysis of Orthogonal Cutting Experiments Using Diamond-Coated Tools with Force and Temperature Measurements . . . . .</b>	<b>33</b>
Robert Ivester, Eric Whitenton, Jill Hershman, Kevin Chou and Qiang Wu	
<b>3 Estimation of Cutting Forces and Tool Wear Using Modified Mechanistic Models in High Performance Turning. . . . .</b>	<b>49</b>
Ana Isabel Fernández-Abia, Joaquín Barreiro García, Luis N. López de Lacalle and Octavio Pereira Neto	
<b>4 Cutting Under Gas Shields: Phenomenological Concepts Versus Industrial Applications . . . . .</b>	<b>109</b>
C.M.A. Silva, V.A.M. Cristino, P.A.R. Rosa and P.A.F. Martins	
<b>5 Machinability of Magnesium and Its Alloys: A Review. . . . .</b>	<b>133</b>
Diego Carou, Eva M. Rubio and J. Paulo Davim	
<b>6 Grinding Science . . . . .</b>	<b>153</b>
Mark J. Jackson	
<b>7 Flexible Integration of Shape and Functional Modelling of Machine Tool Spindles in a Design/Optimisation Framework . . .</b>	<b>209</b>
G.-C. Vosniakos, A. Krimpenis and P. Benardos	
<b>Index . . . . .</b>	<b>235</b>



# Chapter 1

## Polycrystalline Diamond (PCD) Tool Material: Emerging Applications, Problems, and Possible Solutions

Viktor P. Astakhov and Andrew Stanley

**Abstract** This chapter first discusses the challenges with the tool material selection for machining of high-silicon aluminum-matrix composites. It is shown that the combination of a soft easy-to-adhere Al-matrix and highly abrasive particles limits the use of cemented carbide tools due to high rate of adhesion and abrasion wear. The issue becomes intolerable in high-speed machining applications. As a result, polycrystalline diamond (PCD) is slowly becoming a material of choice for such applications. The chapter presents the major research advances in PCD as a tool material. The wear mechanism of PCD is discussed at macro- and micro levels. A discussion on the need and a report on the progress in the development of thermal stable grades of PCD conclude the chapter.

### 1.1 Introduction

The selection of a cutting tool material type and its particular grade is an important factor to consider when planning a successful machining operation. A basic knowledge of each cutting tool material and its performance is therefore important so that the correct selection for each application can be made. Considerations include the type and properties of the material to be machined, the part/blank type and shape, machining conditions, and quality requirements of the machined parts for the considered operation. Note that the cost per machined part (the size of production lot, yearly production, existing machine/machining practice, etc.) should also be considered in the selection of the proper (technically and economically) tool material.

---

V.P. Astakhov (✉)

General Motors Business Unit of PSMi, 1792 Elk Ln, Okemos, MI 48864, USA  
e-mail: astakhov@scientist.com

A. Stanley

General Motors Business Unit of PSMi, 1255 Beach Ct, Saline, MI 48176, USA  
e-mail: astanley@psmicorp.com

© Springer-Verlag Berlin Heidelberg 2015

J.P. Davim (ed.), *Traditional Machining Processes*,

Materials Forming, Machining and Tribology, DOI 10.1007/978-3-662-45088-8\_1

The aim of this chapter is to familiarize readers with problems existing in high-speed machining of abrasive work materials and to present the research advances in polycrystalline diamond (PCD) tool material to address these problems.

## **1.2 Challenges with Work Materials**

There are a number of new work materials that have been in extensive use since the beginning of the 21st century. Among them, two distinctive groups of work materials are of prime concern in many modern manufacturing facilities: metal and polymer base composite materials due to the increased volume of parts made of these materials. Although some types of such materials have been known for a long time, a new challenge in their machining was brought by the necessity of wide implementation of real high-speed, and thus high-efficiency, machining under the pressure to reduce the direct manufacturing cost, on one hand, and significant increase in quality requirements to the machined part, including dimensional accuracy and surface integrity. This chapter concentrates on machining of high-silicon aluminum-matrix metal-matrix composites (HSAM MMCs).

### ***1.2.1 Metal-Matrix Composites (MMCs)***

Progress in design and manufacturing led to the development of new engineering materials including a wide group of composites. One class of composites being looked at more and more by the aerospace and automotive industries is HSAM MMCs. This group of work materials includes lightweight, and relatively low-strength alloys of aluminum, magnesium, or titanium reinforced by adding second-phase particles, whiskers, fibers, wires, or filaments. For the last 20 years, the focus of interest for the more common automotive and aerospace applications seems to be on aluminum reinforced with particles of silicon carbide or alumina fibers. Applications for these materials are being developed in which heavier steel or iron components are replaced by lighter MMC substitutes. Examples in the automotive industry include engine blocks, transmission cases, brake disks, axels, or, in the leisure industry, items such as tennis racquets. Whether the application is a connecting rod or a tennis racquet, efficiency in use is obtained by reduction in weight, and acceleration is improved by reduction in the inertia of the moving mass.

Progress has been made both in the formulation of alloy compositions and in manufacturing routes. Powdered metallurgy, co-spraying, low-pressure liquid metal infiltration, and die-casting techniques have been developed, and in some of these, near net shape components can be made.

MMCs offer high strength-to-weight ratio, high stiffness, and good damage resistance over a wide range of operating conditions, making them an attractive option in replacing conventional material for many engineering applications.

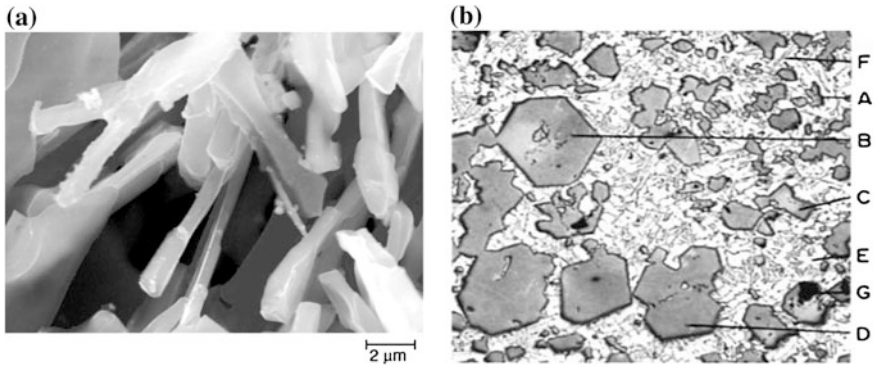
Typically, MMCs are aluminum, titanium, copper, and magnesium alloys, while the reinforcement materials are silicon carbide, aluminum oxide, boron carbide, graphite, etc., in the form of fibers, whiskers, and particles. Probably the single most important difference between fiber-reinforced and particulate composites or conventional metallic materials is the anisotropy or directionality of properties, that is, particulate composites and conventional metallic materials are isotropic, while the fiber-reinforced composites are generally anisotropic. Particulate-reinforced composites offer higher ductility. Their isotropic nature as compared to fiber-reinforced composites makes them an attractive alternative [1]. Although there are a great number of MMCs, HSAM MMCs are of highest usage due to the high volume of automotive manufacturing.

In the context of global competition, manufacturing companies are compelled to improve productivities through the optimizations of their production operations including machining. In the automotive industry, transmission and engine components are made of HSAM MMCs, which have a high strength to weight ratio. Aluminum is cast at a temperature of 650 °C (1,200 °F). It is alloyed with silicon (9 %) and copper (3.5 %) to form the Aluminum Association 380 alloy (UNS A03800) which is widely used in automotive transmissions. Silicon increases the melt fluidity and reduces machinability. Copper increases hardness and reduces ductility. By greatly reducing the amount of copper (less than 0.6 %) the chemical resistance is improved making AA 386 (UNS A03860) well suited for use in marine environments. AA 390 (UNS A03900) with 17 % silicon for high wear resistance is also used in automotive transmissions (for pump covers) and engines (for cylinder castings).

Machining of such alloys presents a great challenge due to their unique properties, namely, a combination of a soft easy-to-adhere Al-matrix and highly abrasive particles including silicon and sludge [2–5]. Figure 1.1a shows a scanning electron microscope (SEM) micrograph of 380 Al—alloy as it is reported to the customer and appears in manufacturing books. In reality, however, real die aluminum castings supplied to automotive plants contain clusters of sludge as shown in Fig. 1.1b. The presence of this sludge and silicon particles make Al-alloys highly abrasive that causes premature tool wear and significant heat generation during machining. The latter causes thermal distortions of the machined parts, resulting in location and diametric errors in machined parts.

### ***1.2.2 Basic Problems with Tools Made of Cemented Carbides***

The tool material of choice in modern manufacturing is cemented carbide. The cemented carbides are a range of composite materials, which consist of hard grains of the carbides of transition metals (Ti, V, Cr, Zr, Mo, Nb, Hf, Ta, and/or W) cemented or bound together by a softer metallic binder consisting of Co, Ni, and/or



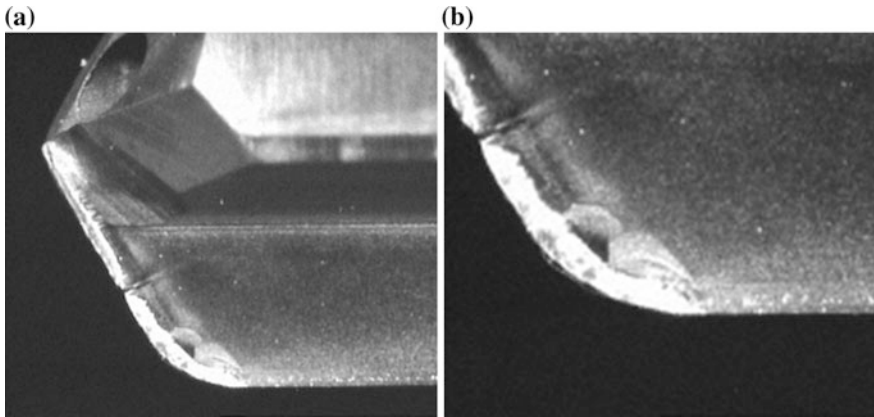
**Fig. 1.1** Micrographs of 380 Al-alloy: **a** SEM image commonly presented to customers, **b** real microstructure that shows coarse crystals of sludge (*A*, *B*, *C*, and *D*). The remainder of the structure consists of aluminum matrix (*E*), eutectic silicon (*F*) and  $\text{Al}_2\text{O}_3$  (*G*)

Fe (or alloys of these metals) known as the matrix. The grades of cemented carbide that include only tungsten carbides (WC) in their composition are known as straight grades. Because most of the commercially important cemented carbides contain mostly WC as the hard phase, the terms “cemented carbide” and “tungsten carbide” are often used interchangeably.

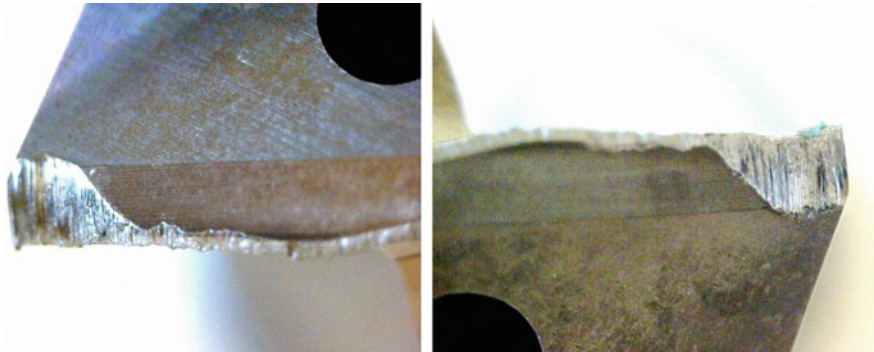
Unfortunately, cutting tools made of cemented carbides do not perform well in machining of HSAM MMCs. Low tool life and subpar quality of the machined surfaces became unbearable with introduction of high-speed machining (HSM) in the automotive industry. In the authors’ opinion, abrasion and adhesion are two basic mechanisms of carbide cutting tool wear in machining of HSAM MMCs, although they are not properly addressed in metal cutting studies/tool applications.

Figure 1.2 shows a worn cutting edge and the rounded drill corner as a result of severe abrasion wear. As can be seen, the drill is completely destroyed. Moreover, a significant amount of the tool material should be ground off to restore the drill to working condition. Figure 1.3 shows the typical appearance of abrasive wear. As can be seen, the worn surface contains deep scratches in the direction of sliding left by abrasive particles/solid phases in the work material.

Generally, adhesive wear is thought of as the mechanical transfer of material from one contacting surface to another. It occurs when high loads, temperatures or pressures cause the asperities on two contacting metal surfaces in relative motion to adhere together then immediately tear apart, shearing the metal in small, discrete areas. The surface may be left rough and jagged or relatively smooth due to smearing/deformation of the metal. In general machinery, adhesion occurs in equipment operating in the mixed and boundary lubrication regimes due to insufficient lubricant supply, inadequate viscosity, incorrect internal clearances, incorrect installation or misalignment. This can occur in rings and cylinders, bearings and gears. Normal break-in is a form of mild adhesive wear, as is frosting. Scuffing usually refers to moderate adhesive wear, while galling, smearing and seizing result



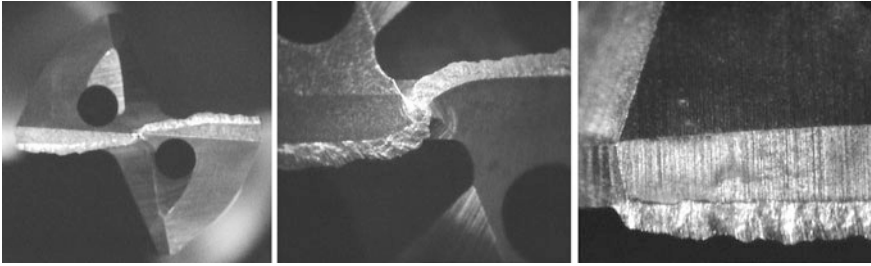
**Fig. 1.2** Rounded drill corner as a result of severe abrasion wear: **a** the drill major cutting edge, and **b** the drill corner



**Fig. 1.3** Abrasive wear of the drill corners

from severe adhesion. Adhesion can be prevented by lower loads, avoiding shock loading and ensuring that the correct oil viscosity grade is being used for lubrication. If necessary, extreme pressure and anti-wear additives are added to the lubrication oil to reduce the damage due to adhesion.

In metal cutting, adhesion occurs due to mechanical bonding of juvenile freshly-formed surface free of oxides. The harder the contact pressure and the rougher the tool contact surface, the stronger the bonding. Such an adhesion can be referred to as pure adhesion in metal cutting. It takes place at low cutting speeds when the built-up edge on the tool rake face is great. Due to high plastic deformation of the chip and high contact pressures at the tool-chip and tool-workpiece interfaces, extreme pressure and anti-wear additives cannot penetrate into these interfaces [6]. As a result of adhesion of the work material converted into the chip and the tool rake face, the so-called built-up edge (commonly referred to as BUE in the literature



**Fig. 1.4** BUE forms in drilling of the first hole

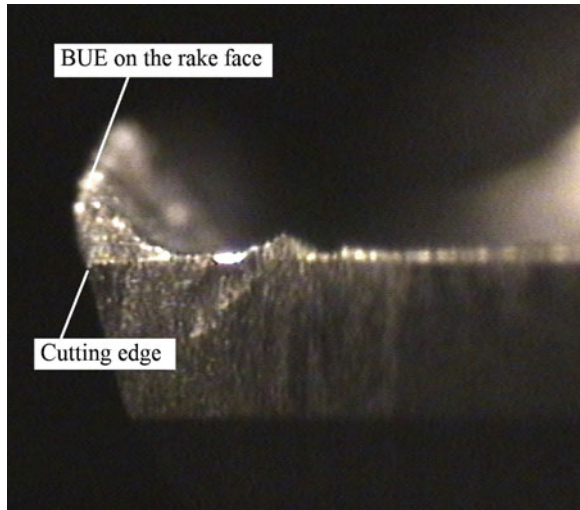
on metal machining) is formed. Its appearance is shown in Fig. 1.4. Note the following particularities:

1. BUE forms in machining of the first part.
2. It is well known in steel machining that BUE exists only at low cutting speed. When cutting speed exceeds 60 m/min, BUE disappears [7]. This is not the case in machining of HSAM MMCs where it exists in the whole range of cutting speed being at a maximum at the drill corner (for the drill shown in Fig. 1.4, it is 300 m/min—the maximum speed allowed by the cemented carbide used as the tool material for the application) to the drill center where the cutting speed converges to virtual zero. All attempts to use the most advanced coatings, including CVD microcrystalline diamond coating, did not result in a noticeable reduction of BUE.

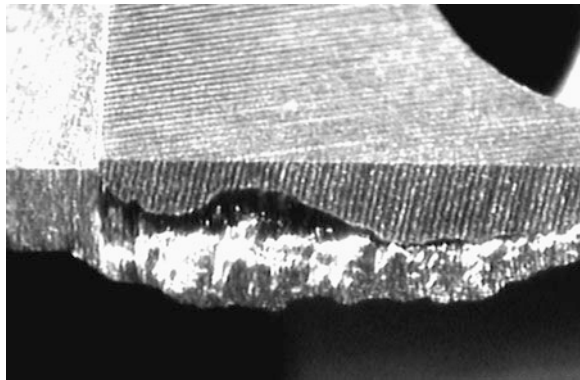
The appearance of BUE (Fig. 1.4) is deceptive so that many literature sources in the past and many specialists up to the present believe that BUE can protect the cutting edge from wear. As it appears as a continuation of the cutting edge as shown in Fig. 1.5, it is believed that “stable” BUE can practically eliminate the contact between the tool flank face and the workpiece so that it “protects” the tool flank face reducing its wear. As discussed by Astakhov earlier [8], this “looks-nice” story ends when one realizes that tool life is lowest for the cutting conditions where BUE is greatest. In machining of steel, a reasonable tool life is achieved at high cutting speeds where BUE does not form at all (greater than 60 m/min for common steels).

Figure 1.6 shows the appearance of adhesion wear of a carbide drill in machining of HSAM MMCs. As can be seen, the drill major cutting edges are completely destroyed by “the protector” BUE. This is because BUE is not stable in metal cutting so it changes within each cycle of chip formation [8]. As BUE adheres to the rake face, the adhesion causes mechanical bonding (as glue with a piece of paper). When BUE is periodically removed by the moving chip (as its height becomes sufficient), it brings a small piece of the tool materials with it (as with glue removed from paper). The process repeats itself many, many times so the tool

**Fig. 1.5** BUE on the rake face of the drill (the view from the margin)



**Fig. 1.6** Appearance of adhesion wear of a carbide drill in machining of HSAM MMCs



becomes worn by this process. Note that no “welding” (the term often used in the literature) or other physical/chemical processes are involved in adhesion wear.

Abrasion and adhesion are the principle problems encountered in the machining of HSAM MMCs where tool life is significantly shortened causing high tooling cost per unit (a machined part). Moreover, the presence of BUE causes poor surface roughness of machined parts. As a result, tungsten carbide tools are used only for roughing operations because achieving the required diametric accuracy and mirror-shiny surface roughness is impossible particularly in modern HSM. Therefore, PCD is slowly becoming a material of choice for such applications particularly with the wider use of HSM in the automotive industry.

## 1.3 PCD as the Tool Material

### 1.3.1 *Brief History*

The 1797 discovery that diamond was pure carbon catalyzed many attempts to make artificial diamond. If the common carbon of commerce could be turned into diamond, a millionfold increase in the value of the starting material would be obtained. There was, in addition, the interest of the scientific achievement. The earliest claim of success (C. Cagniard de la Tour) was made in the year 1823. The diamond synthesis problem has attracted the interest of thousands. Those pursuing the problem have ranged from charlatans through rank amateurs to the world's greatest scientists. Included among the great are Boyle, Bragg, Bridgman, Crookes, Davey, Despretz, Friedel, Liebig, Ludwig, Moissan, Parsons, Taman, and Wohler.

The literature on diamond synthesis is not very extensive. Most of the work has gone unpublished. Many of the world's large industrial organizations have considered the problem and have spent millions of dollars on research and development. So many years passed without success that those working on the problem felt embarrassed to admit that they were so engaged. Another aspect of the problem was chicanery and fraud. Quite a number have claimed to possess a procedure for converting graphite into diamond, invited the unwary to invest their money, and then vanished.

The earliest successes were reported by James Ballantyne Hannay in 1879 [9] and by Ferdinand Frédéric Henri Moissan in 1893 [10]. Their method involved heating charcoal at up to 3,500 °C with iron inside a carbon crucible in a furnace. Whereas Hannay used a flame-heated tube, Moissan applied his newly developed electric arc furnace, in which an electric arc was struck between carbon rods inside blocks of lime. The molten iron was then rapidly cooled by immersion in water. The contraction generated by the cooling supposedly produced the high pressure required to transform graphite into diamond. Moissan published his work in a series of articles in the 1890s [11].

Despite these early successes, many following scientists experienced difficulty in reproducing such results. Spending nearly 30 years of his life and over £30,000, British scientist Charles Algernon Parsons went through great lengths in order to reproduce a high-pressure high-temperature diamond. While claiming to have produced high-pressure high-temperature diamonds, overtime he reluctantly admitted that no scientist, past or present, could create synthetic diamonds and that the best they could create were spinels, or a simple class of minerals crystallized in an octahedral form [12].

Despite past failures and inspired by the vast industrial uses of diamonds, especially during wartime, General Electric (GE) resumed the synthetic diamond project in 1951. Schenectady Laboratories of GE and a high pressure diamond group formed. In 1954, H. Tracy Hall (General Electric) successfully synthesized the first diamond using a high-pressure high-temperature (HPHT) process. The commercial promise of diamond synthesized by HPHT was fulfilled when GE opened their first



production unit in 1956. Since this date, production of HPHT synthetic diamond has increased every year and is currently in excess of 300 tons/year.

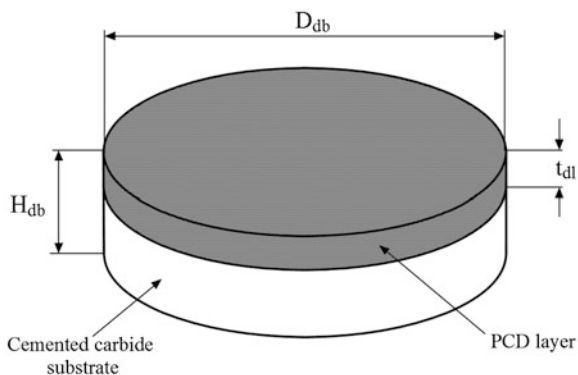
In machining where the wear mechanism is mainly abrasion, PCD made using HPHT synthesis has already proved itself to be a superior tool material. Over the last 20 years, PCD has been accepted for volume production of hypereutectic aluminum–silicon alloy components in the automotive industry, the machining of nonferrous alloys of copper, the machining of abrasive plastics and plastic composites such as glass fiber and printed circuit boards, as well as volume machining of wood composites, such as chipboard.

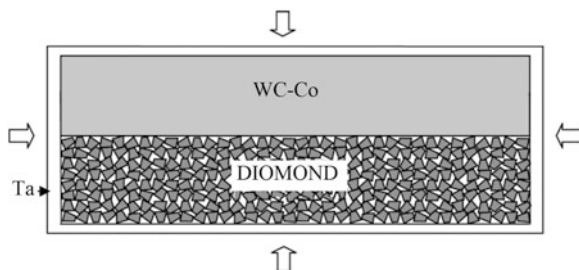
### 1.3.2 Blanks

The vast majority of PCD tools are actually PCD-tipped tools made from PCD discs manufactured using HPHT. Figure 1.7 shows a PCD disk (blank) and its geometrical parameters. Such a blank consists of a layer of fine diamond powder sintered together into a dense uniform mass, approximately 0.5–2.0 mm thick, supported on a substrate of cemented carbide. The expensive and technically difficult HPHT process used to produce the basic disc has been refined over the years and now PCD blanks are made as discs of up to 74 mm in diameter. By using different grain sizes of diamond and by changing the composition of the diamond and carbide layers, it has been possible to optimize the properties of PCD for specific applications. As a result, various grades are now synthesized by a number of companies around the world. The differences are in stability of sizes ( $H_{db}$  and  $t_{dl}$ ), quality including consistency and residual stresses, actual composition, and many others which are not specified by PCD blanks manufacturers.

In manufacturing PCD discs, diamond powder and WC-Co substrate are wrapped up in a tantalum (Ta) shell as shown in Fig. 1.8. Such a wrapping is placed in the assembly composed of a solid pressure salt (NaCl) surrounded by the crucible and graphite heater and then placed in the press for sintering. First, pressure is raised to its nominal level with little or no heating. During this stage, all the crystals

**Fig. 1.7** PCD disk and its geometrical parameters





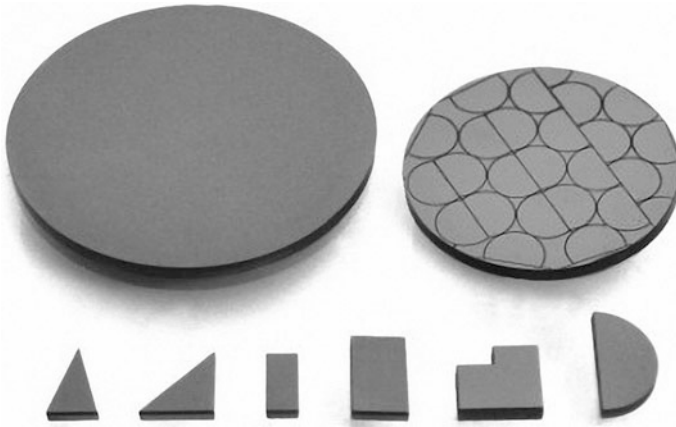
**Fig. 1.8** Diamond powder disc and WC-Co substrate wrapped up in tantalum (Ta) shell (the capsule)

are being pushed against each other with increasing force. Many diamond particles are sliding relative to each other and many are cracking into two or more fragments with the overall effect of increasing powder density [13]. A coarser powder presents a higher degree of crushing than a fine one as the former includes a much smaller average number of contact points and thus much higher contact stresses (compared to fine powders) that cause the described crushing.

After the crushed and compacted powder is under full pressure, the temperature is raised at a heating rate of 60 °C/min to its nominal value (approx. 1,600 °C). The pressure-temperature condition is always kept in the thermodynamically stable region of diamond above the eutectic temperature of carbon and Co. As the diamond powder is packed against the WC-Co substrate, cobalt is the source for the catalyst metal that promotes the sintering process. When the cobalt reaches its melting temperature of 1,435 °C at 5.8 GPa, it is instantaneously squeezed into the open porosity left in the layer of compacted diamond powder. At this point, the sintering process takes place through a mechanism of carbon dissolution and precipitation. Technically, this process is defined as a pressure-assisted liquid-phase sintering. The driving force for the densification under an extreme pressure is determined by the pressure itself and also by the contact area relative to the cross-sectional area of the particles.

The result of the process is a disc (consisting of the WC-Co substrate and diamond layer of certain thickness strongly bonded with this substrate). In this disc PCD composite is a fully dense mass of randomly oriented, intergrown micron-size diamond-particles that are sintered together in the presence of a metallic catalyst phase, usually cobalt. Small pockets of the catalyst phase, which promotes the necessary intergrowth between the diamond particles, are left behind within the composite material.

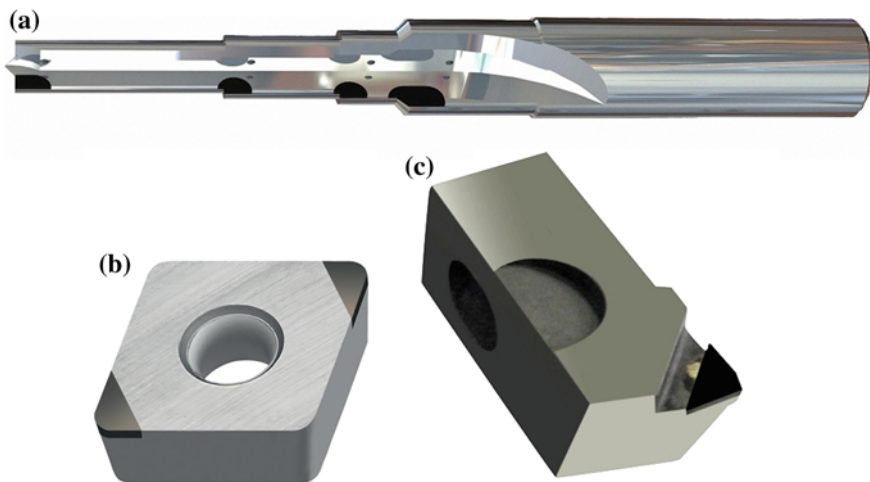
Coarse PCD grades are normally used for interrupted and/or high-impact cutting conditions, e.g. in milling where PCDs with 30 μ or even higher grain sizes are recommended by tool manufacturers. When machining under harsh conditions, the differences in PCD wear resistance become more evident, therefore coarse-grained PCD tends to be used in such conditions. When machining under moderately harsh conditions, the PCD wear resistance is of less importance and factors such as edge



**Fig. 1.9** PCD disc blank, and variety of PCD tips made out of this blank

quality/surface finish must be considered, therefore medium ( $10\text{--}15\ \mu$ ) and fine-grained ( $2\text{--}8\ \mu$ ) PCD grades tend to be used. While an ultra-coarse PCD has the theoretical abrasion resistance required for increased performance, the coarseness of the particles results in a substantially rougher cutting edge, which has a significant negative influence in contributing to overall tool performance.

In PCD tool manufacturing, a PCD disc is cut into inserts using wire electro-discharge machining (known as EDMing) or laser cutting in the manner shown in Fig. 1.9. Then the tips are brazed into the pockets made in tool bodies, trimmed and finished using EDMing, laser cutting, or grinding (polishing). Figure 1.10 shows typical cutting tools with PCD inserts.



**Fig. 1.10** Typical cutting tools with PCD inserts: **a** drill, **b** turning insert, and **c** milling tool cartridge

## 1.4 Research Advances

Although PCD is a relatively new tool material, its application is expanding in an unparalleled pace in the automotive and aerospace industries due to the wide use of challenging work materials combined with machining efficiency requirements imposed by high-speed machining. As a result, a number of problems in the implementation of PCDs are piling up rapidly, and thus require solutions using research advances in the field of machining.

### *1.4.1 Challenges in Tool Life Testing of PCD Tools*

The general mechanisms that govern tool wear of carbide tools are well-known [14]: (1) abrasion, (2) diffusion, (3) oxidation, (4) fatigue, (5) adhesion. The essence of these tool wear mechanisms are well-defined by fundamental research and well documented (for example, Shaw [15], Trent and Wright [16], Astakhov [6]). It is established that one or another mechanism normally prevails in a given machining operation, and thus well-known measures can be taken to reduce tool wear and thus increase tool life [6]. It also allows for the proper selection of the carbide grade and tool geometry, and thus the design of application-specific tools [17]. Unfortunately, no one study has revealed the mechanisms of tool wear of PCD tools. It is pointed out [18] that micro-chipping of the cutting edge due to low toughness of PCD is the prime wear mode [19]. This is particularly true in interrupted cutting of HSAM MMCs, where cutting edges chip readily, and tool consumption is unacceptably high.

Chipping of the cutting edge commonly occurs during the initial stage of an interrupted machining process (common in powertrain veined components such as valve bodies, transmission cases, pump covers, etc.). As these chips accumulate, surface smoothness of the workpiece degrades and burring increases. The composition of conventional PCDs depends on the sintering process by which they are manufactured. Because this process yields unbalanced distributions of diamond particles and a metal catalyst (primarily cobalt), an inverse relationship exists between wear resistance and strength in the tool. Therefore, only very vague recommendations for the selection of PCD grades are available. For example, coarse grades of PCD tools (containing larger diamond particles of 20–30  $\mu$ ) are the most wear-resistant types, but they also have the least strength and toughness. Conversely, fine grades of PCD (normally 5–10  $\mu$ ) tools are very tough, but wear resistance is poor. Because of this performance trade-off, medium grades of conventional PCD tools are typically used to machine aluminum parts. As a result,

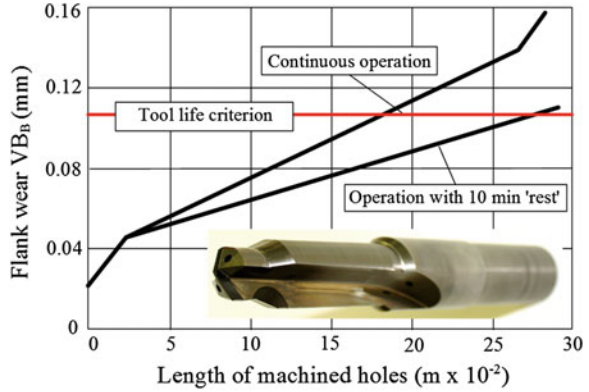
there are no specific recommendations for the selection of a particular PCD grade for a given application. In the automotive industry, a 300–500 % scatter in tool life and unexplained breakage of PCD tools used for similar applications are common. This greatly affects reliability of unattended production lines and manufacturing cells as each premature tool failure results in the scrapping of 10–15 semi-finished parts and up to 30 min line downtime.

In the authors' opinion, which is based on many-years experience in the field, the lack of information on PCD wear mechanisms can be explained by difficulties of conducting experimental studies at universities and R&D facilities. Tool life of carbide tools used in steel machining is measured in minutes. To carry out tool life tests and thus to obtain information on the wear pattern to reveal the wear mechanism, conventional machines, fixtures and inexpensive standard tools are used. A dozen workpieces (normally standard bars) are typically sufficient to complete the study. This is not nearly the case in machining of automotive aluminum alloys with PCD tools where tool life is measured by tens of thousands of parts. A special, expensive high-speed machine with precision bearings (having spindle runout no more than  $0.5 \mu$  at full radial and axial loads with active control and vibration suspensions), special coolants (concentration, filtration, pH, anti-foam and anti-rust additives, etc.), and special non-regrindable cutting tools (cost of a common PCD tool varies from \$1,000 to \$10,000 depending on tool diameters and number of stages) are needed. Each test point requires a new tool. The listed particularities make PCD testing difficult, expensive, time consuming, and thus not feasible in university labs and small R&D facilities.

Unfortunately, the above-listed known mechanisms of wear cannot be modified correspondingly (accounting for the machining conditions and properties of PCD tool material) to reveal wear behavior of PCD. In the author's opinion, the existing theory of wear developed for general machinery cannot be applied in the considered case due to a number of reasons supported by observations of wear behavior of PCDs in machining of HSAM MMCs. Among them, the following two reasons are outstanding:

1. Wear resistance of a PCD insert improves with increasing grain size. This is the opposite of behavior exhibited by any other material used in tribological joints where the wear-resistance improves with decreasing grain sizes of materials in contact. A number of theories of wear are based on this known fact which holds even in metal cutting for carbide and high speed steel tool materials.
2. Tool life of a PCD tool increases when the tool is allowed a 10 min "rest" between drilling successive holes compared to a PCD tool used in an uninterrupted (continuous) operation (5 s for loading/unloading) as it follows from Fig. 1.11. Not one of the known wear mechanisms is able to explain this phenomenon.

**Fig. 1.11** Comparison of tool life (normalized) for a PCD drill used in a continuous operation and a tool used in an operation with 10 min “rest”



**Fig. 1.12** Face milling tool with PCD-tipped cartridges used to represent classification of PCD wear patterns

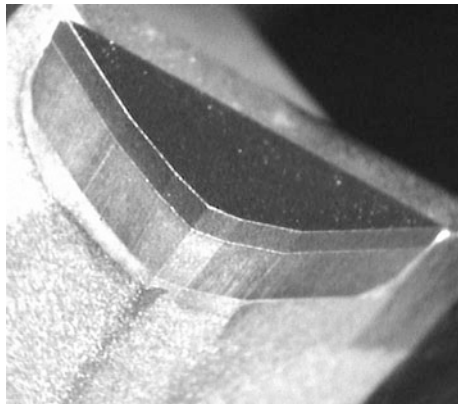


## 1.4.2 Mechanisms of Tool Wear

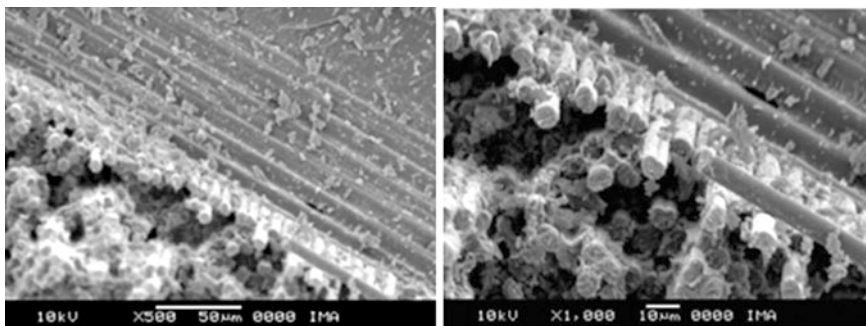
### 1.4.2.1 Macro-Level

A classification of wear patterns of PCD tools is attempted in this chapter in order to help researchers, tool/manufacturing/process engineers and professionals in the field in their assessments of PCD tool quality, wear and operational performance. The face milling tool shown in Fig. 1.12 with PCD-tipped cartridges similar to that shown in Fig. 1.10c is used to represent classification of PCD wear patterns.

Figure 1.13 shows the normal wear pattern of a PCD cartage after completing tool life. Contrary to common perceptions, a detailed microscopic study of this wear pattern shows that when the components of the machining system are coherent and the cutting regime is optimal, chipping does not occur. Rather, a small, pure abrasive-type wear land is the case. This was confirmed with a microscopic study using a scanning-electron microscope (SME).



**Fig. 1.13** Normal wear pattern of a PCD cartridge after completing tool life (15,000 cycles of valve-bodies of a 6-speed automatic transmission, work material—A380)

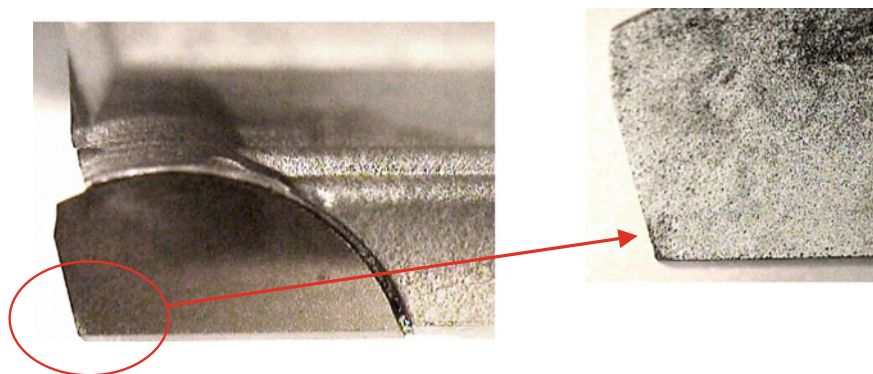


**Fig. 1.14** SME images of the worn surface at two different magnifications

Figure 1.14 shows SME images of the worn surface at two different magnifications. As can be seen, the wear pattern resembles pure abrasion wear with scratches in the direction of the cutting speed.

Figure 1.15 shows the proper wear pattern of a PCD insert obtained when the tool was run at the optimal cutting conditions and tool life of about 200,000 holes in high-silicon aluminum alloy A380. As can be seen, there is no micro-chipping. Rather, a porosity-like structure of tightly-bonded diamond crystals is developed as the catalysis (cobalt) is taken away by aluminum in the sliding chip. In the authors’ opinion, achieving similar wear patterns is the goal in optimization of a machining operation with a PCD tool.

However, the discussed “ideal” wear of PCD tools occurs rather rarely. Problems occur in PCD tool implementations. Such problems originate in their manufacturing and are enhanced by inherent problems of PCD tool material. This chapter discusses some of these problems which are most common in the practice of PCD tool testing and implementation.



**Fig. 1.15** Proper (target) wear pattern of PCD insert

### 1.4.2.2 Microlevel

The scatter in tool life observed in the practice of testing of tool materials of the same composition and bulk properties from different tool material suppliers may reach 300–400 % which is at least an order greater than that for common engineering materials. The existing tool material classifications (within the same type, e.g. cemented carbide and PCD) are too vague, and thus cannot explain this scatter even in principle. For many years, this fact was not noticed in industry as the machining systems were of subpar quality so the tool performance was determined by other components of the machining system rather than the properties of tool materials. The time has changed and so has the quality of machining systems. Many common excuses for poor tool performance were eliminated. As a result, the difference in the tool material of the same grade but from different tool material manufacturers has become more and more noticeable, particularly under challenging applications where tool performance is closely monitored.

If one would attempt to find the difference in the mechanical, physical, chemical, etc. properties of a particular tool material, e.g. a PCD grade, to understand the discussed scatter in tool performance than he or she finds that:

- Only very few, mostly irrelevant to the cutting performance, properties of a particular grade of the tool material are actually available in colorful catalogs of various tool companies.
- Contacting the tool material supplier does not help to answer the questions and/or to resolve the issue with the performance of a particular tool material because: (a) The contactor is not sure what to ask for, and (b) The supplier may not have, or may not willing to reveal, the requested property or properties as they are considered “proprietary information”.

A great number of manufacturing processes and alternatives exist in tool materials manufacturing that may result in the wide range of their performance results although the ingredients of a particular tool material can be absolutely the

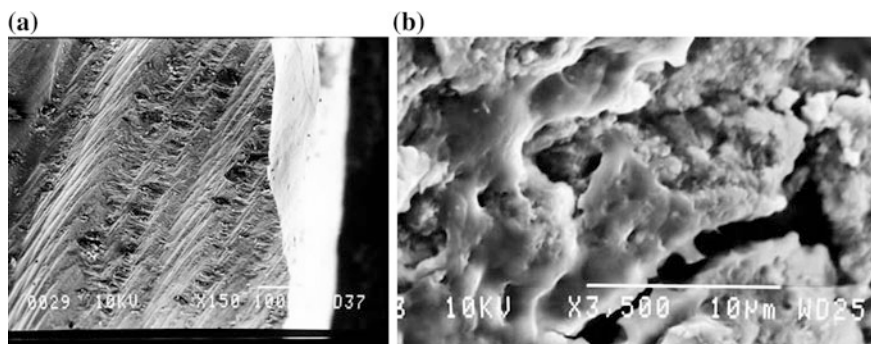


same. The difference in the cost of apparently same tool material from different tool material suppliers can be significant. Moreover, often the bulk mechanical and physical properties of this material are practically the same as reported by various suppliers, so the difference in performance cannot be explained using the known properties and characteristics. As a result, it is rather difficult to justify the higher cost of a tool material of presumable better quality if the reported composition and bulk properties of this material are the same as those of a cheaper one. Unfortunately, many companies do not have time, funding, and sufficiently trained personnel to carry out the full tool life investigation to distinguish the difference in the performance between these two materials so the cheaper tool material is normally selected.

In the authors' opinion, this problem should be solved particularly because the tool materials and cutting tools have become more and more expensive, and because unattended manufacturing is in wider and wider use. To do this, a fresh look at the physics of wear of tool materials should be taken with no blinds imposed by the known mechanisms of wear used in general machinery. This section describes the foundation of such an approach presenting/explaining some known facts and setting the stage for the further research and development on the matter.

Modern tool materials are composite materials so their structure includes at least two distinctive solid phases: extremely hard non-metallic particles (WC, diamond, boron nitride,  $\text{Al}_2\text{O}_3$ , etc.) are held together by the matrix material (for example, cobalt). As these materials are sintered/shaped, great deformation and temperatures are applied, interfacial defects as nano- and microcracks, residual stress and even defects of the atomic structure occur. Microcracking can be attributed to a mismatch of the thermal expansion coefficients between the phases, as well as from thermal expansion anisotropy of the phases.

These defects evolve upon cooling, starting from a stress-free high-temperature state, and specifically in areas with large grain-to-grain misorientation [20]. These defects (examples at different magnifications are shown in Fig. 1.16) lower the



**Fig. 1.16** SME images of surface and internal cracks in the PCD tool material: **a** Surface cracks on a freshly-ground surface. Magnification  $\times 150$ , scale bar is  $100\ \mu$ , and **b** Internal interfacial cracks after tool life run. Magnification  $\times 3,500$ , scale bar is  $10\ \mu$

strength, wear resistance and other useful mechanical and physical properties of tool materials. Moreover, as the population of these defects is of random nature, the great scatter in the performance data is observed in practice. This scatter presents a serious problem in tool materials.

Although inter-granular wear, grain cleavage, peeling and spalling of grains have been suggested as possible wear mechanisms of PCD [21–23], only qualitative descriptions of suggestive nature are normally provided to explain these mechanisms. Moreover, these defects are considered to be formed due to high temperature and stresses in machining while the microdefects due to PCD sintering were not considered. No quantitative characterization of microcracks and their effect on the wear patterns were attempted.

The equation of physical state of solids [20] can be used as the basis to reveal the wear mechanism of PCDs that deals with diamond/diamond interfacial defects (stresses and microcracks) closely coupled in the processes of the generation and propagation of many small cracks occurred at the diamond/cobalt interfaces. However, the role of micro cracking is complex and not well understood on a quantitative basis. Better understanding requires an ability to quantify the crack morphology and how that structure evolves due to stress and temperature fields occurring in metal cutting of high-silicon aluminum alloys.

The complexity and strong coupling of micro cracking to thermal and mechanical properties has been widely recognized [24–27] but is still not well understood and thus correlated with tool wear. Improved understanding is hampered by (a) an inability to quantify micro cracking, (b) limited observations of microcrack array responses to loads, and (c) limited evaluations of the mechanics models which propose to explain the role of microcracks and their role in tool wear mechanisms [28–30]. In the author's opinion, the first and foremost stage in further PCD development should be concerned with the quantification of microcrack structure [31]. Special techniques to classify, count and measure the length, spacing and orientation of microcracks should be developed for PCDs and other tool materials using the available methodologies and test equipment (e.g., the electron channeling contrast methodology using CamScan 44 FE SEM equipped with a Schottky thermal field emission gun [32]). Digital image processing should be applied to take the measurements, thereby providing time effective, reproducible, statistically significant estimates of crack morphology. A key feature of the image processing strategy is to abstract the crack structure to a set of medial axis lines.

As discussed above, abrasive wear is predominant in the practice of PCD applications. Abrasive wear is a phenomenon familiar to all and, like so much which relates to real-life, it is controlled by a subtle interplay of many effects. This makes the task of constructing a generalized model of the process from scratch extremely ambitious. In the author's opinion, this can now be attempted thanks to decades of painstaking research by many workers into different aspects of abrasion and provides the foundation on which a generalized model may be built.

The focus of a new model should be on the interatomic bonds of a solid and their consequences for wear behavior. The theory of the non-equilibrium thermodynamics of solids [20] can be used to understand the response of PCD to forces, heat,

and other energy fields in metal cutting. The internal pressure or stress in PCD is defined as the vector representing the resistance to volume change,  $\mathbf{P} = d\mathbf{F}/ds$ , where  $\mathbf{F}$  is the force of atomic interaction and  $s$  is the surface area enclosing a volume. The thermodynamic equation of state [20]  $PV = s(N, V, T, \mathbf{P})T$ , where  $s$  is the entropy vector and  $P$  is the magnitude of  $\mathbf{P}$ , should be used at the most general level of wear studies. The state of PCD is defined to be the shape of the rotos resulting from the diamond (not PCD) sintering process. A rotos is a closed dynamic cell of solids. The equation of state relates the temperature of the solid structure to its ability to generate resistance forces. Compressions are those atoms located on the decreasing portion of a bond force minimum and provide resistance under heat absorption, and dilatons are those located on the increasing portion to a force maximum and offer resistance in heat radiation. The compression-dilaton pattern of the bonds in a structure determines its response to loads, temperature, and other environmental conditions. Influence on the size effect, stresses, and aging in the wear-resistance response of PCD should be studied accounting for the number of interfacial defects (microcracks and voids) in PCD and the possibility of crack growth and crack coalescence that lead to micro and then to macro chipping of PCD.

The description of dynamic loading and wear due to this loading can be developed from the equation of state to explain the physical nature of the time-dependent response. The increased resistance influences the initiation and propagation of microcracks that, according to this equation, are related to entropy. The thermodynamic potentials of PCDs with varying number of interatomic bonds can then be derived to develop parameters of state using the periodic law of variations in state including mechanical hysteresis and its effects on the dilatons/compressions transformations. The theory of strength in such a development is a generalization of the kinetic theory of strength which postulates that thermal fluctuations are a key in breaking atomic bonds that can be directly correlated with wear. Wear, chipping and fracture are attributed to what is called the Maxwell-Boltzmann factor (from the distribution of energy states), which describes the concentration density and energy of particles in a given region of the solid and which introduces stress-concentrations. Breaking of bonds releases internal energy. Fracture and wear, however, are considered to be thermally dependent processes governed by the intensity of the potential field caused by stress and temperature anisotropy in the presence of dilaton traps.

The first level of the development of such a model uses the equation of physical state of solids [20]. Diffusion self-healing can be briefly explained as follows.

Centuries-old buildings have been said to have survived these centuries because of the inherent self-healing capacity of the binders used for cementing building blocks together. This self-healing capacity has never been termed like that. This is a well-known fact that was seen as the forgiveness of nature rather than self-healing of inherently smart building materials. Today, the field of self-healing is considered a new area of materials research. It was in 2001 that White et al. [33] published their results on self-healing in polymer-based systems by microencapsulated healing agents. This and related research in other fields of materials science was the result

of an initiative by NASA launched amongst selected top institutes in the USA in 1996. Since then the field has been developing rapidly. Because healing presupposes the presence of a defect and a defect generally emerges at a very small scale, probably at the nanoscale, it is not surprising that self-healing is one of the promising application fields of nanotechnology.

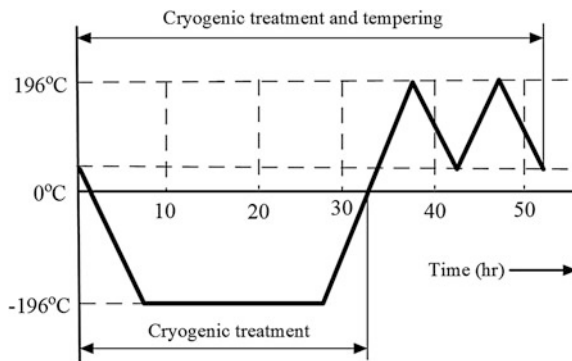
Komarovsky and Astakhov [20] presented the complete theory of diffusion healing of composite materials showing that practically all of these materials can be considered as self-healing materials. A number of advanced methods of self-healing are suggested in this publication. Today our understanding of self-healing materials is as follows. Self-healing materials are man-made materials, which have the built-in capability to repair structural damage autonomously or with some help of an external stimulus (energy fields [20]). The initial stage of failure in materials is often caused by the occurrence of small microcracks/microdefects (even at atomic-molecular scale) throughout the material. The proper characterization of such microdefects can help explain the ranging of tool materials quality formed in their manufacturing so that the cost of better tool materials can be easily and quantitatively justified. The proper application of the external energy fields to enhance diffusion healing of such microdefects in composite tool materials in order to improve their quality should be the goal of the first stage of the development of better tool materials. The next stage can be development of truly self-healing tool materials. In such materials, the occurrence of these microcracks is 'recognized' in some way. Subsequently, mobile species, e.g. atoms, have to be triggered to move to these places and perform their self-healing capacity. These processes are ideally triggered by the occurrence of damage itself, in which case it is called an autonomous self-healing event. In practice one could well imagine self-healing that is triggered by an external stimulus greatly enhances the reliability and durability of tool materials.

The self-healing takes place in machining. For example, tool life of a PCD tool increases when the tool is allowed a 10 min 'rest' between drilling successive holes compared to a PCD tool used in an uninterrupted (continuous) operation (5 s for loading/unloading) as it follows from Fig. 1.11. Not one of the known wear mechanisms is able to explain this phenomenon.

Diffusion healing of tool materials has been known since the 1950s although no one study or other literature source refer to these known treatments as such. This is because such treatments are covered by the generic name "cryogenic treatment". Such a name is misleading as much more complicated thermomechanical processes that involve a combination of deep freezing and tempering cycles. Generally, they can be described as a controlled lowering of temperature from room temperature to cryogenic temperature, maintenance of the temperature for hours, followed by a controlled rising of the temperature. As an example, Fig. 1.17 shows the process diagram of modern cryogenic treatment used to enhance wear resistance of cemented carbides suggested by Gill et al. [34].

The Diffusion© process was developed by Diffusion Ltd. (Windsor ON, Canada) primarily for use in the automotive industry for enhancing and stabilizing properties of the tool materials. This is because severe working conditions and the absence of

**Fig. 1.17** Example of the process diagram of modern cryogenic treatment used to enhance wear resistance of cemented carbides



the so-called safety factor used in the part design can easily contrast the difference in the performance of the original tools and those treated by diffusion. The preliminary testing showed 50–200 % improvement in tool life of various tool materials. Diffusion© process has also been used for improving the performance of structural components of the engines, transmissions, body parts etc. including Canadian NASCAR engines. Preliminary test results showed that the tougher working conditions of a structural component, the greater performance results are achieved due to the treatment.

### ***1.4.3 Casting Defects and PCD Tool Wear/Failure***

Casting defects are principal “enemies” of PCD tools as such tools are very sensitive to these defects. This section attempts to classify the known casting defects and their effects on PCD tool failure.

The casting defects affecting drill performance can be classified as follows:

- Porosity and microinclusions
- Casting cavities
- Macroinclusions

Because the nature of porosity and content of inclusions depends on a particular material, method of casting and many other metallurgical particularities, the further consideration is restricted to HSAM MMCs because they are the materials of choice for many automotive and aerospace parts as well as domestic food and pump part castings. Other applications include components for food handling and marine castings.

Hydrogen is the only gas that is appreciably soluble in aluminum and its alloys. Porosity in aluminum is caused by the precipitation of hydrogen from the melt or by shrinkage during solidification, and most often by a combination of these defects [35]. Dissolution of hydrogen in large amounts in aluminum castings results in

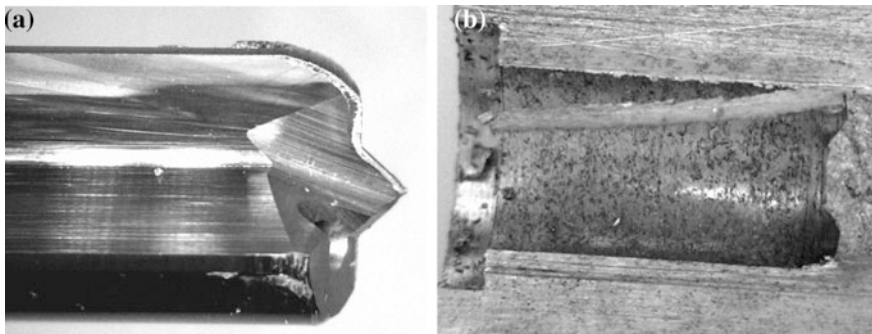
hydrogen gas porosity. For castings that are a few kilograms in weight the pores are usually 0.01–0.5 mm (0.00039–0.020 in) in size [36]. In larger casting they can be up to a millimeter (0.040 in) in diameter. Standard ISO 10049:1992 “Aluminium alloy castings—Visual method for assessing the porosity” specifies a method of inspection and describes the acceptance conditions, tabulates the severity levels, i.e. number and size of pores, and the interpretation of the results.

Pores that form in the matrix of aluminum alloy castings lead to significant deterioration in casting quality. In brief, porosity is formed and distributed in the matrix of the casting. The pore count of aluminum-silicon alloys can be affected by the solidification mode of the alloy, the amount of oxide film and/or particle inclusions, the cooling rate, the atmospheric pressure and the hydrogen level in the melt.

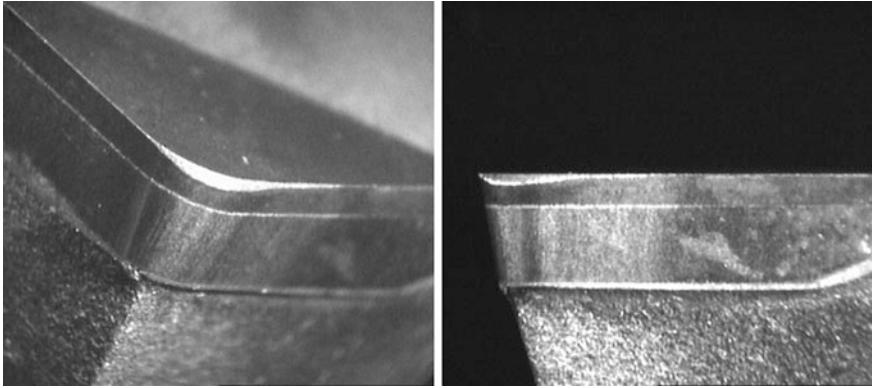
Porosity and porosity-size inclusions present a serious challenge in high-speed machining of HSAM MMCs as a myriad of pores should be thought of as countless number of small sharp razor-type edges enhanced by hard SiC microinclusions. These literally shave the tool when their amount is excessive. It takes its toll heavily on carbide tools. Figure 1.18a shows an example of an excessively worn carbide drill and Fig. 1.18b shows the appearance of severe porosity in the sectioned machined hole. PCD tools, however, can withstand small porosity much better although tool wear is increased. Figure 1.19 shows excessive abrasive wear of a PCD cartage in the presence of casting porosity.

Unfortunately, there is no standard/procedure/methodology for microporosity and microinclusions assessment in terms of their influence on tool wear. As a result, the problem should be dealt with on a case-by-case basis.

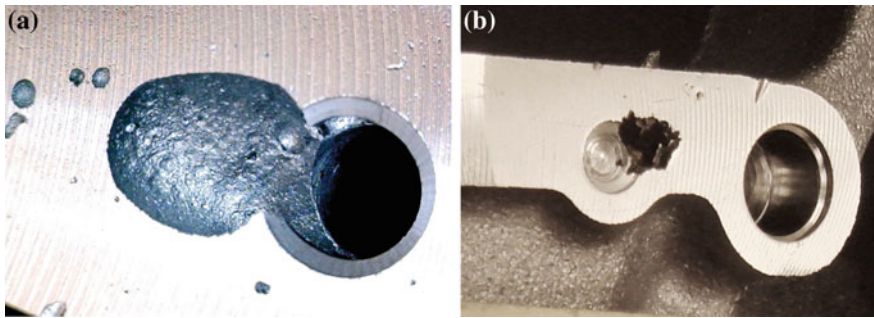
Figure 1.20 shows the appearance of casting cavities and hard inclusions on a milled surface. Casting cavities are large shrinkage cavities. Nonmetallic inclusions are a particular concern in cast aluminum. Because of its reactivity, aluminum oxidizes readily in liquid and solid states. Oxidation rate is greater at molten metal temperatures and increases with temperature and time of exposure. Magnesium in aluminum alloys oxidizes and with time and temperature reacts with oxygen and



**Fig. 1.18** Excessive abrasive wear of a carbide drill due to casting porosity: **a** Appearance of a worn drill, **b** Appearance of severe porosity in the sectioned machined hole



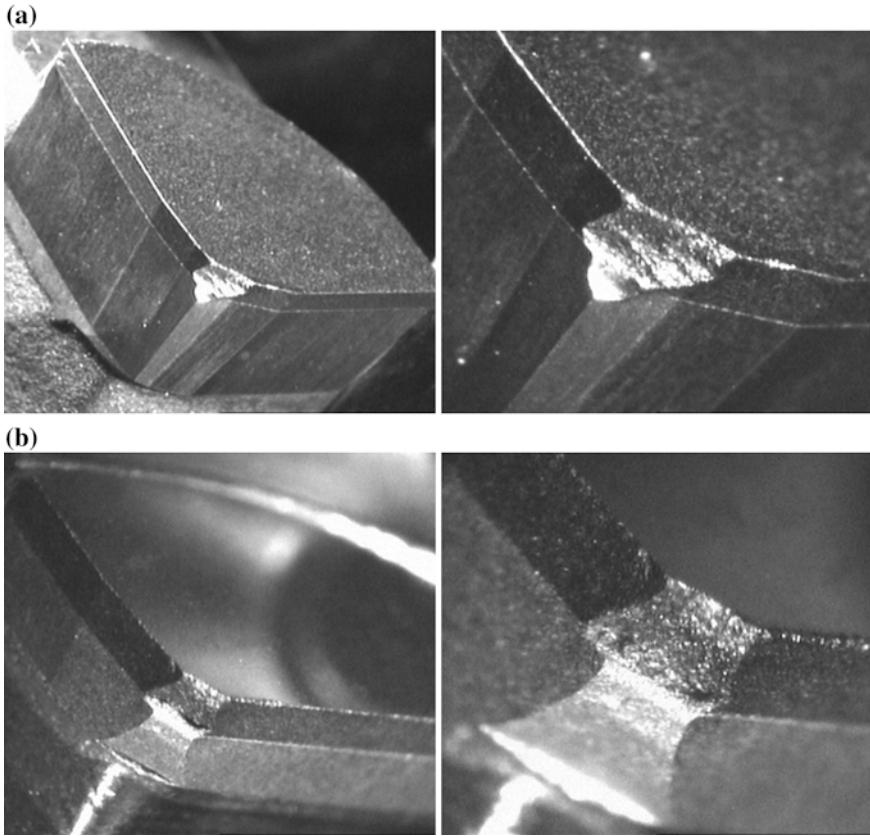
**Fig. 1.19** Excessive abrasive wear of a PCD cartage in the presence of casting porosity



**Fig. 1.20** Appearance of casting defects on the milled surface: **a** casting cavities **b** hard inclusion

aluminum oxide to form spinel. Many oxide forms display densities similar to that of molten aluminum and sizes that reduce the effectiveness of gravimetric separation. Also, most oxides are wet by molten aluminum, reducing the effectiveness of mechanical separation methods. Inclusions occur as varying types with differing sizes and shapes. Aluminum oxides are of different crystallographic or amorphous forms as films, flakes, and agglomerated particles. Magnesium oxide is typically present as a fine particulate. Spinel can be small, hard nodules or large complex shapes.

Surprisingly, PCD tools can handle casting cavities and inclusions much better than carbide tools. However, it is true only for relatively small cavities and inclusions. When the size of these defects increases, PCD inserts are chipped. Figure 1.21a shows chipping of the PCD insert within the PCD layer that happens when the size of defects just exceed what the PCD tool material can handle. Further increases in the size of the discussed casting defects lead to a bulk fracture of PCD inserts through the carbide substrate (Fig. 1.21b).



**Fig. 1.21** Chipping of the PCD insert: **a** within the PCD layer, and **b** through the PCD layer and carbide substrate

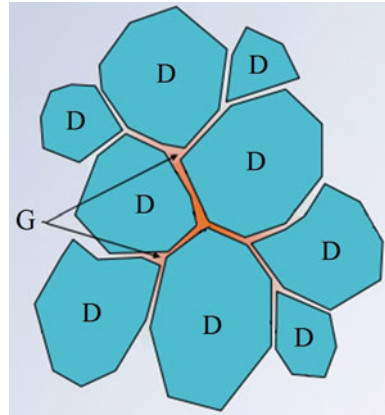
#### ***1.4.4 Thermal Stability as the Weakest Link of Conventional PCDs***

The structure and the origin of strength/hardness of PCD is principally different compared to other tool materials as, for example, cemented carbide. On HPHT sintering of PCD, cobalt acts as a catalyst. It is recognized that this catalytic effect promotes diamond-to-diamond bonds and unitized the diamond layer to the sintered carbide substrate. The result is an abrasion-resistant tool material suitable for machining use. This explains why coarse-grained PCD grades have greater strength and abrasion resistance as such grades have larger areas of diamond-to-diamond interfaces. Formed on HPHT sintering of PCD, the integrity of diamond-to-diamond interfaces should be preserved during PCD tool manufacturing and use.

The major, though not fully recognized and thus not accounted for, problem is that PCD has limited thermal resistance. At atmospheric pressure, a surface of



**Fig. 1.22** Showing graphitization (*G*) of diamond (*D*) crystals boundaries in the presence of high temperature

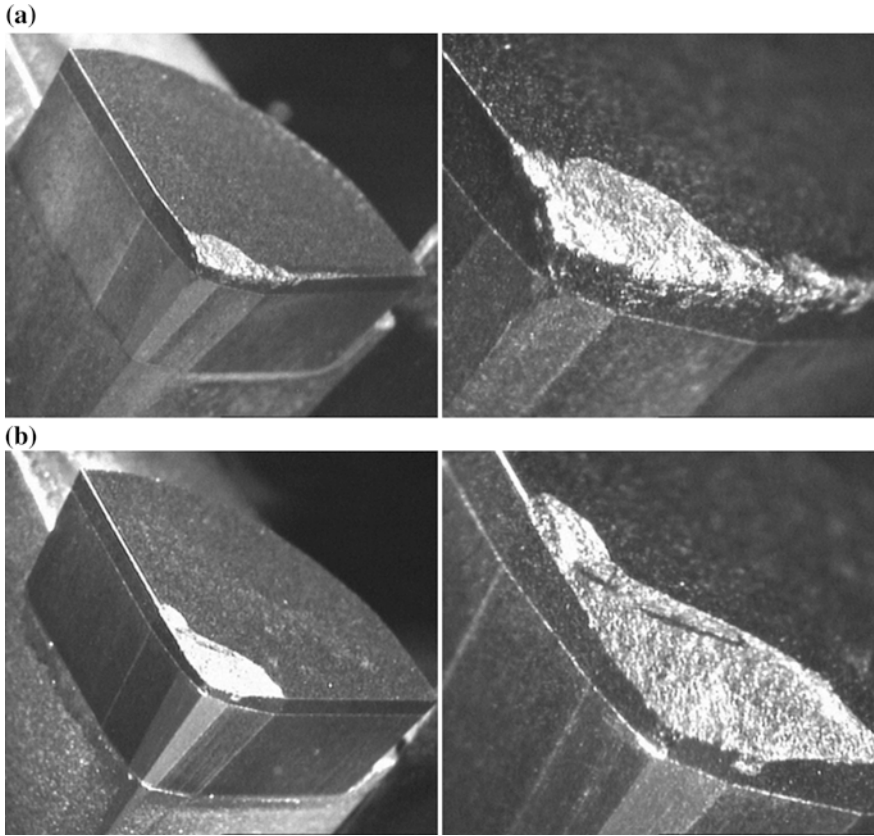


diamond turns to graphite at 900 °C. In a vacuum or inert gas, diamond does not graphitize easily, even at 1,400 °C. But during use, PCD cutters experience a sharp decline in tool performance when they experience temperatures around 700 °C in their manufacturing and/or machining.

The presence of cobalt is the major reason that PCD converts to graphite at a lower temperature than simple diamond. Thermal degradation occurs due to the presence of cobalt in the interstitial regions and the adherence of cobalt to the diamond crystals. Specifically, cobalt is known to cause an undesired catalyzed phase transformation in diamond (converting it to carbon monoxide, carbon dioxide, or graphite) with increasing temperature [37–40]. As temperature increases, graphitization of the diamond in the presence of cobalt becomes a dominant effect. PCD wear is then due to allotropic transformation into graphite or amorphous carbon under influence of cutting force and cutting temperatures. This transformation is accelerated in the presence of cobalt through a combination of mechanical and chemical effects. Figure 1.22 shows a schematic representation of this process.

The second significant cause of thermal degradation of PCDs is a significant difference between the thermal expansion coefficients of cobalt and diamond. Thermal degradation due to differential thermal expansion characteristics between the interstitial catalyst material and the intercrystalline bonded diamond. Such differential thermal expansion is known to occur at temperatures of about 400 °C, causing ruptures to occur in the diamond-to-diamond bonding, and resulting in the formation of cracks and chips in the PCD structure. Chipping and micro-cracking of cutting edges occur as a result [41–43].

These issues limit practical use of conventional PCD tool materials to about 700 °C. This fact presents a significant yet not fully understood, and thus recognized problem, in PCD tool manufacturing and implementation practices. While high temperatures may occur in cutting at high cutting speeds and feeds, it is not likely that it occurs in many cases of machining of high thermal conductivity work material (e.g., aluminum alloys) with high-flow rate water-based coolant supplied



**Fig. 1.23** Results of tool overheating in its manufacturing: **a** plastification of PCD layer, and **b** flaking

through tools. If this was the case, all PCD tools would fail. This is not the case as most of the tools complete tool life.

Therefore, the thermal damage to PCD inserts likely occurs during PCD tool manufacturing. The critical manufacturing operations in terms of thermal damage to PCD are brazing, EDMing and grinding because temperatures generated during these operations can be well above  $700^{\circ}$ . Figure 1.23 shows some results of tool overheating in its manufacturing.

### ***1.4.5 Developing Thermal Stable Grades***

The technologies to manufacture a two-layer composite of diamond-containing/cemented tungsten carbide substrate which has a combination of high wear

resistance and high thermostability are under active development. Up to date, attempts to improve thermal stability of PCD and thus to manufacture thermally stable PCD (TSPCD), can be generally classified as:

1. Removal of the catalyst/solvent phase from the PCD material, either in the bulk of the PCD layer or in a volume adjacent to the working surface of the PCD tool (where the working surface typically sees the highest temperatures in the application because of friction events). This is commonly known as cobalt leaching.
2. Two-step sintering.
3. Use of a ceramic matrix material such as SiC as the catalysis.

#### 1.4.5.1 Cobalt Leaching

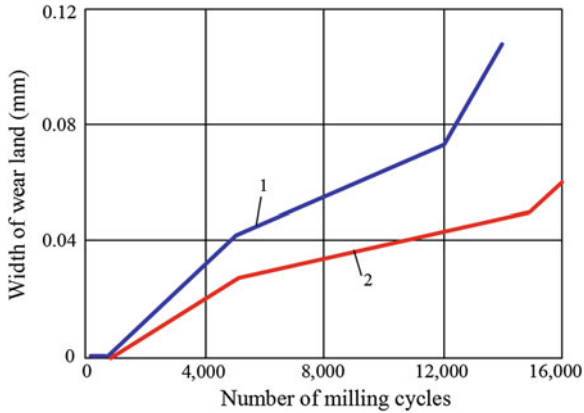
As a means of improving PCD thermal resistance, polycrystalline diamonds have been created that are not bound to metallic base material, i.e. the matrix metal is completely removed by post-process treatments. Although the resultant material can withstand temperatures up to 1,200 °C, it lacks sufficient hardness and impact strength to be used as a cutting tool material. This is due to cavities that remain in the PCD after the catalyst (matrix) metal is removed.

As an alternative, another technology called cobalt leaching has been developed. The essence of cobalt leaching is as follows (U.S. Pat. Nos. 4,224,380 and 4,288,248). After finishing the PCD conventionally, the metallic phase can be removed from the compact by acid treatment, liquid zinc extraction, electrolytic depleting or similar processes, leaving a compact of substantially 100 % abrasive particles. Cobalt is removed up to 200  $\mu$  deep into the PCD layer. As the cobalt phase remains inside the PCD layer, the loss of overall strength is not as significant as with other methods of TSPCD manufactured using other known methods.

Leaching a thin layer at the working surface dramatically reduces diamond degradation and improves the tool's thermal resistance. First, with no cobalt, the diamond-to-diamond bonds remain strong as little graphitization and cracking due to a mismatch of thermal expansion properties occurs at high processing and cutting temperatures. Second, the heat conduction of the contact diamond surface increases, thus the heat is transmitted faster from the tool-chip and tool-workpiece that lowers the maximum cutting temperature.

Figure 1.24 shows wear curves for leached and a non-leached PCD cartridges. As can be seen, after about 12,000 cycles, the wear rate of the unleached cutter increased dramatically. The leached PCD cutter, in contrast, maintained a relatively constant wear rate for about 15,000 cycles.

There are several important issues associated with this approach (cobalt leaching) to achieving improved thermal stability. The prime concern is that a continuous network of empty pores result from the leaching, possessing a substantially increased surface area, which can result in increased vulnerability to oxidation



**Fig. 1.24** Wear curve for: (1) conventional PCD, and (2) leached PCD. Cutting conditions: face milling with the tool shown in Fig. 1.12, work material A380, cutting speed—930 m/min, cartridge tool-in-holder rake angle— $0^\circ$ , normal clearance angle— $10^\circ$ ,  $20\text{-}\mu$  PCD grade

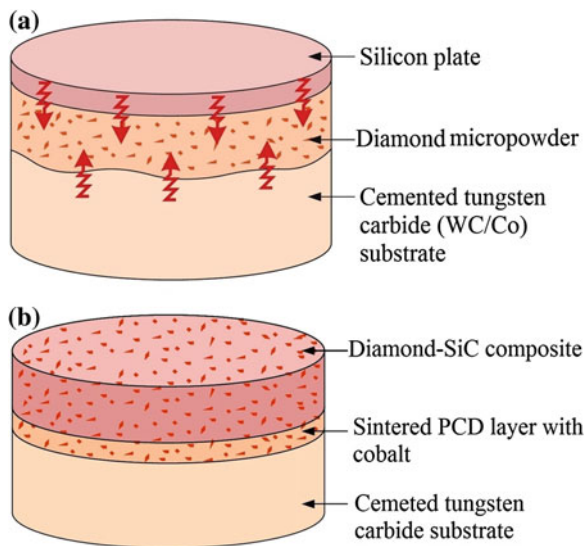
(particularly at higher temperatures). This can then result in reduced strength of the PCD cutter at high temperatures. The second concern is the time needed for leaching, and thus its cost. For example, according to US Patent No. 4,288,248, between 8 and 12 days and strong chemicals are used, e.g., concentrated hot acid solutions.

#### 1.4.5.2 Two-Step Sintering

Two-step sintering results in the formation of a bi-layered sintered PCD disc which includes a thermally stable top layer. According to US Patent No. 4,944,772, a leached PCD compact and a cemented carbide support are separately formed. An interlayer of unsintered diamond crystals (having a largest dimension of  $30\text{--}500\ \mu\text{m}$ ) is placed between the carbide and TSPCD layer. A source of catalyst/sintering aid material is also provided in association with this layer of interposed crystals. This assembly is then subjected to the HPHT process, sintering the interlayer and bonding the whole into a bi-layered supported compact. In this application, appreciable re-infiltration of the TSPCD layer is not seen as advantageous, but the requirement for some small degree of re-infiltration is recognized in order to achieve good bonding.

The method according to US Patent No. 5,127,923 is an improvement to this approach, where a porous TSPCD layer is reattached to a carbide substrate during a second HPHT cycle, with the provision of a second “inert” infiltrant source adjacent to the surface of the TSPCD compact removed from the substrate. Infiltration of the TSPCD body with this second infiltrant prevents significant re-infiltration by the catalyst metal of the carbide substrate. When carefully chosen, it does not compromise the thermal stability of the previously leached body. A suitable infiltrant,

**Fig. 1.25** Starting and finishing stages of structure formation of thermally stable PCD blanks in HPHT-sintering: **a** start of infiltration of the diamond layer from one side by liquid Si and from other side by Co-WC-C melt, **b** finished three-layered composite—top cutting layer is a thermally stable diamond-SiC composite



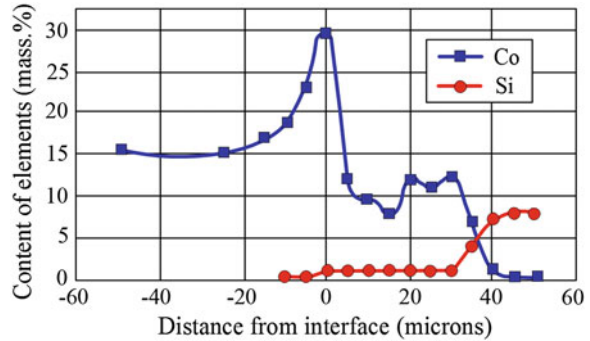
such as silicon for example, must have a melting point lower than that of the substrate binder.

The disadvantage of the bi-layer sintered PCD is the formation of high internal stresses because of the significant differences in properties between the leached/porous layer, the underlying sintered PCD, and carbide substrate. This is exacerbated by the mono-lithic nature of the leached compact and often causes cracking at the PCD-substrate interface or through the PCD layer itself during the second HPHT cycle. Furthermore, the reattachment process itself can be difficult to control such that appreciable re-infiltration of the TSPCD layer does not occur during the second HPHT cycle. Moreover, multi-step sintering processes are both time consuming and labor intensive. It is, therefore, desired that a thermally stable PCD material be developed in a relatively simple single-step manufacturing process.

This ambitious goal can be achieved if two catalyst metals are used simultaneously in the HPHT process. Figure 1.25 shows the model of the HPHT sintering method with double-sided infiltration of diamond micropowder by molten silicon and Co-WC-C melt from cemented tungsten carbide substrate. By changing the pressure and heating rate, this method allows a change in the size of intermediate polycrystalline diamond-Co layer [44].

The SME and X-ray diffraction microanalysis of the structure of the produced samples have shown that a thin transition zone containing 8–12 % cobalt forms between the carbide substrate and the diamond layer during the sintering as shown in Fig. 1.26. The thickness of the transition zone approximately corresponds to the particle size of the initial diamond powder, i.e. the cobalt melt penetrates into the diamond layer to a depth of no more than 40  $\mu\text{m}$ . The amount of cobalt at the carbide-transition zone interface is essentially higher than in the substrate. At a distance of

**Fig. 1.26** Concentration of chemical elements in the sample axial section at the interface between the WC-15 %Co substrate and diamond layer



above 40  $\mu\text{m}$  from the substrate the diamond layer exhibits no cobalt. Free silicon is also not observed and this is supported by X-ray diffraction analysis.

The test results showed considerable increases in tool life (up to 2 times), allowable penetration rate (by 30 %) and thermal stability (up to 1,100  $^{\circ}\text{C}$ ) of the cutters including the thermal stable inserts manufactured using this method.

## References

1. Shin YC, Dandekar C (2012) Mechanics and modeling of chip formation in machining of MMC. In: Davim JP (ed) *Machining of metal matrix composites*. Springer, London, pp 1–50
2. Hung NP, Boey FYC, Khor KA, Phua YS, Lee HF (1996) Machinability of aluminum alloys reinforced with silicon carbide particulates. *J Mater Process Technol* 56(1–4):966–977
3. Andrewesa CJE, Feng H-Y, Laub WM (2000) Machining of an aluminum/SiC composite using diamond inserts. *J Mater Process Technol* 102(1–3):25–29
4. El-Gallab M, Sklad M (1998) Machining of Al/SiC particulate metal matrix composites. Part I. Tool performance. *J Mater Process Technol* 83(2):151–158
5. Tomac N, Tonnessen K (1992) Machinability of particulate aluminum matrix composites. *CIRP Ann Manuf Technol* 41:55–58
6. Astakhov VP (2006) *Tribology of metal cutting*. Elsevier, London
7. Zorev NN (1966) *Metal cutting mechanics*. Pergamon Press, Oxford
8. Astakhov VP (1998/1999) *Metal cutting mechanics*. CRC Press, Boca Raton
9. Hannay JB (1879) On the artificial formation of the diamond. *Proc R Soc Lond* 30 (200–205):450–461
10. Royère C (1999) The electric furnace of Henri Moissan at one hundred years: connection with the electric furnace, the solar furnace, the plasma furnace? *Ann Pharm Fr* 57(2):116–130
11. Moissan H (1994) Nouvelles expériences sur la reproduction du diamant. *C R Acad Sci Paris* 118:320–341
12. Davis RF, Films Diamond (1993) *Diamond films and coating*. Noyes Publications, Park Ridge
13. Uehara K, Yamaya S (1988) High pressure sintering of diamond by cobalt infiltration. *Int J Refract Met H* 7(4):219–223
14. Astakhov VP, Davim PJ (2008) Tools (geometry and material) and tool wear. In: Davim PJ (ed) *Machining: fundamentals and recent advances*. Springer, London, pp 29–58
15. Shaw MC (2004) *Metal cutting principles*, 2nd edn. Oxford University Press, Oxford
16. Trent EM, Wright PK (2000) *Metal cutting*, 4th edn. Butterworth-Heinemann, Woburn

17. Astakhov VP (2010) Geometry of single-point turning tools and drills. Fundamentals and practical applications. Springer, London
18. Stenphenson DA, Agapiou JS (1996) Metal cutting theory and practice. Marcel Dekker, New York
19. El-Gallab M, Sklad M (2000) Machining of Al/SiC particulate metal matrix composites. Part III. Comprehensive tool wear models. *J Mater Process Technol* 101:10–20
20. Komarovskiy AA, Astakhov VP (2002) Physics of strength and fracture control: fundamentals of the adaptation of engineering materials and structures. CRC Press, Boca Raton
21. Miklaszewski S, Zurek M, Beer P, Sokolowska A (2000) Micromechanism of polycrystalline cemented diamond tool wear during milling of wood-based materials. *Diam Relat Mater* 9 (3–6):1125–1128
22. Bai QS, Yao YX, Bex P, Zhang D (2004) Study on wear mechanisms and grain effects of PCD tool in machining laminated flooring. *Int J Refract Met Hard Mater* 2–3:111–115
23. Philbin P, Gordon S (2005) Characterisation of the wear behaviour of polycrystalline diamond (PCD) tools when machining wood-based composites. *J Mater Process Technol* 162–163:665–672
24. Ortiz M, Suresh S (1993) Statistical properties of residual stresses and inter-granular fracture in ceramic materials. *J Appl Mech* 60:77–84
25. Evans AG (1978) Microfracture from thermal expansion anisotropy—I. *Acta Metall* 26:1845–1853
26. Evans AG, Fu Y (1985) Some effects of microcracks on the mechanical properties of brittle solids—II. Microcrack toughening. *Acta Metall* 33(8):1525–1531
27. Laws N, Lee JC (1989) Microcracking in polycrystalline ceramics: elastic isotropy and thermal anisotropy. *J Mech Phys Solids* 37(5):603–618
28. Yousef SG, Rodel J, Fuller ER Jr, Zimmermann A, El-Dasher BS (2005) Microcrack evolution in alumina ceramics: experiment and simulation. *Am Ceram Soc* 88(10):2809–2816
29. Kim BN, Naitoh H, Wakayama S, Kawahara M (1996) Simulation of microfracture process and fracture strength in 2-dimensional polycrystalline materials. *JSME Int J* 39(4):548–554
30. Kim BN, Wakayama S (1997) Simulation of microfracture process of brittle polycrystals: microcracking and crack propagation. *Comput Mater Sci* 8:327–334
31. Yurgartis SW, MacGibbon BS, Mulvaney P (1992) Quantification of microcracking in brittle-matrix composites. *J Mater Sci* 27:6679–6686
32. Crimp MA (2006) Scanning electron microscope imaging of dislocations in bulk materials, using electron channeling contrast. *Microsc Res Tech* 69:374–381
33. White SR, Sottos NR, Moore J, Geubelle P, Kessler M, Brown E, Suresh S, Viswanathan S (2001) Autonomic healing of polymer composites. *Nature* 409:794–797
34. Gill SS, Singh R, Singh H, Singh J (2009) Wear behavior of cryogenically treated tungsten carbide inserts under dry and wet turning conditions. *Int J Mach Tools Manuf* 49:256–260
35. Zolotarevsky VS, Belov NA, Glazoff MV (2007) Casting aluminum alloys. Elsevier, Oxford
36. Chen Y-J (2009) Relationship between ultrasonic characteristics and relative porosity in Al and Al-XSi alloys. *Mater Trans* 50(9):2308–2313
37. Cook MW, Bossom PK (2000) Trends and recent developments in the material manufacture and cutting tool application of polycrystalline diamond and polycrystalline cubic boron nitride. *Int J Refract Metal Hard Mater* 18:147–152
38. Coelho RT, Yamada S, Aspinwall DK, Wise MLH (1995) The application of polycrystalline diamond tool materials when drilling and reaming aluminium based alloys including MMC. *Int J Mach Tool Manuf* 35:761–774
39. Fedoseev DV, Vnukov SP, Bukhovets VL, Anikin BA (1986) Surface graphitization of diamond at high temperatures. *Surf Coat Technol* 28:207–214
40. Shimada S, Tanaka H, Higuchi M, Yamaguchi T, Honda S, Obata K (2004) Thermo-chemical wear mechanism of diamond tool in machining of ferrous metals. *CIRP Ann Manuf Technol* 53:57–60
41. Miess D, Rai G (1996) Fracture toughness and thermal resistance of polycrystalline diamond compacts. *Mater Sci Eng A* 209:270–276

42. Vandembulcke L, De Barros MI (2001) Deposition, structure, mechanical properties and tribological behavior of polycrystalline to smooth fine-grained diamond coatings. *Surf Coat Technol* 146–147:417–424
43. Chen Y, Zhang LC, Arsecularatne JA (2007) Polishing of polycrystalline diamond by the technique of dynamic friction. Part 2: material removal mechanism. *Int J Mach Tool Manuf* 47:1615–1624
44. Osipov AS, Bondarenko NA, Petrusha IA, Mechnik VA (2010) Drill bits with thermostable PCD inserts. *Diam Tooling J* 3:31–34



# Chapter 2

## Analysis of Orthogonal Cutting Experiments Using Diamond-Coated Tools with Force and Temperature Measurements

Robert Ivester, Eric Whitenton, Jill Hershman, Kevin Chou and Qiang Wu

**Abstract** Two dimensional (2D) orthogonal cutting experiments using diamond-coated tools were conducted with forces and tool-tip temperatures measured by dynamometry and infrared thermography, respectively. The objective of this study was to analyze cutting parameter effects on process behavior in diamond-coated tool machining. Special cutting tools and workpieces were prepared to realize orthogonal cutting. The specific cutting energy and the ratio of forces in the normal and cutting directions increased with decreasing uncut chip thickness. The tool temperatures generally increase with the uncut chip thickness. The specific cutting energy decreases slightly with the increase of the cutting speed. The tool temperatures increase significantly with the cutting speed, but level off at a higher cutting speed, 5 m/s. The effect of increasing the edge radius was to increase the specific cutting energy and the force ratio. The tool temperatures were lowest at the middle edge radius value and increase at both the smaller and larger edge radii.

---

R. Ivester · E. Whitenton  
Engineering Laboratory, National Institute of Standards and Technology,  
Gaithersburg, MD, USA

J. Hershman · K. Chou (✉)  
Mechanical Engineering Department, The University of Alabama,  
Tuscaloosa, AL, USA  
e-mail: kchou@eng.ua.edu

Q. Wu  
Global Holmaking Systems Engineering, Kennametal Inc., Latrobe, PA, USA

## 2.1 Introduction

Synthetic polycrystalline diamond (PCD), made by high-pressure high-temperature sintering, is commonly used in the manufacturing industry to machine non-ferrous materials because of its exceptional mechanical and tribological properties.<sup>1</sup> Increased uses of lightweight high-strength components and demands of dry machining have also promoted practices of diamond tools. However, processing and fabrications of PCD tools are of high cost. On the other hand, advanced surface engineering technologies such as chemical vapor deposition (CVD) have been widely explored for wear resistant applications including cutting tools [1, 2]. There have been numerous advancements and studies of coating tools for machining, e.g., [3–5]. In addition, coating has an advantage in fabrications of tools with complex geometry. Diamond coatings, again owing to their extreme properties, have been investigated for cutting tool applications.

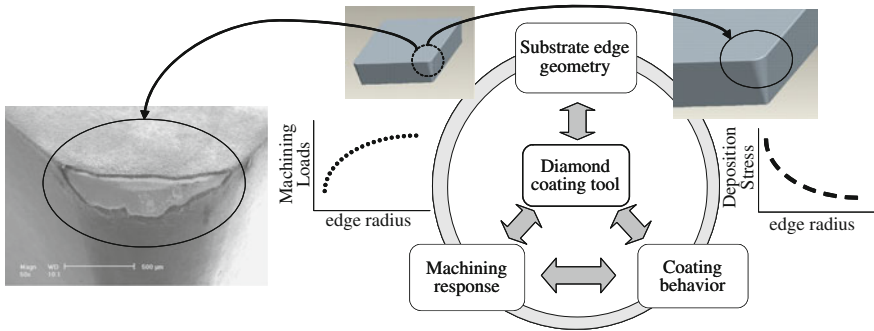
However, current practices for diamond coating cutting tools use off-the-shelf tools as substrates without any consideration of tool edge geometry or the effects of coating properties on machining. To effectively use diamond coated tools, it is necessary to understand the stress modifications around the tool edge due to the deposition process and during machining. Finite element simulations of machining processes have been advanced to study various aspects such as chip formation and cutting forces. On the other hand, there is a gap between the coating process/attributes and machining applications from the tool geometry perspective. Figure 2.1 shows the relations between the tool edge geometry, coating properties, and machining response in diamond-coated tools. In particular, the cutting edge radius has conflicting effects on deposition stresses resulting from mismatched thermal expansions and on thermomechanical loading induced during machining.

A previous study [6] has demonstrated that the cutting edge radius plays a crucial role on the performance of diamond-coated cutting tools, and further, the effect strongly depends upon machining conditions. It is found that by increasing the edge radius from 5 to 65  $\mu\text{m}$ , the tool life of diamond-coated tools can be extended over five times in low-speed, high-feed machining conditions [6]. It is argued that the residual stress from diamond depositions at the coating-substrate interface, in particular, a normal tensile radial stress, results in poor adhesion. A sharp edge will inherit a high residual stress because of stress concentration, and thus, a more rounded edge may be favorable from coating adhesion consideration.

In an earlier numerical study [7], orthogonal cutting simulations with a diamond-coated tungsten carbide (WC) tool were developed to include residual stresses in the tool from depositions. The numerical study investigated the combined

---

<sup>1</sup> Commercial equipment is identified in order to adequately specify certain procedures. In no case does such identification imply recommendation or endorsement by the National Institute of Standards and Technology, nor does it imply that the materials or equipment are necessarily the best available for the purpose. Official contribution of the National Institute of Standards and Technology; not subject to copyright in the United States.



**Fig. 2.1** Conceptual illustration of the edge-geometry importance to diamond-coated tools for machining

deposition and machining effects on the thermal and mechanical states of diamond-coated tools in 2D cutting. In particular, the role of the edge radius was emphasized because of its impact on the resultant interface stresses at different cutting conditions. First, finite element (FE) modeling was used to evaluate the deposition stresses in tools. Second, the tool with deposition stresses was imported into FE software to continue cutting simulations with different cutting conditions. The coating-substrate interface stresses were further analyzed. The stress/strain and temperature fields of a diamond coated tool were analyzed, with the tool edge geometry, the coating thickness, and cutting parameters (cutting speed and uncut chip thickness) investigated. The interfacial stresses were extracted and compared to examine tool and process parameter effects.

In the work described in this paper, a special 2D cutting test-bed at NIST was utilized to conduct a set of machining experiments using specially prepared diamond-coated cutting tools. The test-bed is capable of measuring cutting force and tool temperature distribution. The objective of this work is to investigate the effect of cutting parameters in diamond-coated tool machining through analysis of experimentally measured process behavior and comparison to numerical studies.

## 2.2 Experimental Details

### 2.2.1 Cutting Tool Preparations

The substrates used for diamond coating experiments were grooving type inserts (A4G-U-B-6) from Kennametal Inc. The insert material selected was fine-grain WC with 6 % cobalt by weight (K68 from Kennametal). Three levels of edge radii were selected for evaluations. The edge radius of cutting inserts prior to coating was measured by a commercial white-light interferometer with a  $0.5\times$  objective lens. Measurement results indicate that the uncoated average edge radii were: 5, 25, and

50  $\mu\text{m}$ , with a  $k = 2$  expanded measurement uncertainty of 1  $\mu\text{m}$ . To facilitate temperature distribution measurements, the side relief surface near the cutting edge was precision-ground flat and perpendicular to the cutting edge.

For the coating process, diamond films were deposited using a high-power microwave plasma-assisted CVD process. A gas mixture of methane in hydrogen was used as the feedstock gas. Nitrogen, maintained at a certain ratio to methane, was inserted into the gas mixture to obtain nanostructures by preventing cellular growth. The nominal pressure was 12 kPa and the nominal substrate temperature was 800 °C. The coated inserts were further inspected by the interferometer to measure the edge radius and to estimate the coating thickness. The coating thicknesses of 20 and 25  $\mu\text{m}$  increased the final edge radii accordingly. The average surface roughness,  $R_a$ , of the tools after cutting was approximately 0.5  $\mu\text{m}$ .

### **2.2.2 Workpieces**

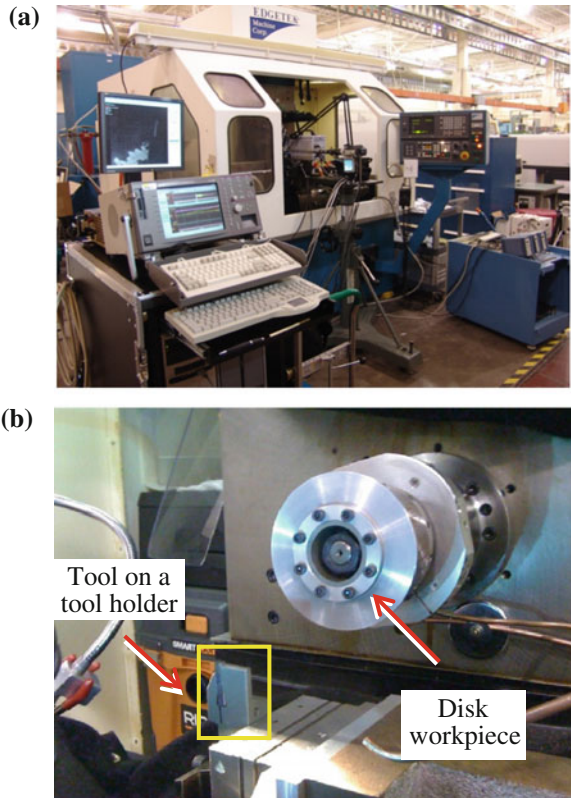
The workpieces were thin disks (127 mm diameter, 3 mm thick) precision machined from a bar stock made of A356 aluminum alloy that was cast and heat treated. The FE cutting simulations used material properties for this particular alloy as reported in the literature [8].

The 2D cutting test-bed was modified from a computer numerical control (CNC) super-abrasive machining center with the addition of multiple sensors. Figure 2.2a shows the machine and Fig. 2.2b shows the cutting tool and workpiece arrangement in the machine. Figure 2.3 depicts (a) the setup of a diamond-coated tool and the disk-shaped workpiece and (b) the side view of a diamond-coated tool tip. A digital oscilloscope records the dynamometer signals at a sampling rate of 2 MHz before down-sampling to 500 Hz for analysis. A high-speed visible light camera (shutter speed of 30,000 frames per second (fps), integration time of 33  $\mu\text{s}$ ) and a medium-speed infrared camera (600 fps shutter speed, 10–25  $\mu\text{s}$  integration time, 3–5  $\mu\text{m}$  wavelength) simultaneously record the cutting process. The disk-shaped workpiece rotates on the horizontal spindle and moves on a vertical axis (feed direction). Synchronizing the dynamometer, visible light camera, and infrared camera signals by reading each signal with an oscilloscope at 2 MHz sampling rate provides confidence the signals represent nearly identical instances in time. The detail of machine and instruments can be found in [9].

### **2.2.3 Testing Parameters**

The toolholder used was A4SML 160624, 25.4 mm steel shank holder. The resulting nominal cutting geometry was 7° of rake angle and 4° of relief angle. The uncut chip thickness (h) values were 0.05, 0.15 and 0.30 mm. The cutting speed (V) tested included 2, 5, and 10 m/s. The linear cutting length was over five revolutions

**Fig. 2.2** **a** 2D orthogonal cutting test-bed, and **b** workpiece and tool arrangement in the machine

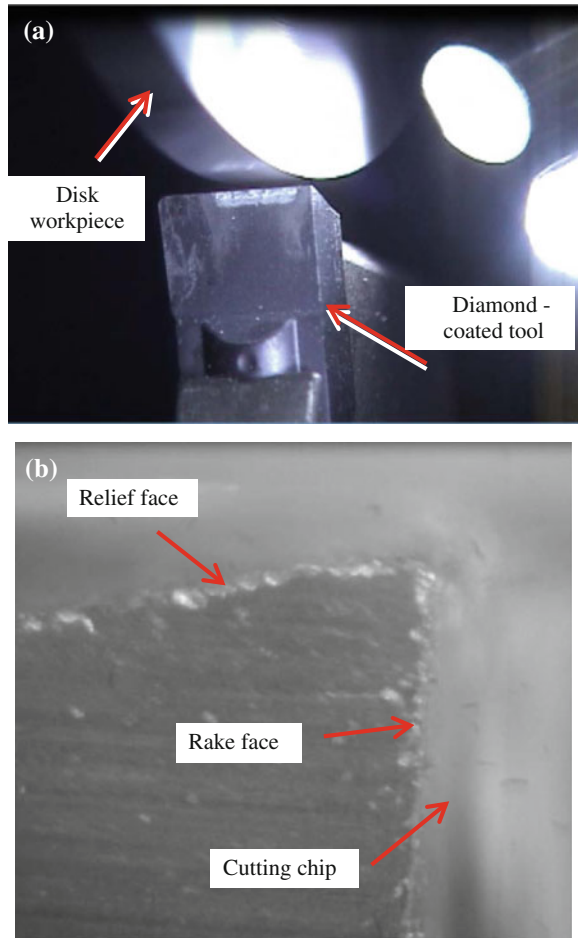


to ensure realization of the full uncut chip thickness. Machining was conducted at room temperature without coolant. In each cutting test, cutting forces and tool temperatures were acquired and further analyzed using MATLAB scripts developed at NIST [10]. For infrared temperature measurements, the emissivity of diamond-coated tools was determined by heating up the tools to a range of temperatures while simultaneously measured by a thermocouple and the infrared camera. The emissivity was between 0.72 and 0.79 ( $k = 2$  expanded measurement uncertainty of 0.02) for the temperature range of 150–200 °C. Linear extrapolation was used for the temperature range outside of the emissivity testing range.

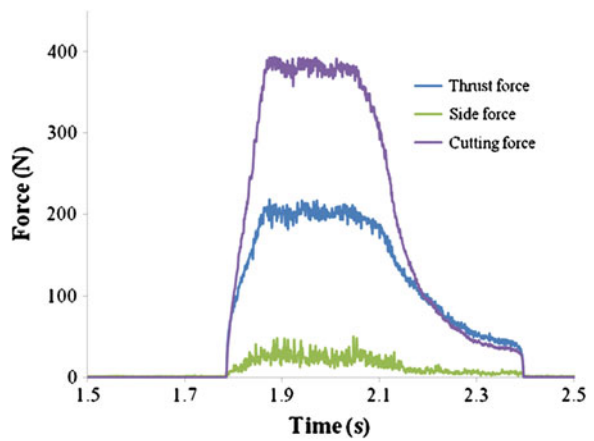
### 2.3 Results and Discussion

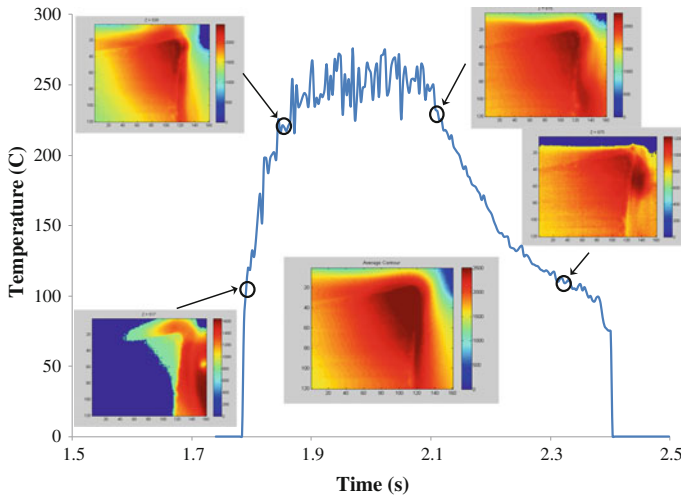
The post-processed data from the experiments were plotted and compared. The section below presents the cutting variable plots/contours for different cutting conditions. Figure 2.4 shows the cutting force history from a typical cutting test (5 m/s cutting speed and 0.15 mm uncut chip thickness) with steady state forces of

**Fig. 2.3** **a** *Close-up view* of tool and workpiece setup, and **b** *side view* of a diamond-coated tool tip



**Fig. 2.4** Cutting force history from one test





**Fig. 2.5** Temperature history at a location close to the tool tip; inserts are thermal images at different times

approximately 400 and 200 N for the cutting and thrust components, respectively. The small side force indicates that the orientation of the cutting edge deviates only slightly from the axis of rotation of the disk. Figure 2.5 shows the temperature, at a specific location on the tool versus the cutting time. The inset thermal images in Fig. 2.5 show the tool temperature distributions corresponding to the indicated times. The temperature contours during the steady state cutting period were averaged to obtain the mean temperature distribution at the tool tip area (inset under the curve in Fig. 2.5).

### 2.3.1 Uncut Chip Thicknesses Effect

Figure 2.6a shows how the specific cutting energy ( $E$ ) varied with the uncut chip thickness at different edge radii with a cutting speed of 5.0 m/s.  $E$  is in the range of 700–1,200 MPa. The trend agrees with conventional knowledge,  $E$  increasing with decreasing uncut chip thickness ( $h$ ), and the effect is manifested at a larger edge radius (50  $\mu\text{m}$  substrate), in particular, at very low uncut chip thickness (0.05 mm). Figure 2.6b shows the ratio of the cutting force to the thrust force (force ratio) varied with the uncut chip thickness at different edge radii. The force ratio also significantly increases with decreasing  $h$ . It is observed that a ratio as high as 0.9 may occur at a large edge radius and small  $h$ . The condition of  $h = 0.15$  mm was duplicated (two data points for 25 and 50  $\mu\text{m}$  edge radii in the figures) and the results show reasonable repeatability.

**Fig. 2.6** **a** Specific cutting energy, and **b** cutting force ratio versus uncut chip thickness,  $h$ , for different edge radii ( $v = 5 \text{ m/s}$ )

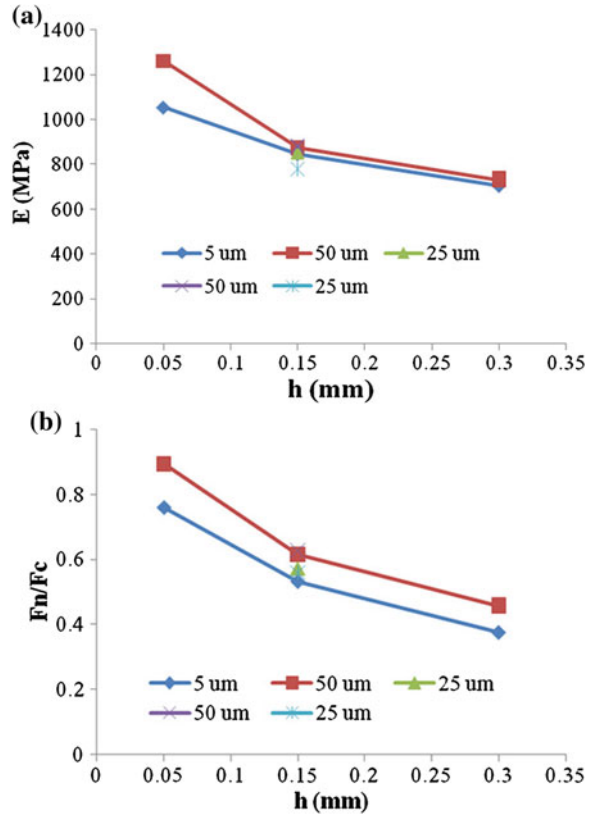


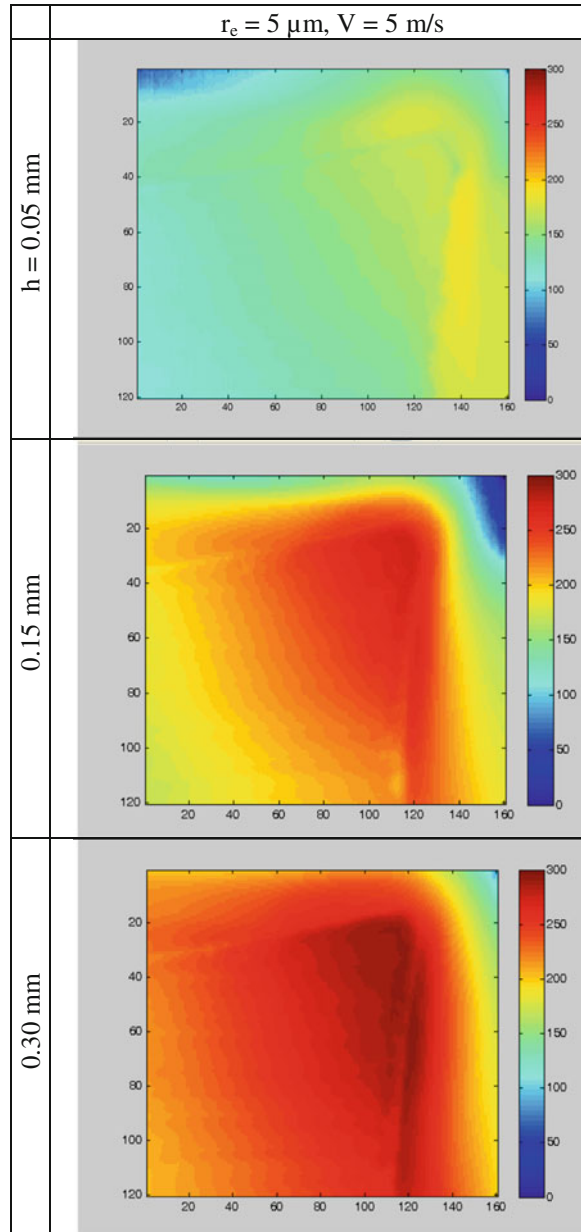
Figure 2.7 displays the temperature distributions at the tool tip (approximately 1 mm wide field of view) at different uncut chip thicknesses for the case of 5  $\mu\text{m}$  edge radius. The tool edge profiles are recognizable from the contours. It is observed that tool temperatures generally increase with the uncut thickness. The maximum temperature of around 300  $^{\circ}\text{C}$  occurred at 0.3 mm  $h$  versus less than 200  $^{\circ}\text{C}$  for 0.05 mm  $h$ . Note that the entire temperature fields were converted to true temperatures using the linear temperature-emissivity relationship of the tools (diamond-coated tools). Therefore, the portions of the temperature fields outside of the tool profile are not correctly represented.

### 2.3.2 Cutting Speed Effect

Figure 2.8a shows the changes in specific cutting energy with cutting speed at different edge radii for an uncut thickness of 0.15 mm.  $E$  is in the range of 800–1,000 MPa. It is also observed that  $E$  decreases slightly with the increase of the cutting speed ( $V$ ).



**Fig. 2.7** Cutting tool temperature contours ( $^{\circ}\text{C}$ ) at different uncut chip thicknesses,  $h$  (x and y scales in pixels)



The effect of the edge radius is small for the range of conditions tested. Similarly, Fig. 2.8b shows changes in the force ratio with cutting speed at different edge radii. The cutting force ratio also decreases slightly with increasing cutting speed, ranging between 0.55 and 0.7. A larger edge radius effect can be noted as well.

**Fig. 2.8 a** Specific cutting energy, and **b** cutting force ratio versus cutting speed for different edge radii (h = 0.15 mm)

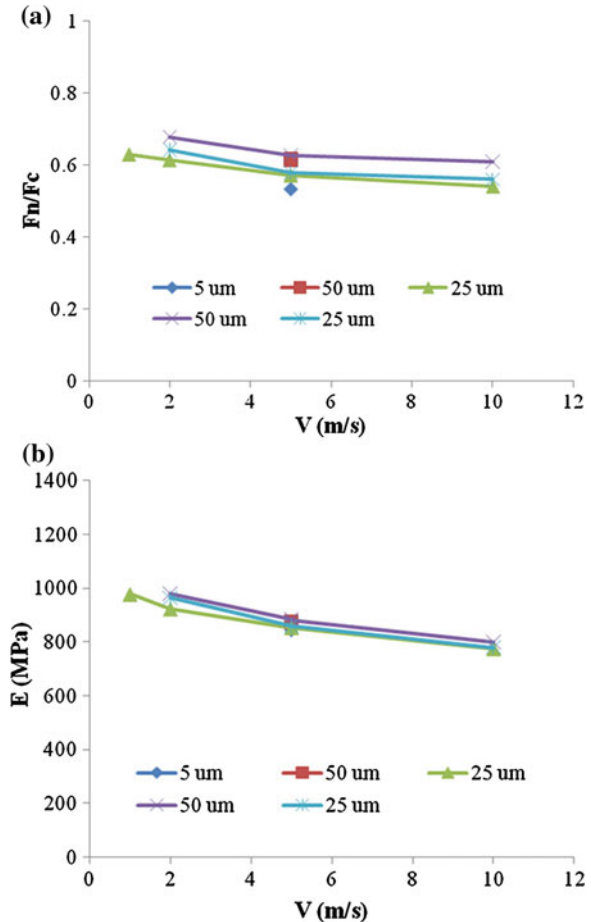
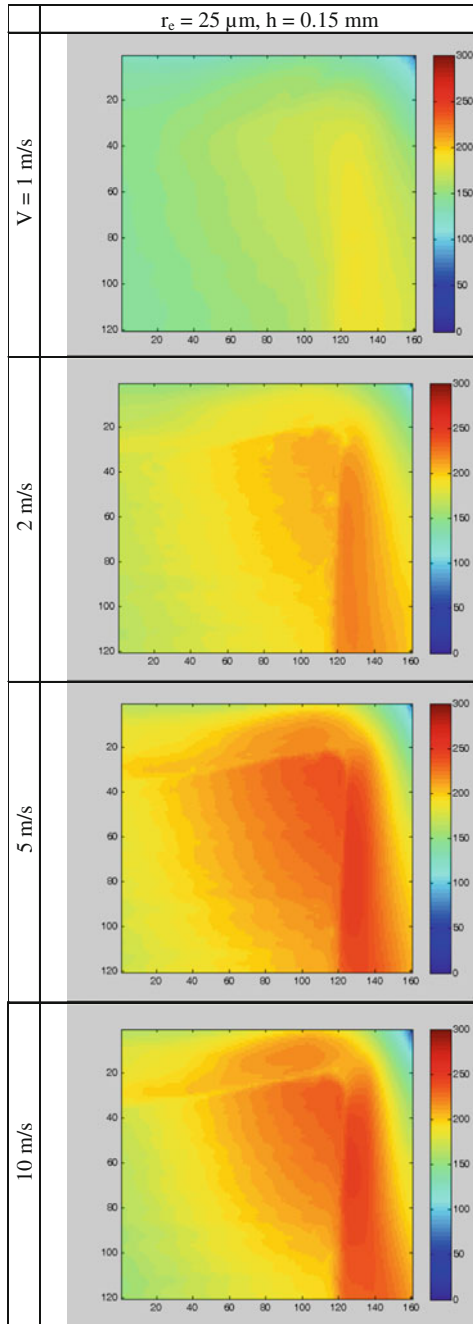


Figure 2.9 displays the effect of the cutting speed on tool tip temperatures at an edge radius of 25  $\mu\text{m}$ . It is observed that tool temperatures increase with cutting speed up to 5 m/s and level off from 5 to 10 m/s. The maximum tool temperatures are in the range of about 175  $^{\circ}\text{C}$  for 1 m/s to about 275  $^{\circ}\text{C}$  for 5 and 10 m/s.

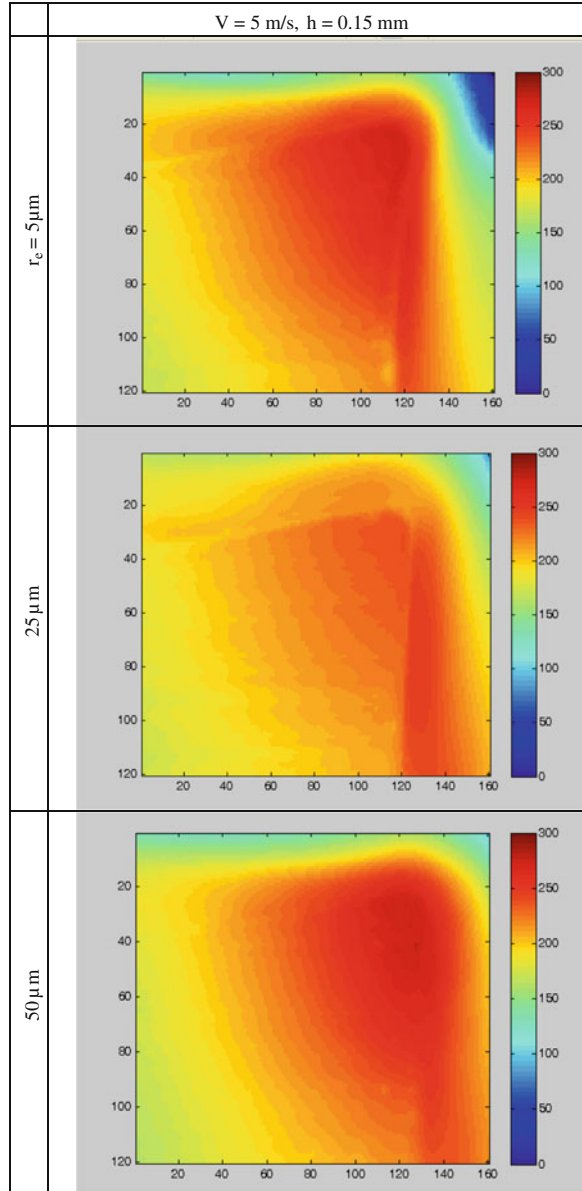
### 2.3.3 Edge Radius Effect on Cutting Tool Temperatures

The measured effects of the edge radius on the specific cutting energy and the force ratio are significant, especially at a smaller uncut thickness. The measured tool temperatures (Fig. 2.10) appear to be minimized at 25  $\mu\text{m}$ , and larger at both 5 and 50  $\mu\text{m}$ .

**Fig. 2.9** Cutting tool temperature contours (°C) at different cutting speeds (x and y scales in pixels)

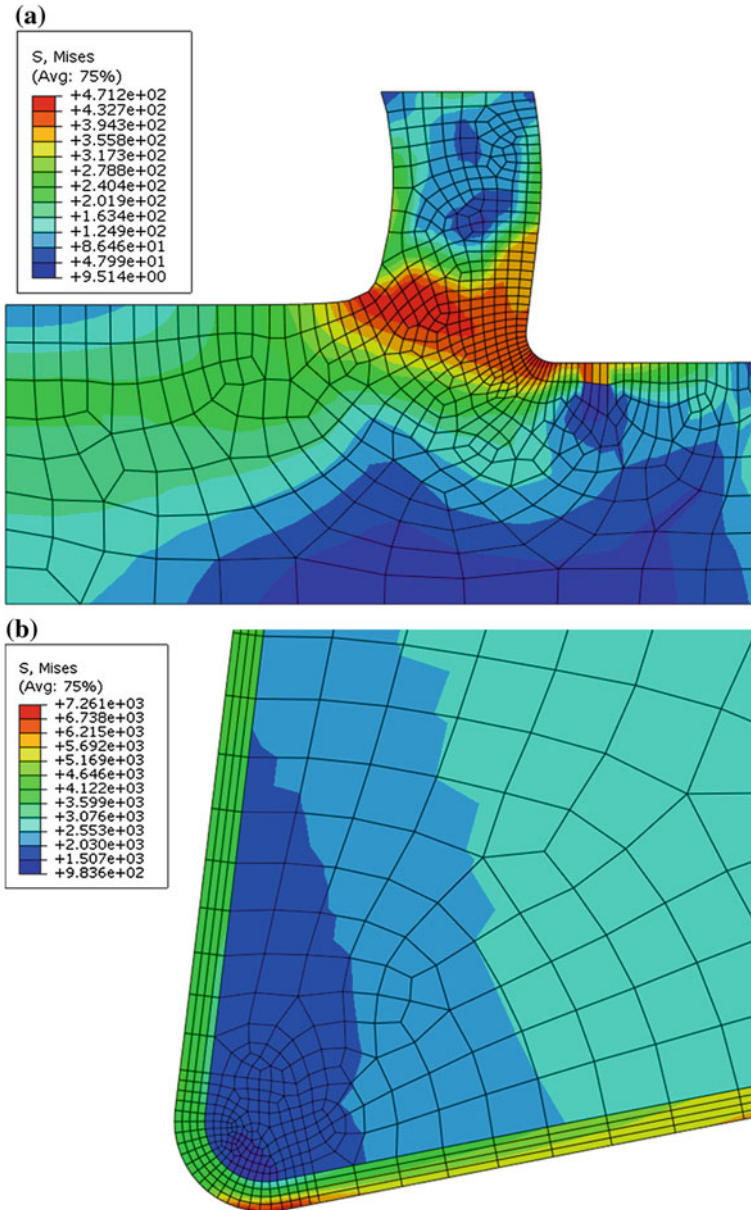


**Fig. 2.10** Cutting tool temperature contours (°C) at different edge radii (x and y scales in pixels)



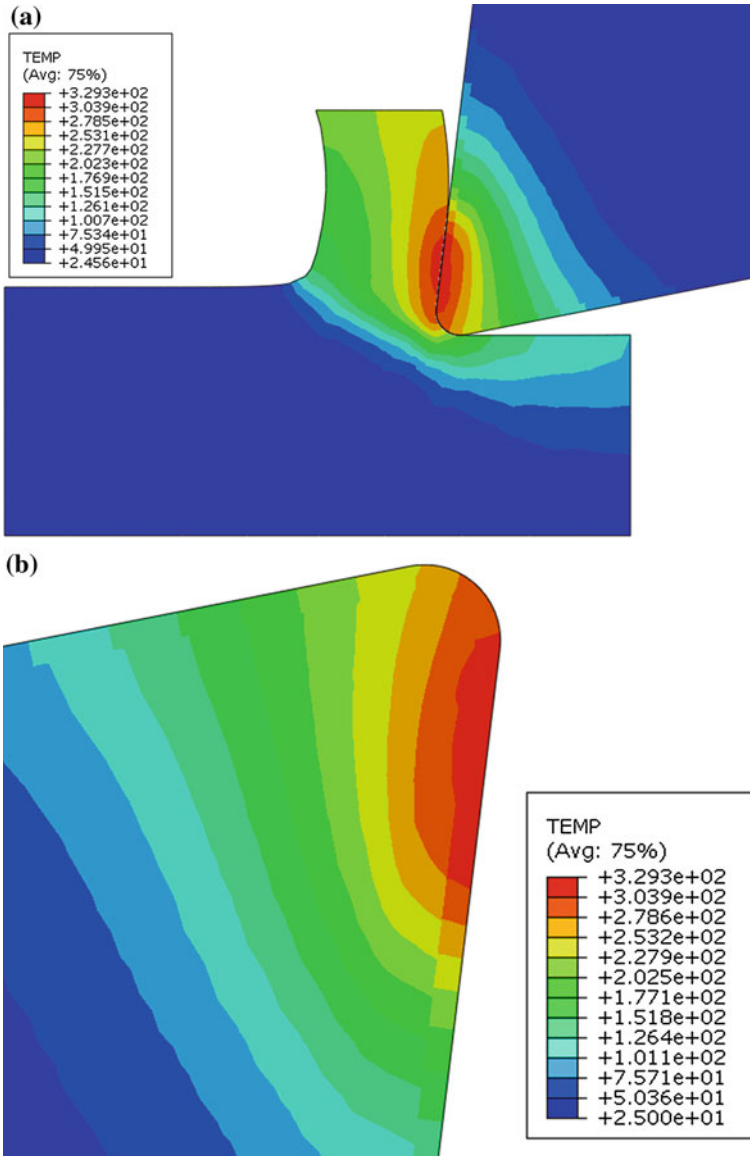
**2.3.4 Simulation Result Example**

FE simulations of 2D cutting with a diamond-coated tool were realized using ABAQUS software. The simulations include a deposition stress analysis with a given deposition temperature and coating and substrate properties, and a subsequent



**Fig. 2.11** Stress contour from cutting simulations: **a** workpiece and chip, and **b** tool alone (unit: MPa)

cutting simulation using the arbitrary Lagrangian Eulerian scheme including the tool with the inherited deposition stresses and a workpiece with given material constitutive model and frictional coefficient. The simulation was conducted in the



**Fig. 2.12** Cutting tool tip temperature contours: **a** overall, and **b** tool alone (unit: °C)

explicit dynamic analysis mode to reach a steady state chip formation. The details of the simulation procedure can be found in a previous publication [7]. The results from an example (25  $\mu\text{m}$  edge radius, 20  $\mu\text{m}$  coating thickness, 5 m/s cutting speed, and 0.15 mm uncut chip thickness) are shown here. Figure 2.11 plots the von Mises stress contours during cutting, (a) in the workpiece and chip and (b) in the diamond-

coated tool. It is noted that the stress level in the primary shear zone is on the order of 300–400 MPa; however, the tool has a very high localized stress, over 7 GPa, in the edge-flank transition area. Note that the residual stress from the diamond deposition can be as high as 4 GPa, as was observed from the previous analysis. Cutting forces calculated from the simulation are 162 and 72 N, respectively, for 1 mm width of cut, which are comparable to the experimental results (128 and 73 N per mm width of cut). Figure 2.12 plots the temperature contour, (a) tool-chip-workpiece, and (b) only tool. The maximum tool temperature is around 330 °C versus 275 °C from the experiment.

## 2.4 Conclusions

Analysis of orthogonal cutting with force and temperature measurements was conducted using the experimental setup at NIST, and a comparison of these measurements to numerical studies was performed. The experimental data were processed to evaluate the effects of process parameters and the tool edge radius. The initial testing sets reveal the major findings summarized below.

- (1) As the uncut chip thickness increases, the tool temperature increases and the specific cutting energy and normal versus cutting force ratio decrease.
- (2) As the cutting speed increases, the specific cutting energy decreases slightly, and the tool temperatures increase substantially.
- (3) The effect of the edge radius on the specific cutting energy and the force ratio is noticeable; however, the effect on the tool temperatures is inconsistent with classical theory.
- (4) The preliminary comparison between the experimental results and simulations indicates reasonable agreement.

The first two findings are consistent with classical metal cutting literature [11]. The third finding indicates a need for further investigation to better understand the underlying phenomena.

For future work, more extensive testing, including systematic repeatability evaluations, a larger uncut chip thickness, and uncoated tool cutting comparisons will be performed. In addition, more thorough quantitative comparisons with FE cutting simulation results will be analyzed.

**Acknowledgments** The University of Alabama portion of this research is supported by NSF, Grant #: 0728228. Vista Engineering LLC, and General Motors generously supplied the diamond coating service and workpieces, respectively, for the experiments. X. Gong conducted the deposition stress and cutting simulations.

## References

1. Kustas FM, Fehrehnbacher LL, Komanduri R (1997) Nanocoatings on cutting tools for dry machining. *Ann CIRP* 46:39–42
2. Arumugam PU, Malshe AP, Batzer SA (2006) Dry machining of aluminum–silicon alloy using polished CVD diamond-coated cutting tools inserts. *Surf Coat Technol* 200:3399–3403
3. Grzesik W, Zalisz Z, Nieslony P (2002) Friction and wear testing of multilayer coatings on carbide substrates for dry machining applications. *Surf Coat Technol* 155:37–45
4. Balaji AK, Jawahir IS (2001) A machining performance study in dry contour turning of aluminum alloys with flat-faced and grooved diamond tools. *Mach Sci Technol* 5:269–289
5. Bouzakis KD, Hadjiyiannis S, Skordaris G, Mirisidis I, Michailidis N, Efstathiou K, Pavlidou E, Erkens G, Cremer R, Rambadt S, Wirth I (2004) The effect of coating thickness, mechanical strength and hardness properties on the milling performance of PVD coated cemented carbides inserts. *Surf Coat Technol* 177–178:657–664
6. Qin F, Chou K, Nolen D, Thompson RG, Ni W (2009) Cutting edge radius effects on diamond coated tools. *Trans NAMRI/SME* 37:653–660
7. Qin F, Chou K (2010) 2D cutting simulations with a diamond-coated tool including deposition residual stresses. *Trans NAMRI/SME* 38:1–8
8. Sartkulvanich P, Sahlan H, Altan T (2007) A finite element analysis of burr formation in face milling of a cast aluminum alloy. *Mach Sci Technol* 11:157–181
9. Heigel JC, Ivester RW, Whinton EP (2008) Temperature measurements of segmented chips using dual-spectrum high-speed microvideography. *Trans NAMRI/SME* 36:73–80
10. Ivester RW (2011) Tool temperatures in orthogonal cutting of alloyed titanium. In: *Proceedings of NAMRI/SME*, vol 39
11. Shaw MC (1984) *Metal cutting principles*. Oxford University Press, New York



# Chapter 3

## Estimation of Cutting Forces and Tool Wear Using Modified Mechanistic Models in High Performance Turning

Ana Isabel Fernández-Abia, Joaquín Barreiro García,  
Luis N. López de Lacalle and Octavio Pereira Neto

**Abstract** In this chapter a model for prediction of cutting forces when turning austenitic stainless steels following the approach of mechanistic models is presented. Mechanistic models, also called semi-empiric, use empiric laws based on the tool geometry and coefficients obtained by experimentation. These coefficients implicitly pick up characteristic data about part and tool materials or tool geometry. Therefore, a series of machining tests is required to calculate these coefficients for each pair tool-workpart, commonly known as characterization tests. This chapter is structured as follows. In Sect. 3.1 a model for prediction of cutting forces without considering the effect of tool wear is presented. This model allows to estimate with reasonable precision the cutting forces. This model can be used, for example, in the scope of machine-tools and fixtures design or optimization of cutting tool geometry. In Sect. 3.2 this model is extended to include the effect of tool wear. So, the model can be used in the scope of monitoring techniques. Both models were developed for turning AISI 303 austenitic stainless steels at high-speed cutting conditions.

---

A.I. Fernández-Abia (✉) · J.B. García · O.P. Neto  
Department of Mechanical, Informatics and Aerospace Engineering,  
University of León, Campus de Vegazana, s/n, 24071 León, Spain  
e-mail: aifera@unileon.es

J.B. García  
e-mail: j barg@unileon.es

O.P. Neto  
e-mail: octavio.pereira.neto@gmail.com

L.N.L. de Lacalle  
Department of Mechanical Engineering, University of the Vasque Country,  
Alameda de Urquijo, s/n, 48013 Bilbao, Spain  
e-mail: norberto.lzlacalle@ehu.es

### 3.1 Model for Prediction of Cutting Forces Without Considering Tool Wear

A mechanistic model is introduced in this section to predict cutting forces in turning operations in the early moments of operation, that is, when the tool is still not worn. This model is adapted to the geometry of the tool. The model is based on the expressions provided by Altintas [1]. This model takes into consideration the fact that tool edge is not perfectly sharp. The rounding of tool edge provokes friction between the tool edge and the workpart surface, which gives an additional friction force to the one due to chip removal. Therefore, force in tool edge is originated by the sum of two effects: the force due to material shearing (identified with subindex “c”) and the force due to the friction (identified with subindex “e”).

According to this statement, the three components of the cutting force ( $F_t$ —tangential,  $F_f$ —axial and  $F_r$ —radial to the edge) can be calculated by means of the following expressions (Eq. 3.1):

$$\begin{aligned} F_t &= F_{tc} + F_{te} = k_{tc}A + k_{te}S \\ F_f &= F_{fc} + F_{fe} = k_{fc}A + k_{fe}S \\ F_r &= F_{rc} + F_{re} = k_{rc}A + k_{re}S \end{aligned} \quad (3.1)$$

where  $k_{tc}$ ,  $k_{fc}$  and  $k_{rc}$  are the specific cutting coefficients related with the material shearing mechanism. These coefficients represent the shearing force for unit of surface;  $k_{te}$ ,  $k_{fe}$  and  $k_{re}$  are the friction coefficients that represent the friction force for unit of length. The term  $A$  is the section of non-deformed chip and  $S$  is the edge length implied in the cutting operation. These parameters are determined based on tool geometry and cutting conditions, since both aspects takes influence in chip section. These empirical coefficients are valid for a specific tool-workpart combination. That is, they depend on (i) workpart material, (ii) material and geometry of tool and (iii) contact conditions between tool and workpart. These coefficients have been determined experimentally through a series of turning tests called characterization tests.

Keeping in mind the aforementioned, the following activities have been carried out to develop the model sequentially:

- (a) Development of the geometric model that defines the turning operation based on cutting conditions and tool geometry. At this stage, the non-deformed chip section and the length of the edge implied in the cut are calculated.
- (b) Development of the mechanistic model for prediction of cutting forces in turning.
- (c) Experimental determination of the specific coefficients related to shearing and friction. From the force model obtained previously and the values of cutting forces recorded in the characterization tests, the values of  $k_{tc}$  and  $k_{te}$

coefficients are obtained. A statistical analysis is carried out to determine the influence of cutting depth ( $a_p$ ) and cutting speed ( $V_c$ ) over these coefficients. Finally, expressions for the specific cutting coefficients are obtained that incorporate the effect of these variables.

(d) Validation of the prediction model.

### 3.1.1 Development of the Geometric Model

In turning operations the cutting geometry changes with cutting depth, feedrate, nose tip radius and main and secondary tool entering angles. Depending on the combination of these parameters different non-deformed chip section geometries can be obtained (Fig. 3.1).

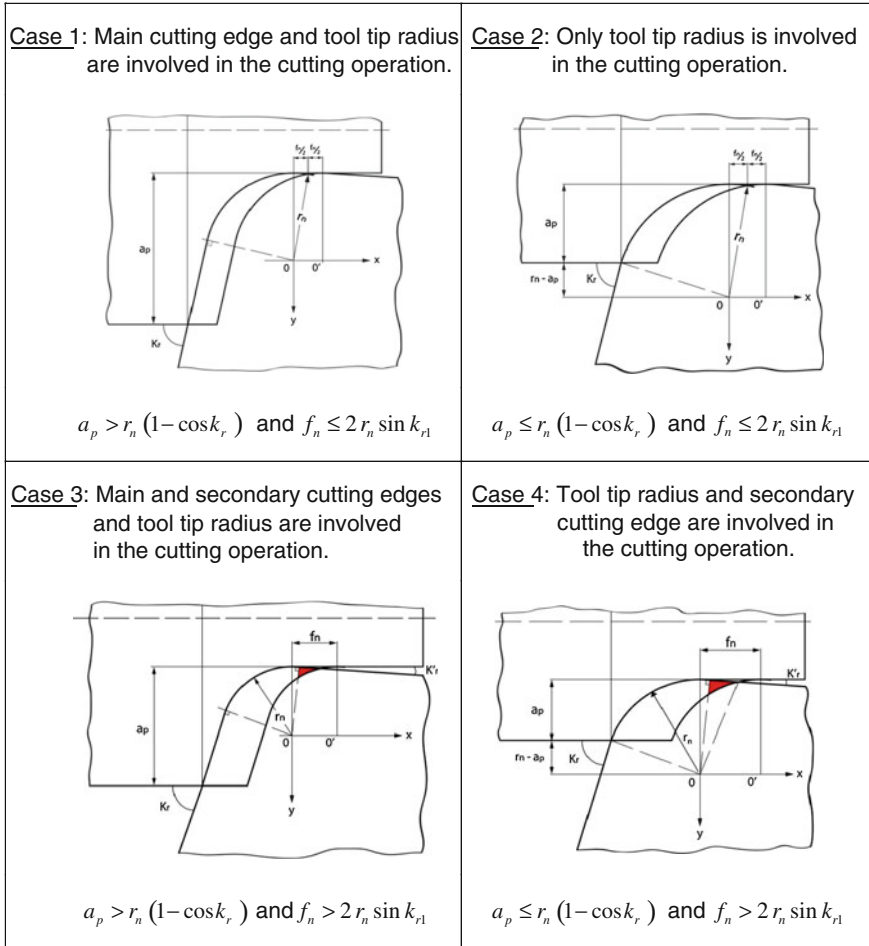
ISO 3685 standard recommends to use feedrate values less than 0.8 times the tool tip radius ( $f_n < 0.8 r_n$ ). The reason is to avoid the involvement of secondary cutting edge in the operation, which could modify the profile roughness in the machined surface. If this recommendation is followed, the only possible conditions correspond to the cases 1 and 2 as indicated in Fig. 3.1.

On the other hand, when turning in roughing or intermediate conditions, cutting depth is usually several times higher than tool tip radius, consequently most of the performed turning operations correspond to the geometry of Case 1. Case 1 geometric model will be used in this chapter due to its wide application. Geometry defined in Case 2 (i.e. cutting depth lower than tool tip radius) is used in finish turning operations or hard turning, outside the scope in this chapter.

#### 3.1.1.1 Cutting Geometry Associated to Case 1

When analysing the geometry of Case 1, it can be observed that chip is featured by variable section. Chip thickness shrinks progressively in the curved segment of the primary cutting edge. Some simplification can be done if ignoring tool tip radius and approximating the rounded tip to a straight linear segment. This simplification allows us to consider a chip with constant section. This simplification can introduce errors to the model depending on the  $a_p/f_n$  relationship. In the work carried out by Denkena and Köler [2] the authors indicate that when the  $a_p/f_n$  relationship is higher than 4 and non-deformed chip thickness ( $h$ ) is higher than 0.1 mm, the effect of tool tip radius over the chip section can be ignored and, consequently, over the cutting forces. However, when the  $a_p/f_n$  relationship is lower than 4, the error introduced in the prediction of axial force is significant and if  $h$  is inferior to 0.1 mm then errors related to tangential and radial forces are considerable.

When tool tip radius is ignored (Fig. 3.2) relationships among  $f_n$  and  $a_p$  with chip thickness ( $h$ ), chip width or edge cutting length ( $S$ ) are expressed as follows (Eqs. 3.2–3.4):



**Fig. 3.1** Cutting geometries as a function of cutting parameters and tool geometry

$$S = \frac{a_p}{\sin k_r} \tag{3.2}$$

$$h = f_n \sin k_r \tag{3.3}$$

$$A = S h = a_p f_n \tag{3.4}$$

When tool tip radius is considered, two different regions are defined in chip section (Fig. 3.3): Region I (along the straight segment in the main cutting edge) and Region II (along the curved segment).

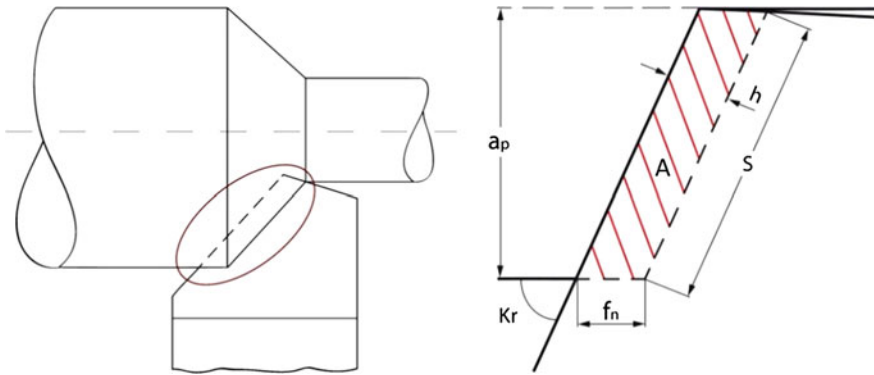


Fig. 3.2 Detailed view of chip section when ignoring tool tip radius

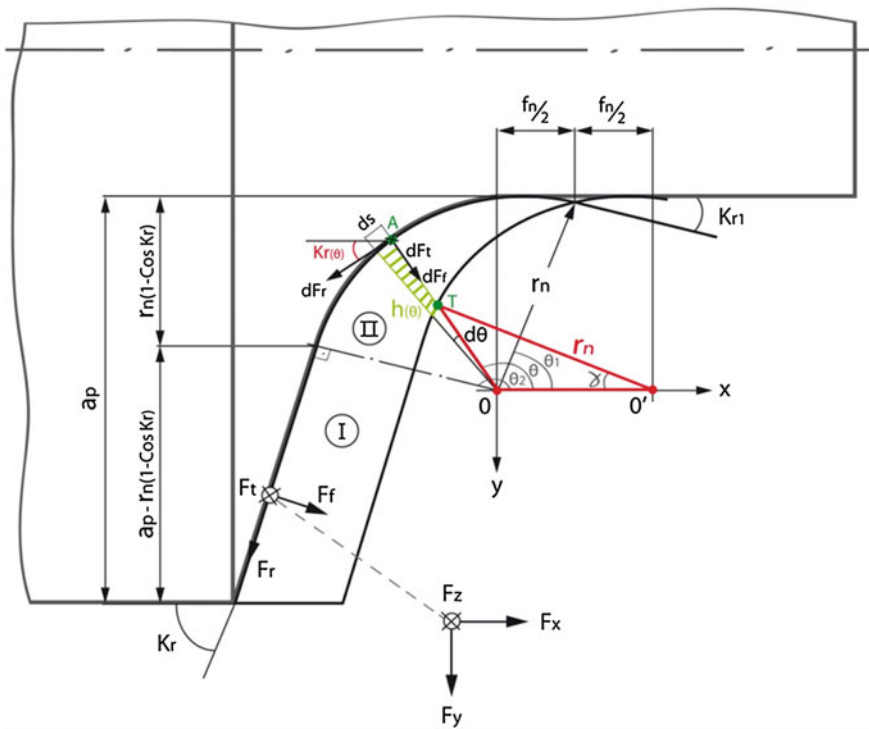


Fig. 3.3 Non-deformed chip section and associated geometrical parameters (Case 1)

In Region I, chip thickness keeps constant and it is determined by the feedrate ( $f_n$ ) and the lead angle ( $k_r$ ). The involved edge length ( $S_I$ ) and the chip section ( $A_I$ ) in this region are calculated using the expressions in Eqs. (3.5)–(3.6).

$$S_I = \frac{a_p - r_n(1 - \cos k_r)}{\sin k_r} \quad (3.5)$$

$$A_I = f_n [a_p - r_n(1 - \cos k_r)] - \frac{1}{4} f_n^2 \sin(2k_r) \quad (3.6)$$

In Region II, chip thickness and lead angle vary constantly. To carry out the geometric analysis in this region, the chip is decomposed into infinitesimal thickness elements. These elements have different thickness and orientation. The length of the edge in the curved segment,  $S_{II}$ , is calculated according to the expression in Eq. (3.7):

$$S_{II} = \int_{\theta_1}^{\theta_2} dS = \int_{\theta_1}^{\theta_2} r_n d\theta \quad (3.7)$$

Section of non-deformed chip,  $A_{II}$ , is calculated with the expression in Eq. (3.8):

$$A_{II} = \int_{\theta_1}^{\theta_2} h(\theta) dS = \int_{\theta_1}^{\theta_2} h(\theta) r_n d\theta \quad (3.8)$$

where integration limits  $\theta_1$  and  $\theta_2$  are given by the expressions in Eq. (3.9):

$$\theta_1 = \cos^{-1} \frac{f_n}{2r_n}; \quad \theta_2 = \frac{\pi}{2} + k_r \quad (3.9)$$

Chip thickness,  $h(\theta)$ , depends on the location of the differential element and it can be approximated by the expression in Eq. (3.10):

$$h(\theta) = \overline{AT} = r_n - \overline{TO} \quad (3.10)$$

If the cosines' law is applied to the OTO' triangle (Eq. 3.11):

$$\overline{TO} = \sqrt{f_n^2 + r_n^2 - 2f_n r_n \cos \gamma} \quad (3.11)$$

Using the sines' law (Fig. 3.4) as indicated in Eq. 3.12, the value of angle  $\gamma$  is obtained (Eq. 3.13):

$$\frac{f_n}{\sin \beta} = \frac{r_n}{\sin \theta} \Rightarrow \frac{f_n}{\sin(\pi - \theta - \gamma)} = \frac{r_n}{\sin \theta} \quad (3.12)$$

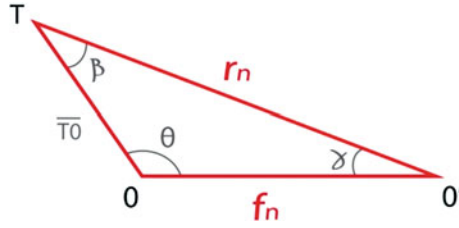


Fig. 3.4 Triangle OTO' extracted from Fig. 3.3 to determine angle  $\gamma$

$$\gamma = \pi - \theta - \sin^{-1} \left( \frac{f_n}{r_n} \sin \theta \right) \quad (3.13)$$

Substituting Eqs. (3.13) and (3.12) into Eq. (3.11), the expression for chip thickness is obtained as a function of angle  $\theta$  (Eq. 3.14):

$$h(\theta) = r_n - \sqrt{f_n^2 + r_n^2 - 2f_n r_n \cos \left[ \pi - \theta - \sin^{-1} \left( \frac{f_n}{r_n} \sin \theta \right) \right]} \quad (3.14)$$

### 3.1.2 Development of a Mechanistic Model for Prediction of Cutting Force

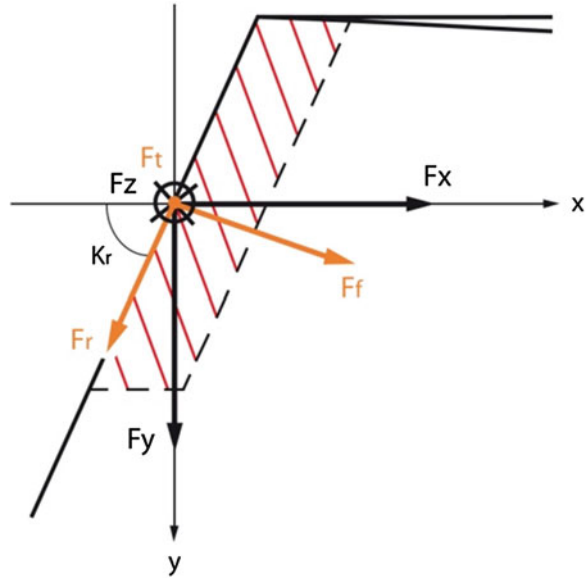
Once the cutting geometry is determined, the following step is to introduce the expressions for the involved edge length ( $S$ ) and the non-deformed chip section ( $A$ ) in the mechanistic model (Eq. 3.1). The model is developed for both cases: (i) the case of simplified geometry, that is, ignoring the tip radius; (ii) the complete case considering the straight and curve segments of the edge.

#### 3.1.2.1 Model for Cutting Force Prediction Ignoring Tool Tip Radius (Simplified Model)

The expressions for the cutting force components in axial, radial and tangential directions are obtained directly by substituting the expressions for  $S$  and  $A$  (Eqs. 3.2 and 3.4) into Eq. 3.1. Therefore:

$$\begin{aligned} F_f &= k_{fc} A + k_{fe} S = k_{fc} a_p f_n + k_{fe} \frac{a_p}{\sin k_r} \\ F_r &= k_{rc} A + k_{re} S = k_{rc} a_p f_n + k_{re} \frac{a_p}{\sin k_r} \\ F_t &= k_{tc} A + k_{te} S = k_{tc} a_p f_n + k_{te} \frac{a_p}{\sin k_r} \end{aligned} \quad (3.15)$$

**Fig. 3.5** Projection of cutting forces into the X-Y-Z reference system



The following step consists on projecting the axial, radial and tangential components on the X-Y-Z- directions (Fig. 3.5). These are the directions of the force components recorded by the dynamometer located under the tool. A rotation transformation between both systems must be applied (Eq. 3.16).

$$\begin{bmatrix} F_x \\ F_y \\ F_z \end{bmatrix} = \begin{bmatrix} \sin k_r & -\cos k_r & 0 \\ \cos k_r & \sin k_r & 0 \\ 0 & 0 & 1 \end{bmatrix} \begin{bmatrix} F_f \\ F_r \\ F_t \end{bmatrix} \quad (3.16)$$

Hence the expressions for the projected forces are (Eq. 3.17):

$$\begin{aligned} F_x &= F_f \sin k_r - F_r \cos k_r \\ F_y &= F_f \cos k_r + F_r \sin k_r \\ F_z &= F_t \end{aligned} \quad (3.17)$$

Then, the expressions in Eq. 3.18 are obtained by substituting Eq. 3.17 into the expressions for  $F_f$ ,  $F_r$ ,  $F_t$  (Eq. 3.15):

$$\begin{aligned} F_x &= \left( k_{fc} a_p f_n + k_{fe} \frac{a_p}{\sin k_r} \right) \sin k_r - \left( k_{rc} a_p f_n + k_{re} \frac{a_p}{\sin k_r} \right) \cos k_r \\ F_y &= \left( k_{fc} a_p f_n + k_{fe} \frac{a_p}{\sin k_r} \right) \cos k_r + \left( k_{rc} a_p f_n + k_{re} \frac{a_p}{\sin k_r} \right) \sin k_r \\ F_z &= k_{tc} a_p f_n + k_{te} \frac{a_p}{\sin k_r} \end{aligned} \quad (3.18)$$



### 3.1.2.2 Model for Cutting Force Prediction Considering the Tool Tip Radius (Complete Model)

If the tool tip radius is considered, the expressions of axial, radial and tangential cutting force components should be considered for each infinitesimal region in which chip section was divided. The total cutting force is then calculated as the sum of forces in Region I plus forces in Region II for each force component.

In Region I, the lead angle keeps constant with a value equal to  $k_r$ . Magnitude of forces and their directions do not vary along the straight segment of the edge. Therefore, expressions for the three components of cutting force in this region are given by Eq. 3.19.

$$\begin{aligned} F_{fI} &= k_{fc} A_I + k_{fe} S_I \\ F_{rI} &= k_{rc} A_I + k_{re} S_I \\ F_{tI} &= k_{tc} A_I + k_{te} S_I \end{aligned} \quad (3.19)$$

In Region II, the lead angle  $k_r(\theta)$  varies continually and, in consequence, direction of cutting forces also changes along the curved edge segment. In this region the force is calculated for each differential element in which the chip was divided, considering that direction of force is normal to each differential element. Expressions for the three force components are given by Eq. 3.20.

$$\begin{aligned} F_{fII} &= \int_{\theta_1}^{\theta_2} k_{fc}(\theta) h(\theta) r_n d\theta + \int_{\theta_1}^{\theta_2} k_{fe}(\theta) r_n d\theta \\ F_{rII} &= \int_{\theta_1}^{\theta_2} k_{rc}(\theta) h(\theta) r_n d\theta + \int_{\theta_1}^{\theta_2} k_{re}(\theta) r_n d\theta \\ F_{tII} &= \int_{\theta_1}^{\theta_2} k_{tc}(\theta) h(\theta) r_n d\theta + \int_{\theta_1}^{\theta_2} k_{te}(\theta) r_n d\theta \end{aligned} \quad (3.20)$$

The total force is the sum of forces in both regions (Eq. 3.21).

$$\begin{aligned} F_f &= F_{fI} + F_{fII} \\ F_r &= F_{rI} + F_{rII} \\ F_t &= F_{tI} + F_{tII} \end{aligned} \quad (3.21)$$

The following step consists again in projecting the axial, radial and tangential force components in the system X-Y-Z, which corresponds to the directions of the forces registered by the dynamometer (Eq. 3.17). Now,  $\varphi$  is constant in the straight segment of the edge with a value of  $k_r$ , but in the curved segment the value of  $\varphi$  depends on the location of each element. It is represented as  $k_r(\theta)$  (Fig. 3.3) and the value can be expressed as indicated in Eq. 3.22.

$$\varphi_{II} \equiv k_r(\theta) = \theta - \frac{\pi}{2} \quad (3.22)$$

The expressions obtained for the cutting force components when applying the transformation are indicated in Eq. 3.23:

$$\begin{aligned} F_x &= F_{fI} \sin k_r + F_{fII} \sin k_r(\theta) - F_{rI} \cos k_r - F_{rII} \cos k_r(\theta) \\ F_y &= F_{fI} \cos k_r + F_{fII} \cos k_r(\theta) + F_{rI} \sin k_r + F_{rII} \sin k_r(\theta) \\ F_z &= F_{tI} + F_{tII} \end{aligned} \quad (3.23)$$

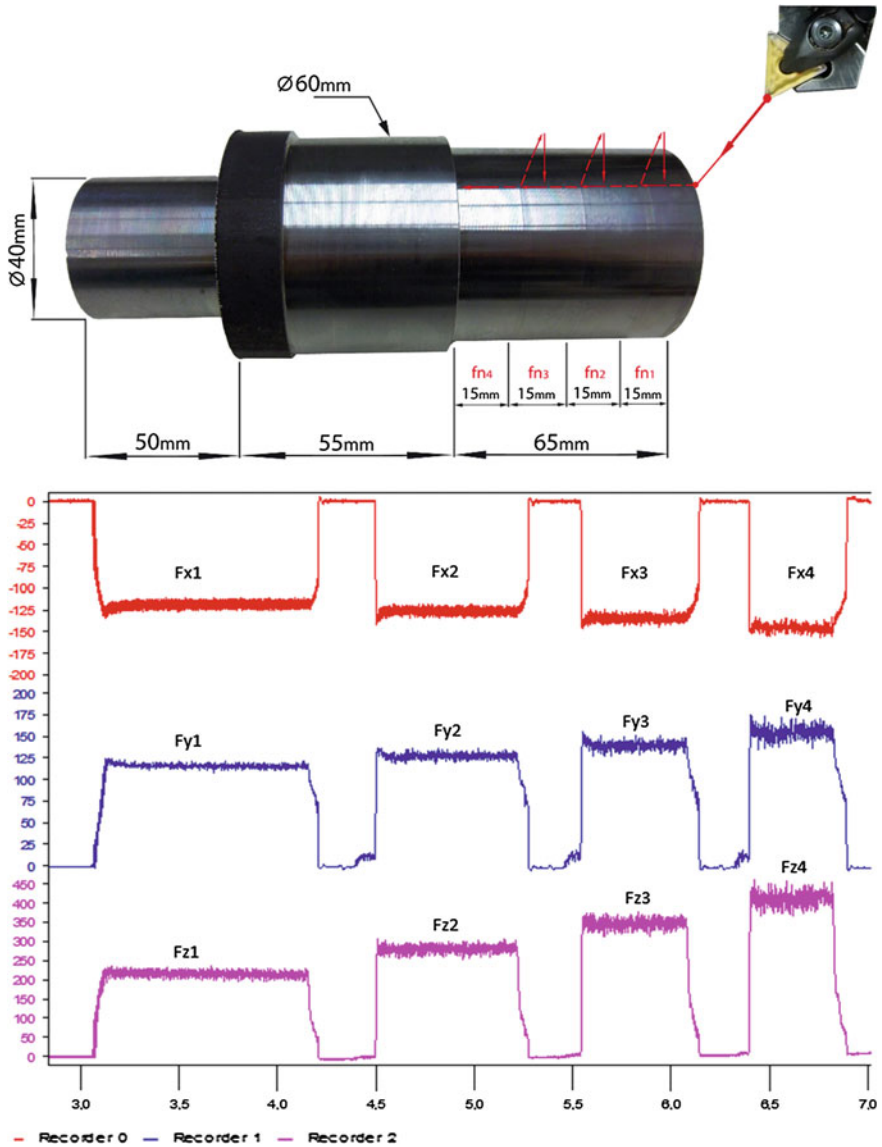
Substituting in Eq. 3.23 the expressions obtained for the  $F_f$ ,  $F_r$  and  $F_t$  components in the Regions I and II, we obtain the expressions in Eq. 3.24.

$$\begin{aligned} F_x &= k_{fc} A_I \sin k_r + k_{fe} S_I \sin k_r + \int_{\theta_1}^{\theta_2} k_{fc}(\theta) h(\theta) r_n \sin k_r(\theta) d\theta + \int_{\theta_1}^{\theta_2} k_{fe}(\theta) r_n \sin k_r(\theta) d\theta \\ &\quad - k_{rc} A_I \cos k_r - k_{re} S_I \cos k_r - \int_{\theta_1}^{\theta_2} k_{rc}(\theta) h(\theta) r_n \cos k_r(\theta) d\theta - \int_{\theta_1}^{\theta_2} k_{re}(\theta) r_n \cos k_r(\theta) d\theta \\ F_y &= k_{fc} A_I \cos k_r + k_{fe} S_I \cos k_r + \int_{\theta_1}^{\theta_2} k_{fc}(\theta) h(\theta) r_n \cos k_r(\theta) d\theta + \int_{\theta_1}^{\theta_2} k_{fe}(\theta) r_n \cos k_r(\theta) d\theta \\ &\quad + k_{rc} A_I \sin k_r + k_{re} S_I \sin k_r + \int_{\theta_1}^{\theta_2} k_{rc}(\theta) h(\theta) r_n \sin k_r(\theta) d\theta + \int_{\theta_1}^{\theta_2} k_{re}(\theta) r_n \sin k_r(\theta) d\theta \\ F_z &= k_{tc} A_I + k_{te} S_I + \int_{\theta_1}^{\theta_2} k_{tc}(\theta) h(\theta) r_n d\theta + \int_{\theta_1}^{\theta_2} k_{te}(\theta) r_n d\theta \end{aligned} \quad (3.24)$$

These expressions allow us to predict the components of the cutting force in the system X-Y-Z using as input data the cutting conditions ( $f_n$  and  $a_p$ ), the tool geometry ( $k_r$  and  $r_n$ ) and the cutting specific coefficients obtained for a particular workpart-tool combination. The cutting conditions and the tool geometry are known a priori. Nevertheless, it is necessary to estimate the cutting specific coefficients by carrying out material characterization tests. This aspect is explained in the next section.

### 3.1.2.3 Material Characterization Tests

The cutting specific coefficients are determined by carrying out machining tests. These tests must be performed in similar conditions to those in the real operation. The experiments to characterize the material consist in longitudinal turning operations over cylindrical stocks by varying only feedrate while keeping constant cutting depth and cutting speed. This operation will be called “series”. Each series is repeated three times to obtain a more precise estimation. A new edge is used for



**Fig. 3.6** Image of the machined part and records of cutting force components during a “series” in material characterization tests

each repetition in order to suppress any effect due to tool wear. During the operation the three components of the cutting force are recorded. Later on, the recorded signals are processed and the average value is calculated for each feedrate. The specimen and the force signals for a particular series are shown in Fig. 3.6.

To enlarge the scope of the model, several series of experiments with different combinations of cutting speed ( $V_c$ ) and feedrate ( $a_p$ ) are carried out. This way the influence of these parameters can be analysed and it is possible to find expressions for the specific coefficients valid for making better predictions in a wider range of cutting conditions.

Table 3.1 shows the cutting conditions used in the characterization tests. Sixteen series were carried out. (with three repetitions for each series) covering a wide range of cutting speed (300–750 m/min), feedrate (0.1–0.25 mm/rev) and cutting depth (1–2.5 mm).

As observed in this table, values of  $V_c$  are outside of the range recommended by tools makers (common values are smaller than 300 m/min). However, the range of  $V_c$  values used in the tests is adequate to reach the objectives of productivity and quality while maintaining an acceptable tool life [3].

With regard to the values chosen for  $a_p$  and  $f_n$ , they satisfy the geometric conditions corresponding to Case I [ $a_p > r_n(1 - \cos k_r)$  and  $f_n \leq 2 r_n \sin k_{r1}$ ] (Fig. 3.1), which assures that cutting action takes place in the straight segment and in the tip radius of the primary cutting edge, that is, without involvement of secondary cutting edge.

**Table 3.1** Characterization tests

$V_c$ (m/min)	$a_p$ (mm)	$f_{n1}$	$f_{n2}$	$f_{n3}$	$f_{n4}$	Series
		(mm/rev)				
750	1	0.1	0.15	0.2	0.25	Series 1
	1.5					Series 2
	2					Series 3
	2.5					Series 4
600	1	0.1	0.15	0.2	0.25	Series 5
	1.5					Series 6
	2					Series 7
	2.5					Series 8
450	1	0.1	0.15	0.2	0.25	Series 9
	1.5					Series 10
	2					Series 11
	2.5					Series 12
300	1	0.1	0.15	0.2	0.25	Series 13
	1.5					Series 14
	2					Series 15
	2.5					Series 16

### 3.1.2.4 Determination of the Cutting Specific Coefficients

As aforementioned, the cutting specific coefficients are obtained empirically using specific material characterization tests. For example, in this work tests are done in a CNC lathe with a dynamometric plate located under the tool holder. The machined material is AISI 303 austenitic stainless steel using coolant at 7 % concentration. The tool is a coated carbide Sandvik (TNMG 160408-MM) with CVD multilayer (TiCN–Al<sub>2</sub>O<sub>3</sub>–TiN). Table 3.2 indicates the main characteristics of the tool assembly.

For estimating the value of the specific cutting coefficients, a dynamometric plate records values of the three force components during the machining. The average values are later on introduced in the mechanistic model together with the geometric data and cutting conditions. This way, values for the specific coefficients are obtained for each series. In the next section the detailed procedure is presented for both predictive models (simplified and complete models).

#### Determination of the Coefficients Using the Simplified Model (Ignoring Tool Tip Radius)

Equation 3.18 can be modified for grouping terms. On one hand those terms related to effect of friction and on the other hand those referring to shearing. So, the expressions in Eq. 3.25 are obtained for the three components of cutting force.

$$\begin{aligned}
 F_x &= (k_{fe} \sin k_r - k_{re} \cos k_r) \frac{a_p}{\sin k_r} + (k_{fc} \sin k_r - k_{rc} \cos k_r) a_p f_n \\
 F_y &= (k_{fe} \cos k_r + k_{re} \sin k_r) \frac{a_p}{\sin k_r} + (k_{fc} \cos k_r + k_{rc} \sin k_r) a_p f_n \quad (3.25) \\
 F_z &= k_{te} \frac{a_p}{\sin k_r} + k_{tc} a_p f_n
 \end{aligned}$$

In these expressions it can be observed that the component of cutting forces associated to material shearing depends on chip thickness, that is, on feedrate  $f_n$ . However, component of cutting forces due to friction keeps constant and independent of feedrate.

**Table 3.2** Geometrical characteristics of the tool assembly for characterization tests

Geometrical characteristics	Value
Rake angle ( $\gamma_n$ )	$-6^\circ$
Inclination angle ( $\lambda_s$ )	$-6^\circ$
Side-cutting edge angle ( $k_r$ )	$91^\circ$
End-cutting edge angle ( $k_{r1}$ )	$29^\circ$
Nose radius ( $r_n$ )	0.8 mm

If mean values of cutting forces are represented in a graph, a linear behaviour is observed when varying  $f_n$ . This linear behaviour repeats for all cutting speeds and cutting depths tested. As higher feedrate as higher cutting section and hence cutting forces.

Figure 3.7 shows this linear behaviour for different cutting depths ( $a_p$ ) corresponding to the evolution of the tangential component ( $F_z$ ) of cutting force with feedrate ( $f_n$ ).

A least squares interpolation is applied to each curve obtained during a series, which provides the equations of the straight lines and the correlation coefficients ( $R^2$ ). Values of  $R^2$  closed to 1 indicate good linear adjustment. This behaviour allows to express cutting forces as follows (Eq. 3.26):

$$F_{x,y,z} = P_{1x,y,z} + P_{2x,y,z}f_n \quad (3.26)$$

If expressions in Eq. 3.25 equal to experimental expressions in Eq. 3.26, the result is (Eq. 3.27):

$$\begin{aligned} F_x &= P_{1x} + P_{2x}f_n = (k_{fe} \sin k_r - k_{re} \cos k_r) \frac{a_p}{\sin k_r} + (k_{fc} \sin k_r a_p - k_{rc} \cos k_r a_p)f_n \\ F_y &= P_{1y} + P_{2y}f_n = (k_{fe} \cos k_r + k_{re} \sin k_r) \frac{a_p}{\sin k_r} + (k_{fc} \cos k_r a_p + k_{rc} \sin k_r a_p)f_n \\ F_z &= P_{1z} + P_{2z}f_n = k_{te} \frac{a_p}{\sin k_r} + k_{tc} a_p f_n \end{aligned} \quad (3.27)$$

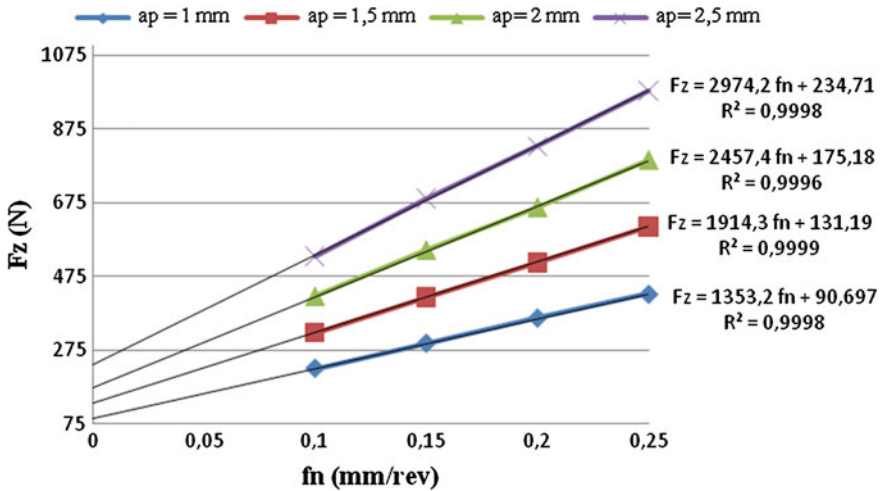


Fig. 3.7 Evolution of cutting force with feedrate ( $V_c = 750$  m/min)

In the previous equalities friction forces are included in  $P_1$  term, which represents the force when feedrate is null, that is, when shearing does not occur. Shearing forces are included in  $P_2$  term, which represents the slope of the regression curve (Fig. 3.8).

Cutting specific coefficients are obtained by solving the system of equations by equalling similar terms (Eq. 3.28).

$$\left\{ \begin{array}{l} P_{1x} = (k_{fe} \sin k_r - k_{re} \cos k_r) \frac{a_p}{\sin k_r} \\ P_{2x} = (k_{fc} \sin k_r - k_{rc} \cos k_r) a_p \\ P_{1y} = (k_{fe} \cos k_r + k_{re} \sin k_r) \frac{a_p}{\sin k_r} \end{array} \right\} \Rightarrow k_{fe}, k_{re}, k_{fc}, k_{rc} \tag{3.28}$$

$$\left\{ \begin{array}{l} P_{1z} = k_{te} \frac{a_p}{\sin k_r} \\ P_{2z} = k_{tc} a_p \end{array} \right\} \Rightarrow k_{te}, k_{tc}$$

This way  $k_{fc}$ ,  $k_{rc}$ ,  $k_{tc}$ ,  $k_{fe}$ ,  $k_{re}$ ,  $k_{te}$  coefficients are obtained corresponding to a specific series, that is, for constant cutting depth ( $a_p$ ) and cutting speed ( $V_c$ ). This process is repeated for the rest of series obtaining different values for the coefficients, what indicates that these coefficients are function of  $V_c$  and  $a_p$ .

Final expressions for cutting specific coefficients incorporating the effect of  $V_c$  and  $a_p$  are obtained applying statistical techniques to improve the reliability of results. Firstly, the sensibility of the six specific coefficients with regard to  $V_c$  and  $a_p$  is by means ANOVA. Once the significant terms are identified for each coefficient, regression analysis is applied to express the relationship between the coefficients and the influence variables. Different regression models can be analysed to check the best fitting. This statistical study is detailed in Sect. 3.1.2.6. Figure 3.9 outlines this sequence for obtaining the cutting specific coefficients.

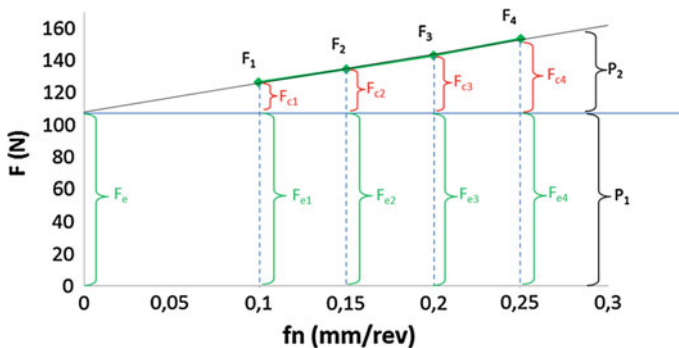


Fig. 3.8 Decomposition of cutting force into shearing force and friction forces (simplified model)

### 3.1.2.5 Determination of the Coefficients Using the Complete Model (Considering Tool Tip Radius)

In this case, expressions for  $F_x$ ,  $F_y$  and  $F_z$  detailed in Eq. 3.25 are used to determine the cutting specific coefficients, that is, those corresponding to the mechanistic model obtained when considering variable chip section by the effect of tool tip radius. To simplify these expressions the equations are rewritten in such a way that the specific coefficients corresponding to the curved segment are considered independent of angle  $\theta$ . Therefore they can be extracted out of the integral (Eq. 3.29):

$$\begin{aligned}
 F_{xexp} &= k_{fe} G_{fx} + k_{re} G_{rx} + k_{fc} Z_{fx} + k_{rc} Z_{rx} \\
 F_{yexp} &= k_{fe} G_{fy} + k_{re} G_{ry} + k_{fc} Z_{fy} + k_{rc} Z_{ry} \\
 F_{zexp} &= k_{te} G_{tz} + k_{tc} Z_{tz}
 \end{aligned}
 \tag{3.29}$$

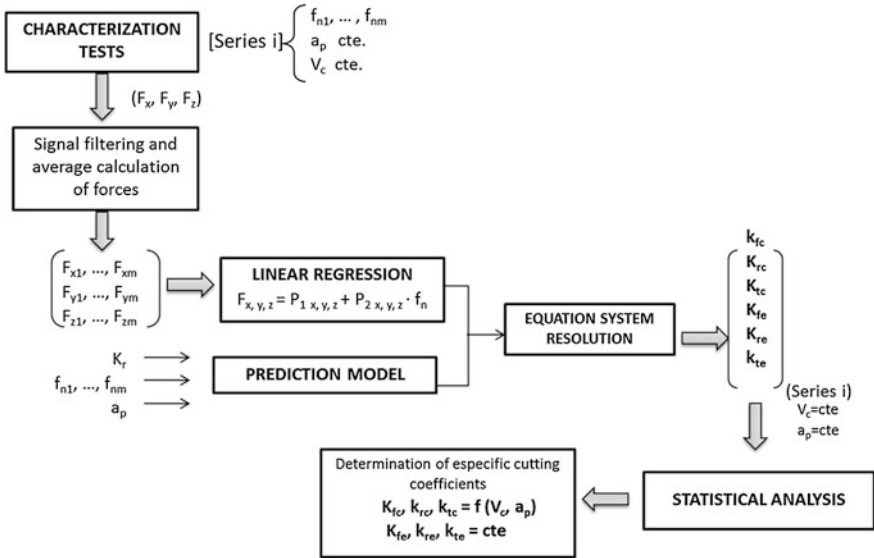


Fig. 3.9 Scheme for the calculation of cutting specific coefficients (simplified model)



where

$$\begin{aligned}
 G_{fx} &= \sin k_r S_I + \int_{\theta_1}^{\theta_2} \sin\left(\theta - \frac{\pi}{2}\right) r_n d\theta; & G_{rx} &= -\cos k_r S_I - \int_{\theta_1}^{\theta_2} \cos\left(\theta - \frac{\pi}{2}\right) r_n d\theta \\
 G_{fy} &= \cos k_r S_I + \int_{\theta_1}^{\theta_2} \cos\left(\theta - \frac{\pi}{2}\right) r_n d\theta; & G_{ry} &= \sin k_r S_I + \int_{\theta_1}^{\theta_2} \sin\left(\theta - \frac{\pi}{2}\right) r_n d\theta \\
 Z_{fx} &= \sin k_r A_I + \int_{\theta_1}^{\theta_2} \sin\left(\theta - \frac{\pi}{2}\right) h(\theta) r_n d\theta; & Z_{rx} &= -\cos k_r A_I - \int_{\theta_1}^{\theta_2} \cos\left(\theta - \frac{\pi}{2}\right) h(\theta) r_n d\theta \\
 Z_{fy} &= \cos k_r A_I + \int_{\theta_1}^{\theta_2} \cos\left(\theta - \frac{\pi}{2}\right) h(\theta) r_n d\theta; & Z_{ry} &= \sin k_r A_I + \int_{\theta_1}^{\theta_2} \sin\left(\theta - \frac{\pi}{2}\right) h(\theta) r_n d\theta \\
 G_{Iz} &= S_I + \int_{\theta_1}^{\theta_2} r_n d\theta; & Z_{Iz} &= A_I + \int_{\theta_1}^{\theta_2} h(\theta) r_n d\theta
 \end{aligned}
 \tag{3.30}$$

Contrary to the simplified model, in this case friction forces increase with  $f_n$  because length of the curved segment involved in the cutting increases also with feedrate. This fact is clear when observing the expression in Eq. 3.7 to calculate  $S_{II}$ , with integration limits affected by  $f_n$ . By solving the integral in Eq. 3.7 the length of the curved segment involved in the cutting is obtained as a function of  $f_n$  (Eq. 3.31).

$$S_{II} = r_n \left[ \frac{\pi}{2} + k_r - \cos^{-1}\left(\frac{f_n}{2r_n}\right) \right]
 \tag{3.31}$$

As aforementioned for the simplified model, the correspondence among the terms of the mechanistic model and the terms experimentally obtained is indicated in Fig. 3.10.

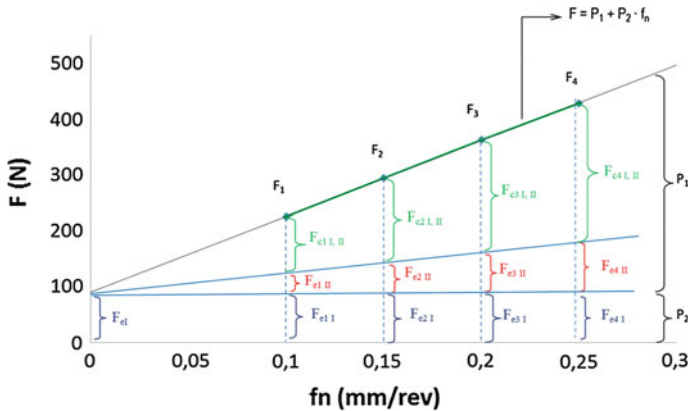


Fig. 3.10 Decomposition of the cutting shearing force and friction force (complete model)

In this Fig. 3.10 friction force corresponding to the straight segment of cutting edge (Area I) is equivalent to cutting force obtained when extrapolating experimental linear regression up to null feedrate. The slope of the linear regression corresponds to the sum of friction force in the edge curved segment (Area II) and the sum of shearing forces along the full edge (areas I and II). In this case, to calculate the cutting specific coefficients the system of equations to solve is indicated in Eq. 3.32.

$$\begin{bmatrix} \left[ \begin{matrix} F_{x1} \\ \vdots \\ F_{xm} \end{matrix} \right]_{exp} \\ \left[ \begin{matrix} F_{y1} \\ \vdots \\ F_{ym} \end{matrix} \right]_{exp} \\ \left[ \begin{matrix} F_{z1} \\ \vdots \\ F_{zm} \end{matrix} \right]_{exp} \end{bmatrix} = \begin{bmatrix} \left[ \begin{matrix} G_{fx1} & G_{rx1} & Z_{fx1} & Z_{rx1} \\ \vdots & \vdots & \vdots & \vdots \\ G_{fxm} & G_{rxm} & Z_{fxm} & Z_{rxm} \end{matrix} \right] \\ \left[ \begin{matrix} G_{fy1} & G_{ry1} & Z_{fy1} & Z_{ry1} \\ \vdots & \vdots & \vdots & \vdots \\ G_{fym} & G_{rym} & Z_{fym} & Z_{rym} \end{matrix} \right] \\ \left[ \begin{matrix} G_{tz1} & Z_{tz1} \\ \vdots & \vdots \\ G_{tzm} & Z_{tzm} \end{matrix} \right] \end{bmatrix} \times \begin{bmatrix} k_{fe} \\ k_{re} \\ k_{fc} \\ k_{rc} \end{bmatrix} \quad (3.32)$$

where  $F_{x1}, \dots, F_{xm}; F_{y1}, \dots, F_{ym}; F_{z1}, \dots, F_{zm}$ , are the mean values of cutting forces recorded during a particular series of tests. Terms  $G_{ij}$  and  $Z_{ij}$  depend only on the cutting geometry and they can be calculated using the expressions indicated in Eq. 3.30. The  $m$  sub-index is the number of levels considered for the feedrate ( $f_{n1}, \dots, f_{nm}$ ) in each series. In this system the number of equations is superior to the number of unknown quantities and it can be solved using the least squares method. Therefor  $k_{fc}, k_{rc}, k_{te}, k_{fe}, k_{re}, k_{te}$  coefficients are obtained for a particular series, that is, for specific cutting speed ( $V_c$ ) and cutting depth ( $a_p$ ). As aforementioned, the process is repeated with several series obtaining different values for the coefficients, what indicates that cutting specific coefficients are function of  $V_c$  and  $a_p$ . Again, statistical techniques are used to find out the final expressions for the specific coefficients that incorporate the effect of  $V_c$  and  $a_p$ , similarly to the process carried out for the simplified model. Figure 3.11 outlines the process for obtaining the cutting specific coefficients using the complete model.

### 3.1.2.6 Effect of Cutting Speed and Feedrate on the Cutting Specific Coefficients

Once the values of the cutting specific coefficients are obtained for each series, the next step is to determine expressions that best fit these coefficients with variations in  $V_c$  and  $a_p$ . Statistical techniques are applied based on regression analysis for obtaining these expressions. In the next paragraphs results of this analysis are presented for both the simplified and the complete models.

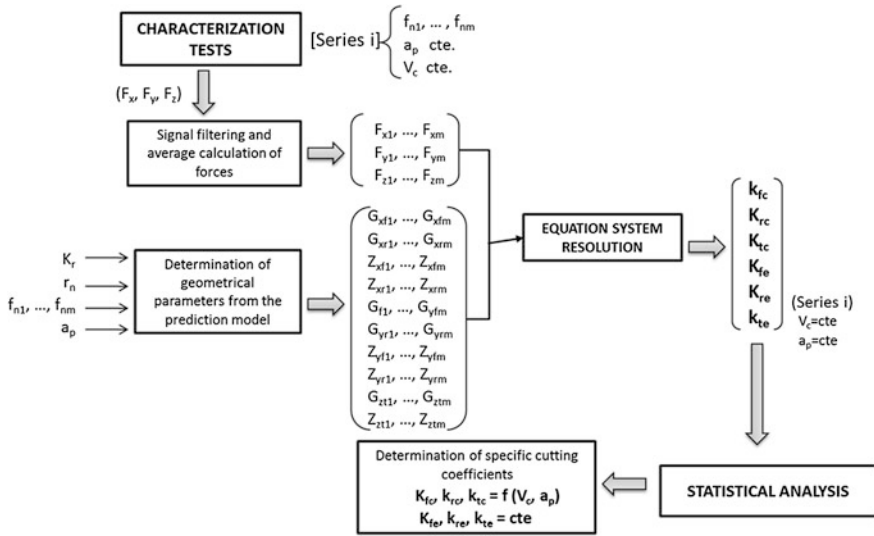


Fig. 3.11 Scheme for the calculation of cutting specific coefficients (complete model)

### Effect of $V_c$ and $a_p$ on the Cutting Specific Coefficients for the Simplified Model (Without Considering Tool Tip Radius)

Since values of cutting specific coefficients obtained for each series of tests are different, the sensibility of these coefficients should be analysed with regard to variations in  $V_c$  and  $a_p$ . Firstly, it is necessary to analyse if  $V_c$  and  $a_p$  parameters affect significantly to the cutting specific coefficients. A variance analysis (ANOVA) is carried out to decompose the total variability into components which are assignable to a specific source of variability. So, the significant variables of influence can be identified.

P-values for the ANOVA carried out on the six cutting specific coefficients with a confidence interval of 95 % are presented in Table 3.3. If P-value is inferior to 0.05 the null hypothesis ( $H_0$ ) of mean equality can be rejected, concluding that such input variable causes a significant effect in the response variable.

Table 3.3 ANOVA results for the cutting specific coefficients (simplified model)

Response	P-value (95 %)		$R^2$	$R^2_{adj}$
	$V_c$	$a_p$		
$k_{fc}$	0.003	0.024	0.84	0.80
$k_{rc}$	0.001	0.000	0.95	0.92
$k_{tc}$	0.000	0.008	0.90	0.86
$k_{fe}$	0.079	0.204	0.63	0.38
$k_{re}$	0.011	0.000	0.98	0.97
$k_{te}$	0.608	0.329	0.40	0

The ANOVA indicates that the three shearing coefficients ( $k_{fc}$ ,  $k_{tc}$ ,  $k_{rc}$ ) suffer significant variations with the two  $V_c$  and  $a_p$  variables and, therefore, it is advisable to adjust the model to consider both variables. The P-value of the variables corresponding to the friction coefficients  $k_{fc}$  and  $k_{tc}$  is superior to 0.05, meaning that these coefficients are not sensitive to variations of  $V_c$  and  $a_p$ . Therefore, the best estimator for  $k_{fc}$  and  $k_{tc}$  is the average value of the values obtained for these coefficients and to consider them constant coefficients. However, the coefficient of friction  $k_{rc}$  is affected significantly by both variables and, therefore, this coefficient should be expressed as a function of  $V_c$  and  $a_p$ . However, if results are analysed from the point of view of cutting process, the three friction coefficients can be considered constant. Many authors propose to use variable shearing coefficients but constant friction coefficients [4]. Lee and Altintas [5] checked experimentally that friction coefficients keep constant for a wide range of cutting conditions. The behaviour of friction force should be the same in the three directions (axial, radial and tangential) and therefore it is more correct to have similar expressions for the three coefficients. On the other hand, in the mechanistic model presented in previous sections, the total force is the sum of shearing force and friction force. The contribution of each of these force components depends on the magnitude of the coefficients. Values obtained for shearing coefficients (Sect. 3.1.2.4) are higher than values for friction coefficients and, consequently, small deviations in the friction coefficients produce insignificant errors in the prediction of the total force. Besides, in the validation stage at the end of the chapter, comparison between force prediction considering  $k_{rc}$  constant and considering  $k_{rc}$  function of  $a_p$  and  $V_c$  provides minor differences.

Once the analysis of sensibility is accomplished, regression analysis is used to define the expressions for the shearing coefficients. The evolution of the three shearing coefficients with  $V_c$  and  $a_p$  is represented in Fig. 3.12.

It is observed that the three coefficients show a linear evolution with both variables. The value of the  $R^2$  coefficient of linear determination is closed to 1, which indicates good linear correlation. Other regression models (polynomial,

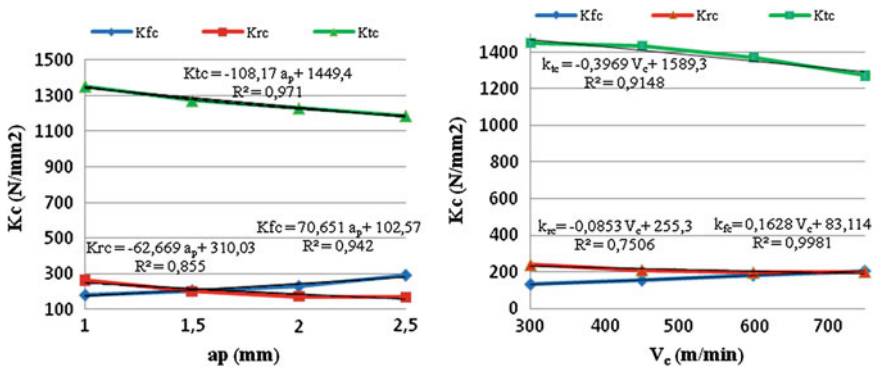


Fig. 3.12 Evolution of shearing specific coefficients with  $a_p$  and  $V_c$

logarithmic) provide lesser adjustment. Therefore, a linear multiple regression is developed for each shearing coefficient with two independent variables  $V_c$  and  $a_p$  (Eq. 3.33).

$$k_{ij} = \beta_0 + \beta_1 V_c + \beta_2 a_p \tag{3.33}$$

This equation represents a linear function where coefficients  $\beta_0$ ,  $\beta_1$  and  $\beta_2$  are unknown. The model describes a plane in the two-dimensional  $V_c$ - $a_p$  space.  $\beta_0$  defines the intersection of the plane with the ordinates axis.  $\beta_1$  represents the expected change in the coefficient  $k_{ij}$  for a unitary change of  $V_c$  when  $a_p$  is constant.  $\beta_2$  represents the expected change in the coefficient  $k_{ij}$  for a unitary change of  $a_p$  when  $V_c$  is constant.

Initially the regression parameters are determined by least squares method. Next the model is verified using the  $R^2$  and adjusted  $R^2$  statistical factors, as well as variance analysis to evaluate significance of the regression and analysis of residuals. Table 3.4 contains a summary of results obtained using multiple linear regression on the three shearing specific coefficients. The Table includes for each coefficient the equation, the P-value corresponding to the t test to evaluate the contribution of each variable and the values of  $R^2$  and adjusted  $R^2$  multiple determination coefficients that evaluate the variability percentage in the response. Finally, the P-value for the test of significance is included to determine if at least one of the variables contributes significantly to the model.

The P-value assigned to both variables ( $V_c$  and  $a_p$ ) is inferior to 0.05, what indicates that their influence on the coefficients is significant. On the other hand, the P-value related to the regression analysis is also inferior to 0.05 and the values of  $R^2$  and  $R^2_{adj}$  are superior to 80 % indicating that the fit is correct.

Additionally, to carry out an analysis of residuals is necessary in order to assure the quality of the model. Four types of residual graphs are analysed:

- Graph of normal probability of residuals, to verify the hypothesis of linearity.
- Graph of residuals-estimated values, to verify the hypothesis of homoscedasticity.
- Histogram of residuals, to verify the hypothesis of normality.
- Graph of residuals in time sequence, to verify the hypothesis of independence.

**Table 3.4** Results of multiple linear regression on the shearing coefficients (simplified model)

Response	Equation	Predictor		$R^2$ (%)	$R^2_{adj}$ (%)	Regression P-value
		$V_c$ (m/ min) P- value	$a_p$ (mm) P- value			
$K_{fc}$	$18.9 + 0.172 V_c + 39.7 a_p$	0.000	0.003	83.2	81.1	0.000
$K_{rc}$	$376 - 0.103 V_c - 63.4 a_p$	0.000	0.013	86.8	84.2	0.000
$K_{tc}$	$1875 - 0.589 V_c - 114 a_p$	0.000	0.001	92.6	90.0	0.000

For example, in Fig. 3.13 four residuals graphs obtained for the  $k_{fc}$  coefficient are presented. These graphs indicate adequate behaviour. The same can be said for the rest of coefficients.

The following conclusions can be drawn from this study:

- Shearing coefficients can be adequately fit through multiple linear regression with  $V_c$  and  $a_p$  variables.
- Friction coefficients  $k_{fc}$  and  $k_{tc}$  are not affected significantly by variations of  $V_c$  and  $a_p$  and, therefore, can be considered constant. The estimator for these coefficients is the average of values obtained in the series.
- Friction coefficient  $k_{rc}$  varies with  $a_p$  and  $V_c$  but can be considered constant. This simplification does not introduce significant errors in the prediction model.

Therefore, the expressions in Table 3.5 are identified for representing the specific cutting coefficients.

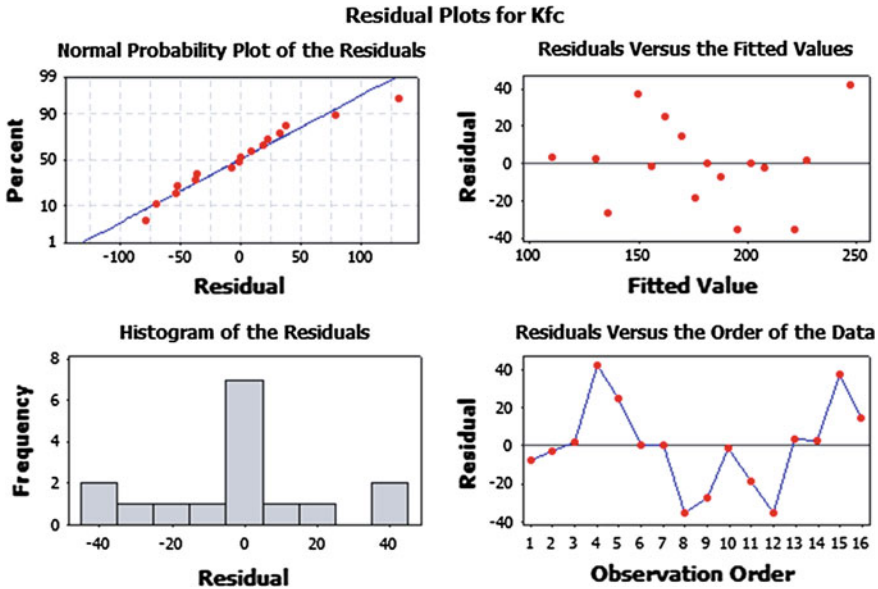


Fig. 3.13 Graphs of residuals for the  $k_{fc}$  coefficient

Table 3.5 Expressions for the specific cutting coefficients (simplified model)

Shearing coefficients	Friction coefficients
$k_{fc} = 18.9 + 0.172 V_c + 39.7 a_p$	$k_{fe} = 113.113$
$k_{rc} = 376 - 0.103 V_c - 63.4 a_p$	$k_{re} = 64.136$
$k_{tc} = 1875 - 0.589 V_c - 114 a_p$	$k_{te} = 91.770$

### Effect of $V_c$ and $a_p$ on the Cutting Specific Coefficients for the Complete Model (Considering Tool Tip Radius)

The same methodology exposed previously is used again. Firstly, an ANOVA analysis is carried out to determine if  $V_c$  and  $a_p$  affect significantly to the specific cutting coefficients. In Table 3.6 the P-values obtained with ANOVA are showed for the six specific cutting coefficients, with a confidence interval of 95 %.

For the three shearing coefficients ( $k_{fc}$ ,  $k_{rc}$  and  $k_{tc}$ ) the independent variable  $a_p$  has a P-value superior to 0.05 which indicates that the null hypothesis ( $H_0$ ) cannot be rejected and therefore this variable does not affect significantly to these coefficients. In spite of it, it is more appropriate to use a linear model that includes both  $V_c$  and  $a_p$  variables, since an explicit dependence of the coefficients with cutting speed and cutting depth assures sensibility of the model to variations of these cutting parameters. The lack of a significant relationship between these coefficients with  $a_p$  does not imply an absence of link. If the variable range is small and the experimental error is high it is common not to observe a significant relationship. The reason is that precision in slope estimation depends on the range of variation of the variable; if this range is small, the variance of slope estimation will be high and it will not allow to conclude that a relationship exists [6]. In many cases, the range of variation is not sufficiently wide to detect variations in the response and, therefore, the significance analysis is negative; but this fact does not mean that the response will not be really affected by the variable when the variation range increases. Consequently, a model that includes the variable will have better predictive capacity outside the tested range of conditions.

For  $k_{fc}$  and  $k_{rc}$  friction coefficients the  $V_c$  and  $a_p$  variables have a P-value superior to 0.05, hence these variables do not affect significantly to the coefficients. Therefore, these coefficients can be considered constant and the best estimator is the average of values. This result is equivalent to the one obtained in the simplified model. Although the  $k_{rc}$  friction coefficient is affected significantly by both variables, it is more appropriate to outline similar expressions for the three friction coefficients, as indicated in the previous section. Therefore, the proposal is to consider variable shearing coefficients and constant friction coefficients. Figure 3.14 shows the evolution of the coefficients with the variables. A linear dependence is observed, similarly to the simplified model.

**Table 3.6** ANOVA results for the cutting specific coefficients (complete model)

Response	P-value (95 %)		$R^2$	$R^2_{adj}$
	$V_c$	$a_p$		
$k_{fc}$	0.005	0.766	0.75	0.58
$k_{rc}$	0.000	0.725	0.91	0.85
$k_{tc}$	0.000	0.804	0.86	0.76
$k_{fe}$	0.064	0.299	0.62	0.37
$k_{re}$	0.009	0.006	0.84	0.73
$k_{te}$	0.603	0.418	0.36	0

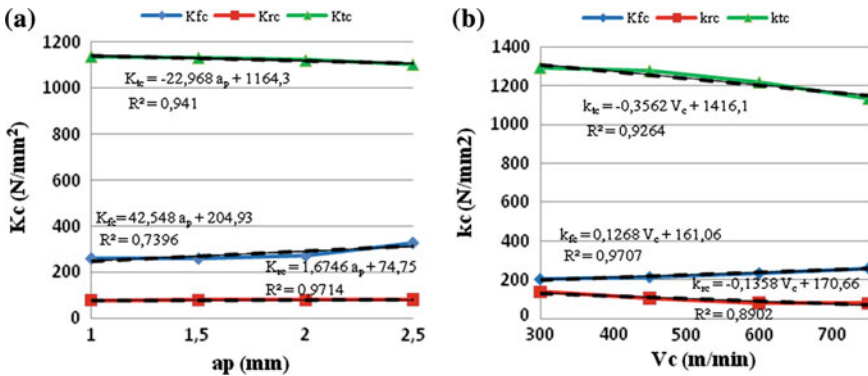


Fig. 3.14 Evolution of shearing coefficients with  $V_c$  and  $a_p$

In view of the results, a multiple linear regression is considered for each specific cutting coefficients, as done in the simplified model. Table 3.7 shows a summary of the results for the three shearing coefficients.

The P-value of the regression model is inferior to 0.05 for the three coefficients, which indicates that the model is adequate to explain the response since at least one of the variables affect significantly ( $V_c$  in this case). On the other hand,  $R^2$  and  $R^2_{adj}$  values are above 70 % and the analysis of residuals is consistent. As conclusion, expressions of the specific cutting coefficients for the complete model are indicated in Table 3.8.

Table 3.7 Results of multiple linear regression on the shearing coefficients (complete model)

Response	Equation	Predictor		$R^2$ (%)	$R^2_{adj}$ (%)	Regression P-value
		$V_c$ (m/min) P-value	$a_p$ (mm) P-value			
$k_{fc}$	$158 + 0.132 V_c + 5.6 a_p$	0.005	0.635	77.9	73.6	0.014
$k_{rc}$	$169 - 0.150 V_c + 5.78 a_p$	0.000	0.414	87.0	83.5	0.000
$k_{tc}$	$1537 - 0.533 V_c - 21.6 a_p$	0.000	0.381	87.9	84.5	0.000

Table 3.8 Expressions for the specific cutting coefficients (complete model)

Shearing coefficients	Friction coefficients
$k_{fc} = 158 + 0.132 V_c + 5.6 a_p$	$k_{fe} = 115.280$
$k_{rc} = 169 - 0.150 V_c + 5.78 a_p$	$k_{re} = 8.674$
$k_{tc} = 1537 - 0.533 V_c - 21.6 a_p$	$k_{te} = 78.835$



### 3.1.2.7 Validation of the Models

In order to confirm the models, a series of validation tests is carried out. The values of specific cutting coefficients calculated in the previous section are introduced in the related mechanistic model (Sects. 3.1.2.1 and 3.1.2.2) together with the cutting conditions and the geometrical characteristics of the tool. This way, values of  $F_x$ ,  $F_y$  and  $F_z$  forces are predicted by the model and they can be compared with the mean values of the experimental forces recorded with the dynamometric plate.

The two outlined mechanistic models are validated comparing the level of precision achieved in each one. The validation test is carried out in four stages:

- First stage: material characterization tests are replicated to estimate the confidence level of the model.
- Second stage: new series of tests are carried out at different conditions than those used in the characterization tests, but always inside the initial interval of cutting conditions and maintaining tool geometry.
- Third stage: additional series of tests outside the initial interval of cutting conditions than those used in the characterization tests, maintaining tool geometry.
- Fourth stage: a last series of tests inside and outside the initial interval of cutting conditions used in the characterization tests, changing tool geometry (lead angle and tip radius).

#### Results of the First Stage of Validation Tests

Table 3.9 contains the force values obtained experimentally and their comparison with estimated values using the simplified and the complete model. The column entitled “% Error” represents the relative error calculated by means of Eq. 3.34.

$$\%Error = \left( \frac{F_{pred} - F_{exp}}{F_{exp}} \right) \cdot 100 \quad (3.34)$$

It can be observed that adjustment of the complete model is better, providing relative errors lower than 5 % for the three components of the cutting force. The capability of prediction of the simplified model is only slightly worse for the  $F_x$  and  $F_z$  components, reaching maximum errors of 6 %. However, for the  $F_y$  component high errors up to 28 % are obtained, which makes necessary to consider the effect of tool tip radius to obtain valid predictions. Figure 3.15 shows the errors obtained for this component. For  $a_p = 1.5$  mm the errors are similar to those for the complete model (tests 3, 6, 10, 13 and 14); when  $a_p$  is lower than 1.5 mm the predicted value is inferior to the experimental value (tests 1, 2, 9); when  $a_p$  is greater than 1.5 mm the predicted value is superior to the experimental value.

**Table 3.9** Comparison between experimental and estimated forces in the first validation stage

Test no	Conditions			$F_x$ (N)					
	$V_c$ (m/min)	$a_p$ (mm)	$f_n$ (mm/rev)	Experimental	Complete model		Simplified model		% Error
				Estimated	Estimated	% Error	Estimated	% Error	
1	750	1	0.1	126.60	129.07	1.95	133.40	5.37	
2	750	1	0.2	143.16	148.05	3.41	152.57	6.57	
3	750	1.5	0.15	210.94	216.27	2.53	218.82	3.73	
4	750	2	0.2	302.42	317.38	4.95	320.57	6.00	
5	750	2.5	0.25	440.38	432.82	-1.72	441.56	0.27	
6	600	1.5	0.15	210.19	210.73	0.25	213.07	1.37	
7	600	2	0.1	273.60	266.77	-2.50	269.41	-1.53	
8	600	2.5	0.25	399.58	418.32	4.69	425.60	6.51	
9	450	1	0.15	128.49	130.45	1.53	135.33	5.32	
10	450	1.5	0.2	208.28	217.41	4.38	219.32	5.30	
11	450	2	0.2	287.12	298.40	3.93	300.15	4.54	
12	450	2.5	0.2	377.61	379.96	0.62	384.83	1.91	
13	300	1.5	0.1	191.02	189.19	-0.96	211.67	0.26	
14	300	1.5	0.2	212.85	209.90	-1.38		-0.56	
15	300	2	0.15	273.22	273.32	0.04	274.57	0.50	
16	300	2.5	0.15	353.57	347.41	-1.74	350.45	-0.88	
Test no	Conditions			$F_y$ (N)					
	$V_c$ (m/min)	$a_p$ (mm)	$f_n$ (mm/rev)	Experimental	Complete model		Simplified model		% Error
				Estimated	Estimated	% Error	Estimated	% Error	
1	750	1	0.1	118.53	121.16	2.22	85.37	-27.98	
2	750	1	0.2	143.83	145.88	1.42	108.57	-24.52	

(continued)

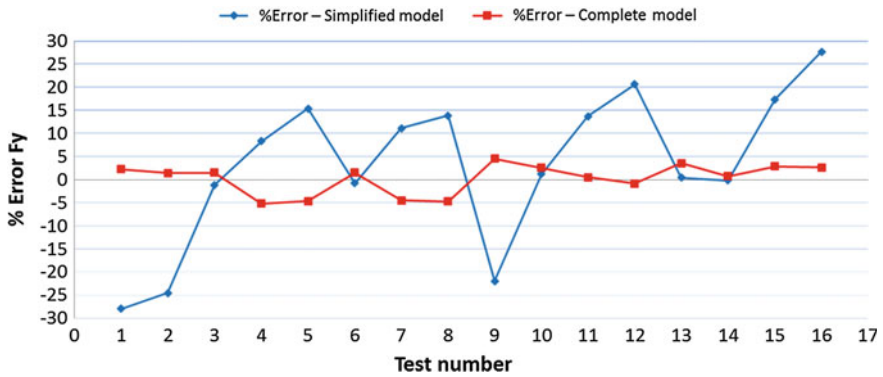
Table 3.9 (continued)

Test no	Conditions			$F_y$ (N)					
	$V_c$ (m/min)	$a_p$ (mm)	$f_n$ (mm/rev)	Experimental	Estimated	% Error	Estimated	% Error	
3	750	1.5	0.15	139.82	141.94	1.51	138.24	-1.13	
4	750	2	0.2	176.81	167.59	-5.22	191.51	8.31	
5	750	2.5	0.25	208.34	198.62	-4.66	240.35	15.36	
6	600	1.5	0.15	142.95	145.13	1.52	141.82	-0.79	
7	600	2	0.1	144.96	138.47	-4.48	161.09	11.13	
8	600	2.5	0.25	219.73	209.42	-4.69	250.29	13.91	
9	450	1	0.15	130.32	136.25	4.55	101.74	-21.93	
10	450	1.5	0.2	160.81	164.87	2.52	162.78	1.23	
11	450	2	0.2	179.59	180.48	0.50	204.22	13.72	
12	450	2.5	0.2	198.37	196.67	-0.86	239.26	20.62	
13	300	1.5	0.1	129.84	134.47	3.57	130.40	0.43	
14	300	1.5	0.2	167.87	169.08	0.72	167.55	-0.19	
15	300	2	0.15	161.04	165.68	2.88	189.02	17.37	
16	300	2.5	0.15	175.65	180.30	2.64	224.26	27.67	
Test no	Conditions			$F_z$ (N)					
	$V_c$ (m/min)	$a_p$ (mm)	$f_n$ (mm/rev)	Experimental	Estimated	% Error	Estimated	% Error	
1	750	1	0.1	225.44	234.94	4.21	223.71	-0.77	
2	750	1	0.2	362.79	365.10	0.64	355.63	-1.97	
3	750	1.5	0.15	418.94	419.26	0.08	421.68	0.65	
4	750	2	0.2	662.49	658.12	-0.66	665.67	0.48	

(continued)

Table 3.9 (continued)

Test no	Conditions			$F_z$ (N)	Complete model			Simplified model		
	$V_c$ (m/min)	$a_p$ (mm)	$f_n$ (mm/rev)		Experimental	Estimated	% Error	Estimated	% Error	
										Estimated
5	750	2.5	0.25	978.31	950.07	-2.89	947.12	-3.19		
6	600	1.5	0.15	445.49	437.96	-1.69	441.56	-0.88		
7	600	2	0.1	445.08	437.26	-1.76	442.29	-0.63		
8	600	2.5	0.25	990.40	1002.14	1.19	1002.33	1.21		
9	450	1	0.15	314.65	324.12	3.01	316.18	0.49		
10	450	1.5	0.2	557.23	563.31	1.09	569.36	2.18		
11	450	2	0.2	717.28	724.70	1.03	736.35	2.66		
12	450	2.5	0.2	887.75	883.93	-0.43	891.93	0.47		
13	300	1.5	0.1	349.05	365.39	4.68	366.77	5.08		
14	300	1.5	0.2	563.15	588.62	4.52	595.87	5.81		
15	300	2	0.15	597.98	612.30	2.39	624.66	4.46		
16	300	2.5	0.15	780.60	747.60	-4.23	759.45	-2.71		



**Fig. 3.15** Comparison between experimental and estimated  $F_y$  for the two models in the first validation stage

### 3.1.2.8 Results of the Second Stage of Validation Tests

In this case predictions are compared to experimental data using different cutting conditions than those used in the characterization tests, but always inside the same range of cutting conditions. Tool geometry is not varied. Table 3.10 contains the results of the comparison.

Errors for the complete model are inferior to 9 % for the three components of cutting force. On contrary, predictions of  $F_x$  and  $F_z$  components with the simplified model present relative errors of 10 % and for the  $F_y$  component rises to 30 %. Figures 3.16, 3.17 and 3.18 show the comparison between the experimental values and the predicted values for the three cutting force components with both models and the relative error.

Therefore, the conclusion is that inside the same range of cutting conditions the capability of prediction of the complete model is good for the three force components. However the simplified model gives important errors for the axial and tangential components ( $F_x$  and  $F_z$ ) and very high errors for the radial component ( $F_y$ ).

### 3.1.2.9 Results of the Third Stage of Validation Tests

Additional series of tests are now carried out in an extended range of cutting conditions than the range used in the characterization tests, but maintaining cutting tool geometry. Table 3.11 shows the results of the validation with this condition.

Figures 3.19, 3.20 and 3.21 show the comparison between experimental values and predicted values for the three cutting force components with both models and the relative errors. Now, the capability of prediction of the complete model for the  $F_x$  component is better for tests 9 and 12, where cutting depth is equal to tool tip radius. However, the capability of prediction of the simplified model diminishes with these conditions, and the estimation error of  $F_y$  component increases substantially.

**Table 3.10** Comparison between experimental and estimated forces in the second validation stage

Test no	Conditions			$F_x$ (N)					
	$V_c$ (m/min)	$a_p$ (mm)	$f_n$ (mm/rev)	Experimental	Complete model		Simplified model		% Error
					Estimated	% Error	Estimated	% Error	
1	375	2.5	0.13		325.75	340.67	4.58	345.95	5.83
2			0.17	344.44	358.74	4.15	364.52	7.76	
3			0.23	364.12	385.62	5.91	392.38	7.29	
4	675	1	0.3	396.03	416.58	5.19	424.89	4.10	
5			0.13	143.37	131.10	8.56	137.49	5.14	
6			0.17	152.48	138.07	9.45	144.65	2.10	
7			0.23	158.72	148.47	6.46	155.38	2.68	
8	600	2.25	0.3	172.53	160.49	6.98	167.91	8.39	
9			0.13	294.99	314.40	6.58	319.73	9.29	
10			0.17	310.22	333.38	7.47	339.03	8.78	
11			0.23	338.25	361.75	6.95	367.97	7.04	
12			0.3	375.30	394.65	5.16	401.73	6.12	
13	750	1.75	0.13	235.68	245.52	4.18	250.10	7.46	
14			0.17	247.10	261.13	5.68	265.54	6.67	
15			0.23	270.66	284.53	5.12	288.71	4.32	
16			0.3	302.66	311.76	3.01	315.73		

(continued)

**Table 3.10** (continued)

Test no	Conditions			$F_x$ (N)				$F_y$ (N)					
	$V_c$ (m/min)	$a_p$ (mm)	$f_n$ (mm/rev)	Experimental	Estimated	% Error	Simplified model Estimated	% Error	Experimental	Estimated	% Error	Simplified model Estimated	% Error
17	500	2.2	0.13	298.85	302.57	1.25	307.21	2.80					
18			0.17	315.11	319.64	1.44	324.41	2.95					
19			0.23	337.91	345.07	2.12	350.20	3.64					
20			0.3	366.53	374.46	2.16	380.30	3.76					
Test no	Conditions			$F_x$ (N)				$F_y$ (N)					
	$V_c$ (m/min)	$a_p$ (mm)	$f_n$ (mm/rev)	Experimental	Estimated	% Error	Simplified model Estimated	% Error	Experimental	Estimated	% Error	Simplified model Estimated	% Error
1	375	2.5	0.13	6.20	171.44	173.15	1.00	212.49					
2			0.17	189.79	192.10	1.22	230.06	21.22					
3			0.23	212.67	221.24	4.03	256.41	20.57					
4	675	1	0.3	241.04	256.40	6.37	287.15	19.13					
5			0.13	141.03	131.21	6.97	93.36	33.80					
6			0.17	151.34	141.28	6.65	102.96	31.97					
7			0.23	166.53	157.12	5.65	117.36	29.53					
8	600	2.25	0.3	184.67	176.83	4.25	134.16	27.35					
9			0.13	168.91	158.94	5.90	188.96	11.87					
10			0.17	184.41	174.22	5.53	204.06	10.66					
11			0.23	203.03	197.88	2.53	226.72	11.67					
12			0.3	233.02	226.74	2.69	253.15	8.64					
13	750	1.75	0.13	158.28	144.33	8.81	150.64	4.83					
14			0.17	170.28	156.46	8.12	163.52	3.97					
15			0.23	191.71	175.43	8.49	182.83	4.63					
16			0.3	217.72	198.85	8.67	205.37	5.67					

(continued)

Table 3.10 (continued)

Test no	Conditions			$F_y$ (N)					
	$V_c$ (m/min)	$a_p$ (mm)	$f_n$ (mm/rev)	Experimental	Estimated	% Error	Estimated	% Error	
17	500	2.2	0.13	168.25	161.02	4.30	188.70	12.16	
18			0.17	184.88	177.05	4.24	204.69	10.71	
19			0.23	202.88	201.82	0.52	228.66	12.71	
20			0.3	227.65	231.94	1.88	256.64	12.73	
Test no	Conditions			$F_z$ (N)					
	$V_c$ (m/min)	$a_p$ (mm)	$f_n$ (mm/rev)	Experimental	Estimated	% Error	Estimated	% Error	
1	375	2.5	0.13	23.94	659.64	664.22	0.70	674.43	
2			0.17	794.69	800.80	0.77	811.34	2.10	
3			0.23	973.14	1009.55	3.74	1016.71	4.48	
4	675	1	0.3	1146.94	1259.62	9.82	1256.30	9.54	
5			0.13	286.52	278.34	2.86	269.03	6.11	
6			0.17	339.41	332.18	2.13	323.57	4.67	
7			0.23	415.28	416.44	0.28	405.37	2.39	
8	600	2.25	0.3	499.06	520.62	4.32	500.81	0.35	
9			0.13	569.66	568.58	0.19	576.56	1.21	
10			0.17	680.70	681.44	0.11	690.41	1.43	
11			0.23	822.82	854.28	3.82	861.20	4.67	
12			0.3	981.26	1061.86	8.21	1060.46	8.07	

(continued)



Table 3.10 (continued)

Test no	Conditions			$F_z$ (N)	Complete model		Simplified model	
	$V_c$ (m/min)	$a_p$ (mm)	$f_n$ (mm/rev)		Estimated	% Error	Estimated	% Error
13	750	1.75	0.13	Experimental	437.00	2.28	441.30	1.32
14			0.17	528.57	521.30	1.37	527.66	0.17
15			0.23	658.99	651.08	1.20	657.21	0.27
16			0.3	793.13	808.08	1.89	808.34	1.92
17	500	2.2	0.13	570.23	572.94	0.47	582.22	2.10
18			0.17	686.91	688.53	0.24	699.23	1.79
19			0.23	834.03	865.61	3.79	874.75	4.88
20			0.3	1002.82	1078.42	7.54	1079.53	7.65

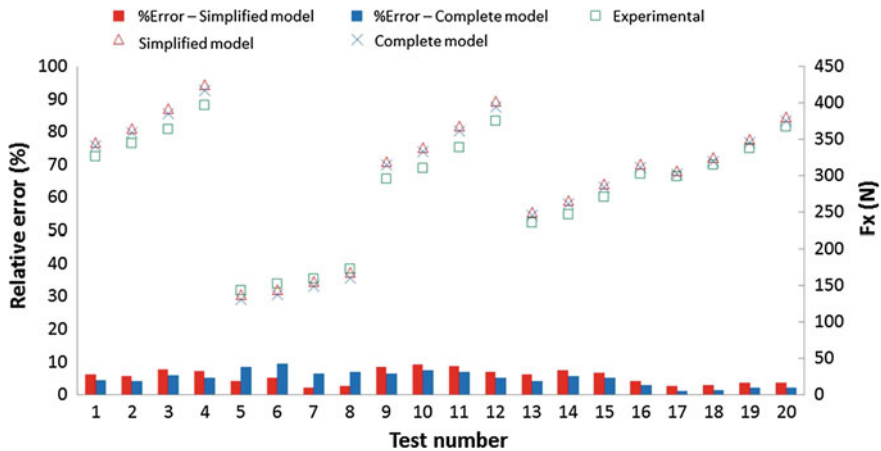


Fig. 3.16 Comparison between experimental and predicted  $F_x$  component for both models in the second stage of validation

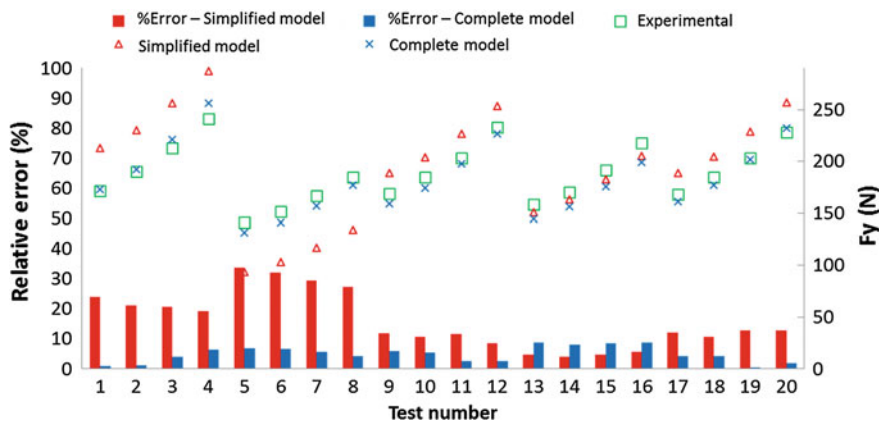


Fig. 3.17 Comparison between experimental and predicted  $F_y$  component for both models in the second stage of validation

Here, the conclusion is that the complete model offers good extrapolation capacity for the three components of cutting force. Errors obtained with this model are similar to errors obtained in the second validation. The simplified model presents acceptable results for the axial and tangential components but errors for the radial component are very high.

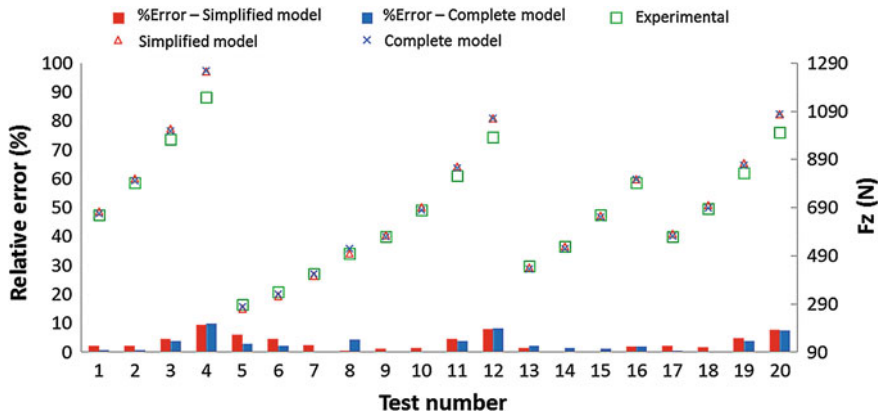


Fig. 3.18 Comparison between experimental and predicted  $F_z$  component for both models in the second stage of validation

### 3.1.2.10 Results of the Fourth Stage of Validation Tests

Finally, a last stage of validation is carried out using different tool geometry. In tests 1–8 tool lead angle is changed; in tests 9–16 the changed parameter is tool tip radius; in tests 17–24 both tool parameters are changed simultaneously. Turning operations are done inside and outside the initial range of cutting conditions as used in the characterization tests. Table 3.12 shows tool geometry, cutting conditions and experimental and predicted forces for both models.

The complete model which considers tool tip radius provides good predictions for those tests where only lead angle or tip radius was modified (tests 1–16). However, in tests where both parameters were modified simultaneously, the relative errors are higher reaching in some case maximum values of 15 % for the  $F_x$  component (although inferior for the other two components). Figures 3.22, 3.23 and 3.24 represent the experimental and estimated forces together with the error.

Finally, it can be concluded that the complete model which considers tool tip radius provides a good capacity of prediction in all conditions, inside and outside the range of initial tested cutting conditions and with different tool geometries. The relative error in all cases is always inferior to 15 % for the axial and radial components, and inferior to 10 % for the tangential component. The capacity of prediction of the simplified model ignoring tool tip radius is inferior for all the tests. This simplified model is valid to predict the tangential force  $F_z$  since similar errors are obtained to those with the complete model. However the prediction errors for the radial component  $F_y$  are very high around 35 %; when tool geometry is modified the prediction errors are also around 35 % for the axial force  $F_x$ .

**Table 3.11** Comparison between experimental and estimated forces in the third validation stage

Test no	Conditions				$F_x$ (N)			
	$V_c$ (m/min)	$a_p$ (mm)	$f_n$ (mm/rev)	Experimental	Estimated	% Error	Estimated	% Error
1	250	2.5	0.13	358.65	334.55	6.72	339.03	5.47
2			0.17	382.27	350.67	8.27	355.48	7.01
3			0.23	403.84	374.56	7.25	380.15	5.87
4			0.3	418.95	401.92	4.07	408.94	2.39
5	850	1	0.13	137.78	135.16	1.90	141.36	2.60
6			0.17	146.61	143.48	2.14	149.71	2.12
7			0.23	158.82	155.99	1.78	162.23	2.15
8			0.3	172.63	170.63	1.16	176.84	2.44
9	775	0.8	0.13	106.00	103.42	2.43	110.96	4.68
10			0.17	109.65	109.03	0.56	116.98	6.69
11			0.23	117.41	117.44	0.02	126.02	7.33
12			0.3	128.75	127.23	1.19	136.56	6.06
Test no	Conditions				$F_y$ (N)			
	$V_c$ (m/min)	$a_p$ (mm)	$f_n$ (mm/rev)	Experimental	Estimated	% Error	Estimated	% Error
1	250	2.5	0.13	185.40	177.89	4.05	216.80	16.94
2			0.17	208.72	198.27	5.01	235.69	12.92
3			0.23	241.53	229.53	4.97	264.03	9.32
4			0.3	263.38	267.13	1.43	297.09	12.80
5	850	1	0.13	135.48	129.67	4.29	90.95	32.87
6			0.17	146.04	139.29	4.62	99.81	31.66

(continued)

Table 3.11 (continued)

Test no	Conditions			$F_y$ (N)				
	$V_c$ (m/min)	$a_p$ (mm)	$f_n$ (mm/rev)	Experimental	Estimated	% Error	Simplified model Estimated	% Error
7			0.23	164.44	154.50	6.04	113.09	31.23
8			0.3	190.26	173.55	8.78	128.59	32.41
9	775	0.8	0.13	123.33	126.89	2.89	74.92	39.25
10			0.17	131.03	136.18	3.93	82.67	36.91
11			0.23	145.05	150.86	4.01	94.30	34.99
12			0.3	162.80	169.26	3.97	107.86	33.75
Test no	Conditions			$F_z$ (N)				
	$V_c$ (m/min)	$a_p$ (mm)	$f_n$ (mm/rev)	Experimental	Estimated	% Error	Simplified model Estimated	% Error
1	250	2.5	0.13	680.71	686.30	0.82	698.35	2.59
2			0.17	835.59	829.87	0.68	842.63	0.84
3			0.23	1043.63	1049.32	0.55	1059.04	1.48
4			0.3	1255.74	1312.20	4.50	1311.52	4.44
5	850	1	0.13	280.44	265.58	5.30	255.63	8.85
6			0.17	332.39	315.21	5.17	306.04	7.93
7			0.23	408.12	392.88	3.73	381.66	6.48
8			0.3	497.24	488.89	1.68	469.89	5.50
9	775	0.8	0.13	221.38	227.09	2.58	211.47	4.48
10			0.17	260.81	269.86	3.47	253.94	2.63
11			0.23	331.94	337.38	1.64	317.65	4.30
12			0.3	411.16	421.78	2.58	391.99	4.66

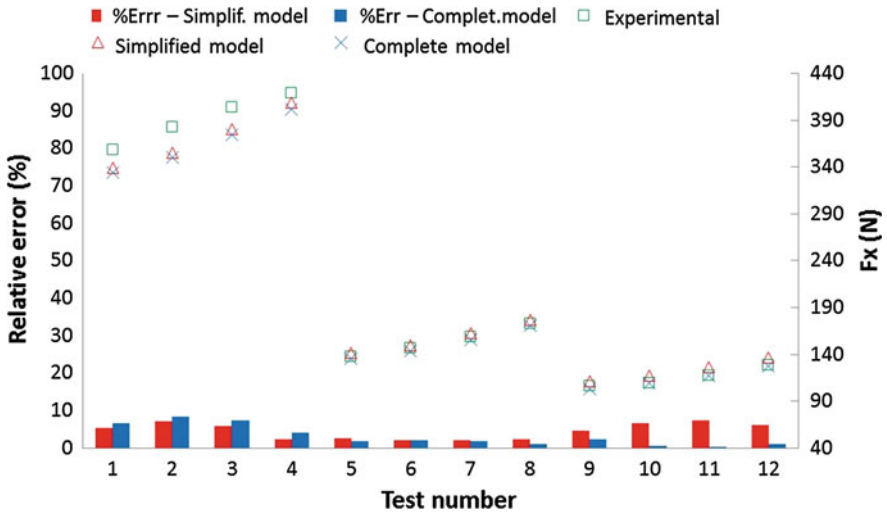


Fig. 3.19 Comparison between experimental and predicted  $F_x$  component for both models in the third stage of validation

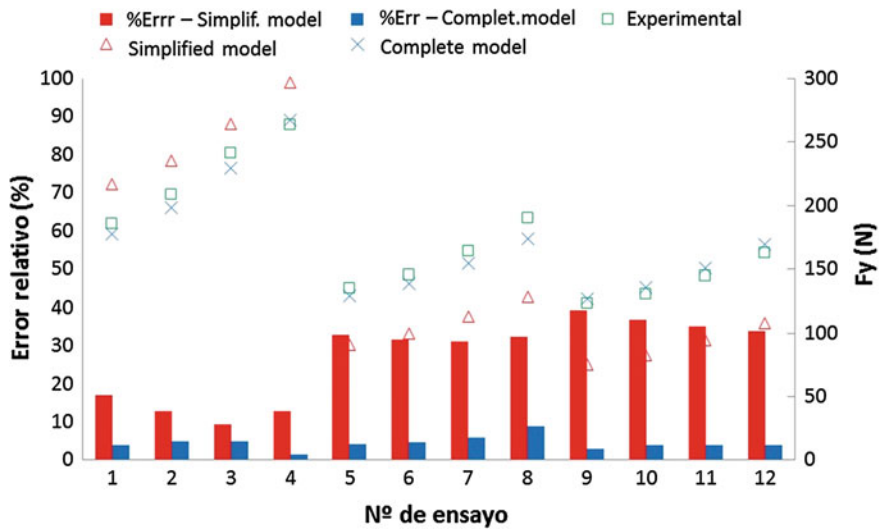


Fig. 3.20 Comparison between experimental and predicted  $F_y$  component for both models in the third stage of validation

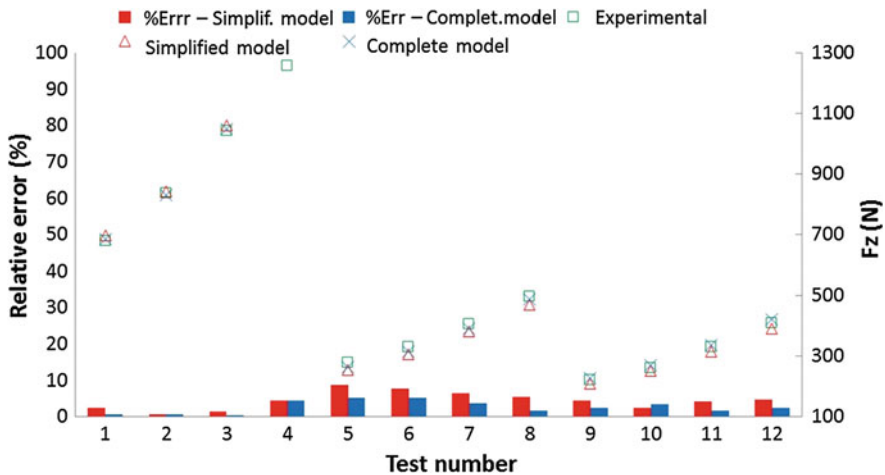


Fig. 3.21 Comparison between experimental and predicted  $F_z$  component for both models in the third stage of validation

## 3.2 Model for Prediction of Cutting Forces Including Tool Wear

The models explained in Sect. 3.1 do not consider tool wear. However, during cutting operations tool wears progressively and consequently tool geometry changes affecting to cutting force. In this section the cutting force prediction model is improved to include the effect of tool wear.

### 3.2.1 Proposed Model for Tool Wear Consideration

Development of a theoretical model for force prediction including tool wear effect is an extremely difficult task due to the no-linear behaviour of wear mechanism. On the other hand, in high speed machining cutting temperature is higher and affects the wear mechanism. That is, typical abrasive wear at low cutting speeds evolves to a complex wear mechanism composed of abrasion, diffusion and oxidation. Complexity due to variations in temperature, properties of material, microscopic and geometric changes in tool caused by built edge and tool wear, makes appropriate to develop prediction models empirically.

The model proposed here considers that cutting force is composed of two factors: (i) a cutting force due to shearing and friction effects in absence of tool wear and (ii) an additional force due to tool wear. This fact is expressed in Eq. 3.35.

Table 3.12 Comparison between experimental and estimated forces in the fourth validation stage

Test no	Tool geometry		Conditions				$F_x$ (N)					
	$k_r$	$f_n$	$V_c$ (m/min)	$a_p$ (mm)	$f_n$ (mm/rev)	Experimental		Complete model		Simplified model		
						Predicha	% Error	Predicha	% Error	Predicha	% Error	
1	60	0.8	450	1.5	0.1	174.10	178.10	2.30	116.78	32.92		
2					0.15	178.14	186.03	4.43	118.11	33.70		
3					0.2	181.19	193.65	6.88	120.23	33.64		
4					0.25	184.14	200.94	9.13	122.09	33.70		
5	60	0.8	600	2	0.1	244.23	246.12	0.77	168.33	31.08		
6					0.15	248.81	260.52	4.70	176.41	29.10		
7					0.2	256.48	274.63	7.08	184.49	28.07		
8					0.25	265.58	288.45	8.61	192.57	27.49		
9	90	1.2	450	1.5	0.1	174.41	183.38	5.14	195.34	12.00		
10					0.15	186.35	193.70	3.95	207.33	11.26		
11					0.2	199.18	203.94	2.39	219.32	10.11		
12					0.25	207.46	214.09	3.19	231.32	11.50		
13	90	1.2	600	2	0.1	250.07	257.52	2.98	269.41	7.74		
14					0.15	266.69	276.18	3.56	289.89	8.70		
15					0.2	281.05	294.80	4.89	310.36	10.43		
16					0.25	300.67	313.39	4.23	330.83	10.03		
17	60	1.2	525	2	0.13	221.90	246.94	11.28	169.27	23.72		
18					0.17	228.99	256.59	12.05	174.53	23.78		
19					0.23	236.71	270.75	14.38	182.42	22.94		
20					0.3	248.69	286.79	15.32	191.63	22.94		
21	60	1.2	800	1.5	0.13	181.34	191.98	5.87	131.26	27.62		

(continued)



Table 3.12 (continued)

Test no	Tool geometry		Conditions		F <sub>x</sub> (N)				
	k <sub>r</sub>	r <sub>n</sub>	V <sub>c</sub> (m/min)	a <sub>p</sub> (mm)	f <sub>n</sub> (mm/rev)	Experimental	Complete model Predicha	Simplified model Predicha	% Error
22					0.17	182.34	201.74	136.53	25.12
23					0.23	192.84	216.15	144.44	25.10
24					0.3	212.78	232.59	153.66	27.79
Test no	Tool geometry		Conditions		F <sub>y</sub> (N)				
	k <sub>r</sub>	r <sub>n</sub>	V <sub>c</sub> (m/min)	a <sub>p</sub> (mm)	f <sub>n</sub> (mm/rev)	Experimental	Complete model Predicha	Simplified model Predicha	% Error
1	60	0.8	450	1.5	0.1	195.87	204.75	236.32	20.65
2					0.15	216.73	224.48	257.40	18.77
3					0.2	235.09	244.52	291.13	23.84
4					0.25	248.54	264.92	320.64	29.01
5	60	0.8	600	2	0.1	254.80	252.17	311.49	22.25
6					0.15	276.08	276.85	337.80	22.36
7					0.2	299.09	301.88	364.10	21.74
8					0.25	319.64	327.31	390.41	22.14
9	90	1.2	450	1.5	0.1	163.24	185.33	128.01	21.58
10					0.15	183.84	203.07	145.40	20.91
11					0.2	200.82	221.34	162.78	18.94
12					0.25	214.79	240.15	180.17	16.12
13	90	1.2	600	2	0.1	176.15	193.21	161.09	8.55
14					0.15	195.57	212.75	179.48	8.23

(continued)

Table 3.12 (continued)

Test no	Tool geometry		Conditions			F <sub>y</sub> (N)				
	k <sub>r</sub>	r <sub>n</sub>	V <sub>c</sub> (m/min)	a <sub>p</sub> (mm)	f <sub>n</sub> (mm/rev)	Experimental	Complete model Predicha	% Error	Simplified model Predicha	% Error
15					0.2	213.56	232.84	9.03	197.87	7.35
16					0.25	230.97	253.52	9.76	216.25	6.37
17	60	1.2	525	2	0.13	271.78	295.32	8.66	327.34	20.44
18					0.17	294.05	315.69	7.36	348.40	18.48
19					0.23	320.98	346.62	7.99	379.99	18.38
20					0.3	350.44	383.32	9.38	416.85	18.95
21	60	1.2	800	1.5	0.13	235.46	241.74	2.66	248.75	5.64
22					0.17	247.88	257.26	3.78	265.55	7.13
23					0.23	272.91	280.99	2.96	290.74	6.53
24					0.3	307.30	309.41	0.69	320.13	4.18
Test no	Tool geometry		Conditions			F <sub>z</sub> (N)				
	k <sub>r</sub>	r <sub>n</sub>	V <sub>c</sub> (m/min)	a <sub>p</sub> (mm)	f <sub>n</sub> (mm/rev)	Experimental	Complete model Predicha	% Error	Simplified model Predicha	% Error
1	60	0.8	450	1.5	0.1	341.00	361.99	6.16	374.79	9.91
2					0.15	447.78	461.79	3.13	482.71	7.80
3					0.2	544.50	563.13	3.42	655.39	20.37
4					0.25	618.45	666.28	7.73	806.48	30.40
5	60	0.8	600	2	0.1	436.34	452.47	3.70	470.65	7.86
6					0.15	563.84	574.62	1.91	600.01	6.42
7					0.2	683.04	698.20	2.22	729.37	6.78
8					0.25	780.99	823.46	5.44	858.73	9.95

(continued)

Table 3.12 (continued)

Test no	Tool geometry		Conditions			$F_z$ (N)				
	$k_r$	$r_n$	Vc (m/min)	$a_p$ (mm)	$f_n$ (mm/rev)	Experimental	Predicha	% Error	Simplified model	% Error
9	90	1.2	450	1.5	0.1	329.75	371.01	12.51	353.52	7.21
10					0.15	440.07	474.39	7.80	461.44	4.86
11					0.2	550.08	580.61	5.55	569.36	3.51
12					0.25	643.61	689.80	7.18	677.28	5.23
13	90	1.2	600	2	0.1	435.44	455.19	4.54	442.29	1.57
14					0.15	571.56	580.66	1.59	571.65	0.02
15					0.2	700.61	708.76	1.16	701.01	0.06
16					0.25	821.66	839.63	2.19	830.37	1.06
17	60	1.2	525	2	0.13	518.54	550.74	6.21	559.76	7.95
18					0.17	622.33	652.07	4.78	666.78	7.14
19					0.23	757.92	805.66	6.30	827.31	9.16
20					0.3	888.85	987.59	11.11	1014.60	14.15
21	60	1.2	800	1.5	0.13	395.29	399.50	1.07	399.35	1.03
22					0.17	466.76	468.12	0.29	473.31	1.40
23					0.23	568.28	572.48	0.74	584.27	2.81
24					0.3	685.53	696.67	1.63	713.71	4.11

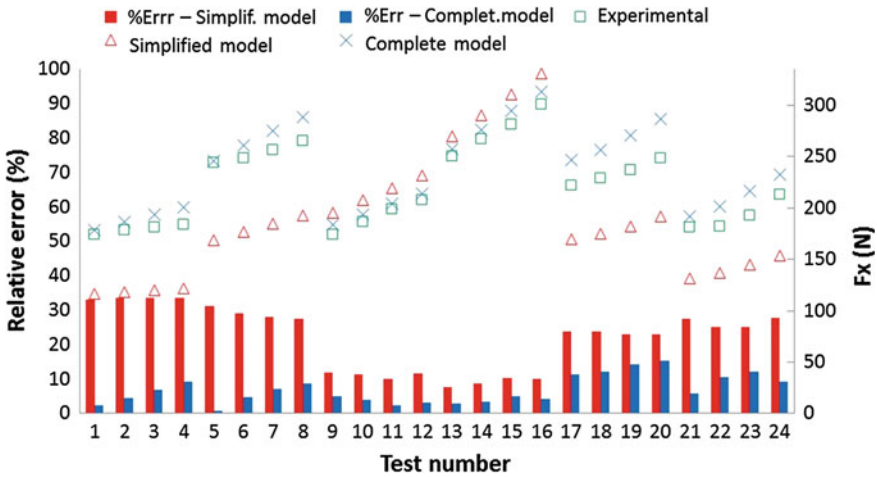


Fig. 3.22 Comparison between experimental and predicted  $F_z$  component for both models in the fourth stage of validation

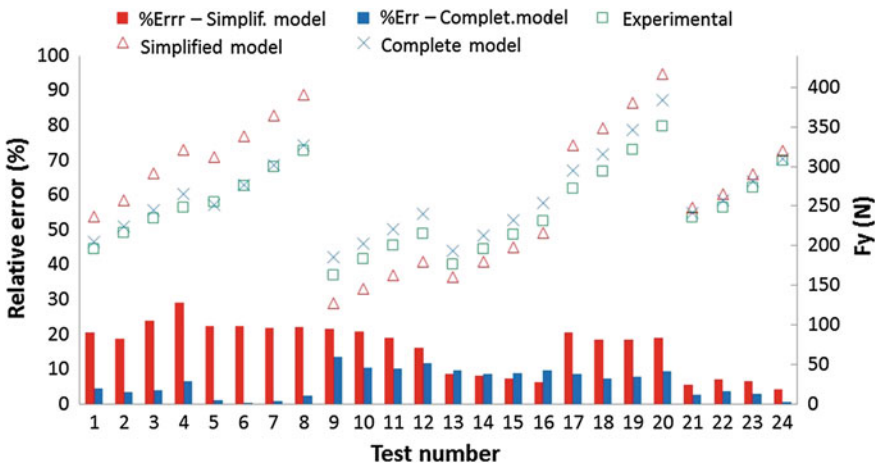
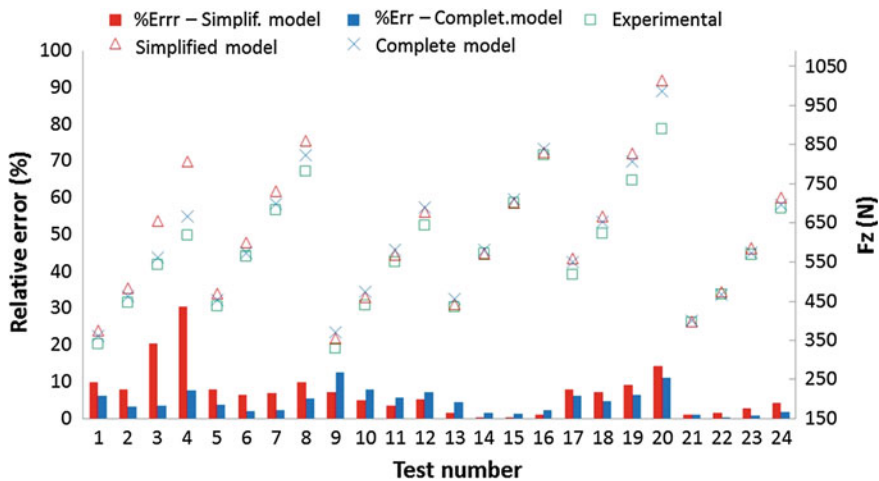


Fig. 3.23 Comparison between experimental and predicted  $F_y$  component for both models in the fourth stage of validation

$$F_i = F_{i0} + F_{iw} \tag{3.35}$$

where sub-index “i” makes reference to the three cutting force components: tangential ( $F_z$ ), axial ( $F_x$ ) and radial ( $F_y$ ).

Term  $F_{i0}$  represents the cutting force in absence of tool wear, that is, the force at the beginning when the edge is new. This force was already determined in the previous section when developing the mechanistic model. It considers the shearing



**Fig. 3.24** Comparison between experimental and predicted  $F_z$  component for both models in the fourth stage of validation

and friction effects between workpart and tool edge.  $F_{i0}$  force is supposed constant along the cutting operation. Research carried out by Kobayashi and Thomsen [7], Thomsen et al. [8] and Shi and Ramalingam [9] demonstrates that local deformation in the primary shearing area and friction located at tool rake face are not affected by wear in tool flank. In the work of Song [10] it is also demonstrated that flank wear does not affect the forces required for chip formation in the shearing area and in the interface chip-tool. Therefore, the cutting force due to shearing and friction processes estimated by the mechanistic model outlined in Sect. 3.1 is considered constant, independently of tool wear state.

Term  $F_{iw}$  represents the increment of cutting force caused by tool wear. When tool wears the contact surface in tool-workpart interface increases and an additional friction force appears.

Many authors have studied the strong correlation that exists between cutting forces and tool wear [11, 12]. Most of the researchers have used flank wear to establish this correlation [13, 14]. Wear in flank increases the contact area in the tool-workpart interface and therefore friction is higher, increasing the cutting forces especially in the normal direction to flank face, that is, in feed direction [1]. Other authors [15] have demonstrated that a relationship can also be settle down between forces and other types of wear (crater, tip). However, the control of flank wear is more important since it affects directly to superficial finish and dimensional precision.

Consequently, a relationship between cutting force increment and the width of flank wear should be defined. Since the increase of force for a specific tool wear depends on the cutting conditions [16], force due to tool wear can be expressed as (Eq. 3.36):

$$F_{iw} = k_{iw} V_c^{a_i} f_n^{b_i} a_p^{c_i} h_f^{d_i} \quad (3.36)$$

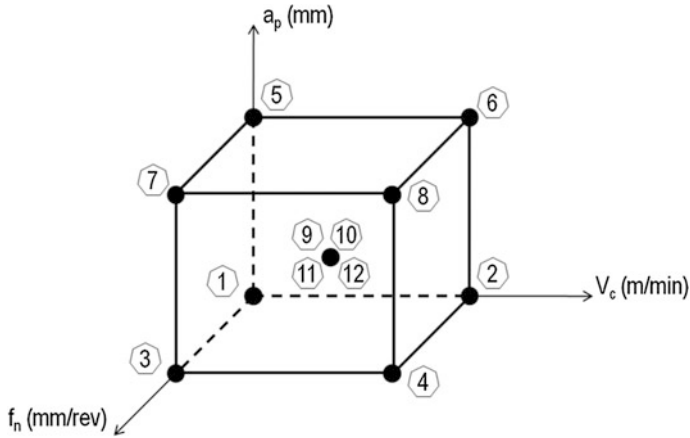
where  $k_{iw}$  is the specific wear coefficient which is function of tool-workpart combination;  $V_c$ ,  $f_n$  and  $a_p$  are the cutting conditions;  $h_f$  is the width of flank wear; exponents  $a_i$ ,  $b_i$ ,  $c_i$  and  $d_i$  represent the influence of cutting speed, feedrate, cutting depth and flank wear on the cutting forces for a specific tool-workpart combination. The values of the  $k_{iw}$  coefficient and the exponents were determined experimentally, as explained in next sections, through a series of wear tests whose methodology is explained in Sect. 3.2.2. The experimental value of the force due to wear ( $F_{xw}$ ,  $F_{yw}$ ,  $F_{zw}$ ) is calculated by removing the value of the force at the beginning of the cutting operation when tool is not worn ( $F_{x0}$ ,  $F_{y0}$ ,  $F_{z0}$ ) using the expressions in Eq. 3.37.

$$\begin{aligned} F_{xw} &= F_x - F_{x0} = k_{xw} V_c^{a_x} f_n^{b_x} a_p^{c_x} h_f^{d_x} \\ F_{yw} &= F_y - F_{y0} = k_{yw} V_c^{a_y} f_n^{b_y} a_p^{c_y} h_f^{d_y} \\ F_{zw} &= F_z - F_{z0} = k_{zw} V_c^{a_z} f_n^{b_z} a_p^{c_z} h_f^{d_z} \end{aligned} \quad (3.37)$$

### 3.2.2 Experimental Methodology

An experimental procedure must be designed in order to obtain a database to build the mathematical model that relates forces to tool wear using different cutting conditions. A factorial design  $2^3$  with addition of central points based on the design of experiments (DOE) method is proposed. This design allows to detect bending in at least one of the studied factors. Besides, this configuration allows to carry out an independent error estimation without performing replicas [17]. The geometric representation of this design can be done with a cube, where eight possible combinations of three tested factors are represented at two levels, plus four repetitions at the centre (Fig. 3.25). The considered three factors are the cutting conditions:  $V_c$ ,  $f_n$  and  $a_p$ . The levels are indicated in Table 3.13. Table 3.14 shows the resulting tests.

It can be observed that the cutting parameters are inside the range of conditions used for the characterization tests (Sect. 3.1.2.3), since the model to obtain must be valid for the same working range. Also, cutting tool, lathe, coolant and part material are also the same as in characterization tests. Tests in this point consist on carrying out longitudinal turning operations while recording cutting forces. Machining is interrupted at regular intervals of 1 min, or shorter for tests at high cutting speeds, to measure tool wear and part roughness. The tests start using a new edge and finish when tool is considered to be closed to catastrophic failure. This condition is denoted for an abrupt increase in the roughness of machined parts or some other incidences (spark observation, uncontrolled chip, vibrations, etc.).



**Fig. 3.25** Factorial design  $2^3$  with addition of four central points

**Table 3.13** Levels for cutting parameters

Levels	$V_c$ (m/min)	$f_n$ (mm/rev)	$a_p$ (mm)
Low	450	0.10	1.0
Medium	600	0.15	1.5
High	750	0.20	2.0

**Table 3.14** Experiments for the wear tests

Test number	$V_c$ (m/min)	$f_n$ (mm/rev)	$a_p$ (mm)
1	450	0.1	1
2	750	0.1	1
3	450	0.2	1
4	750	0.2	1
5	450	0.1	2
6	750	0.1	2
7	450	0.2	2
8	750	0.2	2
9	600	0.15	1.5
10	600	0.15	1.5
11	600	0.15	1.5
12	600	0.15	1.5

### 3.2.3 Analysis of Tool Wear and Effect in Cutting Forces

#### 3.2.3.1 Tool Wear Analysis

Figure 3.26 shows curves of flank wear evolution with cutting time for several tests. Most of the curves are featured by the three common wear regions. Curves corresponding to the tests carried out at the most severe cutting conditions have higher slope.

Images acquired during the tests show that the tool suffers progressive wear in flank up to a certain level, from which the tool becomes unstable with high risk of suffering unexpected breakdown. It has been verified that tools break before reaching a width in flank wear of  $V_{BB} = 0.3$  mm, which is the value indicated by ISO 3685 standard as tool life criteria for this case. As shown in Fig. 3.26, when machining at high cutting speeds (750 m/min) the tool becomes unstable from  $V_{BB} = 0.2$  mm. When cutting speed is around 450 m/min, the tool is able to support cutting efforts with a flank wear around  $V_{BB} = 0.25$  mm, but in most of the cases the edge fails before it reaches  $V_{BB} = 0.3$  mm, without observing any indication in the edge that a catastrophic failure will take place.

The image of the tool used in test number 6 carried out at 750 m/min is presented in Fig. 3.27. The tool shows progressive wear in flank, crater and tip. When  $V_{BB}$  reaches 282  $\mu\text{m}$  the tool does not bear the cutting efforts and an unexpected breakdown takes place during the machining. This behaviour can be caused by cracks (Fig. 3.28) in the edge that leads to sudden fractures. High cutting speed produces a state of high compression stresses in the tool. Carbide tools support limited deformation, even at high temperatures, which produces cracks that cause sudden breakdowns [18].

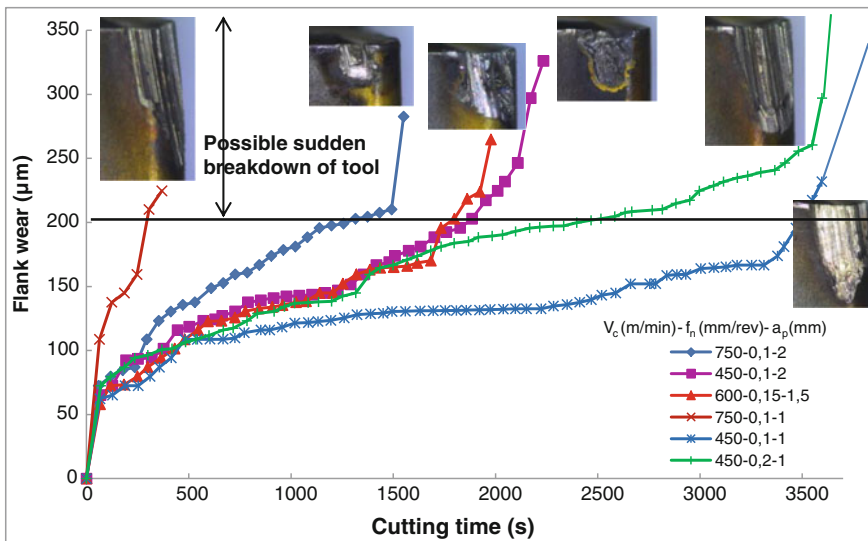


Fig. 3.26 Evolution of flank wear with cutting time



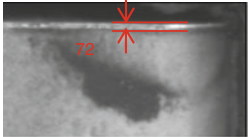
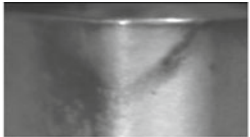
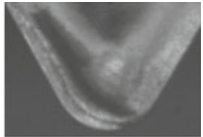
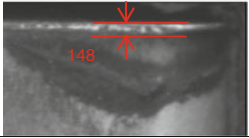
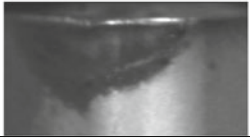
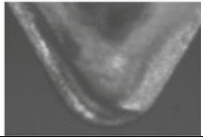
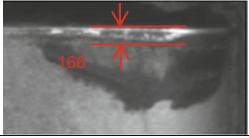
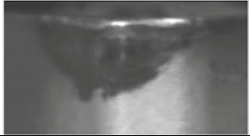
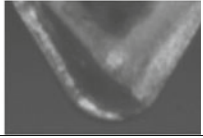
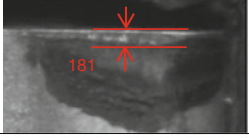
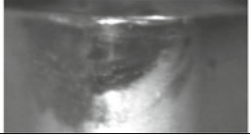
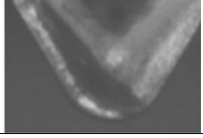

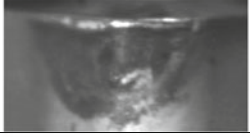
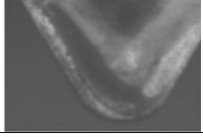
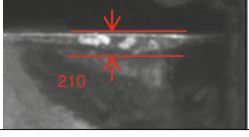
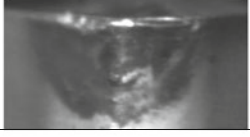
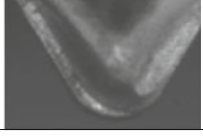

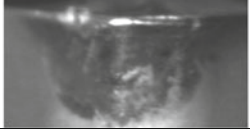

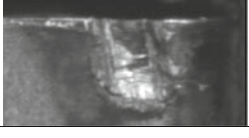
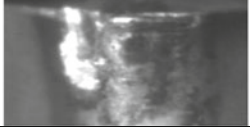
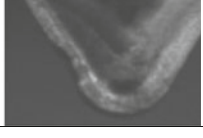
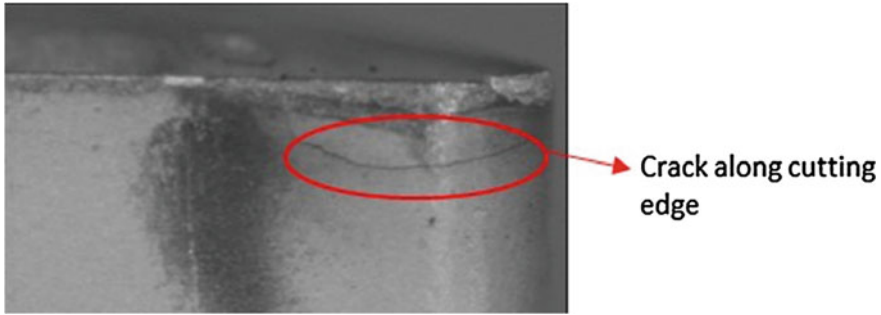
Time(s)	Flank	Tip	Crater
59			
609			
844			
1.021			
1.433			
1.491			
1.550			
1.629			

Fig. 3.27 Images of tool wear for test number 6



**Fig. 3.28** Detail of a crack in the edge of a carbide tool machining AISI 303

Therefore, a value of  $V_{BB} = 0.2$  mm is settled down as tool life criteria when machining austenitic stainless steels at high cutting speeds. This value is more conservative than the one indicated in ISO 3685 standard; it is worth remembering that this standard was developed time ago for machining at inferior cutting speeds, far way the speed admissible by current tools. Consequently, when machining at very high speeds the wear mechanism changes and wear limits should be modified.

### 3.2.3.2 Effect of Flank Wear in Cutting Speeds

Figure 3.29 shows the evolution of tool wear and cutting force with cutting time for several tests.

At the beginning of the operation, recorded forces correspond to values estimated for the mechanistic model presented in Sect. 3.1 and denoted by  $F_0$ . Next, a phase of continuous force growth appears, caused by progressive wear of the tool. The slope of curves in this area depends on the cutting conditions, but it is always higher for severe cutting conditions. In the third stage, closed to the end of tool life, forces are featured by high fluctuations.

It is observed that axial ( $F_x$ ) and radial ( $F_y$ ) components are more sensitive to wear than tangential component ( $F_z$ ). In some extreme cases axial component ( $F_x$ ) is higher to tangential component ( $F_z$ ) (tests 1, 5 and 6). An increase of contact area in tool-workpart interface, caused by flank wear, causes an intensification in the force normal to this area and, consequently, the magnitude of axial and radial components is also higher.

The three components of the force are characterized by an upwards trend during the first and second wear stages in all tests. However in the third stage, with flank wear superior to 0.2 mm, the force components describe different behaviour depending on the tool failure reason. That is, different types of wear (flank, crater, dips and tip) affect in a different way to the force components. In some cases the forces increase suddenly (tests 1 and 5) due to flank wear, while in other cases (tests 6 and 9) the effect is the opposite and force decreases due to crater wear.

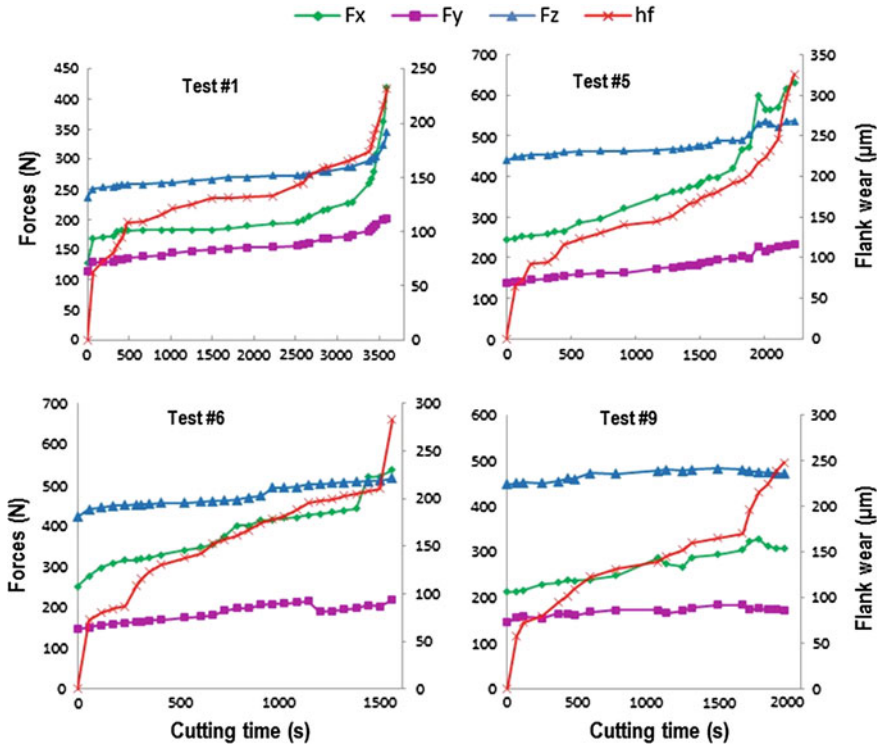
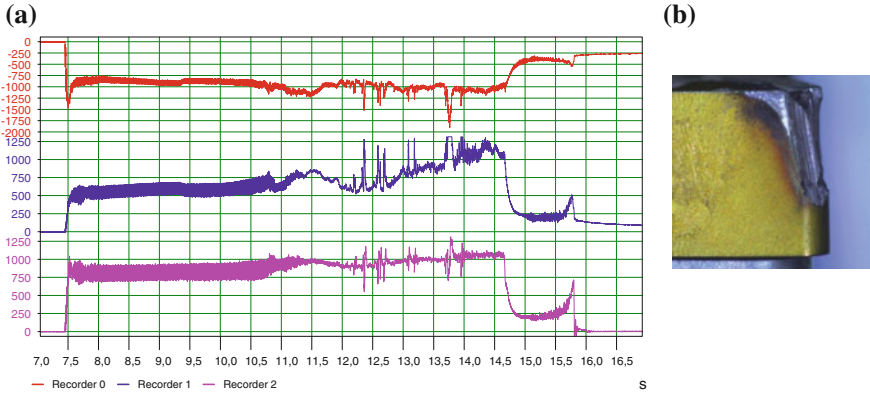


Fig. 3.29 Evolution of cutting forces and tool wear with time

Obikawa [19] observed that cutting forces increase linearly with flank wear, while crater wear produces a force decrement. Ning [20] demonstrated that flank wear produces an increment in the three force components, while crater wear leads to an increment of the effective rake angle and, therefore, a decrement in cutting force components. The reduction is more important in the radial force. Oraby [21] demonstrated that wear in tool tip affects fundamentally to the radial force, flank wear affects equally to the axial and radial force and when machining is unstable and wear is severe, important variations in the tangential component are observed.

The fact that force components exhibit an irregular behaviour during the final stage of tool life makes it difficult to establish a correlation between forces and tool wear above a particular flank wear level. In this section a model is presented that allows to predict cutting forces caused by tool flank wear when work conditions are stable. In previous paragraphs the value of  $V_{BB} = 0.2$  mm was settled down like the maximum wear that assures stable conditions during machining of austenitic stainless steel at high cutting speeds. Therefore, the model developed in this chapter is valid for these conditions (maximum  $V_{BB} = 0.2$  mm).

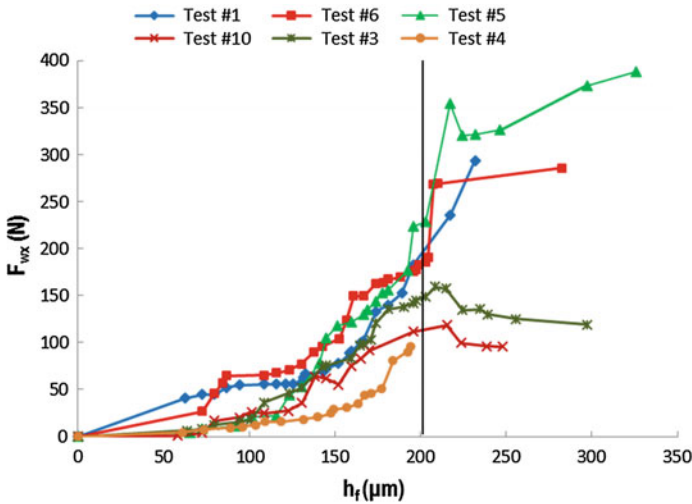
On the other hand, during the tests it was perceptible that cutting forces are sensitive to tool break and therefore they can be used as monitoring system to detect



**Fig. 3.30** **a** Force signals recorded during tool breakdown; **b** image of the broken tool. Test number 8 ( $V_c = 750$  m/min;  $f_n = 0.2$  mm/rev;  $a_p = 2$  mm)

tool failure at the end of tool life. Figure 3.30 shows cutting forces just in the moment of edge breakdown for test number 8. When the tool begins to fail (between 11.5 and 14.5 s), the three components of cutting force experience continuous fluctuations. Finally, when the tool breaks the cutting forces suffer a quick fall down due to the reduction in the cutting section caused by tool tip break.

Figures 3.31, 3.32 and 3.33 represent the value of force components due exclusively to flank wear ( $F_{iw}$ ), where  $h_f$  is the width of flank wear ( $V_{BB}$ ).  $F_{iw}$  is calculated as the difference between the force when the edge is worn and the force at the beginning when the edge is new  $F_{iw} = F_i - F_{i0}$ .



**Fig. 3.31** Evolution of  $F_{wx}$  with flank wear for several tests

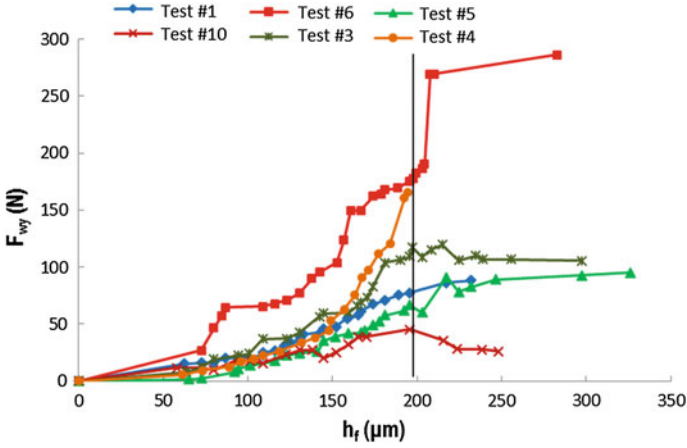


Fig. 3.32 Evolution of  $F_{wy}$  with flank wear for several tests

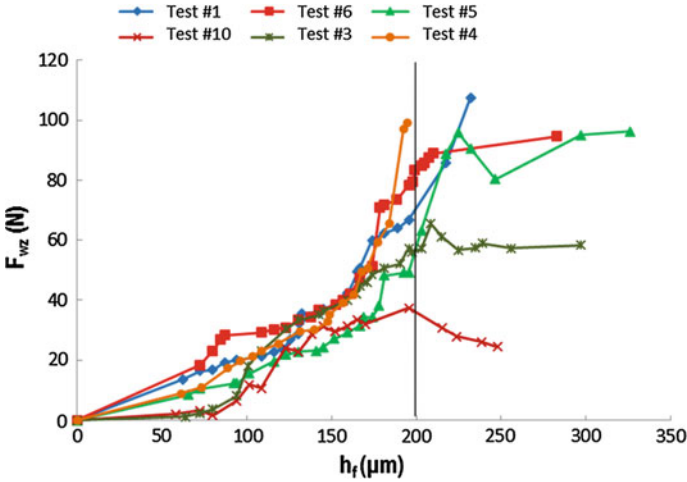


Fig. 3.33 Evolution of  $F_{wz}$  with flank wear for several tests

The three graphs present similar trends. Two regions can be distinguished: in the region where tool wear is lower than  $200 \mu\text{m}$  the forces increase exponentially, whereas in the region where tool wear is higher than  $200 \mu\text{m}$  the forces show fluctuations which are difficult to model. The scope of the correlation model is the first region (machining operation is stable) where the proposed model is valid. Variations are observed in the curves for different cutting conditions, which means a relationship exists between the force due to wear ( $F_{iw}$ ) and the cutting conditions.

The shape of the curves in the first part corresponds to the model proposed in Sect. 3.1 (Eq. 3.36). The procedure for determining the model parameters will be explained in the next section.

### 3.2.4 Parameters Identification and Validation of the Model

The 12 tests done in the previous section provide a total of 267 data with tool wear inferior to 0.2 mm; 142 of these data were chosen randomly to determine the parameters of Eq. 3.36 and the rest of data were used to check the goodness of the model. Firstly, a logarithmic transformation was applied to the expressions in Eq. 3.36 to linearize them (Eq. 3.38).

$$\ln F_{iw} = \ln k_{iw} + a_i \ln V_c + b_i \ln f_n + c_i \ln a_p + d_i \ln h_f \quad (3.38)$$

Then, linear regression techniques were applied to determine the coefficients of the equations using the least squares method. The resulting expressions are indicated in Eqs. 3.39 and 3.40.

$$\begin{aligned} F_{xw} &= 5.42 \times 10^{-4} V_c^{-0.22} f_n^{-0.39} a_p^{0.58} h_f^{2.46} \\ F_{yw} &= 1.71 \times 10^{-3} V_c^{-0.03} f_n^{0.38} a_p^{-0.40} h_f^{2.26} \\ F_{zw} &= 8.25 \times 10^{-4} V_c^{0.33} f_n^{0.61} a_p^{0.71} h_f^{1.93} \end{aligned} \quad (3.39)$$

$$\begin{aligned} F_{xw} &= 5.42 \times 10^{-4} V_c^{-0.22} f_n^{-0.39} a_p^{0.58} h_f^{2.46} \\ F_{yw} &= 1.71 \times 10^{-3} V_c^{-0.03} f_n^{0.38} a_p^{-0.40} h_f^{2.26} \\ F_{zw} &= 8.25 \times 10^{-4} V_c^{0.33} f_n^{0.61} a_p^{0.71} h_f^{1.93} \end{aligned} \quad (3.40)$$

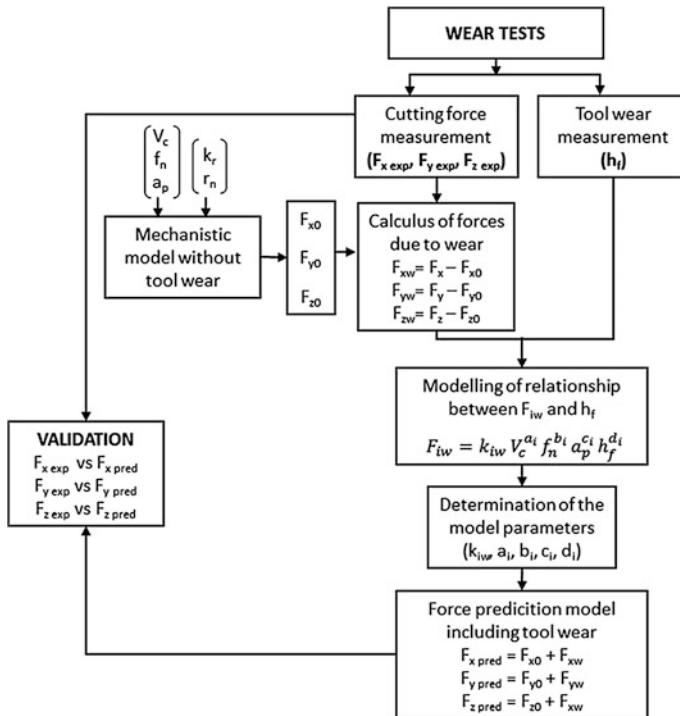
Significance of the model is evaluated through correlation factors  $R^2$  and  $R_{adj}^2$ . Table 3.15 contains the results of a variance analysis for the three equations. The P-value is obtained for a trust interval of 95 %. Also, linearity and independence of residuals, normality and variance equality were studied obtaining appropriate results.

Observing the values of the exponents it can be concluded that  $F_x$  and  $F_y$  components are more sensitive to flank wear than  $F_z$ . However, the  $F_z$  component is the most affected when changing cutting conditions. To consider this behaviour is important for improving the reliability of monitoring systems. In these systems the use of free-noise input variables is necessary, that is, variables insensitive to changes in cutting conditions but very sensitive to tool wear.

Figure 3.34 contains a summary of the tasks to determine the prediction model which considers tool wear.

**Table 3.15** Analysis of variance for the regression

F <sub>wx</sub>					
Source	DF	SS	MS	F	P
Regression	4	101.375	25.344	4231.78	0.000
Residual error	137	0.820	0.006		
Total	141	102.195			
S = 0.0773879	R-Sq = 99.2 %	R-Sq(adj) = 99.2 %			
F <sub>wy</sub>					
Regression	4	82.250	20.562	5498.79	0.000
Residual error	137	0.512	0.004		
Total	141	82.762			
S = 0.0611511	R-Sq = 99.4 %	R-Sq(adj) = 99.4 %			
F <sub>wz</sub>					
Regression	4	69.338	17.335	4287.51	0.000
Residual error	137	0.554	0.004		
Total	141	69.892			
S = 0.0635849	R-Sq = 99.2 %	R-Sq(adj) = 99.2 %			



**Fig. 3.34** Sequence of tasks to determine the prediction model which includes tool wear

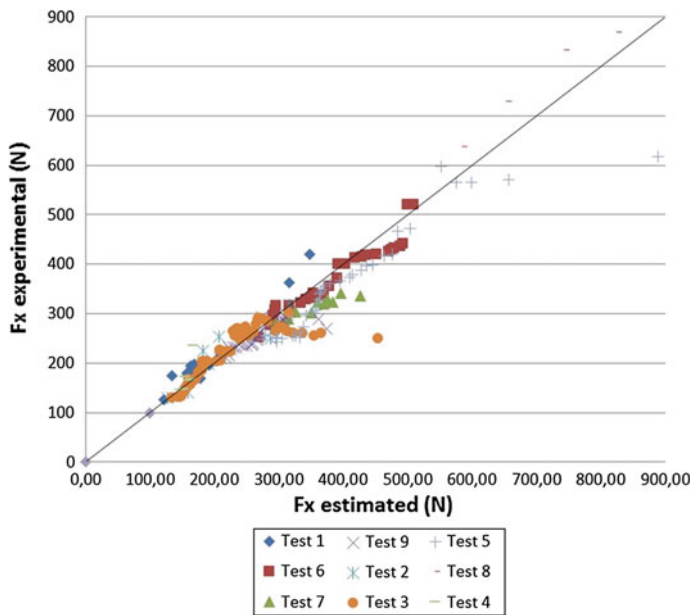


Fig. 3.35 Measured forces versus estimated forces for  $F_x$

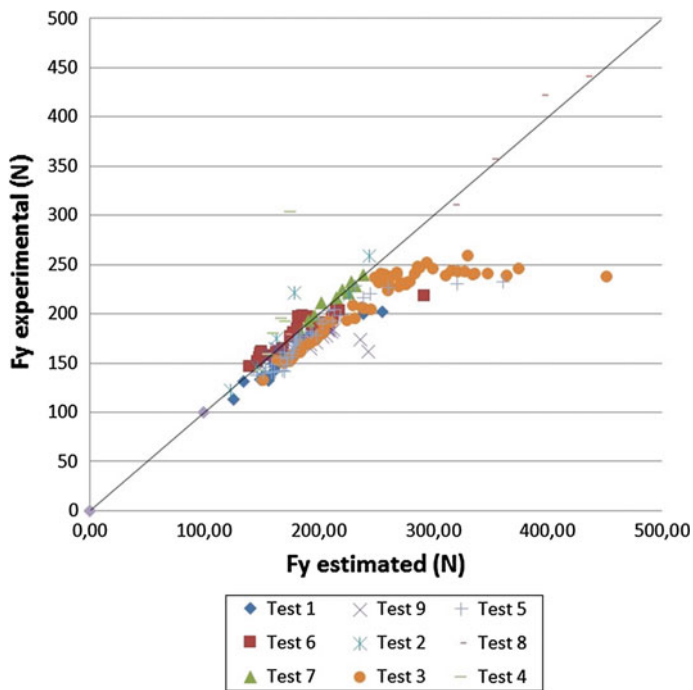


Fig. 3.36 Measured forces versus estimated forces for  $F_y$



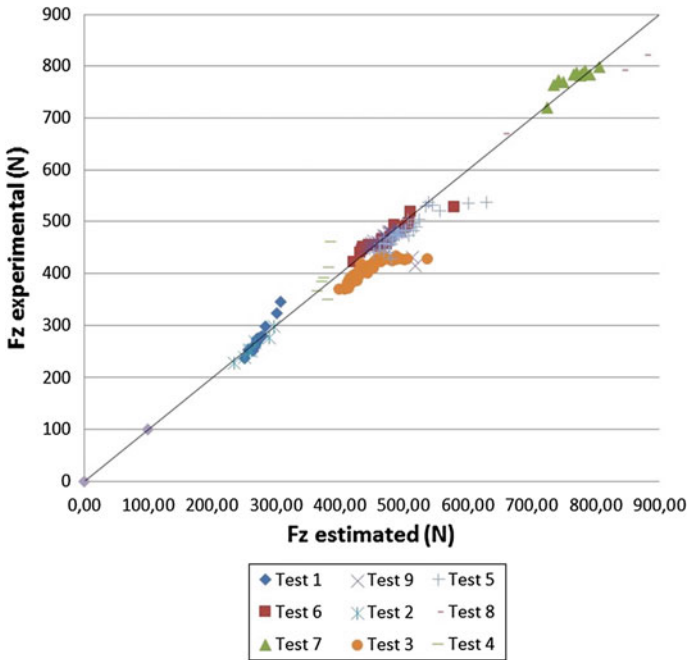


Fig. 3.37 Measured forces versus estimated forces for  $F_z$

Values of cutting forces and flank wear obtained in the 12 remaining tests were used to validate the model. Experimental forces at different levels of flank wear were compared with the ones estimated by the proposed model using the expressions in Eq. 3.41.

$$\begin{aligned}
 F_{xpred} &= F_{x0} + F_{xw} = F_{x0} + 5.42 \times 10^{-4} V_c^{-0.22} f_n^{-0.39} a_p^{0.58} h_f^{2.46} \\
 F_{ypred} &= F_{y0} + F_{yw} = F_{y0} + 1.71 \times 10^{-3} V_c^{-0.03} f_n^{0.38} a_p^{-0.40} h_f^{2.26} \\
 F_{zpred} &= F_{z0} + F_{zw} = F_{z0} + 8.25 \times 10^{-4} V_c^{0.33} f_n^{0.61} a_p^{0.71} h_f^{1.93}
 \end{aligned}
 \tag{3.41}$$

where  $F_{x0}$ ,  $F_{y0}$  and  $F_{z0}$  are the estimated forces obtained with the mechanistic model presented in Sect. 3.1.2.

Figures 3.35, 3.36 and 3.37 show the experimental forces (X-axis) versus forces estimated by the complete model (Y-axis) using the 125 data preserved for validation. The points closed to the 45° line indicate good correlation between experimental and estimated values. The analysis of these results shows discrepancies between estimated and measured forces in the final phase when tool is highly worn, mainly due to the tool unstable behaviour in this phase.

### 3.3 Conclusions

A correlation model is developed to estimate cutting forces in turning. The model considers the influence of wear band width in tool flank. The model is valid in the scope of austenitic stainless steels turning even at high cutting speeds (higher than 450 m/min). The aggressive cutting conditions speed up tool wearing and tool life criterion must be more conservative than the value recommended by ISO 3685 standard, in order to assure a stable operation without unexpected failures. The aggressive cutting conditions produce high compression stresses in the tool that can deform it, causing cracks and sudden edge breakdown. The experiments indicate that this fact happens when  $V_{BB}$  flank wear is superior to 0.2 mm. Therefore, one conclusion drawn from the study is that when turning austenitic stainless steels with coated carbide tools at high cutting speeds it is not desirable to overcome  $V_{BB} = 0.2$  mm flank wear. This value for  $V_{BB}$  redefines the tool life criterion defined in ISO 3685.

As expected, experimental results demonstrate that tool wear produces a significant increment of cutting forces. The axial  $F_x$  and radial  $F_y$  components are the most affected. An important conclusion is that components  $F_x$  and  $F_y$  are valid signals for tool wear monitoring. Besides, since  $F_z$  component is the most affected by changes in cutting conditions, it can be used to normalize the  $F_x$  and  $F_y$  components in order to reduce the influence of changes in cutting conditions.

### References

1. Altintas Y (2000) Manufacturing automation: metal cutting mechanics, machine tool vibrations, and CNC design. Cambridge University Press, Cambridge
2. Denkena B, Köler J (2010) Consideration of the form of the non-deformed section of cut in the calculation of machining forces. *Mach Sci Technol* 14(4):455–470
3. Fernández-Abia AI, Barreiro J, López de Lacalle LN, Martínez S (2011) Effect of very high cutting speeds on shearing, cutting forces and roughness in dry turning of austenitic stainless steels. *Int J Adv Manuf Technol* 57:61–71. doi:[10.1007/s00170-011-3267-9](https://doi.org/10.1007/s00170-011-3267-9)
4. Lamikiz A (2003) Un modelo para la estimación de la fuerza de corte en el fresado de superficies complejas. Ph.D. Thesis, Universidad del País Vasco
5. Lee P, Altintas Y (1996) Prediction of ball-end milling forces from orthogonal cutting data. *Int J Mach Tool Manuf* 36:1059–1072
6. Peña D (2002) Regresión y diseño de experimentos. Alianza Editorial, Madrid
7. Kobayashi S, Thomsen EG (1960) The role of friction in metal cutting. *J Eng Power ASME Trans Ser B* 82:324
8. Thomsen EG, Macdonald AG, Kobayashi S (1962) Flank friction studies with carbide tools reveal sublayer plastic flow. *J Eng Ind* 84:53–62
9. Shi T, Ramalingam S (1991) Slip-line solution for orthogonal cutting with chip breaker and flank wear. *Int J Mech Sci* 33:689–704
10. Song W (2006) Development of predictive force models for classical orthogonal and oblique cutting and turning operations incorporating tool flank wear effects. Ph.D. thesis, Queensland University of Technology

11. Kiouss M, Ouahabi A, Boudraa M, Serra R, Cheknane A (2010) Detection process approach of tool wear high speed milling. *Measurement* 43:1439–1446
12. Remadna M, Rigal JF (2006) Evolution during time of tool wear and cutting forces in the case of hard turning with CBN inserts. *J Mater Process Technol* 178:67–75
13. Sikdar SK, Chen M (2002) Relationship between tool flank wear area and component forces in single point turning. *J Mater Process Technol* 128:210–215
14. Ghani JA, Rizal M, Sayuti A, Nuawi MZ, Rahmam MN, Che Haron CH (2009) New regression model and I-Kaz Method for online cutting tool wear monitoring. *World Acad Sci Eng Technol* 60:420–425
15. Oraby SE, Hayhurst DR (2004) Tool life determination based on the measurement of wear and tool force ratio variation. *Int J Mach Tools Manuf* 44:1261–1269
16. Dimla DE (2004) The impact of cutting conditions on cutting forces and vibration signals in turning with plane face geometry inserts. *J Mater Process Technol* 155–156:1708–1715
17. Montgomery DC (2003) *Diseño y análisis de experimentos*. Limusa, México
18. Trent EM, Wright PK (2000) *Metal cutting*. Butterworth-Heinemann, Boston
19. Obikawa T, Shinozuka J (2004) Monitoring of flank wear of coated tools in high speed machining with a neural network ART2. *Int J Mach Tools Manuf* 44:1311–1318
20. Ning L, Veldhuis SC (2006) Mechanistic modelling of ball end milling including tool wear. *J Manuf Process* 8:21–28
21. Oraby SE, Hayhurst DR (1991) Development of models for tool wear force relationships in metal cutting. *Int J Mech Sci* 33(2):125–138

# Chapter 4

## Cutting Under Gas Shields: Phenomenological Concepts Versus Industrial Applications

C.M.A. Silva, V.A.M. Cristino, P.A.R. Rosa and P.A.F. Martins

**Abstract** This chapter is focused on the interaction between cutting medium and freshly formed surfaces with the aim of providing a new level of understanding on the mechanics of chip flow in orthogonal metal cutting and analyzing its influence on the cutting forces and tool life in conventional milling. The first part of the chapter presents experimental results from an investigation performed with a specially-designed orthogonal metal cutting apparatus and a model material under dry conditions, with the objective of analyzing the influence of active and inert gas shields in the kinematics of chip flow, the friction coefficient, the chip-compression factor and the cutting forces. In particular, authors provide a correlation between surrounding medium, tribological conditions, surface roughness, freshly cut surfaces and chip curling at the tool-chip contact interface. The second part of the chapter extends the investigation to conventional milling of an engineering material in order to study the influence of cutting in the presence of air or under an argon atmosphere in the overall cutting forces and tool wear. Results from the investigation based on orthogonal metal cutting show that cutting in the presence of oxygen leads to higher values of friction, chip compression factor and chip curl radius, and to lower values of the shear plane angle. The presence of oxygen is also responsible for increasing the cutting forces and tool wear in conventional milling.

---

C.M.A. Silva · P.A.R. Rosa · P.A.F. Martins (✉)  
Instituto Superior Técnico, Universidade de Lisboa,  
Av. Rovisco Pais, 1049-001 Lisbon, Portugal  
e-mail: pmartins@ist.utl.pt

C.M.A. Silva  
e-mail: carlos.alves.silva@ist.utl.pt

P.A.R. Rosa  
e-mail: pedro.rosa@ist.utl.pt

V.A.M. Cristino  
Faculty of Science and Technology, University of Macau,  
Av. Padre Tomás Pereira S.J., Taipa, Macau, China  
e-mail: valentino.anok@ist.utl.pt

## 4.1 Introduction

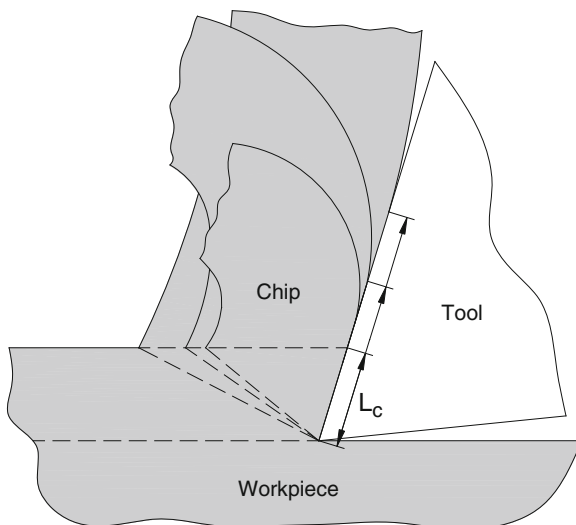
Metal cutting plays a significant role in manufacturing due to its involvement either in the production of components or in the fabrication of tools and equipment utilized by other processes. Metal cutting, like in other metal working processes, is influenced by the tribological conditions at the tool-chip contact interface because they influence the way chip forms and curls, the heat and rise in temperature, the surface quality of the machined workpiece, the cutting forces, the energy requirements and the overall wear and life of the cutting tools.

Knowledge on the mechanics of chip flow has been driven by the study of metal cutting fundamentals, as reported in the state-of-the-art review paper by Jawahir and van Luttervelt [1]. The investigation started in the 1950s when chip curling was studied in connection with tool-chip contact length, restricted contact tools and clamped-on chip formers and, ever since then, there has been an enormous amount of research work in the area because the mechanics of chip flow is the basis for developing analytical and numerical models to predict cutting forces, chip curling, chip breaking, tool-wear and surface integrity.

Friction is also found to significantly influence the mechanics of chip flow. In fact, by reducing the friction coefficient, the shear plane angle  $\phi$  increases, the chip thickness reduces and chip curling increases. Because the area of the shear plane decreases as well as the contact length and the applied pressure, the cutting force required for the process will decrease [2–4] (Fig. 4.1).

Despite the efforts performed by researchers over approximately 50 years, the explanation of how chips are formed, what is the role played by friction and what causes chips to curl are not yet clearly understood. Some of the most significant contributions in the field were systematized in Jawahir and van Luttervelt [1] and

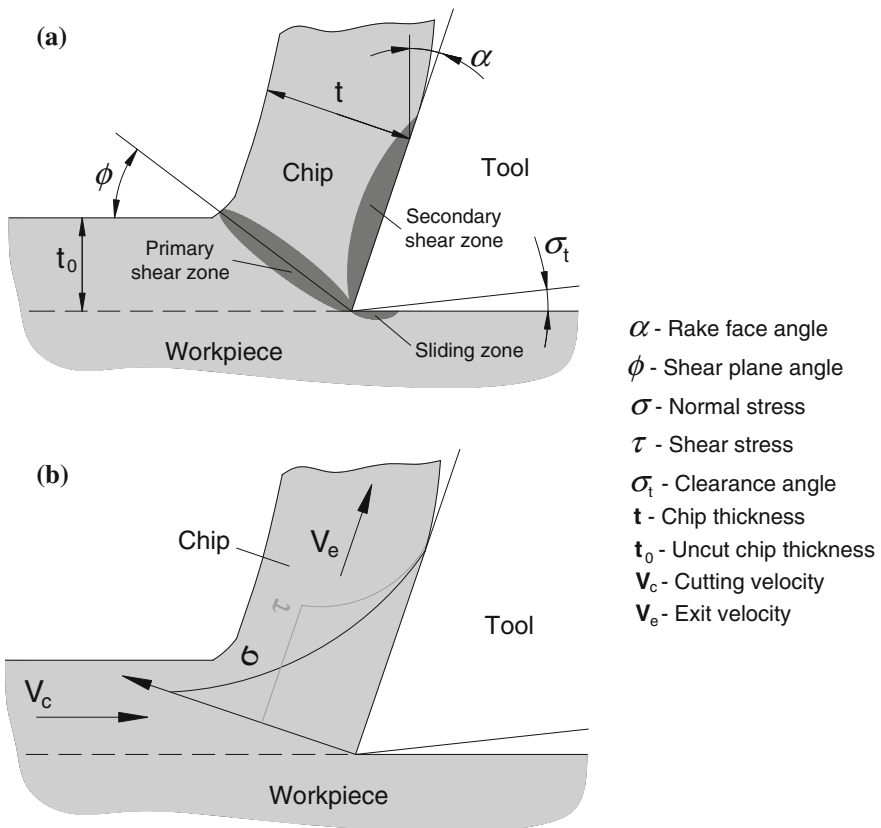
**Fig. 4.1** Influence of the frictional conditions on the contact length and chip curling



van Luttervelt et al. [5] with the aim of saving fragmented and scattered experimental and theoretical knowledge in the mechanics of chip flow for further development.

The commonly accepted mechanism on chip formation in metal cutting consider that (i) new surfaces are formed by plastic flow around the tool edge, (ii) the energy required for cutting is overwhelmingly due to plasticity and friction and (iii) any energy required for the formation of new surfaces is negligible. This mechanism will be hereafter referred as the ‘plasticity and friction only’ view and is inherent in the most significant contributions to the understanding of metal cutting fundamentals made by Zorev [6], Shaw [7] and Oxley [8], among others (Fig. 4.2).

The primary shear zone, shown in Fig. 4.2a, extends from the cutting edge to the surface of the workpiece, and is the zone where the material is plastically deformed under high values of shear strains and stresses. The secondary shear zone occurs on the rake face of the cutting tool and results from plasticity and friction acting along



**Fig. 4.2** Schematic representation of the commonly accepted chip formation mechanism with a basic set of notation that will be used throughout the chapter. **a** Representation of the zones of interest and **b** stress distribution proposed by Zorev [6]

the chip-tool contact interface. As originally developed by Zorev [6], the distribution of the normal and shear stresses on the rake surface gives rise to a region of seizure (or sticking) close to the cutting edge and to a region of sliding in the remaining contact interface (Fig. 4.2b).

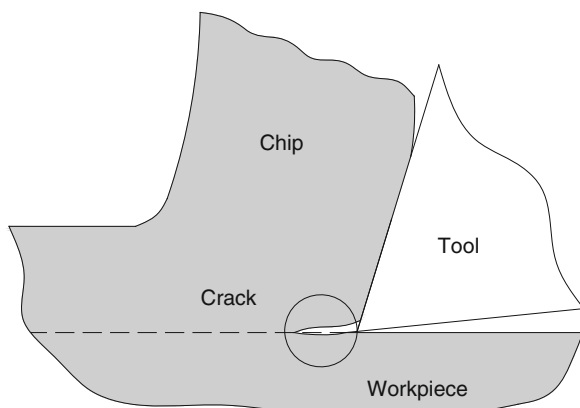
The sliding zone along the clearance surface is caused by friction, increases with the area of contact between the tool and the workpiece, and is mainly responsible for producing flank wear in the cutting tools.

A recent breakthrough in the mechanics of chip formation was made by Atkins [9, 10] by extending traditional analysis to include the work involved in the formation of new surfaces at the tip of the tool (Fig. 4.3). The combination of plasticity and friction with ductile fracture mechanics proved effective for obtaining good estimates of the cutting forces and to solve a longstanding incompatibility problem of the metal cutting theory between the specific cutting pressure and the state-of-stress resulting from the stress-strain/strain rate behaviour of the materials [11].

In addition to what was mentioned previously, there is a common believe among researchers and practitioners that active gases (such as oxygen) acting on the freshly cut surfaces may influence friction, chip compression factor, chip curling and forces to a level that goes significantly beyond what has been said and written in the commonly accepted fundamentals of metal cutting. Despite early experiments conducted by Poletica (Astakhov [12]) on copper and armco iron, indicated that the surrounding medium does not show any influence, there is a necessity of revisiting the subject by identifying and quantifying the type of contaminant films as a function of the surrounding medium and the average surface roughness of the cutting tool.

Indeed, if the interaction between chip and tool in real metal cutting does not take into consideration the reactions of oxygen and nitrogen contained in the air with the freshly cut surfaces of the work material, there is room for misunderstanding the mechanics of chip flow and to consider curling solely as a consequence of static, kinematic and thermal effects caused by the operative cutting parameters. Not taking into account the extremely high sensitivity of metals to oxygen will also

**Fig. 4.3** Schematic representation of crack formation at the tip of the cutting tool



give rise to partial assessment of the role of cutting fluids and to erroneous estimates of the coefficient of friction along the rake surface of the cutting tools. This is probably one of the main reasons why models for chip curling available in the literature are not widely applicable.

In fact, and in contrast to chip formation there has never been a universally accepted mechanism to explain what causes chips to curl. In general, results available in the literature estimate the radius of curvature to decrease with increasing depth of cut, with decreasing cutting velocity and decreasing friction and contact length at the rake face of the tool [1]. Some of these dependencies have been properly modelled by means of finite elements and artificial intelligence [5]. However, investigations by other authors also claim the distribution of stresses in the primary and secondary shear zones, thermal effects and work-hardening characteristics of the workpiece material to influence chip curl [13] and side-curl to be produced when machining dry and inhibited when using a lubricant [14].

This chapter is focused on the interaction between cutting medium and freshly formed surfaces with the aim of providing a new level of understanding on the mechanics of chip flow in orthogonal metal cutting.

The first part of the chapter presents thoroughly experimental results obtained from an investigation performed with a specially-designed orthogonal metal cutting apparatus and a model material under dry conditions, with the objective of analyzing the influence of active and inert gas shields in the kinematics of chip flow, the coefficient of friction, the chip-compression factor and the cutting forces. In particular, authors provide a correlation between surrounding medium, tribological conditions, surface roughness, freshly cut surfaces and chip curling at the tool-chip contact interface that may help assembling the puzzle of chip flow in metal cutting. The presentation enlarges previous published work in the field by the authors [15].

The second part of the chapter extends the investigation to conventional milling of an aluminium alloy AA7050-T7451 under industrial operating conditions. The choice of end milling was due to the fact that operating conditions and chip formation mechanisms differ considerably from those commonly found in steady-state orthogonal metal cutting. In fact, because the cutting edges of an end mill are at some angle of inclination to the direction of motion (oblique metal cutting), the cutting edges are not in constant contact with the workpiece surface and the undeformed chip thickness starts from zero and increases up to some maximum value determined by the chosen value of feed per cutting edge (or is thickest at engagement and tapers out to nothing in case of down or climb milling), it follows that the length of engagement for each cutting edge is short and the overall cutting time and exposure to oxygen for removing the same amount of material is larger than in orthogonal metal cutting. All this, combined with previous investigations by Yamane et al. [16] justify the importance for extending the work on the influence of cutting in the presence of air or under gas shields to conventional milling.



## 4.2 Orthogonal Metal Cutting Under Gas Shields

This section of the chapter is focused on the equipment, methods and procedures that were utilized for obtaining thoroughly researched results and proposing innovative explanations for the tribological conditions at the tool-chip contact interface that arise from the interaction between cutting medium, surface roughness and freshly cut metal surfaces in orthogonal metal cutting.

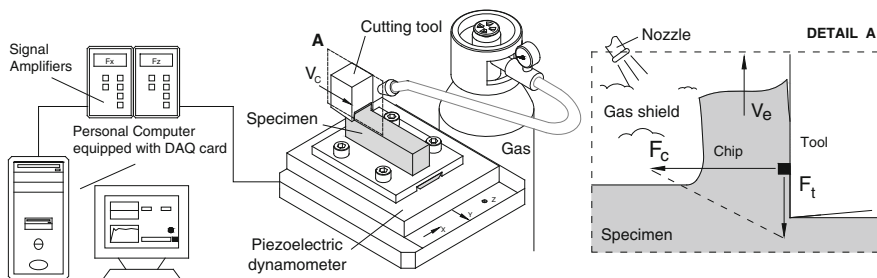
### 4.2.1 Equipment, Methods and Procedures

The experimental apparatus that was developed for performing orthogonal metal cutting under active and inert gas shields is schematically presented in Fig. 4.4, and is essentially composed by a cutting tool, a specimen, a nozzle, a three-dimensional piezoelectric dynamometer and a data acquisition system.

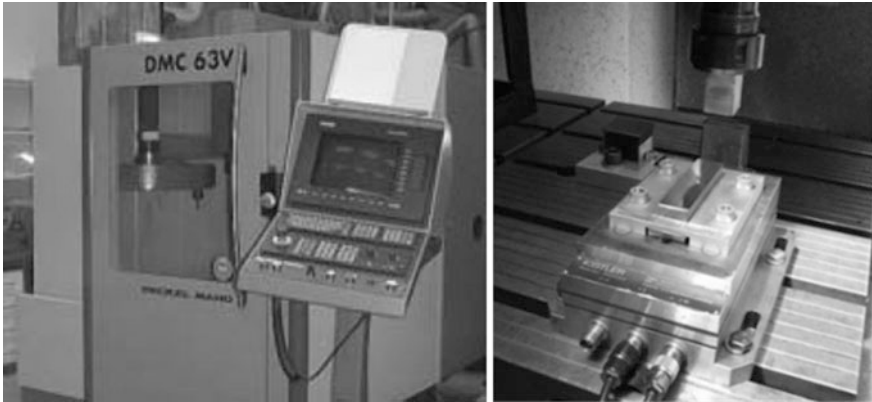
The cutting tool is mounted in the spindle and the specimen is fixed on the three-dimensional piezoelectric dynamometer, which is mounted directly on the work table of the machine. The experimental apparatus was installed in a Deckel-Maho DMC 63V machining center (Fig. 4.5).

The cutting tools were manufactured in AISI 316L stainless steel with a rake face angle  $\alpha = 0^\circ$ , a clearance angle  $\sigma = 0^\circ$  and an edge radius below  $2 \mu\text{m}$  (Fig. 4.6) for minimizing the contact with the clearance surface, where the arithmetical mean roughness  $R_a = 0.04 \mu\text{m}$  in order to ensure a smooth surface.

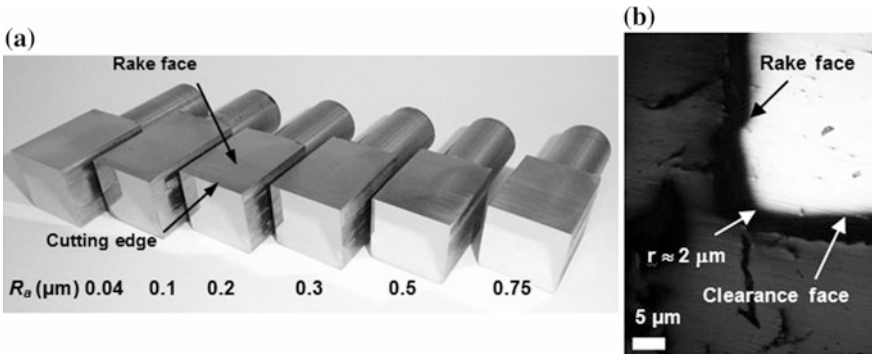
The surface texture, roughness and geometry of the cutting tools were carefully produced and regenerated in the Grinding and Polishing Unit (GPU) after completion of each test in order to ensure repeatability and analogy of surface topography irrespective of the test case. The GPU is schematically shown in Fig. 4.7 and consists in two separated blocks, each one for a respective tool's surface, with a well-defined geometry (rake and clearance angle) guarantying not only the reconditioning of the cutting tool, but also of the cutting edge sharpness.



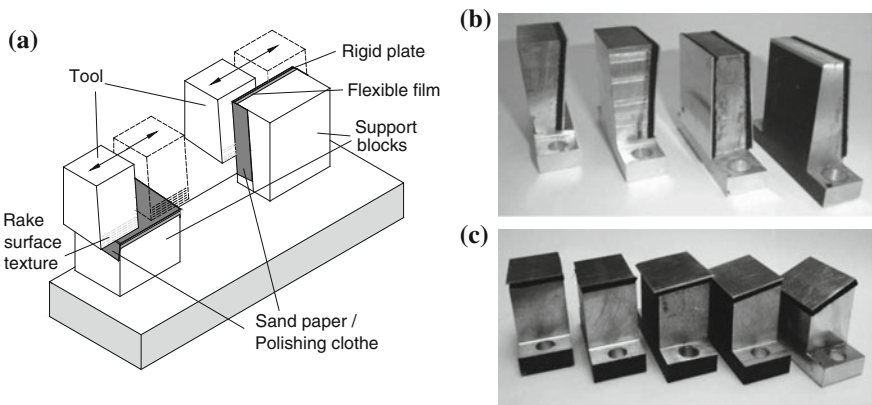
**Fig. 4.4** Schematic representation of the experimental apparatus that was utilized in orthogonal metal cutting



**Fig. 4.5** The Deckel-Maho DMC 63V machining center with a detail of the experimental apparatus where the tests were performed



**Fig. 4.6** **a** Cutting tools in AISI 316L stainless steel with different values of surface roughness and **b** detail of the tip of the tool showing the radius of the cutting edge



**Fig. 4.7** **a** Schematic representation of the Grinding and Polishing Unit (GPU) and of the support blocks utilized for reconditioning the **b** rake and **c** clearance surfaces

The GPU is capable of providing average values of surface roughness ( $R_a$ ) in the rake face within the range 0.04–0.75  $\mu\text{m}$ . These values are measured by a roughness tester along the rake and relief surfaces of the cutting tool in a direction perpendicular to the cutting edge.

The specimens were made from technically-pure lead (99.9 %) with a rectangular cross section of 80 mm  $\times$  20 mm (length  $\times$  width). The choice of technically-pure lead as a model material for the specimens was made in order to ensure narrow zones of intense plastic shearing under low cutting speeds, as required by the ideal orthogonal metal cutting conditions. This requirement is important for reducing the effect of strain-hardening, eliminating the influence of strain-rate sensitivity and keeping temperature rise, induced by energy dissipation due to plasticity and friction, low enough to allow the investigation to be exclusively focused on the influence of the surrounding medium in the mechanics of chip flow. The mechanical behaviour of technically-pure lead under low cutting speeds is not only capable of providing these operating conditions due to its near ideal rigid-plastic stress response as allows replicating the mechanical behaviour of conventional steels at the real manufacturing temperatures [17].

The influence of the surrounding medium was analysed by cutting in the presence of air and by shielding the cutting region by means of active and inert gases (oxygen, nitrogen or argon). The gases were supplied from an external source and applied at a rate of approximately 5 l/min through a nozzle to the cutting region (Fig. 4.4).

The three-dimensional piezoelectric dynamometer (Kistler 9257B) is attached to a signal amplifier (Kistler 5011B) and allows measuring the cutting forces during the tests (Figs. 4.4 and 4.5). The system is linear across its entire range, acquires forces with an accuracy of 1 % and its resolution allows measuring almost any dynamic changes in the forces of great amplitude. A personal computer data logging system based on a multifunction data acquisition card (National Instruments, PCI-6025E) combined with a special purpose LabView software controls testing, acquisition and storage of the experimental data.

Table 4.1 presents the experimental workplan for the entire set of test cases. The experiments were designed in order to correlate the influence of (i) gas shields

**Table 4.1** The plan of experiments

Case	Uncut chip thickness $t_0$ (mm)	Cutting speed $V_c$ (m/min)	Gas shield	Roughness $R_a$ ( $\mu\text{m}$ )
1–6	0.2	0.6	Oxygen	0.04, 0.1, 0.25, 0.35, 0.45, 0.75
7–12	0.2	0.6	Nitrogen	0.04, 0.1, 0.25, 0.35, 0.45, 0.75
13–18	0.2	0.6	Air	0.04, 0.1, 0.25, 0.35, 0.45, 0.75
19–24	0.2	0.6	Argon	0.04, 0.1, 0.25, 0.35, 0.45, 0.75

(active vs. inert) and (ii) surface roughness of the cutting tools with chip curl radius, chip-compression factor, shear angle, friction coefficient and cutting and thrust forces. No lubricants were utilized during the tests.

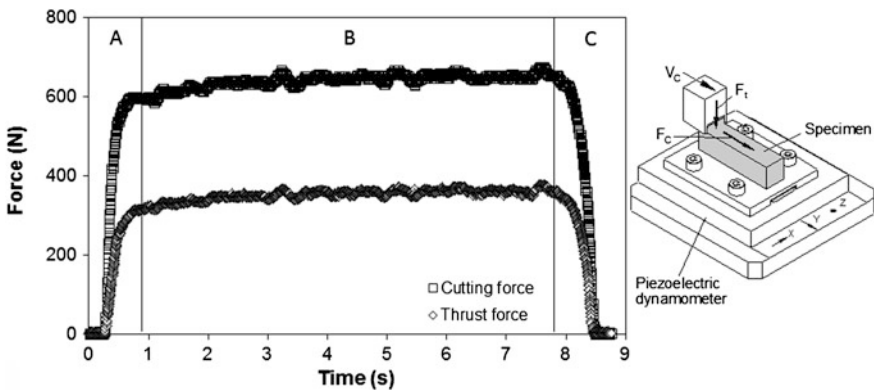
Eliminating the influence of lubrication (dry cutting conditions), temperature and strain-hardening and maintaining the cutting speed (0.6 m/min) and the uncut chip thickness (0.2 mm) identical for all test cases revealed crucial for analysing the overall influence of active and inert gases on the mechanics of chip flow. The influence of size effects was also removed from experimentation because the ratio of the uncut chip thickness to the edge radius of the cutting tools was equal to 100. Otherwise, the number of possible combinations of variables and phenomena would become very large.

The experiments were done in a random order and several replicates were produced for each test configuration in order to provide statistical meaning.

### 4.2.2 Cutting and Thrust Forces

The experimental apparatus and the work plan described in the previous section allowed determining the cutting  $F_c$  and thrust  $F_t$  forces the entire set of test cases that are listed in Table 4.1. Figure 4.8 presents a typical evolution of these forces with time during an orthogonal metal cutting test performed in the presence of air.

As seen in the figure, the cutting and thrust forces increase sharply at the beginning of the test (refer to zone 'A' in Fig. 4.8) and remain almost constant throughout subsequent steady-state cutting conditions (refer to zone 'B' in Fig. 4.8). The sharp decrease in the evolution of the cutting and thrust forces with time that are observed in zone 'C' is not relevant for the overall discussion because it corresponds to unsteady-state cutting conditions that are typical of the end of the cutting test.



**Fig. 4.8** Typical evolution of the cutting and thrust forces during an orthogonal cutting test performed in the presence of air ( $\alpha = 0^\circ$ ,  $\sigma_t = 5^\circ$ ,  $R_a = 0.251 \mu\text{m}$ ,  $t_0 = 0.2 \text{ mm}$ ,  $V_c = 0.6 \text{ m/min}$ )

**Fig. 4.9 a** Cutting and **b** thrust forces as a function of surface roughness and surrounding medium

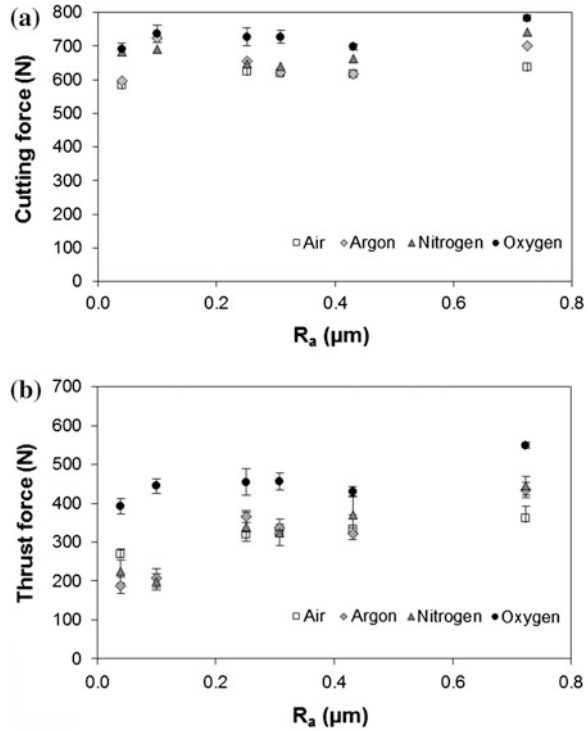


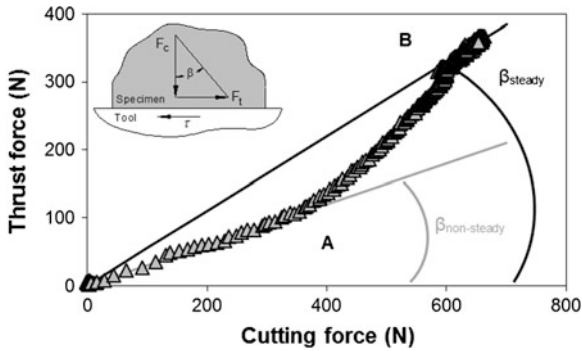
Figure 4.9 shows the experimental steady-state values of the cutting and thrust forces under different active and inert gas shields as a function of surface roughness for the entire set of test cases that are listed in Table 4.1.

As seen, dry cutting under an oxygen-rich atmosphere may require cutting and thrust forces up to 30 % higher than those needed in the presence of air or under an argon atmosphere. This is attributed to chemical reactions of oxygen with lead to form oxide films ( $\text{PbO}$ , the expected product of the chemical reaction between lead and oxygen) on the upper and lower surface boundaries of the chip and unveils the importance of the interactions between active gases and the freshly formed surfaces of the work materials.

Figure 4.9 also shows that cutting in the presence of air generally provides higher forces than those obtained under atmospheres of nitrogen or argon. This is because the low affinity of lead for nitrogen and the inert characteristics of argon avoid the formation of surface films on the freshly formed surfaces.

### 4.2.3 Friction Coefficient

The experimental values of the cutting  $F_c$  and thrust  $F_t$  forces that are acquired during the orthogonal metal cutting tests allow determining the friction coefficient.



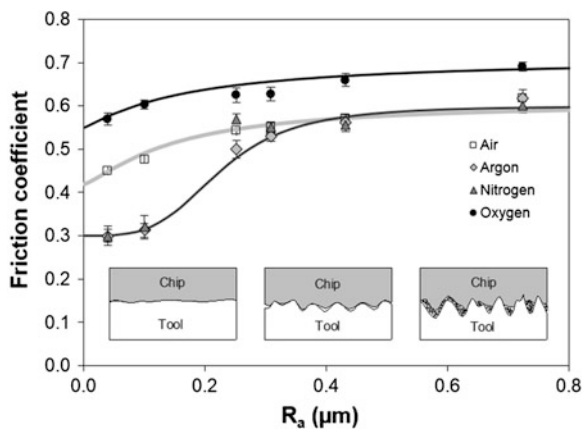
**Fig. 4.10** Thrust force as a function of the cutting force during an orthogonal cutting test performed in the presence of air ( $\alpha = 0^\circ$ ,  $\sigma_t = 5^\circ$ ,  $R_a = 0.251 \mu\text{m}$ ,  $t_0 = 0.2 \text{ mm}$ ,  $V_c = 0.6 \text{ m/min}$ )

Considering, for example, the evolution of the forces with time that is plotted in Fig. 4.8 it is possible to produce a new graphic where the thrust force is plotted as a function of the cutting force that is relevant for the understanding and determination of the friction coefficient (Fig. 4.10).

As seen in Fig. 4.10 there are two different linear trends corresponding to values of the friction coefficient under non-steady state (regions 'A' in Figs. 4.8 and 4.10) and steady-state (regions 'B' in Figs. 4.8 and 4.10) cutting conditions. The friction coefficient is lower at the initial non-steady state conditions and higher at the steady-state cutting regime.

Similarly to what was previously done for the plot of the cutting and thrust forces as a function of surface roughness and surrounding medium, a similar procedure can be used for the friction coefficient  $\mu = \tan \beta$  by taking into consideration the values of the friction coefficient  $\mu_{\text{steady}}$  under steady-state conditions retrieved from the entire set of experimental tests that are listed in Table 4.1. The result is shown in Fig. 4.11 and allows identifying three different regions for the cutting tests

**Fig. 4.11** Friction coefficient  $\mu$  as a function of surface roughness  $R_a$  and surrounding medium



performed under nitrogen and argon gas shields: (i) a leftmost region ( $R_a < 0.1 \mu\text{m}$ ) where the friction coefficient is constant and takes the smallest value among all the test cases, (ii) a rightmost region ( $R_a > 0.3 \mu\text{m}$ ) where the friction coefficient is constant and takes the largest value among all the test cases and (iii) a region in-between where the friction coefficient progressively grows from the smallest to the largest measured values.

In the leftmost region of the graphics the basic source of friction is adhesion ( $\mu \cong \mu_{adh}$ ) and the friction force resulting from the relative sliding movement between the chip and the cutting tool is roughly equal to the force that is needed for shearing the junctions formed by localized pressure welding (cold welding) at the asperities. This is because surface roughness is very small and because the low affinity of lead for nitrogen and the inert characteristics of argon avoid the formation of surface films, allowing the chip to slide smoothly along the rake surface of the cutting tool.

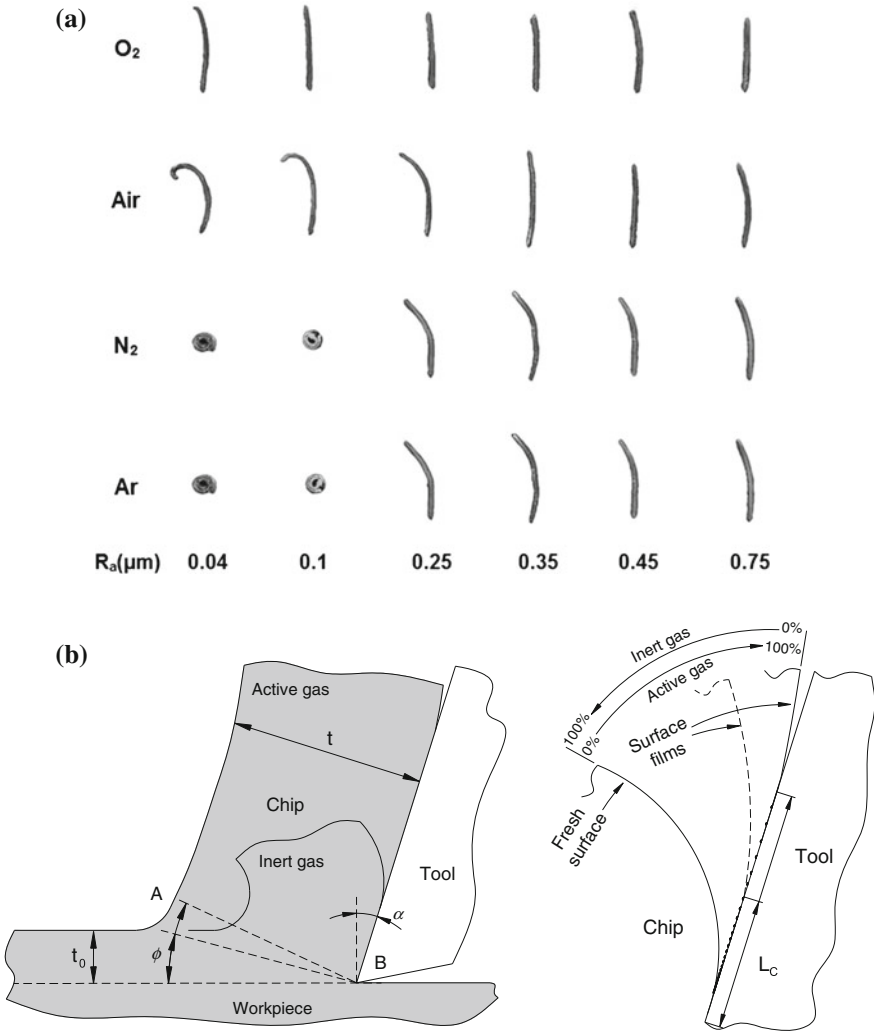
On the contrary, in the rightmost region of the graphic (where surface roughness of the cutting tool is very large) there is a more pronounced interaction between the asperities namely, the penetration and plastic deformation of the boundary surfaces of the chips and, in some cases, the formation of debris from micro-cutting at the asperity level (refer to the rightmost inset detail in Fig. 4.11). The increase of ploughing and the extra resistance to sliding caused by loose debris raise the friction force and, therefore, the friction coefficient for rougher tools is larger than for smoother tools.

The results obtained from the orthogonal cutting tests in the presence of air or under an oxygen-rich atmosphere do not show evidence of the aforementioned first and second regions of the graphic (Fig. 4.11) because both cases show a monotonic increase of the friction coefficient from smaller to larger values of surface roughness. This is attributed to the oxide films of PbO formed in the upper and lower surface boundaries of the chips, which do not allow material to slide smoothly along the rake surface of the cutting tools, even when roughness is very small. Finally, it is worth notice that the affinity of lead for oxygen is responsible for increasing the overall level of friction even when cutting with tools having large surface roughness.

#### 4.2.4 Chip Curling

Although the influence of the surrounding medium in metal cutting is often resumed to its primary function of cooling and lubricating, one important aspect of the cutting medium on the tribological conditions at the tool-chip contact interface is the protection against active gases in air.

Figure 4.12a presents the cross section of the chips obtained for the entire test cases that are listed on Table 4.1. As seen, cutting under nitrogen or argon atmospheres allow chips to curl naturally within the normal range of surface roughness currently found in cutting tools whereas the exposure to oxygen causes the chip curl



**Fig. 4.12** a Pictures of chip cross sections obtained in cutting tests performed under different surface roughness and surrounding medium conditions, and b schematic representation of chip flow as a function of the surrounding medium

radius to become larger. In fact, the exposure to oxygen causes the chips to flow along the rake surface of the cutting tools, increasing the contact length  $L_c$  (Fig. 4.12b), and promoting its curvature away from the cutting edge.

The contact length  $L_c$  in steady-state cutting conditions is due to an energy compromise between the plastic work, a quantity inversely proportional to the radius of curvature of the chip, and the amount of frictional work which is directly proportional to the contact length and, therefore, to the radius of curvature of the chip. Because, cutting in the presence of oxygen increases the friction coefficient



(Fig. 4.11), it follows that frictional work will also increase with the formation of oxide films on the new freshly cut surfaces of lead. The exposure of lead to oxygen also results in larger chip curl radius (Fig. 4.12a).

The influence of the surrounding medium in the mechanics of chip flow can be further understood by analysing the evolution of the chip compression factor  $t/t_0$  and of the primary shear plane angle  $\phi$  as a function surface roughness  $R_a$  for cutting tests performed in the presence of different gas shields (Fig. 4.13):

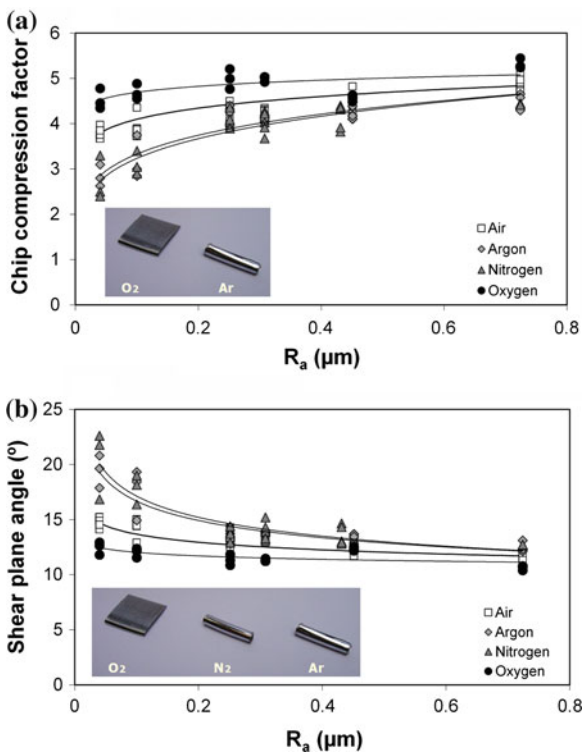
$$\frac{t}{t_0} = \frac{\overline{AB} \cdot \cos(\phi - \alpha)}{\overline{AB} \cdot \sin \phi} = \cot \phi \cos \alpha + \sin \alpha \tag{4.1}$$

where  $\alpha$  is the rake angle,  $t_0$  the uncut chip thickness and  $t$  the chip thickness.

Two different patterns of behaviour can be distinguished; in case of inert gas shields the chip compression factor  $t/t_0$  and the primary shear plane angle  $\phi$  are very sensitive to the surface roughness  $R_a$  whereas in case of cutting in the presence of active gases the aforementioned sensitivity is less important.

In the first pattern type of behaviour, chip thickness decreases (using the original uncut chip thickness as reference) as surface roughness  $R_a$  diminishes due to an increase of the shear plane angle  $\phi$ . As a result of this, the contact length  $L_c$  at the

**Fig. 4.13 a** Chip compression factor and **b** shear plane angle as a function of surface roughness and surrounding medium. *Insets* show pictures of chips produced by cutting in the presence of different gas shields



rake tool surface is diminished and curling of the chip is promoted when cutting in the presence of argon and nitrogen, as shown in the photographs included in Fig. 4.13.

The second pattern type of behaviour in Fig. 4.13 is similar to that of cutting under dry conditions. The curling radius is much larger than that experimentally observed in case of cutting in the presence of inert gas shields and the acquired data points towards the influence of oxide films of PbO to be more important than the diminishing the surface roughness  $R_a$ . As expected, the influence of oxide films in the mechanics of chip flow reaches a maximum when cutting in the presence of an oxygen gas shield.

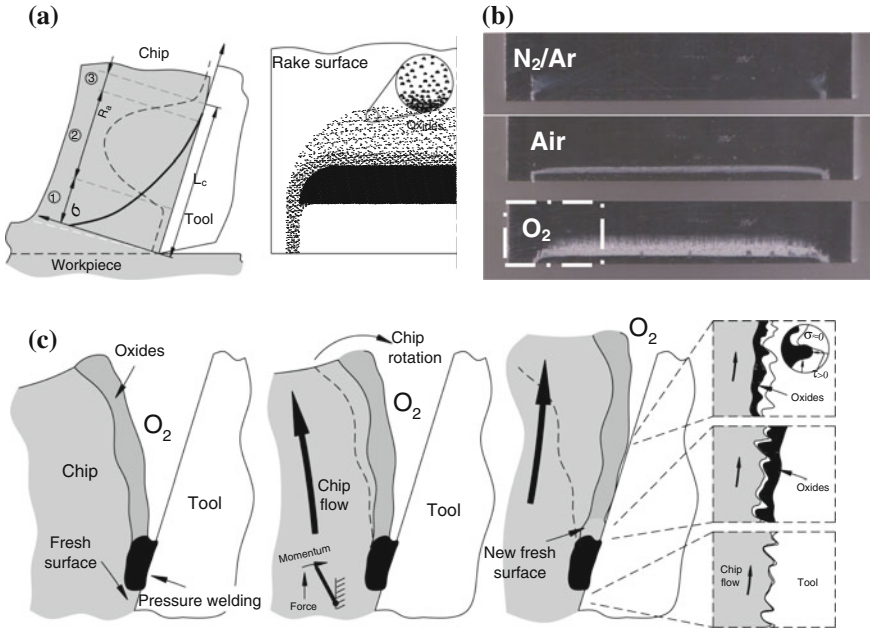
The influence of surface roughness in chip curling can be further analysed in Fig. 4.12. As seen, the higher the roughness, the smaller is the influence of the surrounding medium and the greater are the difficulties for the chips to curl away from the rake face. This is due to a more pronounced interaction between the asperities of the chip and tool and allows us to conclude that cutting in the presence of active gases will diminish the magnitude of the shear plane angle  $\phi$  and will produce thicker chips than in case of cutting under low-affinity or inert atmospheres.

The results supporting these conclusions are in line with common beliefs among researchers and practitioners that oxygen may significantly influence the mechanics of chip flow and go against published research work in the field claiming no influence of the surrounding medium, that was referred in the introduction to this chapter.

The proposed mechanism for explaining the influence of oxygen in the mechanics of chip flow is shown in Fig. 4.14 and requires contact length  $L_c$  to be divided into three main regions; (i) the bottom newly cut surface of the chip (denoted as '1' in Fig. 4.14a), (ii) the intermediate surface of the chip (2) and (iii) the upper surface (3) that extends up to the point where chip separates from tool.

Region '1' is in immediate and intimate contact with the rake face of the tool, is submitted to high normal pressures and is uncontaminated by oxygen. Because its length is small (approximately or slightly greater than  $t_0$ ) and its roughness  $R_a$  is also small the basic source of friction in region '1' is expected to be adhesion.

Region '2' experiences less significant normal pressures than previous region '1' but its exposure to oxygen results in the formation of oxide films in the lower surface boundary of the chip. Figure 4.14a, b show a schematic representation and a photograph of the oxide films that were formed on the surface boundary of the chip and were subsequently smeared over the rake face of the tool (refer to the light coloured strips in Fig. 4.14a) when cutting in the presence of air or under an oxygen-rich atmosphere. Because the average thickness of the oxide films was found to be 3  $\mu\text{m}$ , which is a value significantly larger than the average surface roughness of the rake face of the cutting tool, it is possible to conclude that the interaction between cutting medium and freshly formed surfaces is strong and penetrates deep into the metallic substrate. It is worth notice that in case of cutting under nitrogen or argon atmospheres there is no evidence of surface films left on the



**Fig. 4.14** Cutting under inert and active gas shields: **a** schematic representation of the oxide films that were formed on the freshly cut surface of the chip and are pressure welded onto the rake face of the cutting tool, **b** photographs showing evidence of oxide films on the tool rake face when cutting in the presence of air or under an oxygen gas shield and **c** the proposed mechanism for explaining the influence of oxide films in chip curl

rake face of the tool (Fig. 4.14b) and, therefore, roughness after cutting is similar to that before cutting.

As seen, the oxide films that are pressure welded onto the rake face of the cutting tool are spread throughout a larger area in case of cutting under an oxygen-rich atmosphere than in the presence of air. The increase in surface roughness due to the oxides (Fig. 4.14) in conjunction with the extra force that is needed for shearing the junctions formed between the oxide particles and the asperities gives rise to higher values of friction in region ‘2’. Material flow behaviour approaches sticking conditions, due to a more pronounced interaction between the oxide particles and the asperities and this creates difficulties for the chips to curl away from the rake face of the cutting tools, thereby, increasing its overall contact length  $L_c$  (Fig. 4.14c). This explains the differences observed in the chip cross sections that are pictured in Fig. 4.12.

Region ‘3’ experiences the lowest normal pressures. Scattered oxide films, if present, are likely washed away during sliding of the chip along the rake face of the cutting tools and this explains the reason why Fig. 4.14b shows no signs of contamination arising from the lower surface boundaries of the chips.

The above conclusion helps clarifying the role of cutting fluids in metal cutting. In fact, besides cooling the working area, thereby reducing its temperature, distortion and improving tool life, cutting fluids are also responsible for protecting the freshly formed surfaces of the work material from active gases such as oxygen.

### 4.3 Milling Under Gas Shields

This last section of the chapter extends the investigation to conventional milling of an engineering material and is exclusively focused on the influence of the surrounding medium in the cutting forces and tool wear.

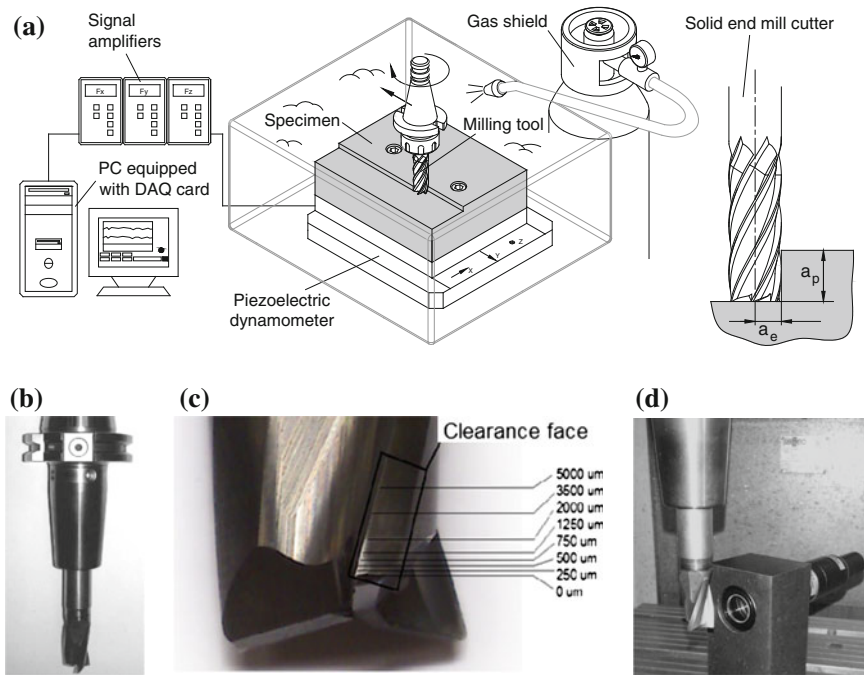
#### 4.3.1 *Equipment, Methods and Procedures*

The experimental apparatus that was developed by the authors to perform conventional milling tests under gas shields is schematically presented in Fig. 4.15a and is essentially composed by a cutting tool, a specimen, a gas chamber, a three-dimensional piezoelectric dynamometer, a data acquisition system and a confocal chromatic imaging measurement system (Fig. 4.15d).

The cutting tool is a solid end mill cutter JS513(51) supplied by Seco Tools with three cutting edges, 16 mm diameter, an helix angle of  $20^\circ$  and a corner radius equal to 0.16 mm (Fig. 4.15b). The selection of an end mill with three cutting edges provides a good compromise between end mills with two cutting edges that have better space for chip ejection and end mills with four cutting edges that ensure better surface finishes. The utilization of a heat shrink tool holder, in which the tool holder clamping area is heated for a few seconds before inserting the end mill cutter, ensures excellent rigidity and concentricity of the end mill with tool run-outs below  $2 \mu\text{m}$ .

The specimens were made from aluminium AA7050-T7451 with a rectangular cross section of  $140 \times 100$  (length  $\times$  width). This choice of material served the dual purpose of carrying out the investigation in an engineering material (widely used in the aerospace industry) and selecting a material with high affinity to oxygen. The affinity of aluminium to oxygen is responsible for the formation of a surface layer of alumina (or, aluminium oxide)  $\text{Al}_2\text{O}_3$  of approximately  $1 \mu\text{m}$  thickness with high hardness and abrasivity.

The cutting parameters employed in the milling tests are summarized in Table 4.2. All tests were performed in dry conditions, in the presence of air or under an argon atmosphere, in end milling conditions. The choice of parameters was performed with the objective of increasing tool wear, reducing the influence of temperature in chip formation and eliminating any extra influence of oxygen beyond that arising from cutting in the presence of air that would result from



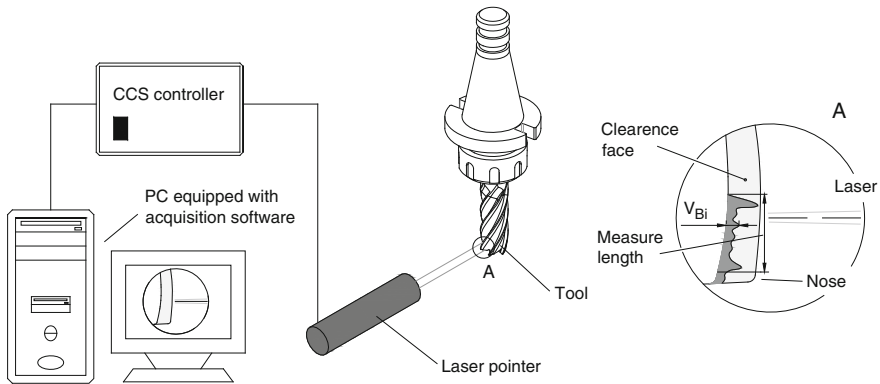
**Fig. 4.15** Milling under gas shields. **a** Schematic representation of the experimental apparatus that was utilized in the tests, **b** the end mill and the heat shrink tool holder, **c** wear measuring locations with reference to distances to the end cutting edge **d** picture of the confocal chromatic imaging measurement system that was utilized for measuring tool wear

**Table 4.2** The cutting parameters for the milling tests

Depth of cut, $a_p$ (mm)	2
Width of cut, $a_e$ (mm)	2
Cutting speed, $V_c$ (m/min)	300
Feed rate, $f$ (mm/min)	600
Feed per tooth, $f_z$ (mm)	0.033

dissociation of water molecules into oxygen and hydrogen, if cutting fluid emulsions were employed.

The cutting forces were measured by means of a three-dimensional piezoelectric dynamometer (Kistler 9257B) attached to a signal amplifier (Kistler 5011B). A personal computer data logging system based on a multifunction data acquisition card (National Instruments, PCI-6025E) combined with a special purpose LabView software was employed for the acquisition and treatment of the experimental data.



**Fig. 4.16** Schematic representation of the experimental set up that was utilized for measuring tool wear in the milling tests

In general, tool wear can take several forms such as flank wear, notch wear, crater wear, edge rounding and edge cracking, among others. All these wear mechanisms play a role in tool life, which is usually characterized by the maximum number of machined parts or the maximum duration (for example, in hours) of operation it takes to reach a specific condition (or criterion).

This section of the chapter is focused on tool wear caused by the intense rubbing of the clearance faces of the milling tool over the freshly formed surfaces of the specimen. This type of wear is commonly designated as ‘flank wear’ and leads to the formation of a wear land.

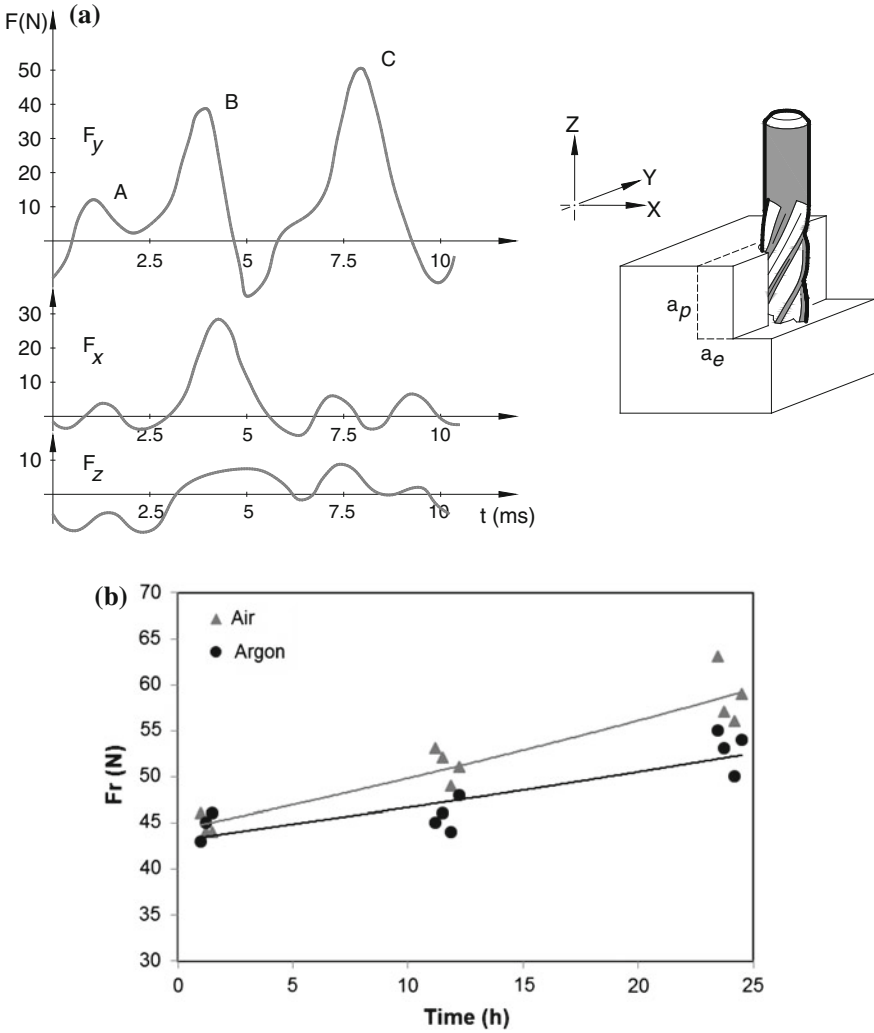
The width  $V_B$  of the wear land was measured by means of a confocal chromatic laser based imaging system (Fig. 4.15d) that employs a white light confocal displacement sensor CL4-MG35 and a controller STIL Initial 4.0 with a resolution of 130 nm and a precision of 300 nm (Fig. 4.15d). The equipment and procedure is schematically shown in Fig. 4.16 and the measuring locations were performed with reference to distances of 250, 500, 750 and 1,250  $\mu\text{m}$  to the end cutting edge (Fig. 4.15c).

The overall experimental apparatus for performing the milling tests was installed in the Deckel-Maho DMC 63V machining center that had been previously utilized in the orthogonal metal cutting tests (refer to Fig. 4.5).

### 4.3.2 Cutting Forces

Figure 4.17a shows the experimental cutting forces  $F_x$ ,  $F_y$  and  $F_z$  measured by means of the three-dimensional piezoelectric dynamometer during one turn performed after 25 h of milling under dry conditions in the presence of air.

The three peaks with increasing amplitudes of the experimental cutting force  $F_y$  that are denoted as ‘A’, ‘B’ and ‘C’ in Fig. 4.17a are associated with the three



**Fig. 4.17** a Three-dimensional cutting forces after 25 h of milling under dry conditions in the presence of air and b resultant force  $F_r$  in the xy-plane as a function of the milling time and the surrounding medium

different cutting edges of the end mill. The evolution of the cutting forces  $F_x$ ,  $F_y$  and  $F_z$  during the 10 ms that are needed for the end mill to complete a full turn allow concluding that the third cutting edge, corresponding to a maximum peak force  $F_y = 50$  N (obtained after 7.5 ms—refer to ‘C’), is the outermost cutting edge of the tool. Moreover, results also show that the instant of time where the maximum peak force ‘C’ is registered is approximately coincident with the instant of time when the

cutting velocity is aligned with the y-axis of the piezoelectric dynamometer ( $F_x \cong 0\text{ N}$ ).

The negative values of the cutting force  $F_y$  are caused by the ejection of chips along the y-axis.

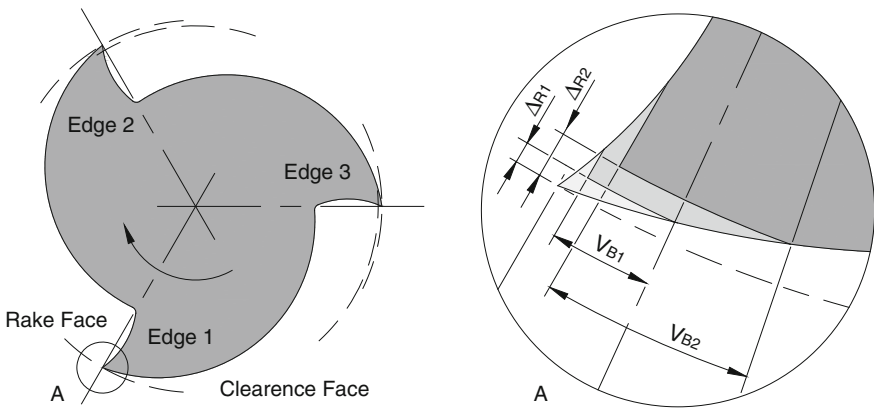
By performing the acquisition of the experimental cutting forces in two other instants of time corresponding to 1 and 24 h of operation and plotting the resultant force  $F_r$  (in the xy-plane),

$$F_r = \sqrt{F_x^2 + F_y^2} \tag{4.2}$$

as a function of time and surrounding medium (Fig. 4.17b), it is possible to conclude that major differences derived from milling in the presence of air or under an argon atmosphere are only noteworthy above 10 h of operation. In fact, only after 10 h of operation the resultant force  $F_r$  experiences a faster growth with time when milling in the presence of air than under an argon atmosphere.

### 4.3.3 Tool Wear

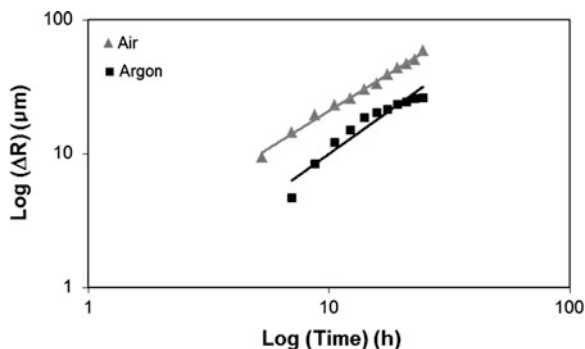
Figure 4.18 presents a schematic representation of tool wear in a solid end mill cutter with three cutting edges. Wear occurs simultaneously in the rake and clearance faces and gives rise to a reduction  $2 \times \Delta R_i$  in the diameter of the end mill and to an increase of the contact width  $V_{Bi}$  between the clearance face and the workpiece. Figure 4.19 shows the evolution of the reduction in the radius of the end mill with the milling time and the surrounding medium.



**Fig. 4.18** Schematic representations of tool wear in a solid end mill cutter with the dimensions that are utilized for its characterization



**Fig. 4.19** Reduction in the radius of the end mill as a function of the milling time and surrounding medium



Tool wear in the rake and clearance faces are caused by abrasive and adhesive mechanisms resulting from the affinity of the freshly formed surfaces to oxygen. They are the most common wear modes in conventional milling and are generally undesirable because dimensional control of the workpiece is lost, surface finished deteriorates and heat generation increases.

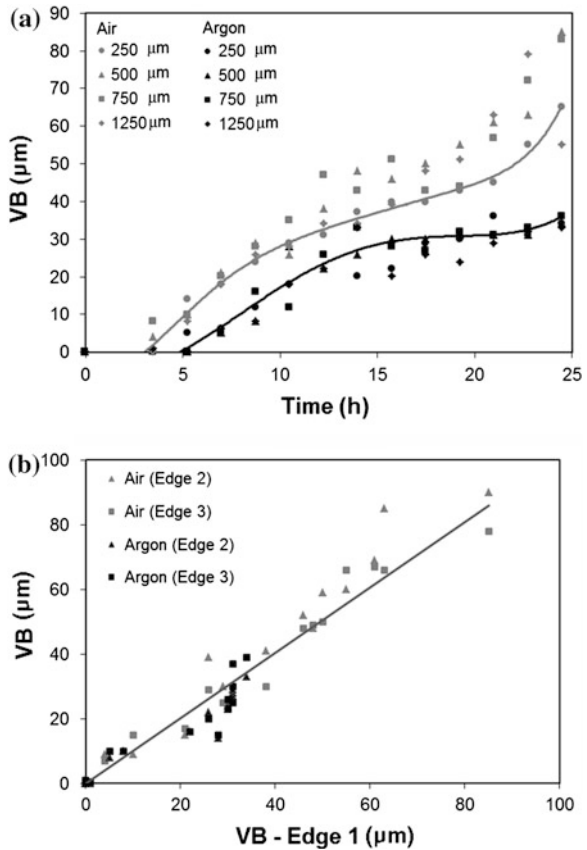
Figure 4.20a shows the widths  $V_{Bi}$  of the flank wear land after  $t_i$  hours of milling that were measured by means of the confocal chromatic imaging system at locations corresponding to 250, 500, 750 and 1,250  $\mu\text{m}$  distance from the end cutting edge. As seen, after the initial 3–5 h of operation wear starts growing rapidly, between 10 and 20 h of operation wear settles down to a nearly steady-state rate, and after 20 h of operation wear accelerates once again towards the end of tool life.

Results in Fig. 4.20a also show that cutting in the presence of air accelerates flank wear, thereby, reducing tool life. In fact, milling under an argon atmosphere allows reducing flank wear by approximately 50 % in 25 h of operation. This result is in good agreement with those obtained by other researchers [16].

The abovementioned evolution of the flank wear with the milling time and surrounding medium for a particular cutting edge can be extrapolated to the other two cutting edges, placed in different radial positions, as proved by the linear interpolation (with a slope equal to 1.01) that is presented in Fig. 4.20b.

The increase of tool life by cutting in the presence of an argon atmosphere may be explained by the prevention of alumina  $\text{Al}_2\text{O}_3$  formation at the contact interface between the cutting edges and the freshly formed surfaces of the workpiece and also by its avoidance during the period of time when the surfaces are not in contact with the cutting edges. The latter is very important because it prevents the cutting edges from engaging the hard and abrasive surface layer of alumina each time a new cut starts. Instead, the cutting edges will always engage the more ductile and less abrasive aluminium alloy.

**Fig. 4.20 a** Flank wear in a cutting edge as a function of the milling time and surrounding medium and **b** Flank wear in cutting edges 2 and 3 as a function of the flank wear in cutting edge 1 (values measured at 500  $\mu\text{m}$  distance from the end cutting edge)



### 4.4 Conclusions

This chapter presented the influence of the surrounding medium in the mechanics of chip flow by performing orthogonal metal cutting and conventional milling under active and inert gas shields. The experimental results obtained from orthogonal metal cutting show that cutting in the presence of oxygen leads to higher values of friction, chip compression factor and chip curl radius and to lower values of the shear plane angle. This indicates that the surface films formed on a freshly cut surface will significantly influence the mechanics of chip flow.

The proposed model for explaining the influence of surface films on the mechanics of chip flow during orthogonal metal cutting that is based on the interaction between chip and tool rake face, allows understanding the reason why cutting in the presence of oxygen will increase the contact length and promote curvature away from the cutting edge.

Similar results obtained in conventional milling of an aluminium alloy allow concluding that oxygen has a significant influence on the overall cutting conditions, namely in the increase of the cutting forces and tool wear.

All these results point towards the importance of taking the interaction between the cutting tools and freshly formed surfaces into account due to chemical reactions with active gases in the atmospheric air. In fact, not taking this interaction into consideration leads to misunderstanding of the mechanics of chip flow, the sources of friction along the rake surface of the cutting tools, the cutting forces, the tool wear and the role of cutting fluids, when used.

**Acknowledgments** The authors would like to acknowledge the support provided by Embraer, Portugal.

## References

1. Jawahir IS, van Luttervelt CA (1993) Recent developments in chip control research and applications. *Ann CIRP* 42:659–693
2. Nakayama K, Ogawa M (1978) Basic rules on form of chip in metal cutting. *Ann CIRP* 27 (1):17–21
3. Klufft W, Konig W, Luthukelt CA, Nakayama K, Pekelkuing AJ (1979) Present knowledge of chip control. *Ann CIRP* 28/2:441–455
4. Pekelharing AJ (1963) Why and how does the chip curl and break. *Ann CIRP* 12(1):144–147
5. van Luttervelt CA, Childs THC, Jawahir IS, Klocke F, Venuvinod PK (1998) Present situation and future trends in modelling of machining operations—progress report of the CIRP working group ‘modelling of machining operations’. *Ann CIRP* 47:587–626
6. Zorev N (1966) *Metal cutting mechanics*. Pergamon Press, Oxford
7. Shaw MC (1984) *Metal cutting principles*. Clarendon Press, Oxford
8. Oxley PLB (1989) *Mechanics of machining: an analytical approach to assessing machinability*. Wiley, New York
9. Atkins AG (2003) Modelling metal cutting using modern ductile fracture mechanics: quantitative explanations for some longstanding problems. *Int J Mech Sci* 45:373–396
10. Atkins AG (2009) *The science and engineering of cutting*. Butterworth-Heinemann, Oxford
11. Rosa PAR, Martins PAF, Atkins AG (2007) Revisiting the fundamentals of metal cutting by means of finite elements and ductile fracture mechanics. *Int J Mach Tools Manuf* 47:607–617
12. Astakhov VP (2006) *Tribology of metal cutting*. Elsevier, Oxford
13. Kalpakjian S (1997) *Manufacturing processes for engineering materials*. Addison-Wesley, Reading
14. de Chiffre L (1990) *Metal cutting mechanics and applications*. DSc. thesis, Technical University of Denmark
15. Cristino VAM, Rosa PAR, Martins PAF (2010) Cutting under active and inert gas shields: a contribution to the mechanics of chip flow. *Int J Mach Tools Manuf* 50:892–900
16. Yamane Y, Narutaki N, Hayashi K (1996) Suppression of tool wear by using an inert gas in face milling. *J Mater Process Technol* 62:380–383
17. Altan T, Henning HJ, Sabroff AM (1970) The use of model materials in predicting forming loads in metalworking. *J Eng Ind Trans ASME* 92:444–452

# Chapter 5

## Machinability of Magnesium and Its Alloys: A Review

Diego Carou, Eva M. Rubio and J. Paulo Davim

**Abstract** In the last decades, the interest for magnesium has increased notably. In particular, the need for weight reduction in the automotive industry has made magnesium a suitable material to replace traditional structural materials because of its low density. But, in addition, magnesium is also finding applications in different sectors as aeronautics, electronics, medical or sports. Thus, machining of magnesium is a topic of great interest for industry and researchers. In the present work, an introduction to the main topics on magnesium machining is presented. The text covers from general topics of magnesium to more specific ones related with the machining process. In this sense, an approximation to the properties of magnesium, magnesium alloys and metal matrix composites of magnesium, and some applications are presented to give a general overview of magnesium. After that, the machining of magnesium is covered addressing general issues and more specific particularities of magnesium machining, such as the ignition risk. To conclude, a brief review of some of the main experimental investigations on magnesium machining is presented, covering drilling, milling and turning processes. In these studies, the machining process is assessed using indicators such as surface finish, temperature or tool wear.

---

D. Carou (✉) · J.P. Davim  
Department of Mechanical Engineering, University of Aveiro,  
Campus Santiago, 3810-193 Aveiro, Portugal  
e-mail: diecapor@gmail.com

J.P. Davim  
e-mail: pdavim@ua.pt

E.M. Rubio  
Department of Manufacturing Engineering, National University  
of Distance Education (UNED), C/Juan Del Rosal, 12, E28040 Madrid, Spain  
e-mail: erubio@ind.uned.es

## 5.1 Introduction

Magnesium is one of the most abundant components of the Earth together with others as the aluminium, calcium and iron [1, 2]. Due to its high reactivity, the natural way of finding it in the nature is in the shape of compounds [3]. Thus, the production industry plays an important role in the use of magnesium.

The utilization of magnesium in industrial applications finds the first references in the World Wars I and II in applications inside the nuclear industry and military aircrafts. But, after the World War II the use of magnesium was reduced greatly [4]. Interest in magnesium has reappeared in the last decades with a great increase in both world primary production and world primary production capacity. Of special relevance is the strong development of the Chinese magnesium industry [5].

The strong development that has been occurring in the field of magnesium alloys makes possible their use in different industries such as the aeronautics, automotive, electronics and medical [6]. The use of magnesium in different industrial sectors encourages getting a better understanding of its use in industrial processes and the expected results of the processes. In particular, it is important to evaluate the use of magnesium in traditional machining processes to deliver new pieces or products, or to perform repair and maintenance operations for magnesium pieces.

## 5.2 Properties

Pure magnesium has a compact hexagonal crystal structure or hexagonal close-packed (HCP) that restricts the movement according to the basal planes. Thus, magnesium is difficult to plastically deform at room temperature. At higher temperatures other slip planes become operational. Therefore, magnesium alloys are formed with temperatures, in general, between 340 and 510 °C. Another feature that provides the HCP structure is the anisotropy for the mechanical properties. Because of the difficulty of cold forming, casting becomes the most suitable method for producing magnesium pieces [7].

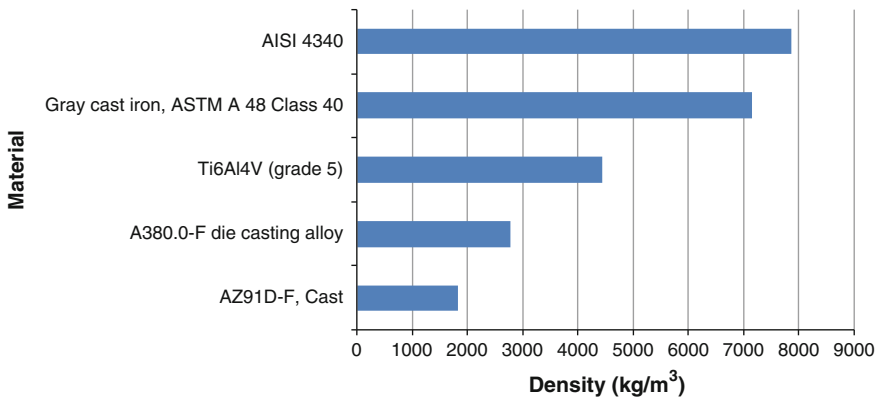
Magnesium has a wide range of advantages that enable its use in different applications. However, there are also several disadvantages that have to be considered. In Table 5.1, the main advantages and disadvantages of magnesium are listed [4, 8, 9].

One of the main advantages of magnesium is its low density. This feature makes it a suitable material to use where the objective is the reduction of weight. In the Fig. 5.1, the density of different usual structural materials is compared. Magnesium has the lowest density of all of the usual structural materials, being 1,810 kg/m<sup>3</sup> for the AZ91D-F cast magnesium alloy. Concretely, the density of the other materials, represented in Fig. 5.1, is between 1.52 and 4.34 times of the density of magnesium.

The mechanical properties of materials play an important role in machining. Thus, the main mechanical properties of magnesium alloys are listed in Table 5.2 along with the properties of other usual structural materials.

**Table 5.1** Main advantages and disadvantages of magnesium

Advantages	Disadvantages
Can be machined (milling/turning) at high speeds	Poor creep resistance at temperatures above 100 °C
High specific strength	Low resistance to corrosion
Good castability	Low elastic modulus
Availability	High degree of shrinkage on solidification
Better resistance to corrosion in the case of pure magnesium	Difficult to be formed at low temperatures and toughness
Good weldability under controlled atmosphere	High chemical reactivity
Lowest density among all structural materials	
In front of the polymeric materials: better mechanical properties, ageing resistance, and better electrical and thermal conductivity	
Recyclable	



**Fig. 5.1** Density of magnesium and other usual structural materials [10–14]

Magnesium competitiveness against other structural materials increases when considering the specific properties because of its low density. Thus, when considering properties such as specific strength, specific stiffness, dent resistance or shell stiffness magnesium performance is closer to other structural materials, or even, higher [7].

In the case of machining processes, the thermal properties are also important because the temperature evolution during the process affects the results and the productivity of the machining process. The main thermal properties are listed in the Table 5.3. In particular, thermal conductivity is one of the most important thermal properties of magnesium because its high value helps to evacuate the heat generated during the machining process.

**Table 5.2** Mechanical properties of magnesium and other usual structural materials [15–19]

Mechanical properties	$\alpha/\beta$ Ti alloy	AISI 4000 series steel	Aluminium alloy	Magnesium alloy	Gray cast iron
Hardness, Brinell	290–411	121–578	28–79	30–600	131–550
Hardness, Vickers	304–480	36–700	29–89	59–100	161–321
Tensile strength, ultimate (MPa)	825–1,580	450–1,970	90–295	90–1,070	118–448
Tensile strength, yield (MPa)	759–1,410	275–1,860	31–285	21–460	65.5–172
Elongation at break (%)	3–18	8–34	1–40	1–75	–
Modulus of elasticity (GPa)	105–125	196–213	68.9–70.0	38–120	62.1–162
Compressive yield strength (MPa)	860–1,280	1650–1,800	0.552–4.60	21–448	572–1,380
Poissons ratio	0.310–0.342	0.270–0.300	0.330–0.350	0.270–0.350	0.240–0.330
Fatigue strength (MPa)	140–1,160	138–772	48.3–110	30–235	68.9–207
Shear modulus (GPa)	41.0–48.3	75–82	0.0483–26.0	16.3–48.0	27.0–65.5

**Table 5.3** Magnesium thermal properties [18]

Thermal properties	Value
Specific heat capacity (J/kg°C)	800–1,450
Thermal conductivity (W/mK)	44.3–159
Melting point (°C)	330–650
Solidus (°C)	330–650
Liquidus (°C)	585–650
Boiling point (°C)	1,090

### 5.3 Magnesium Alloys and Metal Matrix Composites

Drawbacks of pure magnesium make necessary the development of magnesium alloys. The use of alloy elements can improve the properties of the resulting alloy. For instance, they can improve castability (aluminium, rare earths), mechanical and technological properties such as creep properties (silver, calcium, manganese, silicon), or improve corrosion resistance (manganese, rare earths, yttrium). The different properties that the alloy elements give to magnesium alloys and the different requirements of industry lead to several lines of development for magnesium alloys. These lines are focussed on the improvement of the specific strength, ductility, creep resistance or other properties such as the modulus of elasticity, wear or thermal expansion [20].

The use of alloy elements can also help to modify the ignition temperature of magnesium alloys which is important for machining purposes. For instance, alloy elements such as beryllium or calcium allow raising the ignition temperature due to the generation of a surface oxide layer [21]. Other materials such as rare earths: cerium, lanthanum [22] or yttrium [21, 23] let also increase the ignition temperature of magnesium alloys.

In addition to the use of magnesium to produce alloys, magnesium is also used to produce metal matrix composites (MMC). MMCs have many advantages over monolithic metals [24]. The use of magnesium as MMC's matrix material provides advantages such as high specific strength and stiffness, good damping capacities, and dimensional stability [25].

## 5.4 Applications

In its pure composition, magnesium is mainly used as an alloying element in aluminium or as a reducing agent in titanium and zirconium production [26]. When used in alloys, magnesium finds applications for structural products such as die castings or wrought products [5]. In addition, magnesium is also used to produce MMCs that are being widely used to replace conventional materials for a large number of structural applications in sectors such as aeronautics/aerospace, defence, sports and transportation [27, 28].

Next, some of the applications of magnesium in different industrial sectors are highlighted.

### 5.4.1 Automotive

The transportation sector represents, approximately, the 26 % of the total energy consumed globally, depending almost the half, mainly supplied by fossil fuels, on light-duty vehicles. In addition, the transportation sector is also responsible for a high percentage of the emissions to the atmosphere [29]. In the last decades, fuel economy has increased its importance, and energy efficiency is an important line for research and development activities. One of the main strategies to improve fuel consumption in the transportation sector is the reduction of the mass of the vehicles [30]. In this sense, magnesium finds many applications in the automotive industry because of its low density, being a suitable material to replace steel and cast iron [31]. Thus, magnesium is being used more frequently in the transportation industries among other materials such as aluminium, plastics or carbon fibres [32], estimating the average consumption of magnesium per vehicle in 50 kg by 2015 [33]. Additionally, the use of magnesium in vehicle construction provides important benefits as an increased dent and impact resistance compared with aluminium, or a greater ability to dampen noise and vibration [34].



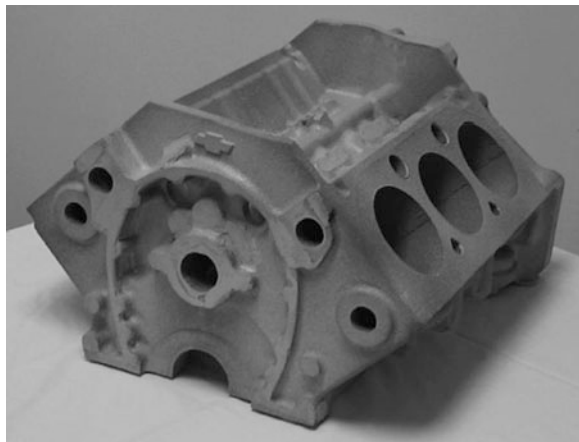
The use of magnesium in cars has a long tradition. One of the first and more noteworthy applications is its use in the Volkswagen Beetle [4]. In addition, the main car manufacturers have used magnesium to produce different parts of their models. To name a few, companies such as Audi, BMW, Ford, Lexus, Toyota or Porsche have used magnesium in their cars [33]. In Table 5.4, some applications of magnesium in car manufacturing are highlighted.

The importance of the weight strategies in car manufacturing is clear when considering the heaviest parts of the cars. For instance, the substitution of traditional cast iron in engine blocks can lead to weight reductions higher than 50 % when using magnesium, letting reduce the weight of the engine by more than 50 kg [38] (Fig. 5.2).

**Table 5.4** Use of magnesium in car manufacturing [35–37]

Part	Magnesium alloy
Wheel	AM60A and AZ81A
Pump	AZ91
Inlet	AZ91
Transmission cover	AZ91 and AZ81A
Cylinder cover	AZ91B
Gearbox	ZE41A
Suspension	ZE41A
Chassis	ZE41A
Steering wheel core	AM60A
Inner door	AM60B

**Fig. 5.2** Block of 3-l V6 engine made of magnesium [38]. Reprinted from Journal of Cleaner Production [38] with permission from Elsevier



### ***5.4.2 Aeronautics/Defence***

The use of magnesium in the aeronautical industry has suffered a reduction in the number of applications in the second half of the 20th century. The development of solutions for the fuselage of the aircrafts has practically disappeared, and the use of magnesium is being limited to engines and transmissions, especially for helicopters [20]. In this sense, it is highlighted the use of the WE43 alloy for the construction of the transmissions for the MD500 and MD600 McDonnell Douglas helicopters [37, 39], or the use of the QE alloy in the nosewheel fork in the Anglo-French Jaguar fighter [40]. The QE22A alloy is also usually employed for the construction of gearboxes in aircraft structures [35].

Another field of use of magnesium is in missile and aerospace applications. The use of the EZ33 alloy in the Skylark research rockets, and the use of various forms of magnesium in the production of many pieces of British and U.S. missiles can be highlighted [41].

### ***5.4.3 Sports***

An important field for magnesium alloys is their use in motor sport competitions. For example, in motorcycling, making wheels for motorcycles by die cast magnesium is a competitive strategy when comparing with the use of carbon compounds [7]. Other applications can be found in Formula 5.1. For instance, in gear covers [39]. In addition to motor applications, magnesium has found space in other applications such as its use in forks, frames and rims for bicycles [42, 43], archery bows and baseball bats [35].

### ***5.4.4 Medical***

Magnesium has also uses in medical applications thanks to its low density, inherent biocompatibility [2] and sufficient mechanical properties [44]. Magnesium and magnesium alloys have been used in different types of implants in animals and humans during the last 130 years [45]. For instance, the AZ31 magnesium alloy has been investigated as a stent material by Mitsuishi et al. [46] and the use of MMCs with the AZ91D magnesium alloy matrix and hydroxyapatite (HA) particles as reinforcements has been investigated in vitro by Witte et al. [47].

### 5.4.5 Other Applications

Various other applications can be found in fields such as electronic devices: cases and covers for computers or mobiles, cameras, mini-disc players, etc. or others as the use of magnesium to produce hand tools and ladders [20, 48, 49].

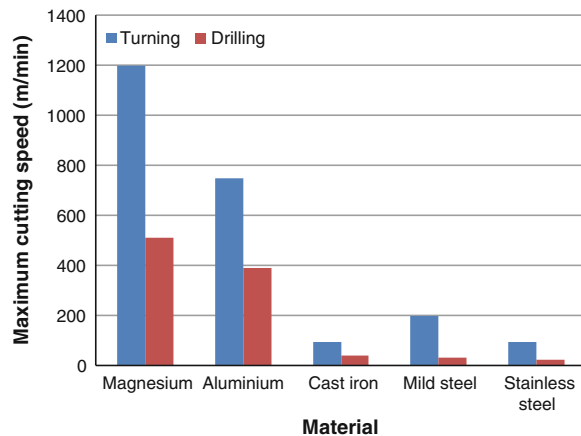
## 5.5 Machining

### 5.5.1 Introduction

Machinability refers to the ease of machining a material. Usually, it is defined from the cutting forces (or power consumption) and the shape of the chips [50]. In terms of machinability, magnesium and its alloys have the best properties compared to all of the other usual structural materials. These properties include: chip formation, cutting forces, cutting speed, depth of cut, surface finish and tool life [20, 51]. The form of the chips in magnesium machining depends mainly on the composition, form and temper of the alloy, and the feed rate [52]. The influence of the tool geometry, in particular, tool rake angle was also identified by Anilchandra and Surappa [53] in the turning of pure magnesium. In relation with the power required for machining, magnesium requires less power than aluminium, cast iron, mild steel and stainless steel, consuming these materials from 1.8 to 10 times the power required in magnesium machining [20].

Higher cutting speeds can also be used in magnesium machining in comparison with other structural materials. In this sense, in Fig. 5.3 the maximum cutting speeds are plotted for both drilling and turning processes. In addition, it is possible to find useful recommendations for machining parameters in the specialised literature or in the technical documentation of tool manufacturers. For instance, Byrne et al. [54]

**Fig. 5.3** Maximum cutting speeds for turning and drilling processes for different structural materials [20]



identify that it is possible to reach cutting speeds between 4,000 and 6,000 m/min and feed per tooth of 0.6 mm in face milling; 1,000 m/min and 0.8 mm/rev in drilling; and in finishing operations, as reaming, cutting speeds superior to 1,500 m/min.

Magnesium alloys, such as the AZ91HP alloy, are practically free of abrasive particles and possess very little susceptibility to adhesion with the cutting tool surfaces. Consequently, low tool wear is expected in magnesium machining [54]. In general, tool life in dry machining of magnesium is five times higher than that obtained in the machining of aluminium using cutting fluids and similar machining conditions [55]. Adhesion processes are more likely when high cutting speeds are used, generating increases in the surface roughness. Adhesion usually occurs in three different ways: built-up edge, built-up layer and flank build-up, being flank build-up the dominating process in magnesium machining [56].

Another aspect to consider in magnesium machining is the generation of burrs. The appearance of burrs is influenced by various factors such as: machining parameters, materials, tool geometry, tool path and tool wear. For instance, in the case of face milling, it is recommended to use moderate cutting speeds to obtain small burrs [57].

The choice of the tool to use in the process has to be made considering the desired level of productivity, acknowledging that tool life is negative correlated with the productivity of the process. The first choice for magnesium is polycrystalline diamond (PCD) not because of tool wear, but rather because of the extremely long tool life attainable and the accompanying consistent surface and dimensional quality of the machined components [54]. In the case of magnesium MMCs, machining is more difficult due to the joint action of the adhesion processes and the abrasion because of the reinforcing elements [55]. However, the good machinability of magnesium facilitates the use of other types of tools. For instance, carbide tools were used with good results in several works [56, 58, 59].

The design of the tools for magnesium machining can use the ones used for aluminium or steel machining. Nevertheless, due to the low resistance of the magnesium and its low heat capacity, it is possible to use designs with smooth faces, large peripheral relief angles, large chip spaces, few blades (as on milling cutters), and small rake angles [52].

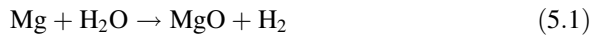
### ***5.5.2 Temperature and Magnesium Ignition***

The importance of the temperature reached in the cutting area is widely recognised in machining processes. The high temperatures at the contact zone of the tool and the workpiece accelerate tool wear and promote the plastic deformation of the machined surface [60]. In the case of magnesium, the temperatures generated during machining are low due to its high specific heat and thermal conductivity that let the heat to be rapidly dissipated [52].

In addition to the influence of temperature on the surface quality and tool wear, the temperature reached in the machining of magnesium is highly important

because magnesium presents a significant ignition risk when the process temperature exceeds 450 °C, being possible to reach temperatures up to 3,000 °C when the fire starts. Additionally, the size of the particles generated in the process is also important. Thus, particle sizes less than 500 µm present imminent explosion danger [61]. Magnesium ignition is determined by various aspects of the process and the environment in which the machining takes place, for instance, the machining parameters, material composition or tool geometry [62]. In general, when using cutting speeds under 300 m/min and feed rates greater than 0.02 mm/rev the possibility of fire occurrence is reduced [63].

Because of the risk of ignition, the decisions related to the use or not of cooling/lubricating systems is a critical element. Additionally, it should be considered the danger associated with the use of water-based fluid due to the magnesium reactivity with water to form hydrogen, flammable and potentially explosive, as shown in the chemical reaction (Eq. 5.1) [33].



Due to the reactivity of the magnesium with water, the use of dry machining or mineral-based oils is usually recommended [52, 64, 65]. However, it should be highlighted the existence of researchers that suggest the possibility of using water-based fluids by appropriate selection of process parameters [66]. In this regard, for instance, the study by Tomac and Tønnessen [56] showed the suitability of the use of water-based emulsions containing 5 % mineral oil, preventing also flank build-up.

The ignition risk requires taking actions to reduce the likelihood of the fire occurrence. Thus, one first recommendation is the reduction of the quantity of chips in the work area to diminish the heat accumulated. The removal of chips and dust generated during machining can be addressed through the use of cutting fluids or, in the case of dry machining, using chip removal systems such as those based on cyclone separators. It is also appropriate to consider the option of placing chips within closed containers [61].

Additionally, to ensure the safety of operators and protect the machines, it is important to have machines with protection systems against explosions and fires, as it can be a frame capable of withstanding the pressure generated in an explosion. Other preventing measures should also be considered, such as the installation of alarm systems [61], the disposal of adequate fire extinguishers (specifically, Class D extinguishers), and containers with dry sand [67].

### 5.5.3 *Experimental Review*

The specialised literature gathers a limited number of studies related to the magnesium machining. However, there are a few noteworthy dealing with different machining processes, such as drilling, milling or turning, in which the behaviour of magnesium alloys and MMCs is studied. In the present section, some of the main

works on magnesium machining are reviewed. In addition, in each machining process section, a summary of the experiments, covering the main topics, machining conditions and materials, is presented. Thus, turning, drilling and milling processes are summarised in Tables 5.5–5.7, respectively.

### 5.5.3.1 Turning

Tönshoff and Winkler [68] studied the influence of tool coatings (uncoated, and TiN and PCD coated tools) in the turning of the AZ91 HP magnesium alloy. The roughness is evaluated using the mean roughness depth ( $R_z$ ). All the values observed were below 30  $\mu\text{m}$ , testing cutting speeds up to 2,400 m/min, using a depth of cut of 1.5 mm and a feed rate of 0.4 mm/rev. In their work, it was identified how the PCD coated tools offered better results than the uncoated and the TiN coated tools, even for high cutting speeds (higher than 900 m/min). In addition, the use of coated PCD tools diminished the adhesion mechanisms and the temperature, therefore diminished the risk of ignition.

The experimentation of Tomac and Tønnessen [56] in the turning of the AZ91 magnesium alloy shows how the application of water-based cutting fluids reduces the temperature and prevent flank build-up. In addition, at low and medium cutting speeds the use of cutting fluids can generate negative effects in form of tool wear and worse surface roughness.

Pu et al. [58] researched the turning process of the AZ31B magnesium alloy, evaluating the influence of the environment (dry machining and cryogenic refrigeration). The cutting speed and feed rate were fixed at 100 m/min and 0.1 mm/rev, respectively. The surface roughness values obtained, in terms of the arithmetic average roughness ( $R_a$ ), were below 0.2  $\mu\text{m}$ , being worse the results obtained when using dry machining. The temperature was also studied using an infrared camera, acknowledging that the cryogenic refrigeration helps to reduce the maximum temperature in the turning process. In all the cases, the maximum temperatures were below 140 °C.

The turning process of Elektron21 magnesium alloy was analysed in the work by Wojtowicz et al. [69] using experimental designs. The research included the evaluation of the influence of the spindle speed, feed rate, depth of cut and tool geometry (tool nose radius) on surface roughness, in terms of the arithmetic average roughness ( $R_a$ ) and maximum roughness height ( $R_t$ ). The results identified feed rate, tool nose radius and the interaction between feed rate and tool nose radius as significant factors.

The study of temperature in magnesium machining was performed by Kurihara et al. [70]. In their work, authors evaluated temperatures in turning of pure magnesium, and AZ31 and AZ80 magnesium alloys under dry machining conditions using the thermocouple method. The cutting speeds tested were between 400 and 2,200 m/min. As the cutting speed is increased, the temperature increases reaching values close to 500 °C in the case of pure magnesium and even above in the case of magnesium alloys.

The study of magnesium for repair and maintenance turning operations was done by several authors. For instance, the dry facing of UNS M11917 magnesium alloy is evaluated in the study by Rubio et al. [71]. In the work, the influence of the machining parameters (feed rate and spindle speed) and tool material was studied, finding that the feed rate is the most important factor to explain surface roughness ( $Ra$ ). The surface roughness values obtained were within the range 0.19–0.82  $\mu\text{m}$  for all the tests performed. From another side, Villeta et al. [72] evaluated the turning of the UNS M11311 magnesium alloy. The influence of the machining parameters and different tool coatings was studied, finding again that the feed rate is the most important factor to explain the surface roughness ( $Ra$ ). The aim of this investigation is to optimise efficiently the dry turning of magnesium pieces to achieve a surface roughness within technical requirements.

**Table 5.5** Main works in magnesium turning processes

Authors	Machining conditions	Materials	Topics
Tönshoff and Winkler [68]	$v$ : 100–2,400 m/min	AZ91 HP and MELRAM 072TS	Cutting forces, surface roughness, tool materials, tool wear
	$f$ : 0.2–0.4 mm/rev		
	$d$ : 0.2–1.5 mm		
Tomac and Tønnessen [56]	$v$ : 400–850 m/min	AZ91	Cutting forces, flank build-up, surface roughness, water-based cutting fluids
	$f$ : 0.1 mm/rev		
	$d$ : 0.4 mm		
Pu et al. [58]	$v$ : 100 m/min	AZ31B	Cryogenic refrigeration, cutting forces, hardness, microstructure, residual stresses, surface roughness, temperature
	$f$ : 0.1 mm/rev		
Kurihara et al. [70]	$v$ : 400–2,200 m/min	Mg, AZ31 and AZ80	Chip morphology, cutting forces, temperature
	$f$ : 0.06–0.65 mm/rev		
	$d$ : 3–5 mm		
Wojtowicz et al. [69] <sup>a, b</sup>	$v$ : 27–107 % of $v^*$	Elektron21	Hardness, microstructure, residual stresses, surface roughness
	$f$ : 25–150 % of $f^*$		
	$d$ : 33–100 % of $d^*$		
Rubio et al. [71] <sup>a</sup>	$v$ : 97–270 m/min	UNS M11917	Surface roughness, tool materials
	$f$ : 0.04–0.12 mm/rev		
	$d$ : 0.25 mm		
Villeta et al. [72]	$v$ : 75–225 m/min	UNS M11311	Surface roughness, tool materials
	$f$ : 0.05–0.15 mm/rev		
	$d$ : 0.25 mm		
Rubio et al. [73] <sup>a</sup>	$v$ : 83–133 m/min	UNS M11917	Intermittent turning, minimum quantity lubrication, surface roughness, tool materials
	$f$ : 0.051–0.1 mm/rev		
	$d$ : 0.25 mm		

<sup>a</sup> Cutting speed is provided as initial cutting speed that was calculated from experimental data

<sup>b</sup> For confidential reasons machining conditions are provided in relation to Mitsubishi's recommendations for aluminium (designated with \*)

Finally, the use of magnesium in intermittent turning processes of the UNS M11917 magnesium alloy was studied by Rubio et al. [73]. In the research, the influence of the cooling/lubricating system, cutting parameters (feed rate and spindle speed), tool material and type of the interruption on surface roughness ( $Ra$ ) was studied. The main results of the investigation let identified several factors and some interactions as significant sources of variability according to the statistical analysis performed. The feed rate was identified as the most important source of surface roughness variability, while the influence of the other significant sources of variability is lower. The surface roughness values obtained were within the range 0.28–0.80  $\mu\text{m}$  for all the tests performed.

### 5.5.3.2 Drilling

An interesting work to mention in magnesium drilling is the study by Wang et al. [27]. Authors evaluated the tool wear during the drilling of the AZ91 magnesium alloy using dry machining. The research let identified a wear map divided into five wear zones. The principal wear mechanisms identified were adhesive, abrasive and diffusion wear. Thus, based on the wear map, it is possible to select the cutting parameters to minimise the expected tool wear.

Other investigations, as the developed by Gariboldi [66] and Bhowmick et al. [31], identified the adhesion on the edge of the tool as a cause of wear during the drilling of the AM60B and AM60 alloys, respectively. Likewise, Gariboldi [66] identified a range of feed rates that guarantees a good tool life and limited surface roughness. From another side, Bhowmick et al. [31] showed how using the minimum quantity lubrication (MQL) system better results are obtained than the ones obtained using dry machining. In addition, the temperature during the process using the MQL system does not overcome the generated when using flooded conditions.

The investigation performed by Bhowmick and Alpas [74] for the drilling of the AZ91 magnesium alloy showed how the use of the MQL system, in combination with the use diamond like carbon coated high speed steel (HSS) tools, offered results comparable to those obtained when using HSS tools under flooded conditions. In the case of dry machining, the tool life obtained during the drilling is considerably lower than when using flooded conditions or the MQL system.

The use of the cryogenic refrigeration was studied by Balout et al. [75]. The investigation in the drilling of the AZ91E magnesium alloy using dry machining and cryogenic pre-cooling showed how the generation of dust during the machining depends to a great extent on the temperature of the workpiece. Especially, the pre-cooling of the workpiece reduces considerably the quantity of dust generated in the process.

The use of magnesium in MMCs was highlighted previously, being tool wear a major concern in MMCs machining due to the hardness of the reinforcing elements. The drilling of magnesium MMCs was analysed by Weinert and Lange [76]. In their work, authors studied the drilling and reaming of magnesium MMCs by means of different types of tools: cemented carbides, and diamond and TiAlN coated tools.



**Table 5.6** Main works in magnesium drilling processes

Authors	Machining conditions	Materials	Topics
Wang et al. [27]	$v$ : 40–73 m/min	AZ91	Chip morphology, tool wear
	$f$ : 0.05–0.3 mm/rev		
	$d$ : 15 mm		
Gariboldi [66]	$v$ : 63 m/min	AM60B	Hardness, surface roughness, tool materials, tool wear
	$f$ : 0.27–0.7 mm/rev		
	$d$ : 40–60 mm		
Bhowmick et al. [31]	$v$ : 50 m/min	AM60	Chip morphology, cutting forces, hardness, minimum quantity lubrication, temperature, torque, surface roughness, wet machining
	$f$ : 0.25 mm/rev		
	$d$ : 19 mm		
Bhowmick and Alpas [74]	$v$ : 50 m/min	AZ91	Coefficient of friction, minimum quantity lubrication, temperature, tool life, tool materials, torque, wet machining
	$f$ : 0.25 mm/rev		
	$d$ : 19 mm		
Balout et al. [75]	$v$ : 35–188 m/min	AZ91E	Chip morphology, cryogenic refrigeration, cutting forces, dust generation, torque
	$f$ : 0.22 mm/rev		
	$d$ : 5–12 mm		
Weinert and Lange [76]	$v$ : 50–100 m/min	AZ91 and ZC63	Metal matrix composites, tool materials, tool wear
	$f$ : 0.05–0.25 mm/rev		
	$d$ : 0.15–20 mm		
Kheireddine et al. [77]	$v = 73$ m/min	AZ31B	Cryogenic refrigeration, cutting forces, hardness
	$f$ : 0.05–0.2 mm/rev		
	$d$ : 10 mm		

A different behaviour was observed depending on the compound considered. In this way, during the machining of an AZ91 alloy, reinforced with 20 % of  $\delta$ - $\text{Al}_2\text{O}_3$ , lower flank wear is observed when using the TiAlN coated tool and the higher is obtained with the cemented carbide tool. In the case of the ZC63 alloy, reinforced with 12 % of SiC, of major hardness, the best results are obtained with the diamond coated tool. In the same way, when machining compounds with mixed reinforcements 5 % of  $\delta$ - $\text{Al}_2\text{O}_3$  and 15 % of SiC, the tools covered with diamond performed better.

The influence of the cryogenic refrigeration on magnesium drilling was studied by Kheireddine et al. [77]. In their work, authors evaluated the drilling process of the AZ31B magnesium alloy using a liquid nitrogen flow rate of 0.6 kg/min. The results of the investigation identified a beneficial effect of the cryogenic refrigeration in the hardness of the specimen when compared with the dry machining case.

**Table 5.7** Main works in magnesium milling processes

Authors	Machining conditions	Materials	Topics
Fang et al. [78]	$v$ : 408–1,088 m/min	AZ91	Chip morphology, cutting forces, temperature
	$f$ : 50–7,000 mm/min		
	$d$ : 0.05–3 mm		
Pedersen and Ramulu [79]	$v$ : 93–122 m/min	ZK60A-T5	Chip morphology, cutting forces, surface roughness, tool wear
	$f$ : 0.112–0.203 mm/rev		
	$d$ : 0.254–0.762 mm		
Salahshoor and Guo [80]	$v$ : 1,200–2,800 m/min	MgCa0.8	Biomedical applications, chip morphology, cutting forces, temperature
	$f$ : 0.2 mm/rev		
	$d$ : 0.2 mm		

### 5.5.3.3 Milling

Fang et al. [78] studied the evolution of the temperature during the milling of the AZ91 magnesium alloy, identifying how the temperature increases when the cutting speed increases and, more emphasised, with a decrease in the undeformed chip thickness. Thus, the average temperature obtained in the flank can become a good indicator to anticipate the generation of fire.

Magnesium MMC facing is studied by Pedersen and Ramulu [79]. Concretely, authors studied the facing process of a composite of ZK60A-T5 magnesium alloy matrix with 20 vol.% SiC particle reinforcement of a nominal 3–4  $\mu\text{m}$  diameter. The main results of the investigation include the recognition of abrasion on the tool flank as the primary tool wear mechanism.

Finally, Salahshoor and Guo [80] investigate the milling of an alloy of application in the field of the biomedicine, the MgCa alloy with a calcium percentage of 0.8 % using PCD tools. In this way, it was observed that chip ignition and sparks did not happen when using high cutting speeds during the process.

## 5.6 Conclusions

Magnesium is increasing its applications in different industrial sectors due its favourable properties in comparison to usual structural materials. Among the main properties of magnesium, its low density makes it a suitable choice to be used in heavy parts in transportation applications. In addition, the mechanical properties, in particular, the specific mechanical properties (specific strength, specific stiffness, dent resistance or shell stiffness) are also competitive in comparison to traditional materials. The increasing use of magnesium is encouraging a great development of magnesium alloys and also metal matrix composites with magnesium matrix that are stimulating the use of magnesium.

Some applications of magnesium have been highlighted in the work. Among them, the automotive sector provides examples such as its use to produce parts as gearboxes, transmission covers or wheels. In the case of aeronautics, some applications in helicopters, rockets or missiles were also highlighted. Other uses of magnesium include electronic, medical or sports applications.

Magnesium is a material with a good machinability in comparison with other usual structural materials. Thus, high cutting speeds can be used consuming low quantities of power and letting attain good surfaces. However, magnesium presents drawbacks for machining such as the ignition risk when temperatures reach 450 °C and the explosion danger when particles of size less than 500 µm are generated. Moreover, the reactivity of magnesium to form hydrogen atmospheres must be also taken into account.

To conclude, the brief review of some of the main experimental investigations on magnesium machining presented let extract several conclusions from the behaviour of magnesium in specific processes:

- In turning processes, it was observed how machining conditions, in particular, cutting speed and feed rate have an important influence on the results of the process. For instance, in terms of surface quality and temperature. Moreover, the use of high cutting speeds with favourable results was observed, but also acknowledging a risk of reaching high temperatures. Regarding the use of cooling/lubricating strategies, it was also identified some beneficial effects of their use. Finally, repair and maintenance operations of magnesium were also analysed, recognising how magnesium can be used in these operations with good surface finish results.
- In drilling processes, the principal wear mechanisms: adhesive, abrasive and diffusion were identified. Several works were also presented in which different cooling/lubricating strategies (MQL or cryogenic refrigeration) were assessed, identifying the main benefits of their use. In addition, the importance of the selection of the tool material was also recognised, especially, when drilling hard materials such as MMCs.
- In milling processes, the important influence of the cutting speed on temperature was recognised. Moreover, the abrasion on the tool flank was identified as the main source of wear in MMCs milling. Finally, the use of magnesium alloys in biomedicine applications has proved that high cutting speeds can be used without risk of ignition.

## References

1. McDonough WF (2001) The composition of the Earth. *Int Geophys* 76:3–23
2. Gray JE, Luan B (2002) Protective coatings on magnesium and its alloys—a critical review. *J Alloy Compd* 336(1–2):88–113
3. Kipouros GJ, Sadoway DR (2001) A thermochemical analysis of the production of anhydrous MgCl<sub>2</sub>. *J Light Met* 1(2):111–117

4. Mordike BL, Ebert T (2001) Magnesium. Properties—applications—potential. *Mater Sci Eng, A* 302(1):37–45
5. Minerals Yearbook (2012) Magnesium. <http://minerals.usgs.gov/minerals/pubs/commodity/magnesium/index.html#myb>. Accessed 23 May 2014
6. Scintilla LD, Tricarico L (2013) Experimental investigation on fiber and CO<sub>2</sub> inert gas fusion cutting of AZ31 magnesium alloy sheets. *Opt Laser Technol* 46:42–52
7. Campbell FC (2006) Magnesium and beryllium. In: Campbell FC (ed) *Manufacturing technology for aerospace structural materials*. Elsevier Science, Oxford
8. Kleiner M, Geiger M, Klaus A (2003) Manufacturing of lightweight components by metal forming. *CIRP Ann—Manuf Technol* 52(2):521–542
9. Shin HW (2011) A feasibility study to replace steel made hood panels by magnesium alloy made hood panels. *Int J Precis Eng Manuf* 13(11):2011–2016
10. AISI 4340 steel, annealed, 25 mm round. <http://www.matweb.com/search/DataSheet.aspx?MatGUID=fd1b43a97a8a44129b32b9de0d7d6c1a>. Accessed 23 May 2014
11. Gray cast iron, ASTM A 48 class 40. <http://www.matweb.com/search/DataSheet.aspx?MatGUID=ec56a89f37f74e2f867a64b0f87f1e9d>. Accessed 23 May 2014
12. Titanium Ti-6Al-4 V (Grade 5), annealed. <http://www.matweb.com/search/DataSheet.aspx?MatGUID=a0655d261898456b958e5f825ae85390>. Accessed 23 May 2014
13. Aluminum A380.0-F die casting alloy. <http://www.matweb.com/search/DataSheet.aspx?MatGUID=5f92a8f7d6ad416c8ce9398cae14a363>. Accessed 23 May 2014
14. Magnesium AZ91D-F, cast. <http://www.matweb.com/search/DataSheet.aspx?MatGUID=07baafb9c364fb18fd413bceced867f>. Accessed 23 May 2014
15. Overview of materials for alpha/beta titanium alloy. <http://www.matweb.com/search/DataSheet.aspx?MatGUID=4dac23c848db4780a067fd556906cae6&ckck=1>. Accessed 23 May 2014
16. Overview of materials for AISI 4000 series steel. <http://www.matweb.com/search/DataSheet.aspx?MatGUID=210fcd12132049d0a3e0cabe7d091eef>. Accessed 23 May 2014
17. Overview of materials for aluminum alloy. <http://www.matweb.com/search/DataSheet.aspx?MatGUID=ab8aeb2d293041c4a844e397b5cfbd4e>. Accessed 23 May 2014
18. Overview of materials for magnesium alloy. <http://www.matweb.com/search/DataSheet.aspx?MatGUID=4e6a4852b14c4b12998acf2f8316c07c>. Accessed 23 May 2014
19. Overview of materials for gray cast iron. <http://www.matweb.com/search/DataSheet.aspx?MatGUID=f3cd25980ab24fdaa5893252cd2bc192>. Accessed 23 May 2014
20. Polmear IJ (2005) Magnesium alloys. In: Polmear IJ (ed) *Light alloys*, 4th edn. Butterworth-Heinemann, Oxford
21. Mebarki N, Kumar NVR, Blandin JJ, Suery M, Pelloux F, Khelifati G (2005) Correlations between ignition and oxidation behaviours of AZ91 magnesium alloys. *Mater Sci Technol* 21(10):1145–1151
22. Rao J, Li H (2010) Oxidation and ignition behavior of a magnesium alloy containing rare earths elements. *Int J Adv Manuf Technol* 51(1–4):225–231
23. Kumar NVR, Blandin JJ, Suéry M, Grosjean E (2003) Effect of alloying elements on the ignition resistance of magnesium alloys. *Scripta Mater* 49(3):225–230
24. Mishra SK, Biswas S, Satapathy A (2014) A study on processing, characterization and erosion wear behavior of silicon carbide particle filled ZA-27 metal matrix composites. *Mater Des* 55:958–965
25. Franco LF, Becerril EB, Ruiz JL, Rodríguez JGG, Guardian R, Rosales I (2011) Wear performance of TiC as reinforcement of a magnesium alloy matrix composite. *Compos B* 42:275–279
26. Westengen H (2001) Magnesium alloys: properties and applications. In: Buschow KHJ, Cahn RW, Flemings MC, Iilschner B, Kramer EJ, Mahajan S, Veyssièrre P (eds) *Encyclopedia of materials: science and technology*, 2nd edn. Elsevier, Oxford
27. Wang J, Liu YB, An J, Wang LM (2008) Wear mechanism map of uncoated HSS tools during drilling die-cast magnesium alloy. *Wear* 265(5–6):685–691

28. Ramnath BV, Elanchezian C, Jaivignesh M, Rajesh S, Parswajinan C, Ghias ASA (2014) Evaluation of mechanical properties of aluminium alloy–alumina–boron carbide metal matrix composites. *Mater Des* 58:332–338
29. Prawoto Y, Djuansjah JRP, Tawi KB, Fanone MM (2013) Tailoring microstructures: a technical note on an eco-friendly approach to weight reduction through heat treatment. *Mater Des* 50:635–645
30. Carvalho I, Baier T, Simoes R, Silva A (2012) Reducing fuel consumption through modular vehicle architectures. *Appl Energy* 93:556–563
31. Bhowmick S, Lukitsch MJ, Alpas AT (2010) Dry and minimum quantity lubrication drilling of cast magnesium alloy (AM60). *Int J Mach Tools Manuf* 50(5):444–457
32. Davim JP, António CAC (2001) Optimal drilling of particulate metal matrix composites based on experimental and numerical procedures. *Int J Mach Tools Manuf* 41:21–31
33. Kulekci MK (2008) Magnesium and its alloys applications in automotive industry. *Int J Adv Manuf Technol* 39(9–10):851–865
34. Du J, Han W, Peng Y (2010) Life cycle greenhouse gases, energy and cost assessment of automobiles using magnesium from Chinese Pidgeon process. *J Clean Prod* 18(2):112–119
35. Ion JC (2005) *Engineering Materials*. In: Ion JC (ed) *Laser processing of engineering materials*. Butterworth-Heinemann, Oxford
36. Trojanová Z, Gärtnerová V, Jäger A, Námesný A, Chalupová M, Palček P, Lukáč P (2009) Mechanical and fracture properties of an AZ91 Magnesium alloy reinforced by Si and SiC particles. *Composites Sci Technol* 69(13):2256–2264
37. Froes FH, Eliezer D, Aghion E (1998) The science, technology, and applications of magnesium. *JOM* 50(9):30–34
38. Tharumarajah A, Koltun P (2007) Is there an environmental of using magnesium of using components for light-weighting cars? *J Clean Prod* 15(11–12):1007–1013
39. Davies G (2003) Future trends in automotive body materials. In: Davies G (ed) *Materials for automobile bodies*. Butterworth-Heinemann, Oxford
40. Charles JA, Crane FAA, Furness JAG (1997) *Materials for airframes*. In: Charles JA, Crane FAA, Furness JAG (eds) *Selection and use of engineering materials*, 3rd edn. Butterworth-Heinemann, Oxford
41. Eliezer D, Aghion E, Froes FH (1998) Magnesium science, technology and applications. *Adv Perform Mater* 5(3):201–212
42. Dobrzański LA, Tański T, Čížek L, Brytan Z (2007) Structure and properties of the magnesium casting alloys. *J Mater Process Technol* 192–193:567–574
43. Deetz J (2005) The use of wrought magnesium in bicycles. *JOM* 57(5):50–53
44. Denkena B, Lucas A (2007) Biocompatible magnesium alloys as absorbable implant materials—adjusted surface and subsurface properties by machining processes. *Ann CIRP* 56(1):113–116
45. Witte F (2010) The history of biodegradable magnesium implants: a review. *Acta Biomater* 6(5):1680–1692
46. Mitsuishi M, Cao J, Bártolo P, Friedrich D, Shih AJ, Rajurkar K, Sugita N, Harada K (2013) Biomanufacturing. *CIRP Ann—Manuf Technol* 62:585–606
47. Witte F, Feyerabend F, Maier P, Fischer J, Störmer M, Blawert C, Dietzel W, Hort N (2007) Biodegradable magnesium–hydroxyapatite metal matrix composites. *Biomaterials* 28:2163–2174
48. Park CW, Kim YH (2012) A study on the manufacturing of digital camera barrel using magnesium alloy. *Int J Precis Eng Manuf* 13(7):1047–1052
49. Pfeifer M (2009) *Material properties and materials science*. In: Pfeifer M (ed) *Materials enabled designs*. Butterworth-Heinemann, Boston
50. Elgallad EM, Samuel FH, Samuel AM, Doty HW (2010) Machinability aspects of new Al–Cu alloys intended for automotive castings. *J Mater Process Technol* 210(13):1754–1766
51. Shokrani A, Dhokia V, Newman ST (2012) Environmentally conscious machining of difficult-to-machine materials with regard to cutting fluids. *Int J Mach Tools Manuf* 57:83–101
52. ASM (1989) *ASM handbook-machining*, vol 16. ASM International, Ohio

53. Anilchandra AR, Surappa MK (2010) Influence of tool rake angle on the quality of pure magnesium chip-consolidated product. *J Mater Process Technol* 210:423–428
54. Byrne G, Dornfeld D, Denkena B (2003) Advancing cutting technology. *CIRP Ann—Manuf Technol* 52(2):483–507
55. Grzesik W (2008) Machinability of engineering materials. In: Grzesik W (ed) *Advanced machining processes of metallic materials*. Elsevier, Amsterdam
56. Tomac N, Tønnessen K (1991) Formation of flank build-up in cutting magnesium alloys. *CIRP Ann—Manuf Technol* 40(1):79–82
57. Aurich JC, Dornfeld D, Arrazola PJ, Franke V, Leitz L, Min S (2009) Burrs-Analysis, control and removal. *CIRP Ann—Manuf Technol* 58(2):519–542
58. Pu Z, Outeiro JC, Batista AC, Dillon OW, Puleo DA, Jawahir IS (2012) Enhanced surface integrity of AZ31B Mg alloy by cryogenic machining towards improved functional performance of machined components. *Int J Mach Tools Manuf* 56:17–27
59. Outeiro JC, Rossi F, Fromentin G, Poulachon G, Germain G, Batista AC (2013) Process mechanics and surface integrity induced by dry and cryogenic machining of AZ31B-O magnesium alloy. *Procedia CIRP* 8:487–492
60. Le Coz G, Marinescu M, Devillez A, Dudzinski D, Velnom L (2012) Measuring temperature of rotating cutting tools: application to MQL drilling and dry milling of aerospace alloys. *Appl Therm Eng* 36:434–441
61. Weinert K, Inasaki I, Sutherland JW, Wakabayashi T (2004) Dry machining and minimum quantity lubrication. *CIRP Ann—Manuf Technol* 53(2):511–537
62. Zhao N, Hou J, Zhu S (2011) Chip ignition in research on high-speed face milling AM50A magnesium alloy. *Second international conference on mechanic automation and control engineering (MACE)*, vol 15–17, pp 1102–1105
63. ASM (1990) *ASM handbook-properties and selection: nonferrous alloys and special purpose materials*, vol 2. ASM International, Ohio
64. Machado AR, Wallbank J (1997) The effect of extremely low lubricant volumes in machining. *Wear* 210(1–2):76–82
65. Villeta M, Rubio EM, Pipaón JMS, Sebastián MA (2011) Surface finish optimization of magnesium pieces obtained by dry turning based on Taguchi techniques and statistical tests. *Mater Manuf Process* 26:1503–1510
66. Gariboldi E (2003) Drilling a magnesium alloy using PVD coated twist drills. *J Mater Process Technol* 134(3):287–295
67. Rubio EM, Valencia JL, Carou D, Saá A (2012) Inserts selection for intermittent turning of magnesium pieces. *Appl Mech Mater* 217–219:1581–1591
68. Tönshoff HK, Winkler J (1997) The influence of tool coatings in machining of magnesium. *Surf Coat Technol* 94–95:610–616
69. Wojtowicz N, Danis I, Monies F, Lamesle P, Chieragatia R (2013) The influence of cutting conditions on surface integrity of a wrought magnesium alloy. *Procedia Eng* 63:20–28
70. Kurihara K, Tozawa T, Kato H (1981) Cutting temperature of magnesium alloys at extremely high cutting speeds. *J Jpn Inst Light Met* 31:255–260
71. Rubio EM, Valencia JL, Saá AJ, Carou D (2013) Experimental study of the dry facing of magnesium pieces based on the surface roughness. *Int J Precis Eng Manuf* 14(6):995–1001
72. Villeta M, Agustina B, Pipaón JMS, Rubio EM (2012) Efficient optimisation of machining processes based on technical specifications for surface roughness: application to magnesium pieces in the aerospace industry. *Int J Adv Manuf Technol* 60:1237–1246
73. Rubio EM, Villeta M, Carou D, Saá A (2014) Comparative analysis of sustainable cooling systems in intermittent turning of magnesium pieces. *Int J Precis Eng Manuf* 15(5):929–940
74. Bhowmick S, Alpas AT (2011) The role of diamond-like carbon coated drills on minimum quantity lubrication drilling of magnesium alloys. *Surf Coat Technol* 205(23–24):5302–5311
75. Balout B, Songmene V, Masounave J (2007) An experimental study of dust generation during dry drilling of pre-cooled and pre-heated workpiece materials. *J Manuf Process* 9(1):23–34
76. Weinert K, Lange M (2001) Machining of magnesium matrix composites. *Adv Eng Mater* 3(12):975–979

77. Kheireddine AH, Ammouri AH, Lu T, Jawahir IS, Hamade RF (2013) An FEM Analysis with Experimental validation to study the hardness of in-process cryogenically cooled drilled holes in Mg AZ31b. *Procedia CIRP* 8:588–593
78. Fang FZ, Lee LC, Liu XD (2005) Mean flank temperature measurement in high speed dry cutting of a magnesium alloy. *J Mater Process Technol* 167(1):119–123
79. Pedersen W, Ramulu M (2006) Facing SiCp/Mg metal matrix composites with carbide tools. *J Mater Process Technol* 172:417–423
80. Salahshoor M, Guo YB (2011) Cutting mechanics in high speed dry machining of biomedical magnesium–calcium alloy using internal state variable plasticity model. *Int J Mach Tools Manuf* 51(7–8):579–590

# Chapter 6

## Grinding Science

Mark J. Jackson

**Abstract** Grinding science is focused on understanding the connectivity between chip formation and the tribology of contact between abrasive grains, bonding agents, fillers, grinding aids and workpiece materials. The chapter reveals information about the nature of real contact by understanding the basic mechanisms of material removal and the nature of sliding contacts during grinding and rubbing of materials. The purpose of this chapter is to provide the reader with: (a) the basic understanding of metal cutting in terms of understanding various plasticity models and by directly observing intimate contact; (b) to explain to the reader the nature of frictional interactions at the machining interface by means of cutting, ploughing and sliding concepts; (c) to explain the effects of frictional heating and lubrication at the contact interface on the ease or difficulty in machining; (d) to provide an analysis of the gaps that are present in the context of the science of grinding; and finally, to provide the reader with a summary of recommendations for stimulate further research activities in order to solve important problems in the area of grinding science.

### 6.1 Introduction

The basic interactions between grinding wheel and workpiece are commonly associated with cutting, ploughing, sliding, interactions between chip and bond, chip and grain, chip and workpiece, bond sliding against workpiece, chip-to-chip interactions, bond-to-bond interactions, metal-to-metal on grain and chip interactions, interactions with coolants, lubricants (solid and liquid), and grinding aids both active and passive. These interactions may operate in series and/or in parallel and some may not operate at all under the conditions of grinding. Grinding process interactions associated with material removal and tribological processes in the

---

M.J. Jackson (✉)

Bonded Abrasives Group, Massachusetts Avenue, Cambridge, MA 02139, USA  
e-mail: bondedabrasive@gmail.com

© Springer-Verlag Berlin Heidelberg 2015

J.P. Davim (ed.), *Traditional Machining Processes*,

Materials Forming, Machining and Tribology, DOI 10.1007/978-3-662-45088-8\_6



grinding zone are associated with cutting of material by the abrasive grain, material displacement between workpiece and abrasive grain, but without chip formation, surface modification due to frictional effects between abrasive grain and workpiece, interaction between chip and bond, interaction between chip and workpiece, and interaction between bond and workpiece. The current approach to product testing and development is a blend of qualitative and quantitative process analyses. The process interactions explain certain events in a qualitative way, but there is a need to better quantify mechanical, thermal, biological and chemical processes that determine calculated grinding parameters and other metrics that describe abrasive product behaviour, especially when microscopic interactions are dominant during time-dependent behaviours. The importance of power as a function of material removal rate with changes in the threshold power and the level of specific grinding energy explained in terms of which interaction mechanism(s) is(are) operating is necessary to explain the behaviour of the grinding system under certain operating conditions. By observing changes in power as a function of material removal rate, it is not clear which interaction is dominant by way of experimental proof, or whether the observed changes are based on intuition, or not. In this particular case, the issue is the inability to apply existing interaction models to quantitatively explain the change in power as a function material removal in terms of grain wear, bond wear, chip/bond friction, etc. The development of models and new testing and measurement techniques to quantify the effects of various process interactions, or combinations of interactions, on product performance is key to the long-term success and improvement in the abrasive product development cycle.

The purpose of this chapter is to provide the reader with the basic understanding of metal cutting at the microscale in terms of various plasticity models and observations, to explain the nature of frictional interactions at the machining interface including the various cutting, ploughing and sliding interactions, to explain the concept of frictional heating and lubrication at the contact interface, to provide an analysis of the gaps that are present in the context of the science of grinding, and to finally provide the reader with a summary of recommendations for further research activities in order to solve important problems in the area of grinding science.

## **6.2 Mechanics of Cutting at the Microscale**

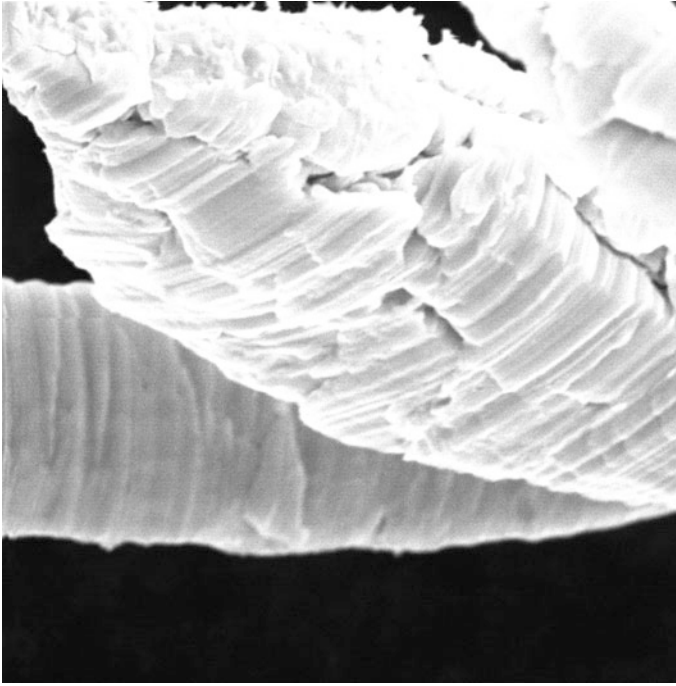
The purpose of this section of the chapter is to introduce the reader to the mechanics of cutting at the microscale that explains chip formation in terms of material response to an applied force, explains how shear plane angle can be predicted, comments on the plastic behaviour of metals at large strains, and introduces the reader to a number of models that explain metal cutting in terms of material response and develops ‘fluid-like’ features of high strain rate phenomena in metal cutting.

There is a substantial increase in the specific energy required with a decrease in chip size during machining. It is believed this is due to the fact that all metals contain defects such as grain boundaries, missing and/or impurity atoms, stacking faults, etc., and when the size of the material removed decreases the probability of encountering a stress-reducing defect decreases. Since the shear stress and strain in metal cutting is unusually high, discontinuous micro-cracks usually form on the primary shear plane. If the material is very brittle, or the compressive stress on the shear plane is relatively low, micro-cracks will grow into larger cracks giving rise to discontinuous chip formation. When discontinuous micro-cracks form on the shear plane they will weld and reform as strain proceeds, thus joining the transport of dislocations in accounting for the total slip of the shear plane. In the presence of a contaminant, such as carbon tetrachloride vapour at a low cutting speed, the re-welding of micro-cracks will decrease, resulting in a decrease in the cutting force required for chip formation. A number of special experiments that support the transport of micro-cracks across the shear plane, and the important role compressive stress plays on the shear plane are explained. An alternative explanation for the size effect in cutting is based on the belief that shear stresses increase with increasing strain rate. When an attempt is made to apply this to metal cutting, it is assumed in the analysis that the von Mises criterion applies to the shear plane. This is inconsistent with the experimental findings by Merchant. Until this difficulty is resolved with the experimental verification of the strain rate approach, it should be assumed that the strain rate effect may be responsible for some portion of the size effect in metal cutting.

It is known that a size effect exists in metal cutting, where the specific energy increases with decrease in deformation size. Backer et al. [1] performed a series of experiments in which the shear energy per unit volume deformed ( $u_s$ ) was determined as a function of specimen size for a ductile metal (SAE 1112 steel). The deformation processes involved were as follows, listed from top to bottom with increasing size of specimen deformed: (a) surface grinding; (b) micro milling; (c) turning; and (d) tensile test.

The surface grinding experiments were performed under relatively mild conditions involving plunge type experiments in which an 8-in (20.3 cm) diameter wheel was directed radially downward against a square specimen of length and width 0.5 in (1.27 cm). The width of the wheel was sufficient to grind the entire surface of the work at different down feed rates ( $t$ ). The vertical and horizontal forces were measured by a dynamometer supporting the workpiece. This enabled the specific energy ( $u_s$ ) and the shear stress on the shear plane ( $\tau$ ) to be obtained for different values of undeformed chip thickness ( $t$ ). The points corresponding to a constant specific energy below a value of down feed of about 28  $\mu\text{in}$  (0.7  $\mu\text{m}$ ) are on a horizontal line due to a constant theoretical strength of the material being reached when the value of  $t$ , goes below approximately 28  $\mu\text{in}$  (0.7  $\mu\text{m}$ ). The reasoning in support of this conclusion is presented in Backer et al. [1].

In the micro milling experiments, a carefully balanced 6-in (152 cm) carbide tipped milling cutter was used with all but one of the teeth relieved so that it operated as a fly milling cutter. Horizontal and vertical forces were measured for a



**Fig. 6.1** Free surface of chip showing regions of discontinuous strain and microfracture. Reprinted with permission from Jackson and Morrell [31]

number of depths of cut ( $t$ ) when machining the same sized surface as in grinding. The shear stress on the shear plane ( $\tau$ ) was estimated by a rather detailed method presented in Backer et al. [1]. Turning experiments were performed on a 2.25-in (5.72 cm) diameter SAE 1112 steel bar pre-machined in the form of a thin-walled tube having a wall thickness of 0.2 in (5 mm). A zero degree rake angle carbide tool was operated in a steady-state two-dimensional orthogonal cutting mode as it machined the end of the tube. Values of shear stress on the shear plane ( $\tau$ ) versus undeformed chip thickness were determined for experiments at a constant cutting speed and different values of axial infeed rate and for variable cutting speeds and a constant axial infeed rate.

A true stress-strain tensile test was performed on a 0.505-in (1.28 cm) diameter by 2-in (5.08 cm) gage length specimen of SAE 1112 steel. The mean shear stress at fracture was 22,000 psi (151.7 MPa) [1]. Shaw [2] discusses the origin of the size effect in metal cutting, which is believed to be primarily due to short-range inhomogeneities present in all engineering metals.

When the back of a metal cutting chip is examined at very high magnification by means of an electron microscope individual slip lines are evident as shown in Fig. 6.1. In deformation studies [3] found that slip does not occur on all atomic planes but only on certain discrete planes. In experiments on deformed aluminium

single crystals the minimum spacing of adjacent slip planes was found to be approximately 50 atomic spaces while the mean slip distance along the active slip planes was found to be about 500 atomic spaces. These experiments further support the observation that metals are not homogeneous and suggest that the planes along which slip occurs are associated with inhomogeneities in the metal. Strain is not uniformly distributed in many cases. For example, the size effect in a tensile test is usually observed only for specimens less than 0.1 in (2.5 mm) in diameter. On the other hand, a size effect in a torsion test occurs for considerably larger samples due to the greater stress gradient present in a torsion test than in a tensile test. This effect and several other related ones are discussed in detail by Shaw [2].

### 6.2.1 Shear Angle Predictions

There have been many notable attempts to derive an equation for the shear angle ( $\phi$ ) for steady-state orthogonal cutting. Ernst and Merchant [4] presented the first quantitative analysis. Forces acting on a chip at the tool point where:  $R$  = the resultant force on the tool face,  $R'$  = the resultant force in the shear plane,  $N_C$  and  $F_C$  are the components of  $R$  normal to and parallel to the tool face,  $N_S$  and  $F_S$  are the components of  $R'$  normal to and parallel to the cutting direction,  $F_Q$  and  $F_P$  are the components of  $R$  normal to and parallel to the cutting direction, and  $\beta = \tan^{-1} F_C/N_C$  (is called the friction angle). Assuming the shear stress on the shear plane ( $\tau$ ) to be uniformly distributed it is evident that:

$$\tau = \frac{F_S}{A_S} = \frac{R' \cos(\phi + \beta - \alpha) \sin \phi}{A} \quad (6.1)$$

where  $A_S$  and  $A$  are the areas of the shear plane and that corresponding to the width of cut ( $b$ ), times the depth of cut ( $t$ ). Ernst and Merchant [4] reasoned that  $\tau$  should be an angle such that  $\tau$  would be a maximum and a relationship for  $\phi$  was obtained by differentiating Eq. 6.1 with respect to  $\phi$  and equating the resulting expression to zero produces,

$$\phi = 45 - \frac{\beta}{2} + \frac{\alpha}{2} \quad (6.2)$$

However, it is to be noted that in differentiating, both  $R'$  and  $\beta$  were considered independent of  $\phi$ . Merchant [5] presented a different derivation that also led to Eq. 6.2. This time an expression for the total power consumed in the cutting process was first written as,

$$P = F_P V = (\tau A V) \frac{\cos(\beta - \alpha)}{\sin \phi \cos(\phi + \beta - \alpha)} \quad (6.3)$$

It was then reasoned that  $\phi$  would be such that the total power would be a minimum. An expression identical to Eq. 6.2 was obtained when  $P$  was differentiated with respect to  $\phi$ , this time considering  $\tau$  and  $\beta$  to be independent of  $\phi$ . Piispanen [6] had done this previously in a graphical way. However, he immediately carried his line of reasoning one step further and assumed that the shear stress  $\tau$  would be influenced directly by normal stress on the shear plane as follows,

$$\tau = \tau_0 + K\sigma \quad (6.4)$$

where,  $K$  is a material constant. Piispanen [6] then incorporated this into his graphical solution for the shear angle. Upon finding Eq. 6.2 to be in poor agreement with experimental data, Merchant also independently (without knowledge of Piispanen's work at the time) assumed that the relationship given in Eq. 6.4, and proceeded to work this into his second analysis as follows. Hence,

$$\sigma = \tau \tan(\phi + \beta - \alpha) \quad (6.5)$$

or, from Eq. 6.4

$$\tau_0 = \tau + K\tau \tan(\phi + \beta - \alpha) \quad (6.6)$$

Hence,

$$\tau = \frac{\tau_0}{1 - K \tan(\phi + \beta - \alpha)} \quad (6.7)$$

when this is substituted into Eq. 6.3 we have,

$$P = \frac{\tau_0 AV \cos(\beta - \alpha)}{[1 - K \tan(\phi + \beta - \alpha)] \sin \phi \cos(\phi + \beta - \alpha)} \quad (6.8)$$

Now, when  $P$  is differentiated with respect to  $\phi$  and equated to zero (with  $\tau_0$  and  $\beta$  considered independent of  $\phi$  we obtain,

$$\phi = \frac{\cot^{-1}(K)}{2} - \frac{\beta}{2} + \frac{\alpha}{2} = \frac{C - \beta + \alpha}{2} \quad (6.9)$$

Merchant called the quantity,  $\cot^{-1} K$ , the machining "constant"  $C$ . The quantity  $C$  is seen to be the angle the assumed line relating  $\tau$  and  $\phi$  makes with the  $\tau$  axis. Merchant [7] has determined the values of  $C$  given in Table 6.1 for materials of different chemistry and structure being turned under finishing conditions with different tool materials. From this table it is evident that  $C$  is not a constant. Merchant's empirical machining "constant"  $C$  that gives rise to Eq. 6.9 with values of  $\phi$  is in reasonably good agreement with experimentally measured values.

While it is well established that the rupture stress of both brittle and ductile materials is increased significantly by the presence of compressive stress (known as

**Table 6.1** Values of C in Eq. 6.9 for a variety of work and tool materials in finish turning without a cutting fluid

Work material	Tool material	C
SAE 1035 Steel	HSS <sup>a</sup>	70
SAE 1035 Steel	Carbide	73
SAE 1035 Steel	Diamond	86
AISI 1022 (lead)	HSS <sup>a</sup>	77
AISI 1022 (lead)	Carbide	75
AISI 1113 (sul.)	HSS <sup>a</sup>	76
AISI 1113 (sul.)	Carbide	75
AISI 1019 (plain)	HSS <sup>a</sup>	75
AISI 1019 (plain)	Carbide	79
Aluminium	HSS <sup>a</sup>	83
Aluminium	Carbide	84
Aluminium	Diamond	90
Copper	HSS <sup>a</sup>	49
Copper	Carbide	47
Copper	Diamond	64
Brass	Diamond	74

Reprinted with permission from Jackson and Morrell [31]

<sup>a</sup> HSS High-speed steel

the Mohr Effect), it is generally believed that a similar relationship for flow stress does not hold. However, an explanation for this paradox with considerable supporting experimental data is presented below. The fact that this discussion is limited to steady-state chip formation rules out the possibility of periodic gross cracks being involved. However, the role of micro-cracks is a possibility consistent with steady-state chip formation and the influence of compressive stress on the flow stress in shear. A discussion of the role micro-cracks can play in steady-state chip formation is presented in the next section. Hydrostatic stress plays no role in the plastic flow of metals if they have no porosity. Yielding then occurs when the von Mises criterion reaches a critical value. Merchant [5] has indicated that Barrett [8] found that for single crystal metals  $\sigma_s$  is independent of  $\tau_s$  when plastics such as celluloid are cut. In general, if a small amount of compressibility is involved yielding will occur when the von Mises criterion reaches a certain value.

However, based on the results of Table 6.1 the role of compressive stress on shear stress on the shear plane in steady-state metal cutting is substantial. The fact there is no outward sign of voids or porosity in steady-state chip formation of a ductile metal during cutting and yet there is a substantial influence of normal stress on shear stress on the shear plane represents an interesting paradox. It is interesting to note that Piispanen [6] had assumed that shear stress on the shear plane would increase with normal stress and had incorporated this into his graphical treatment.

## 6.2.2 Plastic Behaviour at Large Strains

There has been little work done in the region of large plastic strains. Bridgman [9] used hollow tubular notched specimens to perform experiments under combined axial compression and torsion. The specimen was loaded axially in compression as the centre section was rotated relative to the ends. Strain was concentrated in the reduced sections and it was possible to crudely estimate and plot shear stress versus shear strain with different amounts of compressive stress on the shear plane. From these experiments Bridgman concluded that the flow curve for a given material was the same for all values of compressive stress on the shear plane, a result consistent with other materials experiments involving much lower plastic strains. However, the strain at gross fracture was found to be influenced by compressive stress. A number of related results and possible models are considered in the following subsections.

### 6.2.2.1 Langford and Cohen's Model

Langford and Cohen [10] were interested in the behaviour of dislocations at very large plastic strains and whether there was saturation relative to the strain hardening effect with strain, or whether strain hardening continued to occur with strain to the point of fracture. Their experimental approach was an interesting and fortunate one. They performed wire drawing on iron specimens using a large number of progressively smaller dies with remarkably low semi die angle ( $1.5^\circ$ ) and a relatively low (10 %) reduction in area per die pass. After each die pass, a specimen was tested in uniaxial tension and a true stress-strain curve obtained. The drawing and tensile experiments were performed at room temperature and low speeds to avoid heating and specimens were stored in liquid nitrogen between experiments to avoid strain aging effects. All tensile results were plotted in a single diagram, the strain used being that introduced in drawing (0.13 per die pass) plus the plastic strain in the tensile test. The general overlap of the tensile stress-strain curves gives an overall strain-hardening envelope, which indicates that the wire drawing and tensile deformations are approximately equivalent relative to strain hardening [11].

Blazynski and Cole [12] were interested in strain hardening in tube drawing and tube sinking. Drawn tubes were sectioned and tested in plane strain compression. Up to a strain of about 1 the usual strain-hardening curve was obtained that is in good agreement with the generally accepted equation,

$$\sigma = \sigma_1 \varepsilon^n \quad (6.10)$$

However, beyond a strain of 1, the curve was linear corresponding to the equation,

$$\sigma = A + B\varepsilon, (\varepsilon < 1) \quad (6.11)$$

where A and B are constants. It may be shown that,

$$A = (1 - n)\sigma_1 \quad (6.12)$$

$$B = n\sigma_1 \quad (6.13)$$

From transmission electron micrographs of deformed specimens, Langford and Cohen found that cell walls representing concentrations of dislocations began to form at strains below 0.2 and became ribbon shaped with decreasing mean linear intercept cell size as the strain progressed. Dynamic recovery and cell wall migration resulted in only about 7 % of the original cells remaining after a strain of 6. The flow stress of the cold-worked wires was found to vary linearly with the reciprocal of the mean transverse cell size [13].

### 6.2.2.2 Walker and Shaw's Model

Acoustic studies were performed on specimens of the Bridgman type but fortunately, lower levels of axial compressive stress than Bridgman had used were employed in order to more closely simulate the concentrated shear process of metal cutting. The apparatus used that was capable of measuring stresses and strains as well as acoustic signals arising from plastic flow is described in the dissertation of Walker [14]. Two important results were obtained:

1. A region of rather intense acoustical activity occurred at the yield point followed by a quieter region until a shear strain of about 1.5 was reached. At this point there was a rather abrupt increase in acoustic activity that continued to the strain at fracture which was appreciably greater than 1.5; and
2. The shear stress appeared to reach a maximum at strain corresponding to the beginning of the second acoustic activity ( $\gamma \approx 1.5$ ).

The presence of the notches in the Bridgman specimen made interpretation of stress-strain results somewhat uncertain. Therefore, a new specimen was designed which substitutes simple shear for torsion with normal stress on the shear plane. By empirically adjusting distance  $\Delta x$  to a value of 0.25 mm it was possible to confine all the plastic shear strain to the reduced area, thus making it possible to readily determine the shear strain ( $\gamma \approx \Delta y/\Delta x$ ). When the width of minimum section was greater or less than 0.25 mm, the extent of plastic strain observed in a transverse micrograph at the minimum section either did not extend completely across the 0.25 mm dimension or beyond this width.

Similar results were obtained for non-resulfurised steels and other ductile metals. There is little difference in the curves for different values of normal stress on the shear plane ( $\sigma$ ) to a shear strain of about 1.5 [15]. This is in agreement with Bridgman. However, beyond this strain the curves differ substantially with compressive stress on the shear plane. At large strains,  $\tau$ , was found to decrease with increase in ( $\gamma$ ), a result that does not agree with Bridgman [9].



It is seen that for a low value of normal stress on the shear plane of 40 MPa strain hardening appears to be negative at a shear strain of about 1.5; that is, when the normal stress on the shear plane is about 10 % of the maximum shear stress reached, negative strain hardening sets in at a shear strain of about 1.5. On the other hand, strain hardening remains positive to a normal strain of about 8 when the normal stress on the shear plane is about equal to the maximum shear stress.

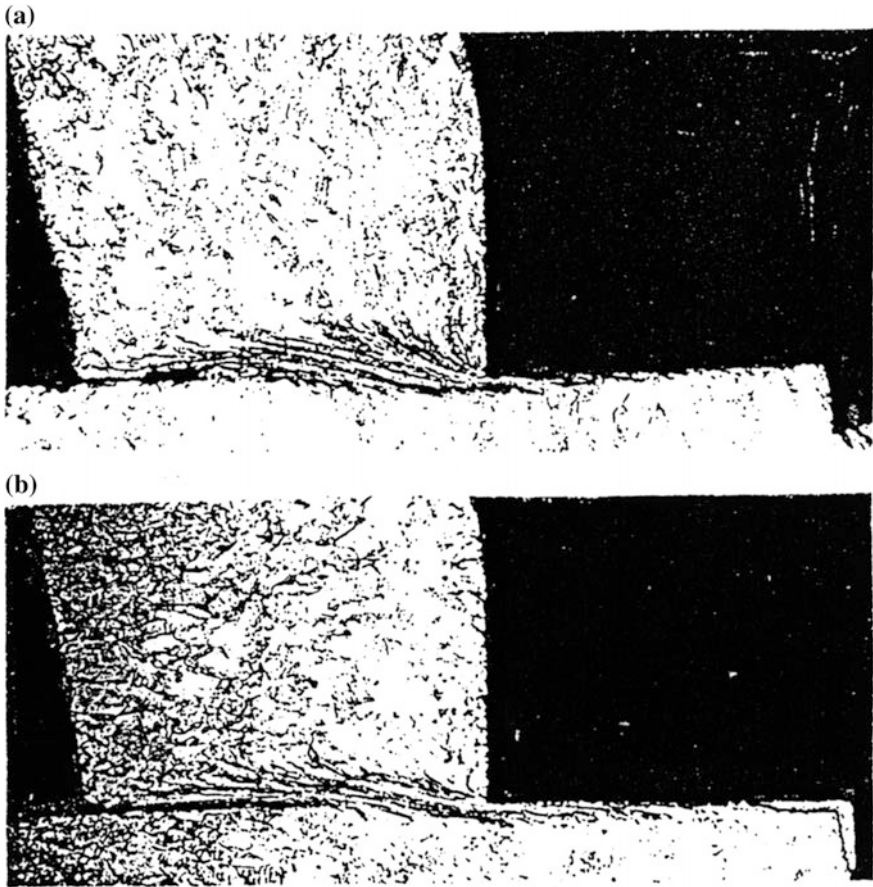
### 6.2.2.3 Usui's Model

In Usui et al. [16] an experiment is described designed to determine why  $\text{CCl}_4$  is such an effective cutting fluid at low cutting speeds. Since this also has a bearing on the role of micro-cracks in large strain deformation, it is considered here. A piece of copper was prepared. The piece that extends upward and appears to be a chip is not a chip but a piece of undeformed material left there when the specimen was prepared. A vertical flat tool was then placed precisely opposite the free surface and fed horizontally. Horizontal  $F_P$  and vertical  $F_Q$  forces were recorded as the shear test proceeded. It was expected that the vertical piece would fall free from the lower material after the vertical region had been displaced a small percentage of its length. However, it went well beyond the original extent of the shear plane and was still firmly attached to the base. This represents a huge shear strain since the shear deformation was confined to a narrow band. When a single drop of  $\text{CCl}_4$  was placed before the shear test was conducted the protrusion could be moved only a fraction of the displacement in air before gross fracture occurred on the shear plane. Figure 6.2 shows photomicrographs of experiments without and with  $\text{CCl}_4$ . It is apparent that  $\text{CCl}_4$  is much more effective than air in preventing micro-cracks from re-welding.

Saw tooth chip formation for hard steel discussed by Vyas and Shaw [17] is another example of the role micro-cracks play. In this case gross cracks periodically form at the free surface and run down along the shear plane until sufficient compressive stress is encountered to cause the gross crack to change to a collection of isolated micro-cracks.

### 6.2.3 Fluid-Like Flow in Chip Formation

An interesting paper was presented by Eugene [18]. Water was pumped into a baffled chamber that removed eddy currents and then caused flow under gravity passed a simulated tool. Powdered bakelite was introduced to make the streamlines visible as the fluid flowed passed the tool. The photographs taken by the camera were remarkably similar to quick stop photomicrographs of actual chips. It was thought by this author at the time that any similarity between fluid flow and plastic flow of a solid was not to be expected. That was long before it was clear that the only logical explanation for the results of Bridgman and Merchant involve



**Fig. 6.2** Photomicrographs of specimens that have been sheared a distance approximately equal to the shear plane length: **a** in air; and **b** with a drop of  $\text{CCl}_4$  applied. Reprinted with permission from Jackson and Morrell [31]

micro-fracture [19]. A more recent paper was presented that again suggests that metal cutting might be modelled by a fluid [20]. However, this paper was concerned with ultra-precision machining (depths of cut  $<4 \mu\text{m}$ ) and potential flow analysis was employed instead of the experimental approach taken by Eugene.

It is interesting to note that chemists relate the flow of liquids to the migration of vacancies (voids) just as physicists relate ordinary plastic flow of solid metals to the migration of dislocations. Eyring et al. [21], Eyring and Ree [22], Eyring and Jhon [23] have studied the marked changes in volume, entropy and fluidity that occur when a solid melts. For example, a 12 % increase in volume accompanies melting of Argon, suggesting the removal of every eighth molecule as a vacancy upon melting. This is consistent with X-ray diffraction of liquid argon that showed good short-range order but poor long-range order. The relative ease of diffusion of these

vacancies accounts for the increased fluidity that accompanies melting. A random distribution of vacancies is also consistent with the increase in entropy observed on melting. Eyring's theory of fluid flow was initially termed the "*hole theory of fluid flow*" but later "*The Significant Structure Theory*" [23]. According to this theory the vacancies in a liquid move through a sea of molecules. Eyring's theory of liquid flow is mentioned here since it explains why the flow of a liquid approximates the flow of metal passed a tool in chip formation. In this case micro-cracks (voids) move through a sea of crystalline solid.

### 6.3 Frictional Interactions at the Machining Interface

Section 6.3 of the chapter focuses on frictional interactions at the machining interface and introduces the reader to understand the mechanics of intimate contact from an experimental viewpoint. Subsections of this viewpoint focus primarily on cutting, ploughing and sliding interactions in terms of static friction and stick-slip phenomena, models for sliding friction, frictional heating and its effect on cutting mechanics, and methods to reduce friction by lubrication.

Initial studies on chip-tool interactions during machining operations were carried out by Professor David Tabor and his team at the Cavendish Laboratory at the University of Cambridge in the United Kingdom during the late 1970s. In their initial studies [24] constructed a transparent sapphire cutting tool bonded to a tool holder that transmitted the action of chip formation so that it could be observed. The reflection of the freshly cut chip is transmitted through the tool by reflecting the image on to a projection face that is highly polished. Doyle et al. [24] reported that they used pure lead and pure tin in air to witness the mechanism of metal transfer to the cutting tool and defined the nature of contact in terms of contact zones as the chip moved across the surface of the tool at low cutting speeds. Initially, two zones were noted, one of sliding across the rake face of the tool (zone 1) and one consisting of the chip material sticking to the rake face (zone 2) ahead of zone 1. On further inspection of the images obtained using a cine camera, zone 1 comprised of two sub zones, namely: zone 1a (where the chip material slides at the edge of the cutting tool on its rake face) and zone 1b (where the chip material sticks to the cutting edge). Further studies by Horne et al. [25], further characterized the nature of contact between the cut chip and the surface of the tool. In an effort to understand the mechanics of chip formation and lubrication, a series of experiments were developed to understand how cooling lubricants provide a thin film between the chip and tool material. In their studies, various lubricants were used and dropped into the chip-tool zone in an effort to provide the means of separation between tool and chip. The lubricant was shown to enter the chip at the side of the material and is absorbed beneath the chip as the chip moves across the rake face. The formation of bubbles is also noticeable when machining aluminium with  $\text{CCl}_4$ , and may significantly contribute to the change in the mechanism of material transfer from chip to tool or the mechanics of machining. The work currently performed at Purdue

University is based on work that was previously conducted at the Cavendish Laboratory and focuses on quantifying the interactions between chip and tool. This work investigates the applicability of applying orthogonal and oblique cutting theories. The initial work was completed by Madhavan [26]. Again, the use of transparent sapphire tools was employed. The cutting tool has a highly polished surface and was used with a research apparatus that is similar in action to the configuration of a metal planer. A Newport slide, model number PM500-4, was used for the linear slide with which to move the workpiece toward the cutting tool. The slide is controlled by a microprocessor. The velocity of the workpiece ranged from 25 to 150 mm/s. The use of an angle plate was necessary to attach the workpiece to the slide. Another slide was used to adjust the depth of cut of the cutting tool. The entire apparatus was mounted to a vibration isolation table. Soda-lime glass tool was used for comparison with the sapphire tool in order to allow for a comparison of frictional constants and sliding mechanisms between the two substrates. These were again highly polished using small cuboids of soda-lime glass for the rough polish. The final polish involved the use of 1  $\mu\text{m}$  diameter cerium oxide particles. The experiments were imaged using an Olympus model OM-4T microscope. The magnification ranged from  $\times 50$  to 200. Force measurements were made with a Kistler piezoelectric transducer. The transducer interestingly enough was configured between the back of the cutting tool and the actual tool holder. The signal produced by the transducer was recorded using an oscilloscope. This was capable of recording the cutting force and the thrust force during machining.

These experiments were conducted for both smooth, polished tools and roughened tools. This was performed to determine if the tool would replicate the rake face of a conventional tool. The tools reflect the image of the rake face to the side of the tool for easy observation as described by Doyle et al. [24]. The initial experiments involved the cutting of wax to develop a basic idea of what may occur. An observation of the process showed that microcracks were formed during the planing of wax. This in turn created a crack along the shear plane. This observation would begin the basis of machining other plastically deformable materials in order to observe the mechanism of machining.

The use of pure lead was considered essential for the experiments concerned with understanding rake face interactions. This was performed using the dry cutting and lubricated conditions. The lubricant was composed of a mixture of 2 parts of oil and 1 part of ink. From these experiments, it was determined that three distinct zones form. The three zones are: Ia, Ib, and II. In zone Ia, the chip interacts with the tool that is known as intimate sliding contact. In zones Ib and II, the chip experiences sticking and metal transfer to the rake face of the tool. When the lubricant is used, metal transfer does not occur in zones Ib and II. It was observed by Doyle et al. [24], that zone II does not form when the experiment is conducted in a vacuum. The idea that there are three distinct zones is puzzling if two of the zones experience the same sliding action. Perhaps two zones with one zone composed of two sub zones would have provided a better explanation of the situation. The magnitude of shear strain is briefly mentioned. The average shear strain for lead is 40–100. The shear strain for aluminium and copper is approximately 20.

There were no calculations included for these values, nor a discussion about the effect of strain causing chip curl. Further experiments were conducted in the later 1990s by Ackroyd [27], who used a new piece of apparatus for characterizing chip-tool interactions. This work further investigated the frictional interactions initially noted by Madhavan [26]. The cutting tool used was again a highly polished sapphire tool bit.

The experimental workpieces used included pure lead as well as pure tin. Both of these materials were obtained from Goodfellow in England. The percentage purity of both materials was 99.95 %. The dimensions of the workpiece were  $50 \text{ mm}^2 \times 2 \text{ mm}$  thick. Ackroyd [27] also investigated the machining of brass and pure aluminium. Sapphire tools were compared to aluminium and high-speed steel tools. With the use of these tools, a comparative analysis was undertaken to determine if the frictional effects were similar for all tool materials. The sapphire tool was once again polished with cerium oxide and then cleaned with acetone. The rake angles of the tools were  $10^\circ$  and  $-5^\circ$ . The experimental apparatus uses a linear drive made by Anorad (model number LW5-750). This unit is capable of a maximum velocity of 2 m/s. The workpiece is similarly mounted to this unit to achieve the maximum workpiece velocity. The vertical stage used was the Newport 433 model. This stage is equipped with the Newport DMH-1, which is a digital micrometer. This allows for measurement of a  $1 \mu\text{m}$  resolution over a 15 mm range. The Newport stage is attached to a Kistler 9254 dynamometer. This is attached to cast iron v-blocks that have been mounted to a worktable. The Kistler unit is used in conjunction with a dual mode amplifier (Kistler 5010B). The optics used for observation can magnify up to  $\times 200$ . The CCD camera used is a Sony DXC-930. The camera was used in conjunction with s-VHS video. The model used was a Panasonic AG-1970 with a capability of 30 frames per second. The digital high-speed camera used was a Kodak Motion Corder Analyzer Sr-Ultra. It is difficult to determine more than two zones resulting from the machining experiment. For the initial experiments, the following are the parameters were used: The depth of cut was  $200 \mu\text{m}$ ; width of cut was 2 mm; length of cut was 50 mm, and the cutting speed ranged from 0.5 to 500 mm/s. It was discovered, and was confirmed by Robinson [28], that the cutting edge plays a significant role in the machining experiments. As the nose radius becomes larger, the depth of cut determines whether the cutting tool cuts, or shears the workpiece material. A large cutting nose radius can create a negative rake angle on the cutting tool if the depth of cut is smaller than the nose radius.

From this work, it can be seen that there are two zones. The first zone involves the chip sliding with no deposit of metal. The second zone involves the chip sticking with some material deposited onto the tool. It was observed that a blunt tool has a higher normal force than a sharp tool. The frictional force versus normal force ratio decreases with the increase in velocity. It was also noted that there were no material deposits to the rake face at higher velocities. The discussion and conclusions of this work show that continual frictional forces increase. This is not a claim that can be substantiated. If frictional force continually increases with friction, it would reach a catastrophic point where the tool would fail. The conclusion was

made using a single machining force measurement to examine both the sticking and sliding regions in question. Both zones cannot be observed simultaneously, therefore a direct comparison cannot be made.

Subsequent work completed by Hwang [29] followed closely the work of Ackroyd [27]. The apparatus that was previously used was upgraded with new components. The use of sapphire and high-speed tools for machining was investigated further by Hwang [29]. The experiments were designed to investigate the sliding and sticking zones. The apparatus was upgraded with a new linear slide. The linear slide was ball screw driven and was supplied by Parker as model number ERB80-B02LAJX-GXS677-A96. This allows for a larger power motor to drive the linear slide. The increased power allowed a larger variety of materials to be investigated. The slide has a maximum speed of 750 mm/s. Again, the vertical stage used was a Newport model number 433. This is actuated using the Newport digital micrometer model number DMH-1. The imaging system remained the same as that used by Ackroyd [27].

A wider variety of plastically deformed materials were used in the experiments. The list includes oxygen free, high conductivity copper (OFHC), cartridge brass, pure lead, Al 1100 aluminium, and Al 6061-T6 aluminium. Hardness values were taken for all materials except for pure lead. The following are the Vickers' hardness values: OFHC =  $89.7 \text{ kg mm}^{-2}$ , cartridge brass =  $153 \text{ kg mm}^{-2}$ , Al 1,100 =  $49.5 \text{ kg mm}^{-2}$ , and Al 6061-T6 =  $116 \text{ kg mm}^{-2}$ . The workpiece specimens investigated closely were pure lead and Al 6061-T6. The depth of cut for the lead was  $200 \text{ }\mu\text{m}$ , while the depth of cut for the 6061 was  $100 \text{ }\mu\text{m}$ . The cutting velocity spanned from 0.5 to 500 mm/s. The exact speeds used were 0.5, 5, 50, and 500 mm/s, respectively. These experiments looked at the effects of lubrication on the chip formation process. The use of lubricant was observed to reduce the length of chip-tool contact length. The investigation focused on the rake face's sliding and sticking regions. This is a continuation of the work performed by Ackroyd [27] and shows the variation in machining different materials. Another aspect of the chip formation process was closely examined. The secondary deformation in a chip was explored with the use of a quick-stop experiment. This is an experiment that stops the cutting tool about three-quarters of the way across the workpiece. This will allow for the examination of the primary shear zone and grain orientation in the chip compared to the substrate. Another segment of the research investigated the use of modulation during machining pure metals with lubricant. The experiment was conducted with a vertical slide as opposed to a horizontal slide. It was not directly observed that the cutting fluid penetrated into the intermittent contact zone during these experiments. This assumption is made due to chip debris remaining static and the elimination of the metal deposit zone. During modulation, frictional forces are much smaller. It was noted that cutting remains under high pressure in the gap ahead of the cutting tool and that the cutting fluid reduced the region of the chip-tool contact. In this region, the contact length reduction promotes a reduction in frictional force. The application of cutting fluid will cause the zone of metal deposits to move further away from the tool edge. This will prevent the expansion of the stagnant metal

zone. This is beneficial to eliminate a partial frictional constant. However, it is questionable as to whether modulation is solely responsible for this action.

The measurement of the rake face temperature was performed using an infra-red imaging system. The signal is reflected at the back of the tool in order to investigate the temperature of the rake face of the tool. The methods of calculating temperature developed by Rapier, Boothroyd, and Loewen and Shaw were used to calculate the rake face temperature. These calculations were then compared to the measured data. From these results, it can be reasoned that modulation does not solve the frictional contact problem. However, modulation does create a constant cutting length and constant values of friction between chip and tool. However, this action alone is dependent upon the stroke length chosen, and will be different for each material machined and the corresponding depth of cut.

The research conducted by Lee [30] follows closely the work of both Ackroyd [27] and Hwang [29]. Lee's study included using particle image velocimetry to measure chip velocity. This utilized a linear slide with a ball screw and allows for an adjustment of the depth of cut as little as 1  $\mu\text{m}$ . A charge-coupled device (CCD) was used for high-speed imaging. Similar to the Hwang's work, a Kodak Motion Corder Analyzer Sr-Ultra was used. An optical microscope records the chip formation process, and employs a Nikon Optiphot that can examine the specimen up to  $\times 200$  magnification. The CCD can capture images of up to 10,000 fps using a black and white format. The spatial resolution is 3.3  $\mu\text{m}$  pixel size. The experiments were conducted dry. The workpiece specimens used were commercially pure lead and copper that is 99.95 % pure. These were both obtained from Goodfellow, UK. In the initial investigation using 6061-T6 aluminium, a built-up edge (BUE) was observed on the rake face. The BUE changes the rake angle thus increasing the chip velocity more than in the machining of other materials.

The velocity of the chip was inspected using constrained workpiece specimens. These areas show the rake face and the side view of the cut chip. This allows for the investigation of the metal deposit on the rake face and the effects of deformation in the secondary zone. A vertical stage moves the tool into contact with the workpiece. This is made possible through the use of a micrometer. At the foundation is the ball screw drive that brings the workpiece into contact with the cutting tool. This is a satisfactory experimental apparatus. However, there remains much to be desired with this particular apparatus in terms of rigidity and range of workpiece cutting speeds.

### ***6.3.1 Cutting, Ploughing and Sliding Interactions***

The nature of the contact between surfaces is an important aspect of understanding the function of tribology in machining [31]. The properties of the materials in contact are homogeneous and isotropic. Macro-contact conditions are most useful in models for friction when there is lubrication and the effects of surface heterogeneities are of little importance. Hertz's equations allow engineers to calculate the

**Table 6.2** Equations for calculating elastic (Hertz) contact stress

Symbol	Definition	
$P$	Normal force	
$p$	Normal force per unit contact length	
$E_{1,2}$	Modulus of elasticity for bodies 1 and 2, respectively	
$\nu_{1,2}$	Poisson's ratios for bodies 1 and 2, respectively	
$D$	Diameter of the curved body, if only one if curved	
$D_{1,2}$	Diameters of bodies 1 and 2, where $D_1 > D_2$ by convention	
$S_c$	Maximum compressive stress	
$a$	Radius of the elastic contact	
$b$	Width of a contact (for cylinders)	
$E^*$	Composite modulus of bodies 1 and 2	
$A, B$	Functions of the diameters of bodies 1 and 2	
Geometry	Contact dimension	Contact stress
Sphere-on-flat	$a = 0.721 \sqrt{[3]PDE^*}$	$S_c = 0.918 \sqrt{[3]P/(D^2E^*)^2}$
Cylinder-on-flat	$b = 1.6 \sqrt{pDE^*}$	$S_c = 0.798 \sqrt{p/DE^*}$
Cylinder-on-cylinder (axes parallel)	$b = 1.6 \sqrt{pE^*/A}$	$S_c = 0.798 \sqrt{pA/E^*}$
Sphere in a spherical socket	$a = 0.721 \sqrt{[3]PE^*/B}$	$S_c = 0.918 \sqrt{[3]P(B/E^*)^2}$
Cylinder in a circular groove	$b = 1.6 \sqrt{pE^*/B}$	$S_c = 0.798 \sqrt{pB/E^*}$

Reprinted with permission from Jackson and Morrell [31]

maximum compressive contact stresses and contact dimensions for non-conforming bodies in elastic contact. The parameters required to calculate the quantities and the algebraic equations used for simple geometries are given in Table 6.2 [32]. It should be noted that Hertz's equations apply to static, or quasi-static, elastic cases. In the case of sliding, plastic deformation, contact of very rough surfaces, or significant fracture, both the distribution of stresses and the contact geometry will be altered. Hertz's contact equations have been used in a range of component design applications, and in friction and wear models in which the individual asperities are modeled as simple geometric contacts.

Greenwood and Williamson [33] developed a surface geometry model that modeled contacts as being composed of a distribution of asperities. From that assumption, contact between such a surface and a smooth, rigid plane could be determined by three parameters: the asperity radius ( $R$ ), the standard deviation of asperity heights ( $\sigma^*$ ), and the number of asperities per unit area. To predict the extent of the plastic deformation of asperities, the plasticity index ( $\psi$ ), also a function of the hardness ( $H$ ), elastic modulus ( $E$ ), and Poisson's ratio ( $\nu$ ), was introduced.



$$\psi = \left(\frac{E'}{H}\right) \left(\frac{\sigma^*}{R}\right)^{1/2} \quad (6.14)$$

where,  $E' = E/(1-\nu^2)$ . This basic formulation was refined by various investigators such as Whitehouse and Archard [34] to incorporate other forms of height distributions, and the incorporation of a distribution of asperity radii, represented by the correlation distance  $\beta^*$ , which produced higher contact pressures and increased plastic flow. Therefore,

$$\psi = \left(\frac{E'}{H}\right) \left(\frac{\sigma^*}{\beta}\right)^{1/2} \quad (6.15)$$

Hirst and Hollander [35] used the plasticity index to develop diagrams to predict the start of scuffing wear. Other parameters, such as the average or root mean square slope of asperities, have been incorporated into wear models to account for such peculiarities [36]. Worn surfaces are observed to be much more complex than simple arrangements of spheres, or spheres resting on flat planes, and Greenwood readily acknowledged some of the problems associated with simplifying assumptions about surface roughness [37]. A comprehensive review of surface texture measurement methods have been given by Song and Vorburger [38]. The most commonly used roughness parameters are listed in Table 6.3. Parameters such as skewness are useful for determining lubricant retention qualities of surfaces, since they reflect the presence of cavities. However, one parameter alone cannot precisely model the geometry of surfaces. It is possible to have the same average roughness (or RMS roughness) for two different surfaces.

Small amounts of wear can change the roughness of surfaces on the microscale and disrupt the nanoscale structure as well. Some of the following quantities have been used in models for friction:

1. The true area of contact;
2. The number of instantaneous contacts comprising the true area of contact;
3. The typical shapes of contacts (under load);
4. The arrangement of contacts within the nominal area of contact; and
5. The time needed to create new points of contact.

Finally, contact geometry-based models for friction generally assume that the normal load is constant. This assumption may be unjustified, especially when sliding speeds are relatively high, or when there are significant friction and vibration interactions in the tribosystem. As the sliding speed increases, frictional heating increases and surface thermal expansion can cause intermittent contact. The growth and excessive wear of intermittent contact points is termed thermoelastic instability (TEI) [39]. TEI is only one potential source of the interfacial dynamics responsible for stimulating vibrations and normal force variations in sliding contacts. Another major cause is the eccentricity of rotating shafts, run-out, and the transmission of external vibrations. Static friction and stick-slip behaviour are

**Table 6.3** Definitions of surface roughness parameters

Let $y_i$ = vertical distance from the $i$ th point on the surface profile to the mean line	
$N$ = number of points measured along the surface profile	
Thus, the following are defined:	
Arithmetic average roughness	$R_a = \frac{1}{N} \sum_{i=1}^N  y_i $
Root-mean-square roughness	$R_q = \left[ \frac{1}{N} \sum_{i=1}^N y_i^2 \right]^{1/2}$
Skewness	$R_{sk} = \frac{1}{NR_q^3} \sum_{i=1}^N y_i^3$
	A measure of the symmetry of the profile
	$R_{sk} = 0$ for a Gaussian height distribution
Kurtosis	$R_{kurtosis} = \frac{1}{NR_q^4} \sum_{i=1}^N y_i^4$
	A measure of the sharpness of the profile
	$R_{kurtosis} = 3.0$ for a Gaussian height distribution
	$R_{kurtosis} < 3.0$ for a broad distribution of heights
	$R_{kurtosis} > 3.0$ for a sharply-peaked distribution

Reprinted with permission from Jackson and Morrell [31]

considered, and as with kinetic friction, the causes for such phenomena can be interpreted on several scales.

### 6.3.1.1 Static Friction and Stick-Slip Phenomena

If all possible causes for friction are to be considered, it is reasonable to find out whether there are other means to cause bodies to stay together without the requirement for molecular bonding. Surfaces may adhere, but adherence is not identical to adhesion, because there is no requirement for molecular bonding. If a certain material is cast between two surfaces and, after penetrating and filling irregular voids in the two surfaces, solidifies to form a network of interlocking contacting points there may be strong mechanical joint produced, but no adhesion. Adhesion (i.e., electrostatically balanced attraction/chemical bonding) in friction theory meets the need for an explanation of how one body can transfer shear forces to another. Clearly, it is convenient to assume that molecular attraction is strong enough to allow the transfer of force between bodies, and in fact this assumption has led to many of the most widely used friction theories. From another perspective, is it not equally valid to consider that if one pushes two rough bodies together so that asperities penetrate, and then attempts to move those bodies tangentially, the atoms may approach each other closely enough to repel strongly, thus causing a backlash against the bulk materials and away from the interface. The repulsive force parallel to the sliding direction must be overcome to move the bodies tangentially,

whether accommodation occurs by asperities climbing over one another, or by deforming one another. In the latter, it is repulsive forces and not adhesive bonding that produces sliding resistance. This section focuses on static friction and stick slip phenomena.

Ferrante et al. [40] have provided a comprehensive review of the subject. A discussion of adhesion and its relationship to friction has been conducted by Buckley [41]. Atomic probe microscopes permit investigators to study adhesion and lateral forces between surfaces on the atomic scale. The force required to shift the two bodies tangentially must overcome bonds holding the surfaces together. In the case of dissimilar metals with a strong bonding preference, the shear strength of the interfacial bonds can exceed the shear strength of the weaker of the two metals, and the static friction force ( $\mathbf{F}_s$ ) will depend on the shear strength of the weaker material ( $\tau_m$ ) and the area of contact ( $A$ ). In terms of the static friction coefficient  $\mu_s$ ,

$$\mathbf{F}_s = \mu_s \mathbf{P}^* = \tau_m A \quad (6.16)$$

or,

$$\mu_s = (\tau_m / \mathbf{P}^*) A \quad (6.17)$$

where  $\mathbf{P}^*$ , the normal force is comprised of the applied load and the adhesive contribution normal to the interface. Under specially controlled conditions, such as friction experiments with clean surfaces in vacuum, the static friction coefficients can be greater than 1.0, and the experiment becomes a test of the shear strength of the solid materials than of interfacial friction. Scientific understanding and approaches to modeling friction has been strongly influenced by concepts of solid surfaces and by the instruments available to study them. Atomic-force microscopes and scanning tunneling microscopes permit views of surface atoms with high resolution and detail. Among the first to study nanocontact frictional phenomena were McClellan et al. [42, 43]. A tungsten wire with a very fine tip is brought down to the surface of a highly oriented, cleaved basal plane of pyrolytic graphite as the specimen is oscillated at 10 Hz using a piezoelectric driver system. The cantilevered wire is calibrated so that its spring constant is known (2,500 N/m) and the normal force could be determined by measuring the deflection of the tip using a reflected laser beam. As the normal force is decreased, the contributions of individual atoms to the tangential force became apparent. At the same time, it appeared that the motion of the tip became less uniform, exhibiting atomic-scale stick-slip.

Thompson and Robbins [44] discussed the origins of nanocontact stick-slip when analyzing the behaviour of molecularly thin fluid films trapped between flat surfaces of face-centered cubic solids. At that scale, stick-slip was believed to arise from the periodic phase transitions between ordered static and disordered kinetic states. Immediately adjacent to the surface of the solid, the fluid assumed a regular, crystalline structure, but this was disrupted during each slip event. The experimental data points of friction force per unit area versus time exhibited extremely uniform classical stick-slip appearance. Once slip occurred, all the kinetic energy must be

converted into potential energy in the film. In subsequent papers [45] this group of authors used this argument to calculate the critical velocity,  $v_c$ , below which the stick-slip occurs is:

$$v_c = c(\sigma \mathbf{F}_s / M)^{1/2} \quad (6.18)$$

where  $\sigma$  is the lattice constant of the wall,  $\mathbf{F}_s$  is the static friction force,  $M$  is the mass of the moving wall, and  $c$  is a constant.

Friction is defined as the resistance to relative motion between two contacting bodies parallel to a surface that separates them. Motion at the atomic scale is unsteady. In nanocontact, accounting for the tangential components of thermal vibrations of the atoms thus affects our ability to clearly define relative motion between surfaces. Under some conditions it may be possible to translate the surface laterally while the adhesive force between the probe tip and the opposite surface exceeds the externally applied tensile force. Landman et al. [46] reviewed progress in the field of molecular dynamics (MD). By conducting MD simulations of nickel rubbing a flat gold surface, Landman illustrated how the tip can attract atoms from the surface simply by close approach without actual indentation. A connective neck or bridge of surface atoms was observed to form as the indenter was withdrawn. The neck can exert a force to counteract the withdrawal force on the tip, and the MD simulations clearly model transfer of material between opposing asperities under pristine surface conditions. Landman has subsequently conducted numerous other MD simulations, including complete indentation and indentation in the presence of organic species between the indenter and substrate. Belak and Stowers [47], using a material volume containing 43,440 atoms in 160 layers, simulated many of the deformational features associated with metals, such as edge dislocations, plastic zones, and point defect generation. Calculated shear stresses for a triangular indenter passing along the surface exhibited erratic behaviour, not unlike that observed during metallic sliding under clean conditions. Pollock and Singer [48] compiled a series of papers on atomic-scale approaches to friction.

While MD simulations and atomic-scale experiments continue to provide fascinating insights into frictional behaviour, under idealized conditions, most engineering tribosystems are non-uniform. Not only are surfaces not atomically flat, but the materials are not homogeneous, and surface films and contaminant particles of many kinds, much larger than the atomic scale, may influence interfacial behaviour. Static friction coefficients measured experimentally under ambient or contaminated conditions probably will not assume the values obtained in controlled environments. In a series of carefully conducted experiments on the role of adsorbed oxygen and chlorine on the shear strength of metallic junctions [49] showed how,  $\mu_s$ , can be reduced in the presence of adsorbed gases. On the other hand, static friction coefficients for pure, well-cleaned metal surfaces in the presence of non-reactive gases like He can be relatively high. It is interesting to note that the friction of copper on nickel and the friction of nickel on copper are quite different. This is not an error, but rather a demonstration of the fact that reversing the materials of the sliding specimen and the counterface surface can affect the measured friction,

**Table 6.4** Static friction coefficients for clean metals in helium gas at two temperatures

Static friction coefficient		
Material combination	300 K	80 K
Fe (99.9 %) on Fe (99.99 %)	1.09	1.04
Al (99 %) on Al (99 %)	1.62	1.60
Cu (99.95 %) on Cu (99.95 %)	1.76	1.70
Ni (99.95 %) on Ni (99.95 %)	2.11	2.00
Au (99.98 %) on Au (99.98 %)	1.88	1.77
Ni (99.95 %) on Cu (99.95 %)	2.34	2.35
Cu (99.95 %) on Ni (99.95 %)	0.85	0.85
Au (99.98 %) on Al (99 %)	1.42	1.50
Fe (99.9 %) on Cu (99.95 %)	1.99	2.03

Reprinted with permission from Jackson and Morrell [31]

confirming the assertion that friction is a property of the tribosystem and not of the materials in contact. A cryotribometer was used to obtain the data in Table 6.4. The length of time that two solids are in contact can also affect the relative role that adhesion plays in establishing the value of the static friction coefficient. Two distinct possibilities can occur: (a) if the contact becomes contaminated with a lower shear-strength species, the friction will decline; and (b) if the contact is clean and a more tenacious interfacial bond develops, the static friction will tend to increase. Akhmatov [50] demonstrated that by using cleaved rock salt that the formation of surface films over time lowers static friction. The opposite effect has been demonstrated for metals. A first approximation of rising static friction behaviour is given by,

$$\mu_{S(t)} = \mu_{S(t=\infty)} - \left[ \mu_{S(t=\infty)} - \mu_{S(t=0)} \right] e^{-ut} \quad (6.19)$$

where,  $\mu_s(t)$ , is the current value of the static friction coefficient at time  $t$ ,  $\mu_s(t = \infty)$  is the limiting value of the static friction coefficient at long times,  $\mu_s(t = 0)$  is the initial static friction coefficient, and  $u$  is a rate constant. In contrast to exponential dependence on time, Buckley showed that by using data for tests of single-crystal Au touching Cu-5 % Al alloy that junction growth can cause the adhesive force to increase linearly with time.

When materials are placed in intimate contact, it is not unexpected that the atoms on their surfaces will begin to interact. The degree of this interaction will depend on the contact pressure, temperature, and the degree of chemical reactivity that the species have for each other, hence, static friction can change with the duration of contact. Despite the two opposite dependencies of static friction on time of contact, observations are consistent from a thermodynamic standpoint. Systems tend toward the lowest energetic state. In the case of interfaces, this state can be achieved either by forming bonds between the solids, or by forming bonds with other species (adsorbates and films) in the interface. The former process tends to strengthen the

shear strength of the system, and the latter tends to weaken it. Sikorski [51] reported the results of experiments designed to compare friction coefficients of metals with their coefficients of adhesion (defined as the ratio of the force needed to break the bond between two specimens to the force which initially compressed them together). Rabinowicz [52] conducted a series of simple, tilting-plane tests with milligram- to kilogram-sized specimens of a variety of metals. Results demonstrated the static friction coefficient to increase as slider weight (normal force) decreased. For metal couples such as Au/Rh, Au/Au, Au/Pd, Ag/Ag, and Ag/Au, as the normal force increased over about six orders of magnitude (1 mg–1 kg), the static friction coefficients tended to decrease by nearly one order of magnitude.

Under low contact pressures, surface chemistry effects can play a relatively large role in governing static friction behaviour. However, under more severe contact conditions, such as extreme pressures and high temperatures, other factors, more directly related to bulk properties of the solids, dominate static friction behaviour. When very high pressures and temperatures are applied to solid contacts, diffusion bonds or solid-state welds can form between solids, and the term static friction ceases to be applicable. Table 6.5 lists a series of reported static friction coefficients. Note that in certain cases, the table references list quite different values for these coefficients. The temperature of sliding contact can affect the static friction coefficient. This behaviour was demonstrated for single crystal ceramics by Miyoshi and Buckley [41], who conducted static friction tests of pure iron sliding on cleaned {0001} crystal surfaces of silicon carbide in a vacuum ( $10^{-8}$  Pa). For both <1010> and <1120> sliding directions, the static friction coefficients remained about level (0.4 and 0.5, respectively) from room temperature up to about 400 °C; then they each rose by about 50 % as the temperature rose to 800 °C. The authors attributed this effect to increased adhesion and plastic flow. The role of adsorbed films on static friction suggests that one effective strategy for alleviating or reducing static friction is to introduce a lubricant or other surface treatment to impede the formation of adhesive bonds between mating surfaces. Contamination of surfaces from exposure to the ambient environment performs essentially the same function, but is usually less reproducible. Campbell [53] demonstrated how the treatment of metallic surfaces by oxidation can reduce the static friction coefficient. Oxide films were produced by heating metals in air. Sulfide films were produced by immersing the metals in sodium sulfide solution.

Except for the film on steel, film thicknesses were estimated to be 100–200 nm. Results from ten experiments, using a three ball-on-flat plate apparatus, were averaged to obtain static friction coefficients. In addition to producing oxides and sulfides, Campbell also tested oxide and sulfide films with Acto oil. The results of this investigation are shown in Table 6.6. For copper, the static friction coefficient ( $\mu_s = 1.21$ , with no film) decreased when the sulfide film thickness was increased from 0 to about 300 nm, after which the static friction coefficient remained about constant at 0.66.

The extent to which the solid lubricant can reduce static friction may be dependent on temperature, as confirmed by Hardy's earlier studies on the static friction of palmitic acid films on quartz. Between 20 and 50 °C the static friction

**Table 6.5** Static friction coefficients for metals and non-metals (dry or unlubricated conditions)

Material combination			
Fixed specimen	Moving specimen	$\mu_s$	Table reference number
<i>Metals and alloys on various materials</i>			
Aluminium	Aluminium	1.05	1
	Steel, mild	0.61	1
	Titanium	0.54	3
Al, 6061-T6	Al, 6061-T6	0.42	4
	Copper	0.28	4
	Steel, 1032	0.35	4
	Ti-6Al-4 V	0.34	4
Copper	Cast iron	1.05	1
Steel	Cast iron	0.4	2
Steel, hardened	Steel, hardened	0.78	1
	Babbitt	0.42, 0.70	1
	Graphite	0.21	1
Steel, mild	Steel, mild	0.74	1
	Lead	0.95	1
Steel, 1032	Aluminium	0.47	4
	Copper	0.32	4
	Steel, 1032	0.31	4
	Ti-6Al-4 V	0.36	4
Steel, stainless 304	Copper	0.33	4
Tin	Iron	0.55	3
	Tin	0.74	3
Titanium	Aluminium	0.54	3
	Titanium	0.55	3

Reprinted with permission from Jackson and Morrell [31]

1. Bhushan and Gupta [104]
2. Handbook of Chemistry and Physics, 48th Ed., CRC Press (1967)
3. E. Rabinowicz, ASLE Trans., Vol. 14, p. 198; plate sliding on inclined plate at 50 % rel. humidity (1971)
4. "Friction Data Guide," General Magnaplate Corp., Ventura, California 93003, TMI Model 98-5 Slip and Friction Tester, 200 grams load, ground specimens, 54 % rel. humidity, average of 5 tests (1988)

**Table 6.6** Reduction of static friction by surface films

Material combination	$\mu_s$ , No film	$\mu_s$ , Oxide film	$\mu_s$ , Sulfide film
Copper-on-copper	1.21	0.76	0.66
Steel on steel	0.78	0.27	0.39
Steel on steel	0.78	0.19 <sup>a</sup>	0.16 <sup>a</sup>

Reprinted with permission from Jackson and Morrell [31]

<sup>a</sup> film and oil

coefficient decreases until melting occurs, at which time the lubricant loses its effectiveness.

Stick-slip is often referred to as a relaxation-oscillation phenomenon, and consequently, some degree of elasticity is needed in the sliding contact in order for stick-slip to occur. Israelachvili [54] considered stick-slip on a molecular level, as measured with surface forces apparatus. He considers the order-disorder transformations described by Thompson and Robbins [44], 1991) in terms of simulations. Most classical treatments of stick-slip take a mechanics approach, considering that the behaviour in unlubricated solid sliding is caused by forming and breaking adhesive bonds.

Stick-slip behaviour can be modeled in several ways. Generally, the system is represented schematically as a spring-loaded contact, sometimes including a dashpot element to account for viscoelastic response [55]. The effects of time-dependent material properties on stick-slip behaviour of metals are provided by Kosterin and Kragelski [56] and Kragelski [57]. Bowden and Tabor's analysis [58] considers a free surface of inertial mass  $m$  being driven with a uniform speed  $v$  in the positive  $x$  direction against an elastic constant  $k$ . Then the instantaneous resisting force  $\mathbf{F}$  over distance  $x$  equals  $-kx$ . With no damping of the resultant oscillation,

$$ma = -kx \quad (6.20)$$

where acceleration  $a = (d^2x/dt^2)$ . The frequency  $n$  of simple harmonic motion is given by

$$n = (1/2 \pi)(k/m)^{1/2} \quad (6.21)$$

Under the influence of a load  $\mathbf{P}$  (mass  $\mathbf{W}$  acting downward with the help of gravity  $g$ ), the static friction force  $\mathbf{F}_s$  can be represented as

$$\mathbf{F}_s = \mu_s \mathbf{P} \quad (6.22)$$

In terms of the deflection at the point of slip ( $x$ ),

$$x = \mathbf{F}_s/k \quad (6.23)$$

If the kinetic friction coefficient  $\mu$  is assumed to be constant during slip, then

$$ma - \mu \mathbf{P} = -kx \quad (6.24)$$

Letting time = 0 at the point of slip (where  $x = F_s/k$ ), and the forward velocity  $v \ll$  the velocity of slip, then,

$$x = (\mathbf{P}/k)[(\mu_s - \mu) \cos \omega t + \mu] \quad (6.25)$$

where,  $\omega = (k/m)^{1/2}$ . In this case, the magnitude of slip,  $\delta$ , is



$$\delta = [\mathbf{P}(2\mu_s - 2\mu)/k] \quad (6.26)$$

From this equation, the larger the  $\mu$  relative to  $\mu_s$ , the less the effects of stick-slip, and when they are equal, the sliding becomes completely steady. Kudinov and Tolstoy [59] derived a critical velocity above which stick-slip could be suppressed. This critical velocity  $v_c$  was directly proportional to the difference in the static and kinetic friction coefficients  $\Delta\mu$  and inversely proportional to the square root of the product of the relative dissipation of energy during oscillation ( $\psi = 4\pi\tau$ ), the stiffness of the system  $k$ , and the slider mass  $m$ . Thus,

$$v_c = \Delta\mu N / \sqrt{\psi km} \quad (6.27)$$

where  $N$  is the factor of safety. The authors report several characteristic values of  $\Delta\mu$  for slideways on machine tools: cast iron on cast iron = 0.08, steel on cast iron = 0.05, bronze on cast iron = 0.02, and PTFE on cast iron = 0.04.

System resonance within limited stick-slip oscillation ranges was discussed by Bartenev and Lavrentev [60], who cited experiments in which an oscillating normal load was applied to a system in which stick-slip was occurring. The minimum in stick-slip amplitude and friction force occurred over a range of about 1.5–2.5 kHz, the approximate value predicted by  $(1/2\pi)(k/m)^{-1/2}$ . Rabinowicz [61] suggested two possible solutions:

1. Decrease the slip amplitude or slip velocity by increasing contact stiffness, increasing system damping, or increasing inertia; and
2. Lubricate or otherwise form a surface film to ensure a positive  $\mu$  versus velocity relationship.

The latter solution requires that effective lubrication be maintained, and stick-slip can return if the lubricant becomes depleted. The fact that stick-slip is associated with a significant difference between static and kinetic friction coefficients suggest that strategies that lower the former or raise the latter can be equally effective.

### 6.3.1.2 Sliding Friction

Sliding friction plays a very important role in many manufacturing processes. Sliding friction models, other than empirical models, can generally be grouped into five categories:

1. Ploughing and cutting-based models;
2. Adhesion, junction-growth, and shear models;
3. Single- and multiple-layer shear models;
4. Debris layer and transfer layer models; and
5. Molecular dynamics' models.

Each type of model was developed to explain frictional phenomena. Some of the models are based on observations that contact surfaces contain grooves that are suggestive of a dominant contribution from ploughing. Single-layer models rely on a view of the interface showing flat surfaces separated by a layer whose shear strength controls friction. Some models involve combinations, such as adhesion plus ploughing. Recent friction models contain molecular-level phenomena. Lubrication-oriented models and the debris-based models describe phenomena that take place in zone I, whereas most of the classical models for solid friction concern zone II phenomena. There are few models that take into account the effects of both the interfacial properties and the surrounding mechanical systems such as zone III models.

### Models for Sliding Friction

Sliding friction models are summarized in this section of the chapter and fall into one, or more, of the five categories explained in the previous section.

- (a) **Ploughing Models:** Ploughing models assume that the dominant contribution to friction is the energy required to displace material ahead of a rigid protuberance or protuberances moving along a surface. One of the simplest models for ploughing is that of a rigid cone of slant angle  $\theta$  ploughing through a surface under a normal load  $\mathbf{P}$  [61]. If we assign a groove width  $w$  (i.e., twice the radius  $r$  of the circular section of the penetrating cone at surface level), the triangular projected area,  $A_p$ , swept out as the cone moves along is as follows:

$$A_p = \frac{1}{2}w(r \tan \theta) = \frac{1}{2}(2r)(r \tan \theta) = r^2 \tan \theta \quad (6.28)$$

The friction force  $\mathbf{F}_p$  for this ploughing contribution to sliding is found by multiplying the swept-out area by the compressive strength  $p$ . Thus,  $\mathbf{F}_p = (r^2 \tan \theta)p$ , and the friction coefficient, if this were the only contribution, is  $\mu_p = \mathbf{F}_p/\mathbf{P}$ . From the definition of the compressive strength  $p$  as force per unit area, we can write:

$$p = \mathbf{P}/\pi r^2 \quad (6.29)$$

And

$$\mu_p = \mathbf{F}_p/\mathbf{P} = (r^2 \tan \theta)p/\pi r^2 p = (\tan \theta)/\pi \quad (6.30)$$

This expression can also be written in terms of the apex angle of the cone ( $\alpha = 90^\circ - \theta$ ):

**Table 6.7** Estimates of the maximum ploughing contribution to friction

Metal	Critical rake angle <sup>a</sup> (°)	$\mu_p$
Aluminium	-5	0.03
Nickel	-5	0.03
Lead	-35	0.22
$\alpha$ -Brass	-35	0.22
Copper	-45	0.32

Reprinted with permission from Jackson and Morrell [31]

<sup>a</sup> For a cone, the absolute value of the critical rake angle is 90 minus angle  $\theta$

$$\mu_p = (2 \cot \alpha)/\pi \quad (6.31)$$

Note that the friction coefficient calculated is for the ploughing of a hard asperity and is not necessarily the same as the friction coefficient of the material sliding along the sides of the conical surface. Table 6.7 shows the maximum ploughing contribution to friction for various metals.

- (b) **Adhesion, Junction Growth, and Shear (AJS) Models:** The AJS interpretations of friction are based on a scenario in which two rough surfaces are brought close together, causing the highest peaks (asperities) to touch. As the normal force increases, the contact area increases and the peaks are flattened. Asperity junctions grow until they are able to support the applied load. Adhesive bonds form at the contact points. When a tangential force is applied, the bonds must be broken, and overcoming the shear strength of the bonds results in the friction force. Early calculations comparing bond strengths to friction forces obtained in experiments raised questions as to the general validity of such models. Observations of material transfer and similar phenomena suggested that the adhesive bonds might be stronger than the softer of the two bonded materials, and that the shear strength of the softer material, not the bond strength, should be used in friction models.

Traditional friction models, largely developed for metal-on-metal sliding, have added the force contribution due to the shear of junctions to the contribution from ploughing, giving the extended expression:

$$\mu = (\tau A_r)/\mathbf{P} + (\tan \theta)/\pi \quad (6.32)$$

where  $A_r$  is the real area of contact and  $\tau$  is the shear strength of the material being plowed. This type of expression has met with relatively widespread acceptance in the academic community and is often used as the basis for other sliding friction models. But if the tip of the cone wears down, three contributions to the ploughing process can be identified: the force needed to displace material from in front of the cone, the friction force along the leading face of the cone (i.e., the component in the macroscopic sliding direction), and the friction associated with shear of the interface along the worm frustum of the cone. From this analysis, it is clear that friction

on two scales is involved: the macroscopic friction force for the entire system, and the friction forces associated with the flow of material along the face of the cone and across its frustum. That situation is somewhat analogous to the interpretation of orthogonal cutting of metals in which the friction force of the chip moving up along the rake face of the tool and friction along the wear land are not in general the same as the cutting force for the tool as a whole [62]. Considering the three contributions to the friction of a flat-tipped cone gives

$$\mu = (\tau/\mathbf{P})(\pi r^2) + \mu_i \cos^2\theta + (\tan \theta)/\pi \quad (6.33)$$

where  $r$  is defined as the radius of the top of the worn cone and  $\mu_i$  is the friction coefficient of the cone against the material flowing across its face. Equation 6.33 helps explain why the friction coefficients for ceramics and metals sliding on faceted diamond films are 10 or more times higher than the friction coefficients reported for smooth surfaces of the same materials sliding against smooth surfaces of diamond (i.e.,  $\mu \gg \mu_i$ ). When the rake angle  $\theta$  is small,  $\cos^2 \theta$  is close to 1.0. The second term is only slightly less than  $\mu_i$  (0.02–0.12 typically). If one assumes that the friction coefficient for the material sliding across the frustum of the cone is the same as that for sliding along its face ( $\mu_i$ ), then Eq. 6.33 can be re-written:

$$\mu = 2\mu_i + (\tan \theta)/\pi \quad (6.34)$$

Thus, this implies that the friction coefficient for a rigid sliding cone is more than twice that for sliding a flat surface of the same two materials. It is interesting to note that Eq. 6.34 does not account for the depth of penetration, a factor that seems critical for accounting for the energy required to plow through the surface (displace the volume of material ahead of the slider), and at  $\theta = 90^\circ$ , which implies infinitely deep penetration of the cone, it would be impossible to move the slider at all as  $\mu$  tends toward infinity.

When one of the complexities of surface finish it seems remarkable that Eqs. 6.33 and 6.34, which depend on a single quantity  $[(\tan \theta)/\pi]$ , should be able to predict the friction coefficient with any degree of accuracy. The model is based on a single conical asperity cutting through a surface that makes no obvious accountability for multiple contacts and differences in contact angle. The model is also based on a surface's relatively ductile response to a perfectly rigid asperity and can neither account for fracture during wear nor account for the change in the groove geometry that one would expect for multiple passes over the same surface.

Mulhearn and Samuels [63] published a paper on the transition between abrasive asperities cutting through a surface and ploughing through it. The results of their experiments suggested that there exists a critical rake angle for that type of transition. (Note: The rake angle is the angle between the normal to the surface and the leading face of the asperity, with negative values indicating a tilt toward the direction of travel). If ploughing can occur only up to the critical rake angle, then we may compute the maximum contribution to friction due to ploughing from the data of Mulhearn and Samuels and Eq. 6.31 (Table 6.7). This approach suggests

**Table 6.8** Critical degree of penetration ( $D_p$ ) for unlubricated friction mode transitions

Material	Value of $D_p$ for the transition	
	Ploughing to wedge formation	Wedge formation to cutting
Brass	0.17 (tip radius 62 $\mu\text{m}$ )	0.23 (tip radius 62, 27 $\mu\text{m}$ )
Carbon steel	0.12 (tip radius 62 $\mu\text{m}$ )	0.23 (tip radius 27 $\mu\text{m}$ )
Stainless steel	0.13 (tip radius 62, 27 $\mu\text{m}$ )	0.26 (tip radius 27 $\mu\text{m}$ )

Reprinted with permission from Jackson and Morrell [31]

that the maximum contribution of ploughing to the friction coefficient of aluminium or nickel is about 0.03 in contrast to copper, whose maximum ploughing contribution is 0.32. Since the sliding friction coefficient for aluminium can be quite high (over 1.0 in some cases), the implication is that factors other than ploughing, such as the shearing of strongly adhering junctions, would be the major contributor. Examination of unlubricated sliding wear surfaces of both Al and Cu often reveals a host of ductile-appearing features not in any way resembling cones, and despite the similar appearances in the microscope of worn Cu and Al, one finds from the first and last rows in Table 6.8 that the contribution of ploughing to friction should be different by a factor of 10. Again, the simple cone model appears to be too simple to account for the difference.

Hokkirigawa and Kato [64] carried the analysis of abrasive contributions to sliding friction even further using observations of single hemispherical sliding contacts (quenched steel, tip radius 26 or 62  $\mu\text{m}$ ) on brass, carbon steel, and stainless steel in a scanning electron microscope. They identified three modes: (a) ploughing, (b) wedge formation and (c) cutting (chip formation). The tendency of the slider to produce the various modes was related to the degree of penetration,  $D_p$ . Here,  $D_p = h/a$ , where  $h$  is the groove depth and  $a$  is the radius of the sliding contact. The sliding friction coefficient was modeled in three ways depending upon the regime of sliding. Three parameters were introduced:

$$f = p/\tau \quad \theta = \sin^{-1}(a/R)$$

and  $\beta$ , the angle of the stress discontinuity (shear zone) from Challen and Oxley's [65] analysis. Where  $p$  is the contact pressure,  $\tau$  is the bulk shear stress of the flat specimen, and  $R$  is the slider tip radius. The friction coefficient was given as follows for each mode:

Cutting mode:

$$\mu = \tan \left[ \theta - (\pi/4) + \frac{1}{2} \cos^{-1} f \right] \quad (6.35)$$

Wedge-forming mode:

$$\mu = \frac{\left\{1 - \sin 2\beta + (1 - f^2)^{1/2}\right\} \sin \theta + f \cos \theta}{\left\{1 - \sin 2\beta + (1 - f^2)^{1/2}\right\} \cos \theta + f \sin \theta} \quad (6.36)$$

Ploughing mode:

$$\mu = \frac{A \sin \theta + \cos(\cos^{-1} f - \theta)}{A \sin \theta + \cos(\cos^{-1} f - \theta)} \quad (6.37)$$

where

$$A = 1 + (\pi/2) + \cos^{-1} f - 2\theta - 2 \sin^{-1} \frac{\sin \theta}{(1 - f)^{-1/2}} \quad (6.38)$$

For unlubricated conditions, the transitions between the various modes were experimentally determined by observation in the scanning electron microscope. Table 6.8 summarizes those results. Results of the study illustrate the point that the analytical form of the frictional dependence on the shape of asperities cannot ignore the mode of surface deformation. In summary, the foregoing treatments of the ploughing contribution to friction assumed that asperities could be modeled as regular geometric shapes. However, rarely do such shapes appear on actual sliding surfaces. The asperities present on most sliding surfaces are irregular in shape, as viewed with a scanning electron microscope.

- (c) **Ploughing with Debris Generation:** Even when the predominant contribution to friction is initially from cutting and ploughing of hard asperities through the surface, the generation of wear debris that submerges the asperities can reduce the severity of ploughing. Table 6.9 shows that starting with multiple hard asperities of the same geometric characteristics produced different initial and steady-state friction coefficients for the three slider materials. Wear debris accumulation in the contact region affected the frictional behaviour. In the case of abrasive papers and grinding wheels, this is called loading. Loading is extremely important in grinding, and a great deal of effort has been focused on dressing grinding wheels to improve their material removal efficiency. One measure of the need for grinding wheel dressing is an increase in the tangential grinding force or an increase in the power drawn by the grinding spindle.

As wear progresses, the wear debris accumulates between the asperities and alters the effectiveness of the cutting and ploughing action by covering the active points. If the cone model is to be useful at all for other than pristine surfaces, the effective value of  $\theta$  must be given as a function of time or number of sliding passes. Not only is the wear rate affected, but the presence of debris affects the interfacial shear strength, as is explained later in this chapter in regard to third-body particle

**Table 6.9** Effects of material type on friction during abrasive sliding

Slider material	24 $\mu\text{m}$ grit size		16 $\mu\text{m}$ grit size	
	Starting ( $\mu$ )	Ending ( $\mu$ )	Starting ( $\mu$ )	Ending ( $\mu$ )
AISI 52100 steel	0.47	0.35	0.45	0.29
2014-T4 aluminium	0.69	0.56	0.64	0.62
PMMA	0.73	0.64	0.72	0.60

Reprinted with permission from Jackson and Morrell [31]

<sup>a</sup> Normal force 2.49 N, sliding speed 5 mm/s, multiple strokes 20 mm long

effects on friction. The observation that wear debris can accumulate and so affect friction has led investigators to try patterning surfaces to create pockets where debris can be collected [66]. The orientation and depths of the ridges and grooves in a surface affect the effectiveness of the debris-trapping mechanism.

- (d) **Ploughing with Adhesion:** Traditional models for sliding friction have historically been developed with metallic materials in mind. Classically, the friction force is said to be an additive contribution of adhesive ( $S$ ) and ploughing forces ( $F_{\text{pl}}$ ) [58]:

$$\mathbf{F} = \mathbf{S} + \mathbf{F}_{\text{pl}} \quad (6.39)$$

The adhesive force derives from the shear strength of adhesive metallic junctions that are created when surfaces touch one another under a normal force. Thus, by dividing by the normal force we find that  $\mu = \mu_{\text{adhesion}} + \mu_{\text{ploughing}}$ . If the shear strength of the junction is  $\tau$  and the contact area is  $A$ , then

$$\mathbf{S} = \tau A \quad (6.40)$$

The ploughing force  $F_{\text{pl}}$  is given by

$$\mathbf{F}_{\text{pl}} = pA' \quad (6.41)$$

where  $p$  is the mean pressure to displace the metal in the surface and  $A'$  is the cross section of the grooved wear track. While helpful in understanding the results of experiments in the sliding friction of metals, the approach involves several applicability-limiting assumptions, for example, that adhesion between the surfaces results in bonds that are continually forming and breaking, that the protuberances of the harder of the two contacting surfaces remain perfectly rigid as they plow through the softer counterface, and perhaps most limiting of all, that the friction coefficient for a tribosystem is determined only from the shear strength properties of materials.

- (e) **Single-Layer Shear (SLS) Models:** SLS models for friction depict an interface as a layer whose shear strength determines the friction force, and hence, the friction coefficient. The layer can be a separate film, like a solid lubricant, or simply the near surface zone of the softer material that is shearing during friction. The friction force  $\mathbf{F}$  is the product of the contact area  $A$  and the shear strength of the layer:

$$\mathbf{F} = \tau A \quad (6.42)$$

The concept that the friction force is linearly related to the shear strength of the interfacial material has a number of useful implications, especially as regards the role of thin lubricating layers, including oxides and tarnish films. It is known from the work of Bridgman [67] on the effects of pressure on mechanical properties that  $\tau$  is affected by contact pressure,  $p$ :

$$\tau = \tau_0 + \alpha p \quad (6.43)$$

Table 6.10 lists several values for the shear stress and the constant  $\alpha$  [68].

- (f) **Multiple-Layer Shear (MLS) Models:** SLS models presume that the sliding friction can be explained on the basis of the shear strength on a single layer interposed between solid surfaces. Evidence revealed by the examination of frictional surfaces suggests that shear can occur at various positions in the interface: for example, at the upper interface between the solid and the debris layer, within the entrapped debris or transfer layer itself, at the lower interface, or even below the original surfaces where extended delaminations may occur. Therefore, one may construct a picture of sliding friction that involves a series of shear layers (sliding resistances) in parallel. Certainly, one would expect the predominant frictional contribution to be the lowest shear strength in the shear

**Table 6.10** Measured values for the shear stress dependence on pressure

Material	$\tau_0$ (kgf/mm <sup>2</sup> )	$\alpha$
Aluminium	3.00	0.043
Beryllium	0.45	0.250
Chromium	5.00	0.240
Copper	1.00	0.110
Lead	0.90	0.014
Platinum	9.50	0.100
Silver	6.50	0.090
Tin	1.25	0.012
Vanadium	1.80	0.250
Zinc	8.00	0.020

Reprinted with permission from Jackson and Morrell [31]



layers. Yet the shear forces transmitted across the weakest interface may still be sufficient to permit some displacement to occur at one or more of the other layers above or below it, particularly if the difference in shear strengths between those layers is small.

The MLS models can be treated like electrical resistances in a series. The overall resistance of such a circuit is less than any of the individual resistances because multiple current paths exist. Consider, for example, the case where there are three possible operable shear planes stacked up parallel to the sliding direction in the interface. Then,

$$\frac{1}{\mathbf{F}} = \frac{1}{\mathbf{F}_1} + \frac{1}{\mathbf{F}_2} + \frac{1}{\mathbf{F}_3} \quad (6.44)$$

And, solving for the total friction force  $\mathbf{F}$ , in terms of the friction forces acting on the three layers, is

$$\mathbf{F} = \frac{\mathbf{F}_1 \mathbf{F}_2 \mathbf{F}_3}{\mathbf{F}_1 \mathbf{F}_2 + \mathbf{F}_2 \mathbf{F}_3 + \mathbf{F}_1 \mathbf{F}_3} \quad (6.45)$$

If the area of contact  $A$  is the same across each layer, then Eq. 6.45 can be written in terms of the friction coefficient of the interface, the shear stresses of each layer, and the normal load  $\mathbf{P}$  as follows:

$$\mu = \left( \frac{A}{\mathbf{P}} \right) \left[ \frac{\tau_1 \tau_2 \tau_3}{\tau_1 \tau_2 + \tau_2 \tau_3 + \tau_1 \tau_3} \right] \quad (6.46)$$

If one of the shear planes suddenly became unable to deform (say, by work hardening or by clogging with a compressed clump of wear debris), the location of the governing plane of shear may shift quickly, causing the friction to fluctuate. Thus, by writing the shear stresses of each layer as functions of time, the MLS model has the advantage of being able to account for variations in friction force with time and may account for some of the features observed in microscopic examinations of wear tracks.

- (g) ***Molecular Dynamics' Models***: When coupled with information from nanoprobe instruments, such as the atomic force microscope, the scanning tunneling microscope, the surface-forces apparatus, and the lateral-force microscope, MD studies have made possible insights into the behaviour of pristine surfaces on the atomic scale. Molecular dynamics models of friction for assemblages of even a few hundred atoms tend to require millions upon millions of individual, iterative computations to predict frictional interactions taking place over only a fraction of a second in real time, because they begin with very specific arrangements of atoms, usually in single crystal form with a

specific sliding orientation, results are often periodic with sliding distance. Some of the calculation results are remarkably similar to certain types of behaviour observed in real materials, simulating such phenomena as dislocations (localized slip on preferred planes) and the adhesive transfer of material to the opposing counterface. However, molecular dynamics models are not presently capable of handling such contact surface features as surface fatigue-induced delaminations, wear debris particles compacting and deforming in the interface, high-strain-rate phenomena, work hardening of near-surface layers, and effects of inclusions and other artifacts present in the microstructures of commercial engineering materials.

The models presented up to this point use either interfacial geometric parameters or materials properties (i.e., bonding energies, shear strengths, or other mechanical properties) to predict friction. Clearly, frictional heating and the chemical environment may affect some of the variables used in these models. For example, the shear strength of many metals decreases as the temperature increases and increases as the speed of deformation increases. Certainly, wear and its consequences (debris) will affect friction. Thus, any of the previously described models will probably require some sort of modification, depending on the actual conditions of sliding contact. In general, the following can be said about friction models:

1. No existing friction model explicitly accounts for all the possible factors that can affect friction;
2. Even very simple friction models may work to some degree under well-defined, limited ranges of conditions, but their applicability must be tested in specific cases;
3. Accurately predictive, comprehensive tribosystem-level models that account for interface geometry, materials properties, lubrication aspects, thermal, chemical, and external mechanical system response, all in a time-dependent context, do not exist;
4. Friction models should be selected and used based on an understanding of their limitations and on as complete as possible an understanding of the dominant influences in the tribosystem to which the models will be applied; and
5. Current quantitative models produce a single value for the friction force, or friction coefficient. Since the friction force in nearly all known tribosystems varies to some degree, any model that predicts a single value is questionable.

If no existing model is deemed appropriate, the investigator could either modify a current model to account for the additional variables, develop a new system-specific model, or revert to simulative testing and/or field experiments to obtain the approximate value. An alternative to modeling is to estimate frictional behaviour using a graphical, or statistical approach.

### 6.3.2 Frictional Heating

Heat generation and rising surface temperatures are intuitively associated with friction. When a friction force  $\mathbf{F}$  moves through a distance  $x$ , an amount of energy  $\mathbf{F}x$  is produced. The laws of thermodynamics require that the energy so produced be dissipated to the surroundings. At equilibrium, the energy into a system  $U_{\text{in}}$  equals the sum of the energy output to the surroundings  $U_{\text{out}}$  (dissipated externally) and the energy accumulated  $U_{\text{accumulated}}$  (consumed or stored internally):

$$U_{\text{in}} = U_{\text{out}} + U_{\text{accumulated}} \quad (6.47)$$

The rate of energy input in friction is the product of  $\mathbf{F}$  and the sliding velocity  $v$  whose units work out to energy per unit time (e.g., Nm/s). This energy input rate at the frictional interface is balanced almost completely by heat conduction away from the interface, either into the contacting solids or by radiation or convection to the surroundings. In general, only a small amount of frictional energy, perhaps only 5 %, is consumed or stored in the material as microstructural defects such as dislocations, the energy to produce phase transformations, surface energy of new wear particles and propagating subsurface cracks, etc. Most of the frictional energy is dissipated as heat. Under certain conditions, there is enough heat to melt the sliding interface. Energy that cannot readily be conducted away from the interface raises the temperature locally. Assuming that the proportionality of friction force  $\mathbf{F}$  to normal force  $\mathbf{P}$  (i.e., by definition,  $\mathbf{F} = \mu\mathbf{P}$ ) holds over a range of normal forces, we would expect that the temperature rise in a constant-velocity sliding system should increase linearly with the normal force. Tribologists distinguish between two temperatures, the flash temperature and the mean surface temperature. The former is localized, the latter averaged out over the nominal contact zone. Since sliding surfaces touch at only a few locations at any instant, the energy is concentrated there and the heating is particularly intense—thus, the name flash temperature. The combined effect of many such flashes dissipating their energy in the interface under steady state is to heat a near-surface layer to an average temperature that is determined by the energy transport conditions embodied in Eq. 6.47 given earlier. Blok [69] discussed the concept and calculation of flash temperature in a review article. The early work of Blok [70] and Jaeger [71] is still cited as a basis for more recent work, and it has been reviewed in a simplified form by Bowden and Tabor [58]. Basically, the temperature rise in the interface is given as a function of the total heat developed,  $Q$ :

$$Q = \frac{\mu \mathbf{W} g v}{J} \quad (6.48)$$

where,  $\mu$  is the sliding friction coefficient,  $\mathbf{W}$  is the load,  $g$  the acceleration due to gravity,  $v$  the sliding velocity, and  $J$  the mechanical equivalent of heat (4.186 J/cal). Expressions for various heat flow conditions are then developed based on Eq. 6.48. Some of these are given in Table 6.11.

**Table 6.11** Temperature rise during sliding

Conditions	Temperature rise <sup>a</sup> ( $T = T_o$ )
Circular junction of radius $a$	$= \frac{Q}{4a(k_1+k_2)}$
Square junction of side = $2l$ , at low speed	$= \frac{Q}{4.24l(k_1+k_2)}$
Square junction of side = $2l$ , at high speed wherein the slider is being cooled by the incoming surface of the flat disk specimen	$= \frac{Qx^{1/2}}{3.76l[k_1(l/v)^{1/2}+1.125x^{1/2}k_2]}$
	Where $x = (k_1/\rho_1c_1)$ for the disk material

After Jaeger [71]. Reprinted with permission from Jackson and Morrell [31]

<sup>a</sup>  $T$  = steady-state junction temperature,  $T_o$  = initial temperature,  $k_{1,2}$  = thermal conductivity of the slider and flat bodies,  $\rho$  = density,  $c$  = specific heat

As Table 6.11 shows, the expressions become more complicated when the cooling effects of the incoming, cooler surface are accounted for. Rabinowicz [61] published an expression for estimating the flash temperature rise in sliding:

$$\theta_m = \frac{v}{2} (\pm \text{a factor of 2 to 3}) \quad (6.49)$$

where,  $v$  is sliding velocity (ft/min) and  $\theta_m$  is the estimated surface flash temperature ( $^{\circ}\text{F}$ ). A comparison of the results of using Eq. 6.49 with several other, more complicated models for frictional heating has provided similar results, but more rigorous treatments are sometimes required to account for the variables left out of this rule of thumb. In general, nearly all models for flash or mean temperature rise during sliding contain the friction force-velocity product. Sometimes, the friction force is written as the product of the normal force and friction coefficients.

A review of frictional heating calculations has been provided by Cowan and Winer [72], along with representative materials properties data to be used in those calculations. Their approach involves the use of two heat partition coefficients ( $\gamma_1$  and  $\gamma_2$ ) that describe the relative fractions of the total heat that go into each of the contacting bodies, such that  $\gamma_1 + \gamma_2 = 1$ . The time that a surface is exposed to frictional heating will obviously affect the amount of heat it receives. The Fourier modulus,  $F_o$ , a dimensionless parameter, is introduced to establish whether or not steady-state conditions have been reached at each surface. For a contact radius  $a$ , an exposure time  $t$ , and a thermal diffusivity for body  $i$  of  $D_i$ ,

$$F_o = \frac{D_i t}{a^2} \quad (6.50)$$

The Fourier modulus is taken to be 100 for a surface at steady state conditions. Another useful parameter grouping is the Peclet number  $P_e$ , defined in terms of the density of the solid  $\rho$ , the specific heat  $c_p$ , the sliding velocity  $v$ , the thermal conductivity  $k$ , and the characteristic length  $L_c$ :

$$P_e = \frac{\rho c_p v L_c}{k} \quad (6.51)$$

The characteristic length is the contact width for a line contact or the contact radius for a circular contact. The Peclet number relates the thermal energy removed by the surrounding medium to that conducted away from the region in which frictional energy is being dissipated. As  $D_i = (\rho c_p/k)$  yields the following,

$$P_e = \frac{v L_c}{D_i} \quad (6.52)$$

The Peclet number is sometimes used as a criterion for determining when to apply various forms of frictional heating models. Peclet number is used in understanding frictional heating problems associated with grinding and machining processes. It is important to compare the forms of models derived by different authors for calculating flash temperature rise. Four treatments for a pin moving along a stationary flat specimen are briefly compared: Rabinowicz's derivation based on surface energy considerations, a single case from Cowan and Winer's review, Kuhlmann-Wilsdorf's model, and the model provided by Ashby. Based on considerations of junctions of radius  $r$  and surface energy of the softer material  $\Gamma$ , Rabinowicz arrived at the following expression:

$$T_f = \frac{3000 \pi \mu \Gamma v}{J(k_1 + k_2)} \quad (6.53)$$

where  $J$  is the mechanical equivalent of heat,  $v$  is sliding velocity,  $\mu$  is the friction coefficient, and  $k_1$  and  $k_2$  represent the thermal conductivities of the two bodies. The constant 3,000 obtained from the calculation of the effective contact radius  $r$  in terms of the surface energy of the circular junctions  $\Gamma$  and their hardness  $H$  (i.e.,  $r = 12,000 \Gamma/H$ ) and the load carried by each asperity ( $\mathbf{P} = \pi r^2 H$ ). Thus, the numerator is actually the equivalent of  $\mathbf{F}v$  expressed in terms of the surface energy model. The equation provided by Cowan and Winer, for the case of a circular contact with one body in motion is

$$T_f = \frac{\gamma_1 \mu \mathbf{P} v}{\pi a k_1} \quad (6.54)$$

where  $\gamma_1$  is the heat partition coefficient, described earlier,  $\mathbf{P}$  is the normal force,  $a$  is the radius of contact, and  $k_1$  is as defined earlier. The value of  $\gamma_1$  takes various forms depending on the specific case. The presence of elastic, or plastic contact, can also affect the form of the average flash temperature, as Table 6.12 demonstrates. Here, the exponents of normal force and velocity are not unity in all cases. Kuhlmann-Wilsdorf [73] considered an elliptical contact area as the planar moving heat source. The flash temperature is given in terms of the average temperature in the interface  $T_{ave}$ :

**Table 6.12** Effects of deformation type and Peclet number on flash temperature calculation for the circular contact case

Type of deformation	Peclet number	Average flash temperature <sup>a</sup>
Plastic	$P_e < 0.02$	$T_f = \mu \mathbf{P}^{0.5} v \frac{\sqrt{\pi \rho}}{8k}$
Plastic	$P_e > 200$	$T_f = 0.31 \mu \mathbf{P}^{0.25} v^{0.5} \left[ \frac{(\pi \rho)^{0.75}}{(k \rho c)^{0.5}} \right]$
Elastic	$P_e < 0.02$	$T_f = 0.13 \mu \mathbf{P}^{0.667} v \left( \frac{1}{k} \right) \left( \frac{E_v}{R} \right)^{0.333}$
Elastic	$P_e > 200$	$T_f = 0.36 \mu \mathbf{P}^{0.5} v^{0.5} \left( \frac{1}{\sqrt{k \rho c}} \right) \left( \frac{E_v}{R} \right)^{0.5}$

Reprinted with permission from Jackson and Morrell [31]

<sup>a</sup> Key  $\mu$  = friction coefficient,  $\mathbf{P}$  = load,  $v$  = velocity,  $k$  = thermal conductivity,  $\pi$  = density,  $c$  = heat capacity,  $E_v$  = the reduced elastic modulus =  $E/(1 - \nu^2)$ ,  $\nu$  = Poisson's ratio,  $\rho$  = flow pressure of the softer material

$$T_{\text{ave}} = \frac{\pi q r}{4k_1} \quad (6.55)$$

where  $q$  is the rate of heat input per unit area (related to the product of friction force and velocity),  $r$  is the contact spot radius, and  $k_1$  is the thermal conductivity, as given earlier. Then

$$T_f = \frac{T_{\text{ave}}}{(1/ZS) + (k_1/S_0)} \quad (6.56)$$

where  $Z$  is a velocity function and  $S$  and  $S_0$  are contact area shape functions (both = 1.0 for circular contact). At low speeds, where the relative velocity of the surfaces  $v_r < 2(v_r = v/\mathbf{P}_e)$ ,  $Z$  can be approximated by  $1/[1 + (v_r/3)]$ . The differences between models for frictional heating arise from the following:

1. Assuming different shapes for the heat source on the surface;
2. Different ways to partition the flow (dissipation) of heat between sliding bodies;
3. Different ways to account for thermal properties of materials (e.g., using thermal diffusivity instead of thermal conductivity, etc.);
4. Different contact geometry (sphere-on-plane, flat-on-flat, cylinder-on-flat, etc.);
5. Assuming heat is produced from a layer (volume) instead of a planar area; and
6. Changes in the form of the expression as the sliding velocity increases.

Comparing the temperature rises predicted by different models for low sliding speeds produces accurate results, even with the uncertainties in the values of the material properties that go into the calculations. At higher speeds, the predictions become unreliable since materials properties change as a function of temperature and the likelihood of the interface reaching a steady state is much lower. Experimental studies have provided very useful information in validating the forms of frictional heating models. Experimental scientists have often used embedded thermocouples in one or both members of the sliding contact to measure surface

temperatures, and others sometimes made thermocouples out of the contacts themselves. However, techniques using infrared sensors have been used as well. Dow and Stockwell [74] used infrared detectors with a thin, transparent sapphire blade sliding on a 15-cm-diameter ground cylindrical drum to study the movements and temperatures of hot spots. Griffioen et al. [75] and Quinn and Winer [76] used an infrared technique with a sphere-on-transparent sapphire disk geometry. A similar arrangement was also developed and used by Furey with copper, iron, and silver spheres sliding on sapphire, and Enthoven et al. [77] used an infrared system with a ball-on-flat arrangement to study the relationship between scuffing and the critical temperature for its onset.

Frictional heating is important because it changes the shear strengths of the materials in the sliding contact, promotes reactions of the sliding surfaces with chemical species in the environment, enhances diffusion of species, and can result in the breakdown or failure of the lubricant to perform its functions. Under extreme conditions, such as plastic extrusion, frictional heating can result in molten layer formation that serves as a liquid lubricant.

### ***6.3.3 Lubrication to Control Friction in Machining***

The frictional characteristics of liquid and solid lubricants and their interaction with materials are reviewed. Comprehensive discussions of the mechanical and chemical engineering aspects of lubrication are available in the literature [78]. The following section was originally published by Jackson and Morrell [31] and appears hereafter.

#### **6.3.3.1 Liquid Lubrication**

The process of lubrication is one of supporting the contact pressure between opposing surfaces, helping to separate them, and at the same time reducing the sliding or rolling resistance in the interface. There are several ways to accomplish this. One way is to create in the gap between the bodies geometric conditions that produce a fluid pressure sufficient to prevent the opposing asperities from touching while still permitting shear to be fully accommodated within the fluid. That method relies on fluid mechanics and modifications of the lubricant chemistry to tailor the liquid's properties. Another way to create favorable lubrication conditions is to formulate the liquid lubricant in such a way that chemical species within it react with the surface of the bodies to form shearable solid films. Surface species need not react with the lubricant, but catalyze the reactions that produce these protective films.

Several attributes of liquids make them either suitable or unsuitable as lubricants. Klaus and Tewksbury [79] have discussed these characteristics in some detail. They include:

1. Density;
2. Bulk modulus;
3. Gas solubility;
4. Foaming and air entrainment tendencies;
5. Viscosity and its relationships to temperature and pressure;
6. Vapour pressure;
7. Thermal properties and stability; and
8. Oxidation stability.

The viscosity of fluids usually decreases with temperature and therefore can reduce the usefulness of a lubricant as temperature rises. The term viscosity index, abbreviated VI, is a means to express this variation. The higher the VI, the less the change in viscosity with temperature. One of the types of additives used to reduce the sensitivity of lubricant viscosity to temperature changes is called a VI improver. ASTM test method D 2270 is one procedure used to calculate the VI. The process is described step-by-step in the article by Klaus and Tewksbury [79]. The method involves references to two test oils, the use of two different methods of calculation (depending on the magnitude of VI), and relies on charts and tables.

ASTM Standard D341 recommends using the Walther equation to represent the dependence of lubricant viscosity on temperature. Defining  $Z$  as the viscosity in cSt plus a constant (typically ranging from 0.6 to 0.8 with ASTM specifying 0.7),  $T$  equal to the temperature in Kelvin or Rankin, and  $A$  and  $B$  being constants for a given oil, then

$$\log_{10}(\log_{10} Z) = A + B(\log_{10} T) \quad (6.57)$$

Sanchez-Rubio et al. [80] have suggested an alternative method in which the Walther equation is used. In this case, they define a viscosity number (VN) as follows:

$$\text{VN} = \left[ 1 + \frac{(3.55 + B)}{3.55} \right] \times 100 \quad (6.58)$$

The value of 3.55 was selected because lubricating oils with a VI of 100 have a value of  $B$  about equal to  $-3.55$ . Using this expression implies that  $\text{VN} = 200$  would correspond to an idealized oil whose viscosity has no dependence of viscosity on temperature (i.e.,  $B = 0$ ). The pressure to which oil is subjected can influence its viscosity. The relationship between dynamic viscosity and hydrostatic pressure  $p$  can be represented by

$$\eta = \eta_0 \exp(\alpha p) \quad (6.59)$$

where  $\eta$  and  $\alpha$  vary with the type of oil. Table 6.13 illustrates the wide range of viscosities possible for several liquid lubricants under various temperatures and pressures. The viscosity indices for these oils range from  $-132$  to  $195$ . Viscosity



**Table 6.13** Effects of temperature and pressure on viscosity of selected lubricants having various viscosity indexes (All fluids have viscosities of 20 cSt at 40 °C and 0.1 MPa pressure)

Quantity	Fluorolube	Hydrocarbon	Ester	Silicone
Viscosity index	-132	100	151	195
Viscosity (cSt) at -40 °C	500,000	14,000	3600	150
Viscosity (cSt) at -100 °C	2.9	3.9	4.4	9.5
Viscosity (cSt) at -40 °C and 138 MPa	2700	340	110	160
Viscosity (cSt) at -40 °C and 552 MPa	>1,000,000	270,000	4900	48,000

Reprinted with permission from Jackson and Morrell [31]

has a large effect on determining the regime of lubrication and the resultant friction coefficient. Similarly to the effect of strain rate on the shear strength of certain metals, like aluminium, the rate of shear in the fluid can also alter the viscosity of a lubricant.

Ramesh and Clifton [81] constructed a plate impact device to study the shear strength of lubricants at strain rates as high as 900,000/s and found significant effects of shear rate on the critical shear stress of lubricants. In a Newtonian fluid, the ratio of shear stress to shear strain does not vary with stress, but there are other cases, such as for greases and solid dispersions in liquids, where the viscosity varies with the rate of shear. Such fluids are termed non-Newtonian and the standard methods for measuring viscosity cannot be used.

Lubrication regimes determine the effectiveness of fluid film formation, and hence, surface separation. In the first decade of the twentieth century, Stribeck developed a systematic method to understand and depict regimes of journal bearing lubrication, linking the properties of lubricant viscosity ( $\eta$ ), rotational velocity of a journal ( $\omega$ ), and contact pressure ( $p$ ) with the coefficient of friction. Based on the work of Mersey, McKee, and others, the dimension-less group of parameters has evolved into the more recent notation ( $ZN/p$ ), where  $Z$  is viscosity,  $N$  is rotational speed, and  $p$  is pressure. The Stribeck curve has been widely used in the design of bearings and to explain various types of behaviour in the field of lubrication. At high pressures, or when the lubricant viscosity and/or speed are very low, surfaces may touch, leading to high friction. In that case, friction coefficients are typically in the range of 0.5–2.0. The level plateau at the left of the curve represents the boundary lubrication regime in which friction is lower than for unlubricated sliding contact ( $\mu = 0.05$  to about 0.15). The drop-off in friction is called the mixed film regime. The mixed regime refers to a combination of boundary lubrication with hydrodynamic or elastohydrodynamic lubrication. Beyond the minimum in the curve, hydrodynamic and elastohydrodynamic lubrication regimes are said to occur. Friction coefficients under such conditions can be very low. Typical friction coefficients for various types of rolling element bearings range between 0.001 and 0.0018.

The conditions under which a journal bearing of length  $L$ , diameter  $D$ , and radial clearance  $C$  (bore radius minus bearing shaft radius) operates in the hydrodynamic regime can be summarized using a dimensionless parameter known as the Sommerfeld number  $S$ , defined by

$$S = \frac{\eta NLD}{P} \left(\frac{R}{C}\right)^2 \quad (6.60)$$

where  $P$  is the load on the bearing perpendicular to the axis of rotation,  $N$  is the rotational speed,  $\eta$  is the dynamic viscosity of the lubricant, and  $R$  is the radius of the bore. The more concentrically the bearing operates, the higher the value of  $S$ , but as  $S$  approaches 0, the lubrication may fail, leading to high friction. Sometimes Stribeck curves are plotted using  $S$  instead of  $(ZN/p)$  as the abscissa. Raimondi [82] added leakage considerations when they developed design charts in which the logarithm of the Sommerfeld number is plotted against the logarithm of either the friction coefficient or the dimensionless film thickness.

Using small journal bearings, McKee developed the following expression for the coefficient of friction  $\mu$  based on the journal diameter  $D$ , the diametral clearance  $C$ , and an experimental variable  $k$ , which varies with the length to diameter ratio ( $L/D$ ) of the bearing [83]:

$$\mu = (4.73 \times 10^{-8}) \left(\frac{ZN}{P}\right) \left(\frac{D}{C}\right) + k \quad (6.61)$$

The value of  $k$  is about 0.015 at  $(L/D) = 0.2$ , drops rapidly to a minimum of about 0.0013 at  $(L/D) = 1.0$ , and rises nearly linearly to about 0.0035 at  $(L/D) = 3.0$ . A simpler expression, discussed by Hutchings [84], can be used for bearings that have no significant eccentricity:

$$\mu = \frac{2\pi h}{S R} \quad (6.62)$$

where  $S$  is the Sommerfeld number,  $h$  is the mean film thickness, and  $R$  is the journal radius. With good hydrodynamic lubrication and good bearing design,  $\mu$  can be as low as 0.001.

Hydrodynamic lubrication, sometimes called thick-film lubrication, generally depends on the development of a converging wedge of lubricant in the inlet of the interface. This wedge generates a pressure profile to force the surfaces apart. When the elastic deformation of the solid bodies is similar in extent to the thickness of the lubricant film, then elastohydrodynamic lubrication is said to occur. This latter regime is common in rolling element bearings and gears where high Hertz contact stresses occur. If the contact pressure exceeds the elastic limit of the surfaces, plastic deformation and increasing friction occur. One way to understand and control the various lubrication regimes is by using the specific film thickness (also

called the lambda ratio), defined as the ratio of the minimum film thickness in the interface ( $h$ ) to the composite root-mean-square (rms) surface roughness  $\sigma^*$ :

$$\Lambda = h/\sigma^* \quad (6.63)$$

where the composite surface roughness is defined in terms of the rms roughness ( $\sigma_{1,2}$ ) of surfaces 1 and 2, respectively:

$$\sigma^* = \sqrt{(\sigma_1^2 + \sigma_2^2)} \quad (6.64)$$

For the boundary regime,  $\Lambda \ll 1$ . For the mixed regime  $1 < \Lambda < 3$ . For the hydrodynamic regime,  $\Lambda \gg 6$ , and for the elasto-hydrodynamic regime,  $3 < \Lambda < 10$ . Boundary lubrication produces friction coefficients that are lower than those for unlubricated sliding but higher than those for effective hydrodynamic lubrication, typically in the range  $0.05 < \mu < 0.2$ . Briscoe and Stolarski [85] have reviewed friction under boundary-lubricated conditions. They cited the earlier work of Bowden, which gave the following expression for the friction coefficient under conditions of boundary lubrication:

$$\mu = \beta\mu_a + (1 - \beta)\mu_1 \quad (6.65)$$

where the adhesive component  $\mu_a$  and the viscous component of friction  $\mu_1$  are given in terms of the shear stress of the adhesive junctions in the solid (metal)  $\tau_m$  and the shear strength of the boundary film  $\tau_1$  under the influence of a contact pressure  $\sigma_p$ :

$$\mu_a = \frac{\tau_m}{\sigma_p} \quad (6.66)$$

The parameter,  $\beta$ , is called the fractional film defect [85] and is:

$$\beta = 1 - \exp \left\{ - \left[ \frac{(300.9 \times 10^5) T_m^{1/2}}{VM^{1/2}} \right] \exp \left( - \frac{E_c}{RT} \right) \right\} \quad (6.67)$$

where  $M$  is the molecular weight of the lubricant,  $V$  is the sliding velocity,  $T_m$  is the melting temperature of the lubricant,  $E_c$  is the energy to desorb the lubricant molecules,  $R$  is the universal gas constant, and  $T$  is the absolute temperature. Various graphical methods have been developed to help select boundary lubricants and to help simplify the task of bearing designers. These methods are based on the design parameters of bearing stress (or normal load) and velocity. One method, developed by Glaeser and Dufrane [86] involves the use of design charts for different bearing materials. An alternate but similar approach was used in developing the so-called IRG transitions diagrams (subsequently abbreviated ITDs), an approach that evolved in the early 1980s, was applied to various bearing steels, and

is still being used to define the conditions under which boundary-lubricated tribosystems operate effectively. Instead of pressure, load is plotted on the ordinate. Three regions of ITDs are defined in terms of their frictional behaviour: Region I, in which the friction trace is relatively low and smooth, Region II, in which the friction trace begins with a high level then settles down to a lower, smoother level, and Region III, in which the friction trace is irregular and remains high. The transitions between Regions I and II or between Regions I and III are described as a collapse of liquid film lubrication. The locations of these transition boundaries for steels were seen to depend more on the surface roughness of the materials and the composition of the lubricants and less on microstructure and composition of the alloys. Any of the following testing geometries can be used to develop ITDs: four-ball machines, ball-on-cylinder machines, crossed-cylinders machines, and flat-on-flat testing machines (including flat-ended pin-on-disk). One important aspect of the use of liquid lubricants is how they are applied, filtered, circulated, and replenished. Lubricants can also be formed on surfaces by the chemical reaction of vapour-phase precursor species in argon and nitrogen environments”.

#### **6.4 Analysis of Gaps in the Literature and Their Relationship to Grinding Process Interactions**

This section allows the reader to identify and understand the gaps in the research literature that pertains to the application of tribological theories to the area of grinding practice. The section explains where the gaps are in the science of grinding by interpreting the results shown and explained in Sects. 6.2 and 6.3 of this chapter. The first part of the gap analysis focuses on models associated with chip formation, while the second part focuses on tribological interactions associated with ploughing and sliding.

Interaction models associated with chip formation in machining were reviewed and the following observations made:

1. Models associated with understanding the mechanics of cutting with single point tools are very well documented and are reviewed by [87–92]. The common assumptions associated with these models include: orthogonal cutting is dominant, a shear plane exists, the shear plane angle takes a value such that the work done is a minimum, the shear strength along the shear plane is constant, continuous chip formation is apparent, the behaviour of the material is independent of the rate of deformation, the effects of temperature are negligible, and the material properties do not change during deformation. However, depending on the size of the undeformed chip, these models may not be applicable due to the ‘size effect’ that is prevalent in grinding processes (the size effect is stated as the increase in specific cutting energy (energy required to remove a unit volume of work material) owing to an increase in energy associated with ploughing and sliding (non-chip making interactions) as the uncut

chip thickness decreases for a cutting tool of finite edge sharpness). Therefore, further studies will be required to test the validity of these models. Models explained in this chapter may be applicable as they account for the size effect in grinding. In this context, models can be classed as blends of physical, mathematical, and computational solutions;

2. Chemical models appear to be absent from the classical models. The effect of grain, workpiece and bond chemistry should be considered significant especially when one considers the significance of the size effect on chip formation;
3. Effects of shear strain rates and shear strains on the 'size effect' in grinding have not been thoroughly investigated. Such studies could yield insights into optimizing kinematics conditions, and developing new products that exploit the effects of very high shear strains on chip formation, i.e. grains that fracture with rake angles designed to induce very thin and long chips that can be captured by large pores that accommodate them;
4. Reducing the magnitude of shear stress as a function of chip size is a technical challenge that does not appear to have been addressed in the form of any models. This may be the domain of tribochemistry where mechanical-chemical models need to be developed in order to understand how to design improved products and modify the grinding process. The gaps in the literature exist owing to the lack of scientific understanding of the 'size effect'. Gaps may be filled by combining machining and material structure models with tribochemical effects;
5. Treatment of the 'size effect' in machining literature certainly shows that there is a lack of models describing how surface treatments or the effects of adsorbed chemical species might affect the activation of slip planes in the shear zone. There are no reported models that describe how these complex reactions affect chip forming at the microscopic scale. Indeed, there are no models describing the effect of shear stresses and compressive stresses on the size of the shear plane with regard to chemical effects. Again, tribochemical models are lacking in these areas;
6. The effects of very large plastic strains on chip formation and ramifications for abrasive product design and grinding system performance are not very well understood. This is unfortunate since the plastic strain at fracture is heavily influenced by compressive stresses set up in the shear zone. Models shown in the literature appear to be limited to shear strains in the range of 1–8 (In grinding, shear strains range from 4 to 20);
7. Traditionally, the amount of specific energy as a function of undeformed chip thickness is well understood. However, according to Kececioğlu [93], the specific energy is better described by considering it as a function of shear plane area because it is a function of: (i) the mean normal stress on the shear plane; (ii) the shear volume of the shear zone; (iii) The strain rate in the shear zone; (iv) the temperature of the shear plane; and (v) the degree of strain hardening before cutting. Clearly, models will need to be developed in this area to understand chip formation in grinding;

8. Zhang and Bagchi [94] propose the use of a void nucleation model in understanding the ‘size effect’ in chip formation. However, there are no models that describe how to prevent the re-welding of microcracks in such thin shear zones. Again, filling a gap in the application of suitable tribochemical models may yield benefits in the design of products when considering the role of surface treatments or chemisorbed species on products during chip formation;
9. It is noted that inhomogeneous microstrains may prevent chip formation at extremely low undeformed chip thickness levels. The challenge here is to promote homogeneous microstrains to aid chip formation. Models need to be developed in this regard to understand how to create chips and how they aid product design;
10. There is no mention of the Rebinder effect in any discussion on chip formation, and certainly no models to describe it (The Rebinder effect is the improvement of surface properties of a material caused by a reduction in surface energy). This area of modeling should be linked to tribochemical effects and how it relates to enhancing grinding system performance and product design; and
11. A paper by Duwell and McDonald of the 3 M Company published in Duwell and MacDonal [95] appears to have recognized the complexity of grinding process interactions (mechanical, chemical, thermal). The authors decided to take an empirical approach to abrasive product evaluation in grinding since the late 1950s. Later papers appear to confirm this approach and are shown in the reference section [96–103].

Interaction models associated with grit ploughing and sliding were reviewed and the following observations made:

1. Ploughing and sliding models have been reviewed and appear to be well understood for very simple tribological interactions and should be applied to simple grinding situations to test their validity. However, models are required for more complex situations such as grinding where the following information is required: (i) the true area of contact; (ii) the number of instantaneous contacting points; (iii) the arrangement of contacts with the nominal area of contact; (iv) and the time required to create new points of contact. It may be possible to use simple models that incorporate limitations imposed by certain grinding conditions that may be classified as ‘special cases’. However, more complex models may enhance the ability to develop better abrasive products;
2. Thermoelastic behaviour is shown to be responsible for sliding interactions, but models that describe complex situations associated with stick-slip and static contacts are less common. The role of contaminant films are critical in reducing or increasing the coefficient of friction and models are required to describe the role of adhesive bonding and reducing surface energy. There appears to be little modeling conducted related to chip and bond interactions, especially in abrasive machining where sliding speeds are much higher than tribological testing conditions;
3. Sliding friction models that account for the effect of debris generation at high speeds especially for the purpose of chip making (chips clearing from the

grinding zone) are not available. This is an area that may be particularly fruitful for abrasive product design, such as the design of pore networks that capture certain forms of chips, or the formation of grooves on abrasive grains to maintain a pathway for chips to enter pore networks. Surface treatments may aid in chip gelling, which may be useful although not investigated. Few models are available to test these conditions;

4. Temperature models for sliding are well developed and may be used to calculate heat at the interfaces between workpiece, chip, abrasive grain and bond. The temperatures generated and the flow of heat may be controlled by the shape of the grains and may lead to the design of products where a particular shape of grain of known conductivity/diffusivity can be used to form a composite wheel designed to take heat away from the contact zone. These models do not appear to account for heat flow associated with ploughing;
5. In addition to sliding models and their applicability to improving the chip formation process in grinding, there are a lack of models that describe tribochemical effects and the type of lubrication required for a particular chip-forming situation (solid, liquid or gaseous lubrication); and
6. Tribochemistry is a very important aspect of lubrication as well as unlubricated grinding conditions. One of the most comprehensive treatments of tribochemistry is the text by Heinicke [104]. Heinicke identifies a number of sub-topics of tribochemistry, including tribodiffusion, tribosorption, tribodesorption, triboreactions, tribooxidation, tribocatalysis, etc. Tribochemistry is a very challenging discipline, since multiple chemical processes can be occurring simultaneously in lubricated tribosystems and models that describe these complex situations are lacking. Adapting existing sliding and ploughing models or developing new sliding and ploughing models may further enhance how chip and bond interactions can be manipulated to improve the performance of existing abrasive products and/or develop new products and develop new applications.

Interaction models associated with other frictional interactions (chip/bond, chip/work, bond/work) were reviewed and the following observations made:

1. There appears to be a lack of models that describe chip-bond interactions, chip-workpiece interactions and bond-workpiece interactions in the open literature especially when operating at speeds associated with grinding; and
2. Tribological models of sliding for systems such as glass-on-metal, metal-on-metal, polymer-on-metal and other material sliding systems could be adapted to describe slow-speed interactions in areas such as lapping, honing and polishing. However, there is a need to understand these interactions at intermediate and high speeds in order to apply them to higher speed grinding processes. Adapting existing sliding and ploughing models to operate at higher speeds or developing new sliding and ploughing models may further enhance how chip and bond interactions can be manipulated to improve the performance of existing abrasive products and/or develop new products and develop new applications. In this respect, further studies are required to identify tribological models that could effectively describe chip and bond interactions;

On further inspection of the various cutting and sliding models, no account is taken of the following interactions and are identified as gaps in the model (the following are not fundamental process interactions, but are consequences of process interactions, such as that between the grit and the workpiece): (1) initiation modes of abrasive grain failure—could be due to small amount of attritious wear, poor thermal shock resistance, chemical reactions with bond and workpiece, coolant reactions, eutectic reactions, chemical wear of grain, low fracture toughness of grain, cracks induced in abrasive microstructure; (2) completion modes of abrasive grain failure—could be due to grain pull-out, poor thermal shock resistance, reactions with chemistry of coolant/workpiece; (3) initiation modes of abrasive grain and bond failure—could be due to bond material subjected to too high tangential and normal forces, heat transfer through grain to bond determined by grinding power intensity and thermal energy partitions, grain-bond interfacial activity, bond-workpiece friction initiated by grain wear, large scale fracture of grains; (4) completion modes of abrasive grain and bond failure—could be due to grain release from bond, grain composite (collection of grains) released from the bond also known as ‘wheel surface collapse’, bond fracture due to erosion or corrosion of bond, fractures in the bond due to heat treatment; and (5) initiation modes of failure initiated through the bond—could be due to poor bond and grain adhesion, thermal expansion mismatch between bond and grain, poor thermal shock resistant bonds, microcracking in bonds, crack propagation from grain to bonding phase. It is suggested that existing models should be augmented by additional models to quantify interaction processes in the grinding zone. It is predicted that doing so would yield a better understanding of abrasive product performance, on an application-by-application basis.

## 6.5 Summary of Research Recommendations

In summary, the following recommendations are made:

1. Models describing chip formation and models that explain tribological interactions at grinding length scales should be validated and compared to traditional cutting and sliding models. As an example, an initial study could be performed to compare known force and shear plane models developed for single point cutting tools with positive rake angles to that of abrasive grains that predominantly have negative, zero, and positive rake angles. This could be achieved by using a single grain platform by measuring forces and visualizing in-process and post-process shear plane angles to compare and contrast predicted and actual forces, shear plane angles, friction coefficients, and other useful information that characterize the grinding process in terms of frictional interactions along rake, clearance and shear faces/planes. Models that can be compared with experimental data have been developed by research workers such as Ernst and Merchant, Merchant, Stabler, Lee and Shaffer, and Hucks;



It should be noted that further studies be conducted to investigate the applicability of using finite element models to describe specific grinding applications;

2. Shear strain and strain rate models that encompass size effects should be developed. As an example, models could be developed that relate strain and strain rates in terms of the nature of the lamellar spacing from a microstructural viewpoint rather than lamellar spacing alone. Experimental procedures need to be developed that prove or refute the existence of the size effect in terms of identifying the dynamic interactions between workpiece materials, abrasive grains and bonding systems;
3. Size effect dominated chip formation models should be developed that account for tribochemical and microstructural effects, thereby extending physical models of crack formation in materials developed by Argon et al. [105] and Anderson [106];
4. Very large plastic strain models should be developed to explain chip formation by microfracture;
5. The effects of surface treatment should be modeled as a way to describe chip formation due to the size effect, where the size effect is explicitly described as a function of geometry of the cutting tool, its geometry relative to the depth of cut, and the microstructural condition of the workpiece material, i.e., mapping the relationship between geometrical and microstructural features and ease or difficulty in forming a chip thereby extending the work of Argon et al. [105] and Anderson [106];
6. Ploughing and sliding models should be extended to describe complex tribological conditions such as abrasive machining. Models developed by Challen and Oxley and Samuels on ploughing should be adopted and compared with experimental grinding conditions;
7. Sliding friction models should be developed that account for debris generation, chip-workpiece contact and bond-workpiece interactions;
8. Tribochemical models should be developed that predict the performance of lubricants and coolants during grinding processes. Thermal models should be used to control the flow of heat in the contact zone. Thermal models exist for single and multi-point tools and grinding wheels, but do not appear to be used in the course of product development by relating thermal conditions with dynamic material conditions of the abrasive;
9. Gaps identified in cutting and sliding models include: initiation and completion modes of abrasive grain failure; initiation and completion modes of abrasive grain and bond failure; and initiation and completion of modes of failure that act through the bonding system, and models that explain wheel surface collapse. These models can be further developed to include interactions involving multiple contact points between abrasive grains, bonds, chips, workpiece material, and fluids;
10. Models that provide connectivity between microscopic interactions and macroscopic interactions should be developed. In addition to this, models that relate models at different length scales to grinding performance measures should also

be developed. Techno-economic models also need to be developed, i.e. linking cost per component models with micro and macroscopic interaction models would be most useful to product design and selection;

11. Specific models that describe the microscopic interactions should be identified from the literature and applied in the laboratory and compared with observations using a variety of test platforms;
12. Model development should be prioritized by focusing on models that have been developed for micromachining (considering size effects) and applied to grinding conditions. Thereafter, models should be developed that explain the role of bond and chip interactions and how these interactions affect product design and grinding process understanding. Are there size effects associated with these interactions? If so, they should be developed with a view to developing products that exploits that knowledge; and
13. Gap analysis studies should be extended to continue to identify applicable models published in the academic literature and potential models described in patents and sales literature provided by manufacturers of abrasives and abrasive products.

The conclusions drawn from this study show that further work is needed to connect ‘size effect’ models to grinding models in order to understand grinding system dynamics and to develop products based on size effect cutting, ploughing, and sliding interactions. The identified gaps in existing models are associated with initiation and failure of the bonding system and abrasive grains and their interaction with workpiece materials and chips. Gaps in the models should be filled by identifying mechanisms and potential models that adequately describe the observed gaps. This chapter identifies areas of tribology that may contribute to sliding interactions and it is stated that further work is required to review and apply applicable fretting, corrosion, erosion, fatigue, creep, stress corrosion models and other applicable models that describe sliding interactions between abrasive grain, workpiece, bonding systems, and chips.

In conclusion, it is stated that the gap analysis should be completed and that the newly developed models of those identified gaps be proven, or refuted, through rigorous experimentation, initially by understanding the effects of grit geometry and sharpness on chip formation. Further identification of gaps in the area of grinding science could be achieved by building an experimental apparatus that visualizes the process interactions together with enhanced measurement techniques so that thermo-mechanical interactions for specific grain-work systems can be explored.

**Acknowledgments** The author acknowledges with thanks the permission to reproduce a selection of figures and tables of data published by Woodhead Publishing, Cambridge, UK. The figures and tables of data were used from the publication: M. J. Jackson and J. S. Morrell, ‘Tribology in Manufacturing’, Chapter 5, pp 161–242, published in Jackson and Morrell [31]. *ISBN 0 85709 114 X and ISBN-13: 978 0 85709 114 7*. The author of this work also thanks Springer publishers for permission to reproduce and adapt Sects. 6.2 and 6.3 from the work entitled, “Tribology of Machining”, (*Published under Springer license number: 3412871241727, June 20, 2014*) published in, “Tribology in Manufacturing Technology”, Edited by J. P. Davim, pp. 67–02, Heidelberg, Germany, 2012. *ISBN 978-3-642-31682-1*.

## References

1. Backer WR, Marshall ER, Shaw MC (1952) *Trans ASME* 74:61
2. Shaw MC (1952) *J Franklin Inst* 254:109
3. Heidenreich RO, Shockley W (1948) Report on strength of solids. *Phys Soc Lond* 57
4. Ernst HJ, Merchant ME (1941) *Trans Am Soc Met* 29:299
5. Merchant ME (1945) *J Appl Phys* 16:318–324
6. Piispanen V (1937) *Teknillinen Aikakaushetki (Finland)* 27:315
7. Merchant ME (1950) *Machining theory and practice*. *Am Soc Met* 9:5–44
8. Barrett CS (1943) *Structure of Met*. McGraw Hill Co, New York, p 295
9. Bridgman PW (1952) *Studies in large plastic flow and fracture*. McGraw Hill Co, New York
10. Langford G, Cohen M (1969) *Trans ASM* 62:623
11. Piispanen V (1948) *J Appl Phys* 19:876
12. Blazynski, TZ, Cole JM (1960) *Proc Instn Mech Eng* 1(74):757
13. Shaw MC (1950) *J Appl Phys* 21:599
14. Walker TJ (1967) PhD Dissertation, Carnegie-Mellon University, PA
15. Walker TJ, Shaw MC (1969) *Advances in machine tool design and research*. Pergamon Press, Oxford, pp 241–252
16. Usui E, Gujral A, Shaw MC (1960) *Int J Mach Tools Res* 1:187–197
17. Vyas A, Shaw MC (1999) *Trans ASME-J Mech Sci* 21(1):63–72
18. Eugene F (1952) *Ann CIRP* 52(11):13–17
19. Shaw MC (1980) *Int J Mech Sci* 22:673–686
20. Kwon KB, Cho DW, Lee SJ, Chu CN (1999) *Ann CIRP* 47(1):43–46
21. Eyring H, Ree T, Harai N (1958) *Proc Nat Acad Sci* 44:683
22. Eyring H, Ree T (1961) *Proc Nat Acad Sci* 47:526–537
23. Eyring H, Jhon MS (1969) *Significant theory of liquids*. Wiley, New York
24. Doyle ED, Horne JG, Tabor D (1979) Frictional interactions between chip and rake face in continuous chip formation. *Proc R Soc Lond A* 366:173–187
25. Horne JG, Doyle ED, Tabor D (1978) Direct observation of the contact and lubrication at the chip-tool interface. In: *Proceedings of the first international conference on lubrication challenges in metalworking and processing*. IIT Research Institute, Chicago, USA, June 1978, pp 1–6
26. Madhavan V (1993) School of industrial engineering. MS thesis, Purdue University, West Lafayette, Indiana
27. Ackroyd B (1999) School of industrial engineering. PhD thesis, Purdue University, West Lafayette, Indiana
28. Robinson GM (2007) *Mixed scale machining with nanostructured coated cutting tools*. PhD thesis, Purdue University, West Lafayette, Indiana
29. Hwang J (2005) School of industrial engineering. PhD thesis, Purdue University, West Lafayette, Indiana
30. Lee S (2006) School of industrial engineering. PhD thesis, Purdue University, West Lafayette, Indiana
31. Jackson MJ, Morrell JS (2011) Tribology in manufacturing, Chap. 5. In: Davim J (ed) *Tribology for engineers: a practical guide*. Wood Head Publishing, Cambridge, UK, pp 161–242
32. Young WC (1989) *Roark's formulas for stress and strain*, 6th edn. McGraw-Hill, New York
33. Greenwood JA, Williamson JBP (1966) Contact of nominally flat surfaces. *Proc R Soc Lond A* 295:300–319
34. Whitehouse DJ, Archard JF (1970) The properties of random surfaces of significance in their contact. *Proc R Soc Lond A* 316:97–121
35. Hirst W, Hollander AE (1974) *Proc R Soc Lond A* 233:379
36. McCool J (1986) Comparison of models for the contact of rough surfaces. *Wear* 107:37–60

37. Greenwood JA (1992) Problems with surface roughness. In: Singer IL, Pollock HM (eds) *Fundamentals of friction: macroscopic and microscopic processes*. Kluwer, Dordrecht, pp 57–76
38. Song JF, Vorburger TV (1992) Surface texture. In: *Friction, lubrication, and wear technology*, ASM handbook, vol 18, 10th edn. ASM International, Materials Park, pp 334–345
39. Burton RA (1980) Thermal deformation in frictionally-heated systems. Elsevier, Lausanne, p 290
40. Ferrante J, Bozzolo GH, Finley CW, Banerjea A (1988) Interfacial adhesion: theory and experiment. In: Mattox DM, Baglin JEE, Gottschall RJ, Batich CD (eds) *Adhesion in Solids*. Materials research society, Pittsburgh, pp 3–16
41. Buckley DF (1981) Surface effects in adhesion, friction, wear, and lubrication. Elsevier, New York, pp 245–313
42. McClelland GM, Mate CM, Erlandsson R, Chiang S (1988) Direct observation of friction at the atomic scale. In: Mattox DM, Baglin JEE, Gottschall RJ, Batich CD (eds) *Adhesion in solids*. Materials Research Society, Pittsburgh, pp 81–86
43. McClelland GM, Mate CM, Erlandsson R, Chiang S (1987) *Phys Rev Lett* 59:1942
44. Thompson PA, Robbins MO (1990) Origin of stick-slip motion in boundary lubrication. *Science* 250:792–794
45. Robbins MO, Thompson PA, Grest GS (1993) Simulations of nanometer-thick lubricating films. *Mater Res Soc Bull* XVIII(5):45–49
46. Landman U, Luetke WD, Burnham NA, Colton RJ (1990) Atomistic mechanisms and dynamics of adhesion, nanoindentation, and fracture. *Science* 248:454–461
47. Belak J, Stowers JF (1992) The indentation and scraping of a metal surface: a molecular dynamics study. In: Pollock HM, Singer IL (eds) *Fundamentals of friction: macroscopic and microscopic processes*. Kluwer, Dordrecht, pp 511–520
48. Pollock HM, Singer IL eds (1992) *Fundamentals of friction: macroscopic and microscopic processes*. Kluwer, Dordrecht, p 621
49. Wheeler DR (1975) The effect of adsorbed chlorine and oxygen on the shear strength of iron and copper junctions, NASA TN D-7894
50. Akhmatov AS (1939) Some items in the investigation of the external friction of solids, Trudy Stankina. In: Kragelski IV (ed) (1965) *Friction and wear*, Butterworths, London, p 159
51. Sikorski ME (1964) The adhesion of metals and factors that influence it. In: Bryant PJ, Lavik L, Salomon G (eds) *Mechanisms of solid friction*. Elsevier, Amsterdam, pp 144–162
52. Rabinowicz E (1992) Friction coefficients of noble metals over a range of loads. *Wear* 159:89–94
53. Campbell WE (1940) Remarks printed in proceedings of M.I.T. conference on friction and surface finish. MIT Press, Cambridge, p 197
54. Israelachvili JN (1992) Adhesion, friction, and lubrication of molecularly smooth surfaces. In: Pollock HM, Singer IL (eds) *Fundamentals of friction: macroscopic and microscopic processes*. Kluwer, Dordrecht, pp 351–381
55. Moore DF (1975) *Principles and applications of tribology*. Pergamon Press, Oxford, p 152
56. Kosterin JI, Kraghelski IV (1962) Rheological phenomena in dry friction. *Wear* 5:190–197
57. Kragelski IV (1965) *Friction and wear*. Butterworths, London, p 200
58. Bowden FP, Tabor D (1986) *The friction and lubrication of solids*. Clarendon Press, Oxford
59. Kudinov VA, Tolstoy DM (1986) Friction and oscillations. In: Kragelski IV (ed) *Tribology handbook*. Mir, Moscow, p 122
60. Bartenev GM, Lavrentev VV (1981) *Friction and Wear of Polymers*. Elsevier, New York, pp 53–61
61. Rabinowicz E (1965) *Friction and wear of materials*. Wiley, New York, p 69, 89, 99–102
62. Black PH (1961) *Theory of metal cutting*. McGraw-Hill, New York, pp 45–72 (Chap. 5)
63. Mulhearn TO, Samuels LE (1962) *Wear* 5:478
64. Hokkirigawa K, Kato K (1988) An experimental and theoretical investigation of ploughing, cutting and wedge formation during abrasive wear. *Tribol Int* 21(1):51–57

65. Challen JM, Oxley PLB (1979) An explanation of the different regimes of friction and wear using asperity deformation models. *Wear* 53:229–243
66. Suh NP (1986) *Tribophysics*. Prentice-Hall, Englewood Cliffs, pp 416–424
67. Bridgman PW (1931) *The physics of high pressure*. Macmillan Press, New York
68. Kragelskii IV, Dobychin MN, Kombatov VS (1982) *Friction and wear calculation methods*. Pergamon Press, Oxford, pp 178–180
69. Blok H (1963) The flash temperature concept. *Wear* 6:483–494
70. Blok H (1937) General discussion on lubrication. *Inst Mech Eng* 2:222
71. Jaeger JC (1942) *J Proc R Soc N South Wales* 76:203
72. Cowan RS, Winer WO (1992) Frictional heating calculations. In: *Friction, lubrication, and wear technology*, ASM handbook, vol 18, 10th edn. ASM International, Materials Park, pp 39–44
73. Kuhlmann-Wilsdorf D (1987) Demystifying flash temperatures I. Analytical expressions based on a simple model. *Mater Sci Eng* 93:107–117
74. Dow TA, Stockwell RD (1977) Experimental verification of thermoelastic instabilities in sliding contact. *J Lubr Technol* 99(3):359
75. Griffioen JA, Bair S, Winer WO (1985) Infrared surface temperature in a sliding ceramic-ceramic contact. In: Dowson D et al (eds) *Mechanisms of surface distress*. Butterworths, London, pp 238–245
76. Quinn TFJ, Winer WO (1987) An experimental study of the ‘hot spots’ occurring during the oxidational wear of tool steel on sapphire. *J Tribol* 109(2):315–320
77. Enthoven JC, Cann PM, Spikes HA (1993) Temperature and scuffing. *Tribol Trans* 36 (2):258–266
78. Wills JG (1980) *Lubrication fundamentals*. Marcel Dekker, New York
79. Klaus EE, Tewksbury EJ (1984) Liquid lubricants. In: Booser ER (ed) *The handbook of lubrication (Theory and practice of tribology)*, vol II. CRC Press, Boca Raton, pp 229–254
80. Sanchez-Rubio M, Heredia-Veloz A, Puig JE, Gonzalez-Lozano S (1992) A better viscosity-temperature relationship for petroleum products. *Lubr Eng* 48(10):821–826
81. Ramesh KT, Clifton RJ (1987) A pressure-shear plate impact experiment for studying the rheology of lubricants at high pressures and high shear rates. *J. Tribol.* 109:215–222
82. Raimondi AA (1968) Analysis and design of sliding bearings, Chap. 5 in *standard handbook of lubrication engineering*. McGraw-Hill, New York
83. Hall AS, Holowenko AR, Laughlin HG (1961) *Lubrication and bearing design*, in *Machine design*, Schaum’s outline series. McGraw-Hill, New York, p 279
84. Hutchings IM (1992) *Tribology—friction and wear of engineering materials*. CRC Press, Boca Raton, p 65
85. Briscoe BJ, Stolarski TA (1993) Friction, Chap. 3 in *characterization of tribological materials*. In: Glaeser WA. Butterworth Heinemann, Boston, pp 48–51
86. Glaeser WA, Dufrane KF (1978) New design methods for boundary lubricated sleeve bearings. *Machine Design*, April 6, pp 207–213
87. Zorev NN (1966) *Metal Cutting Mechanics*. Pergamon Press, Oxford, England
88. Komanduri R (1993) NSF Report on US Contributions to Machining and Grinding Research in the 20th Century, Oklahoma, USA
89. Trent E, Wright P (2000) *Metal Cutting*, 4th edn. Butterworth Heinemann, New York
90. Shaw MC (2005) *Metal cutting principles*, 2nd edn, Oxford University Press, New York
91. Astakov V (2006) *Tribology of metal cutting*, Elsevier, New York
92. Atkins A (2009) *The science and engineering of cutting*, Butterworth Heineman, New York
93. Kececioglu D (1960) *Trans. ASME-J. Eng for Industry*, 82, 79–86
94. Zhang B, Bagchi A (1994) *Trans. ASME- J. of Eng for Industry*, 116, 289
95. Duwell EJ, McDonald WJ (1961) Some factors that affect the resistance of abrasive grits to wear. *J Wear* 4:371–383
96. Duwell EJ (1990) Ceramic Aluminium Oxide—a new abrasive grit for coated and bonded abrasive tooling, SME paper MS90-304. In: *International manufacturing technology conference*. Chicago, Illinois

97. Duwell EJ, McDonald WJ (1971) Performance and evaluation of coated abrasives in heavy duty grinding operations, SME paper MR . In: International grinding conference. Dearborn, Michigan, pp 71–412
98. Duwell EJ, Cosmano R, Abrahamson G (1984) Dynamics of grinding with coated abrasives, SME paper MR84-546. In: International grinding conference, August 1984. Fontana, Wisconsin
99. Duwell EJ, Gagliardi JJ (1990) Belt grinding with ceramic oxide aluminium oxide, SME paper MR90-543. In: International grinding conference, October 1990. Dearborn, Michigan
100. Gagliardi JJ, Duwell EJ (1989) Coated abrasives made with abrasive grit clusters for constant performance surface finishing, SME Paper MR89-139. In: Deburring and surface conditioning conference, February 1989, San Diego, California
101. Hong IS, Duwell EJ (1975) Centerless grinding with coated abrasive belts, SME paper MR 75-616. In: International grinding conference. Dearborn, Michigan
102. Yoon SC Laramie HA (1990) Use of sintered ceramic oxides in vitrified bonded wheels, SME paper EM90-360. In: International manufacturing technology conference. Chicago, Illinois
103. Heinicke G (1984) Tribochemistry. Carl Hanser Verlag, Munich, p 446
104. Bhushan B, Gupta BK (1991) Handbook of Tribology. McGraw-Hill, New York pp 5–11, pp 5–12
105. Argon AS, Im J, Safoglu R, 1975, Metallurgical transactions, 6A, 825
106. Anderson TL (1991) Fracture mechanics, CRC Press, Florida

# Chapter 7

## Flexible Integration of Shape and Functional Modelling of Machine Tool Spindles in a Design/Optimisation Framework

G.-C. Vosniakos, A. Krimpenis and P. Benardos

**Abstract** In this work a streamlined design process of a machining centre spindle assembly is advocated in a flexible, yet standardised manner. This enables automatic construction of a structured 3D mesh, following a consistent numbering scheme of mesh regions so as to automate load application (bearings reactions and machining force) in parametrically variable spindle models. In this way, numerical analysis of any desired range of candidate design variants can be performed. Two groups of parameters are considered in spindle modelling: design and functional. Important design parameters are: number of bearings, bearings span and spindle diameters. A Design of Experiments (DoE) orthogonal array is a good way to discover favourable combinations of design parameter values as well as their relative importance through modal analysis without exhausting all possible combinations. Important functional parameters are: rotation speed and machining force pattern. Their effect is explored by transient dynamic analysis for targeted loading scenarios studying deflection at points of interest such as tool tip, bearings interface, coupling interface etc. Illustrative examples are given concerning 18 variants of a typical machining centre spindle.

---

G.-C. Vosniakos (✉)

School of Mechanical Engineering, National Technical University of Athens, Athens, Greece  
e-mail: vosniak@central.ntua.gr

A. Krimpenis

Department of Mechanical Engineering, School of Technological Applications,  
Technical Education Institute of Central Greece, Lamia, Greece

P. Benardos

Department of Mechanical, Materials and Manufacturing Engineering,  
University of Nottingham, Nottingham, UK

© Springer-Verlag Berlin Heidelberg 2015

J.P. Davim (ed.), *Traditional Machining Processes*,

Materials Forming, Machining and Tribology, DOI 10.1007/978-3-662-45088-8\_7

## 7.1 Introduction

In CNC machining practice the main consideration is high quality part production at reasonably low cost. Machined part quality is usually synonymous to very low values of surface roughness. It has been shown [1, 2] that this can be achieved by smooth cutting forces that generally excite on the CNC machine tool assembly mild vibrations especially at the cutting region. However, all machines with moving or rotating parts suffer from vibrations that are identified either as forced or as self-excited and that are strongly connected to machine tool design. In this light, it is desirable that the machine designed modal frequencies lie as far as possible from the functional frequencies associated with the machining process.

Various approaches are adopted for studying the dynamic behaviour of CNC machines and spindles. The most popular is the use of finite element analysis (FEA) method in order to develop models that calculate deformations, temperature distribution in the spindle assembly and determine the frequency response function (FRF) at the tool tip. The development of analytical models that focus on design choices and their impact on dynamics is also widely spread in literature; most notable factors include the types of bearings, their positions and preloading as well as the effects of different rotational speeds, especially in the case of high speed machining. Experimental investigations are also common involving modal analysis, mechanical excitation and subsequent displacement measurement in order to determine individual dynamic characteristics and the FRF as such. Finally, there have been attempts to develop methodologies and systems that employ combinations of the above in order to aid the overall design of machine tools and/or spindles through a unified environment. The most recent of these developments are presented in Sect. 7.2.

In this work, parametric design of a machining centre spindle assembly (spindle, bearings, tool holder and cutting tool) is advocated in a flexible, yet standardised manner, so as to enable automatic construction of a 3D mesh that is key to performing numerical analysis of any candidate design. Such flexibility in the design-analysis cycle enables various optimisation procedures, starting from Taguchi-based evaluation of a finite set of representative alternative spindles and reaching ultimately automation of the evaluation cycle, for instance in an evolutionary algorithm. Geometric modelling of the spindle is presented in Sect. 7.3. This approach may be used not only in classic design of spindles but also in reconfiguring spindles according to their application on a particular machine tool. Any spindle design is evaluated as a FEA model. Its construction is discussed in Sect. 7.4. First modal analysis reveals a number of modal frequencies, their type (bending, torsional etc.) as well as their values and span characterising quality of the design. This exercise is run for all variants of interest as discussed in Sect. 7.5. Applying transient analysis for a variety of loading scenarios gives an insight into the functional response of the spindle, as outlined in Sect. 7.6, but is computationally heavy. An overall framework for spindle performance assessment at the design stage is given in Sect. 7.7 as a practical conclusion of the parametric modelling approach advocated.



## 7.2 State-of-the-Art

In [3] Abele et al. present a complete review of the current state-of-the-art in machine tool spindle design, modelling and ongoing research. Topics covered include spindle mechanical and thermal modelling, design of various bearing types and interfaces, drive concepts as well as future trends especially considering sensor integration and mechatronic concepts such as active balancing, preload control and tool deflection compensation.

Results of Finite Element Analysis (FEA) implementation strongly depend on the accuracy of spindle assembly modeling, so that it represents the assembly's actual functional behavior. Besides, modeling friction at the contact surfaces of the bearings and the spindle is crucial, since it affects assembly temperature and, thus, spindle dimensions, machine tool stiffness and machining tolerances.

Cao and Altintas [4] propose an approach based on a detailed Finite Element Model (FEM) of the spindle assembly that includes spindle, tool holder, angular contact ball bearings and their fixing on both the spindle and the casing. The model predicts bearing stiffness, assembly modes, FRF, static and dynamic deviations along the tool axis, bearing loads and contact forces in simulation environment before the actual manufacturing and testing of the spindle assembly. Validation of the model through experiments has shown that bearing pre-load increases bearing stiffness, which in turn leads to higher natural frequencies for the system and drives stability lobes to frequency areas of higher spindle speeds. However, higher bearing pre-loads also lead to less damping. Thus, dynamic stiffness at the tool tip is smaller and self-excited vibrations manifest themselves for smaller depth of cut. Hence, pre-loading does not necessarily improve the situation recorded by stability lobes; it just improves static stiffness and may decrease self-excited vibrations.

An optimization methodology was proposed that achieves maximum depth of cut or best dynamic stiffness [5]. This was achieved by regulating spindle modes so that no self-excited vibrations exist, while finding optimal positioning of bearings and necessary motor properties.

A methodology based on reduced order models is developed by Law et al. [6] in order to decrease the computational load while evaluating the dynamic performance of a machine tool in respect to various relative positions of spindle nose and table within the machine work volume. The aim is to identify the components that can cause stability problems and chatter and subsequently modify their design in order to maximise machine tool productivity.

Coupled thermo-mechanical FEA of high speed spindles taking into consideration the bearings, shaft and housing is presented in [7]. Validation of the model is done by comparison with other published results and a study of a typical spindle system for various rotational speeds is also performed. Another approach that takes into account the variation of spindle dynamics for high rotational speeds is given in [8]. The proposed model takes into account the gyroscopic moment and centrifugal forces on both the spindle shaft and bearings in order to calculate the frequency response function (FRF) at the tool tip. It is shown that the former can increase

cross FRFs but not the direct FRFs while the latter reduces overall stiffness as speed increases. Similar conclusions were also obtained by Rantatalo et al. [9] after analysing lateral vibrations of a milling machine spindle through magnetic excitation and conductive displacement measurements. Their model was validated through comparison with FEA.

Ertürk et al. [10] developed an analytical model that measures the effect of lathe spindle design (spindle diameter and length, bearing stiffness and positioning) and functional parameters (tool and holder type, tool length and holding torque) on the dynamic behavior of the tooltip and the stability of the assembly as far as self-excited vibrations are concerned. Tool point FRF analysis proves that increasing spindle diameter displaces elastic mode frequencies towards positive values and increases elasticity. It was also observed that a larger tool holder diameter leads to modes of the spindle in smaller frequency areas, while tool modes are affected in amplitude, not in frequency.

In [11] a milling machine model was created that predicts the limits of parameter values—spindle speed and depth of cut—at which no self-excited vibrations appear. Although stability lobes of the model accurately fitted the experimental results, the model is more conservative than the actual experiments; predicted frequencies of self-excited vibrations deviate only about 3 % relatively to the experimentally measured frequencies.

Chang et al. [12] positioned sensors at the spindle casing in order to conduct experiments that correlate spindle displacement and machined part surface roughness. Parameters taken into account were spindle speed, feedrate and radial depth of cut. Ultimately, a simplified function that correlates part roughness to spindle displacement was obtained by linear interpolation.

Brecher et al. [13] present an experimental investigation of several bearing designs highlighting their effect on achieving high spindle rotational speeds. Among the examined parameters are bearing geometry, type of rollers and tribological characteristics during operation (i.e. lubrication). Specific modifications to existing bearing types are suggested to improve their performance.

A strategy based on fuzzy logic, FRF determination at the spindle's tool tip and sequential quadratic programming (SQP) forms an expert design system that leads to automatic generation of spindle configuration [14]. In essence, transmission and lubrication type are selected through seven fuzzy logic rules based on cutting condition data and past experience, while location of the bearings is optimised through SQP by iteratively determining the FRF for different combinations of cutting tools and depths of cut.

A spindle design system is presented by Lin and Tu [15] as a systematic way of optimizing its natural frequencies. The multiple stage approach involves identification of design parameters, subsequent sensitivity analysis based on FEA and optimization based on Maximum Improvement First rule. Out of the eight identified parameters the most influential were the distance between the bearings, distance between the bearings axis and tool tip and length of spindle shaft.

Since the deformation mechanism of CNC machine tools is complicated it may not be practical to express analytically thermal error models. Temperatures can be

quite high in high-speed CNC machine tools, for which spindle load is dynamic and non-linear and depends on the rotating speed. Most modeling methods are based on finding a correlation between thermal errors and temperature at specific points on the machine tool. Chen and Hsu [16] propose various models that accurately predict thermal errors—multi-parametric interpolation, Artificial Neural Networks, Fuzzy Logic, etc.—concerning spindle dimensional deviations owing to temperature change. Centrifugal forces and thermal expansion of the bearings and the rotor change the thermal characteristics of the motor, the bearings and the housings.

### 7.3 Parametric Shape Modelling Principles

Parts and assemblies to be used in FEA can be modelled either within the FEA software as such or in a generic, preferably parametric, CAD modeller. However, since the main focus of FEA software is not the detailed part and assembly modelling, the respective user interface may render this a lengthy and resource consuming process.

Design principles in FEA software, e.g. ANSYS, include the creation of points (keypoints), lines or curves, areas and volumes in a sequential bottom-up manner. This can be achieved through the graphics environment, through data insertion in appropriate forms or through issuing specific commands. An alternative top-down approach can also be performed using area (rectangular, circular, polygonal etc.) or volume (blocks, cylindrical, prisms etc.) primitives and Boolean operations (union, subtraction and intersection). Additionally, more complex solid objects can be created taking advantage of extrude and sweep operations.

Despite the available modelling tools and methods, FEA software usually lacks key elements that are readily available in modern CAD modellers such as parametric design, feature based design etc. However, when FEA is employed in order to optimize part geometry or assembly configuration, increased detail is needed and a lot of design variants may be evaluated. Therefore, it is suggested that the FEA environment should be used in the following modelling use cases:

- Parts that can easily be produced from 2D area primitives
- Non-complex 2.5D/3D parts
- Single part evaluation (no need to investigate variations)
- Editing of parts created by external CAD modellers to repair import errors, e.g. using de-featuring, detail removal etc.

The 3D part or assembly can alternatively be created using a dedicated CAD modeller, exploiting its specialized features and capabilities, and then imported in the FEA software. However, this approach is frequently hindered by the fact that errors (gaps, sliver faces, very acute angles etc.) are likely to occur after the import of complex 3D geometry in the FEA software. These errors either result in poor meshing or prevent meshing altogether [17]. The geometry has to be repaired within the FEA software, which is typically a very time consuming process.

In this work, a two-step approach is adopted that results in a parametric (flexible) shape modelling procedure for machine tool spindles, which can produce an error-free, high quality 3D mesh suitable for FEA and evaluation. In the first step, a 2D drawing of the spindle assembly profile is parametrically designed in a dedicated CAD modeller (Solidworks™ in this case). In the second step, this 2D geometry is imported by the FEA software (ANSYS™ in this case) as an IGES file and is subsequently revolved around its axis of symmetry in order to create the final solid model.

In this way, two important advantages are obtained: firstly, it is possible to easily modify the spindle assembly geometry to account for any desired variation of its features without the need to start over each time. Secondly, the probability of errors occurring in the final 3D model and the resulting mesh is minimized since these are created inside the FEA software using its own tools.

### 7.3.1 Selection of Design Parameters

Design of a sample spindle assembly is based on the model introduced in [4]. The spindle assembly consists of the main spindle, the cutting tool and the collet chuck. The respective 2D drawing can be seen in Fig. 7.1. Only half of the profile is presented taking into consideration axial symmetry. The final solid 3D model can be obtained using the “sweep” function.

In order to produce a desired number of configurations out of all possible permutations, specific design parameters are selected that influence the overall spindle assembly geometry. These parameters refer to geometric characteristics of the spindle assembly as well as to its mounting on the machine tool body.

Note that the geometric model of the spindle assembly does not have a constant outer diameter, thus the first selected design parameter is the outer spindle diameter at the areas where the bearings are located. Parametric design of the assembly allows for the outer diameter in the remaining sections of the spindle to be automatically modified in order to maintain the scaling of the initial model. The partitioning of the initial model for this operation and the bearings locations are shown in Fig. 7.2. Similarly, the inner spindle assembly diameter is set to vary so that the ratio of inner to outer diameter of the original model is kept constant for each of the above sections separately.

Design parameters influence both static and dynamic behaviour of the spindle, the former due to a change in the total mass of the assembly and the latter due to a change in the distribution of the total mass.

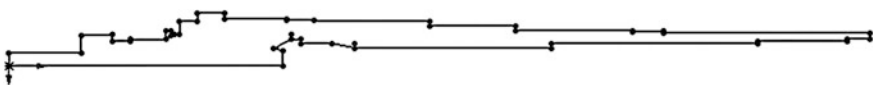


Fig. 7.1 The 2D drawing of the spindle



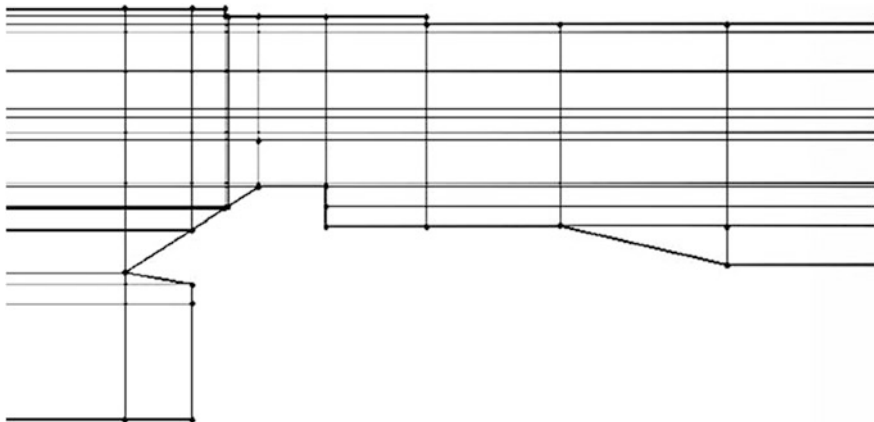
**Fig. 7.2** Initial spindle assembly model partitioning and bearing location

Following the same line of thought the second design parameter involves the total number of bearings used since this changes the type of assembly support on the machine tool body, thus affecting the boundary conditions applicable in FEA.

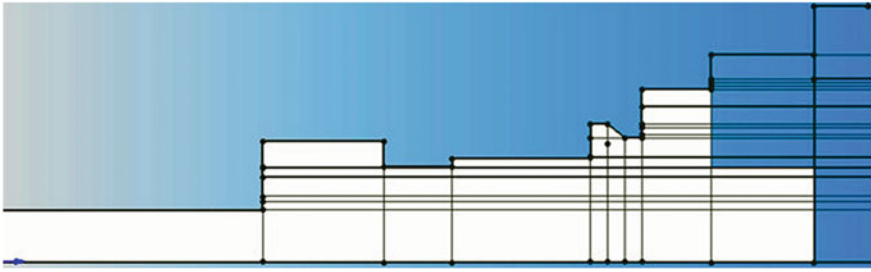
Finally, for a given total length of the assembly and a given distance between location A and the cutting tool tip the distance between the bearings' locations A and B is considered as a design parameter.

Normally, the final step in the CAD modeller would be to produce the actual 3D spindle assembly model and then export it to the FEA environment. Nevertheless, to overcome the pertinent problems mentioned previously a different approach is adopted in this work, namely defining planar surfaces inside the spindle assembly, which when imported by the FEA environment and revolved around the axis of symmetry will result in well-defined volumes.

These surfaces can be defined through a series of projection and contour lines (vertical and horizontal) originating at specific points located on the assembly's boundary. The required points are those that correspond to changes in distance from the axis of symmetry, see Fig. 7.3. The intersections of these lines form rectangular regions inside the assembly's boundary that are used to easily define the required surfaces.



**Fig. 7.3** Horizontal and vertical (auxiliary) lines originating at the spindle assembly's boundary points



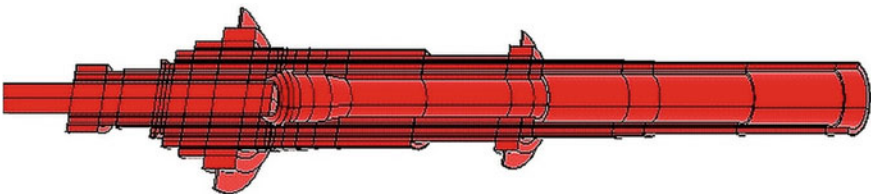
**Fig. 7.4** Area creation in sequential manner

It should be noted that these areas should be created in a uniform sequential manner rather than randomly. The numbering scheme that was implemented dictated starting from bottom to top (i.e. from the tool tip towards the top of the spindle assembly) and from the axis of revolution towards the assembly's outer diameter (Fig. 7.4). This intermediate 'mesh' is exported into the FEA environment as a neutral format file, in this case an IGES file.

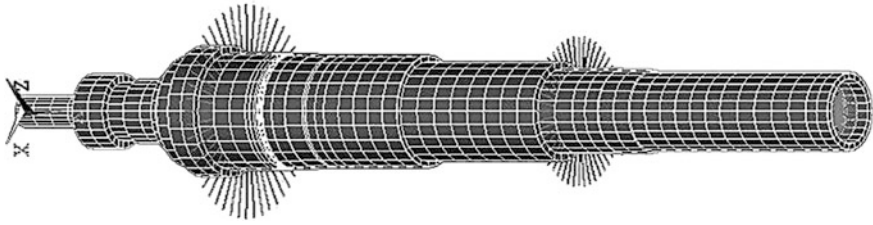
### ***7.3.2 Solid Modelling of Spindle Assembly in FEA Software***

After importing the file to the FEM software, the planar surfaces are identified as 'areas' and each is allocated a unique number that corresponds to the order in which that specific surface was created in the CAD modeller.

By revolving the imported geometry around the axis of symmetry, the final solid model of the spindle assembly is created (see Fig. 7.5). It should be noted that each of the volumes that are created is also numbered in a unique way. The order in which these numbers are allocated to each volume corresponds to the order that each area is numbered. This numbering scheme is particularly important because it enables fast identification and accurate application of boundary conditions at any desired model section.



**Fig. 7.5** Cross-section of the 3D solid model of the spindle assembly



**Fig. 7.6** A 3D aspect of the meshed spindle in ANSYS

## 7.4 Functional Modelling and Analysis Principles

Figure 7.6 presents an aspect of the 3D spindle model in ANSYS, including the solid mesh. All dimensions are parametrically defined, so that changes in total spindle length and/or in diameters where bearings are positioned automatically lead to new spindle drawings.

### 7.4.1 Material Models

The spindle and the bearings are made of steel, each of different type and properties. Material behaviour is considered isotropic. The material of the spindle is AISI 4000 steel (Material1), whilst bearing material is 100Cr6 steel (Material2) see Table 7.1.

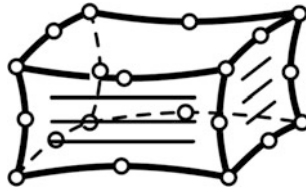
Especially for Material2, Friction Coefficient and Emissivity must also be defined. The latter are automatically defined by the software when the contact areas between spindle and bearings are defined.

### 7.4.2 Choice of Finite Element and Mesh Types

There is a great variety of Finite Element types, which can be used depending on the type of analysis. For structural analysis, there is a number of both planar and

**Table 7.1** Material properties

Material property	Spindle	Bearings
Density (g/cm <sup>3</sup> )	7.85	7.8
Expansion coefficient (10 <sup>-6</sup> /K)	12.7	11.5
Young modulus (GPa)	205	210
Poisson ratio	0.29	0.3
Hardness vickers (HV10)	300	700
Thermal conductivity (W/mK)	44.3	40–45



**Fig. 7.7** The utilised finite element type (SOLID186)

solid finite elements in ANSYS, out of which SOLID186 was chosen for this study, see Fig. 7.7. This is three-dimensional, comprising of 20 nodes per element and behaving as a tetrahedral displacement element. In each of the 20 nodes three degrees of freedom (DoF) can be applied corresponding to the displacement along X, Y and Z axes. The elements also support plastic and hyperelastic behaviour, creeping, large form deviations and large deformations. FE types for contact areas must be defined, too.

Owing to the axial symmetry of the assembly but not so regarding loading conditions a structured mesh can be applied, see Fig. 7.6. After experimentation with element size element side length of 20 mm seemed sufficient for the analysis.

Note that in this example total spindle length nears 1,000 mm and the resulting mesh contains about 18,000 elements thus enabling FEA at a reasonable computational cost.

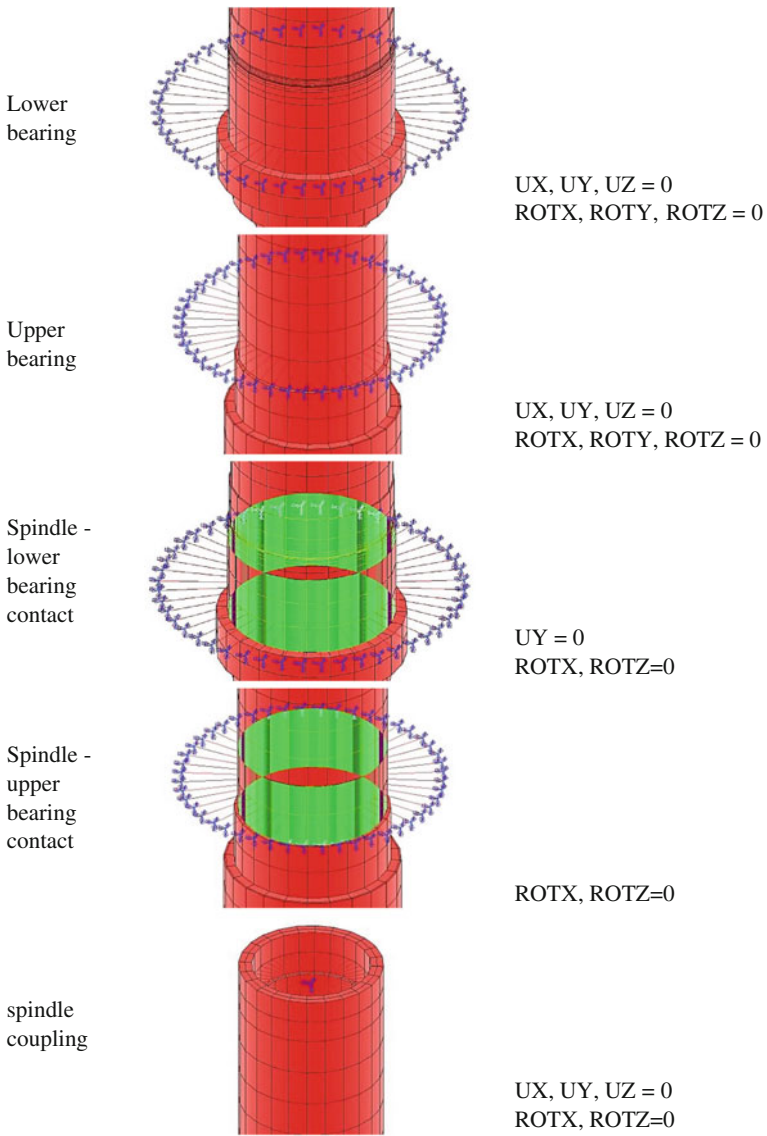
### 7.4.3 Loads

#### 7.4.3.1 Degrees of Freedom (DoF)

In structural analysis, the involved DoFs are the displacement in the three main axes (UX, UY and UZ) and the rotation around the three main axes (ROTX, ROTY and ROTZ). Thus, at each node of the assembly DoFs are positioned so as to reflect movement and deformation of the nodes during loading. DoFs can indirectly define the assembly's fixed points; hence, specific values for the DoFs on nodes and surfaces are given where needed. Specifically, DoFs of fixed points are of zero displacement and zero rotation, see Fig. 7.8. The DoF values of the rest nodes are calculated in the analysis.

Inner rings of the bearing are considered to have a tight fit to the spindle, so there is no need to define DoFs in the contact area between spindle and bearing. In the upper part of the assembly, as seen in Fig. 7.8, the coupling between the spindle and the motor of the machine tool is rigid, thus displacement DoF are set to zero and so are rotational DoF about X and Z axes. In order to ensure that the outer rings can





**Fig. 7.8** Boundary conditions (DoF values) in various regions of the assembly

partially absorb loads, apart from the external surface that is fixed, DoFs of the rest outer ring surfaces are only allowed displacements on the XZ plane. The external surface of the lower bearing inner ring can only revolve around Y axis, while all the other DoFs are locked. This surface is the one that contacts the internal surface of the outer ring.

### 7.4.3.2 Inertia Forces

The inner rings of the bearings rotate along with the spindle, having exactly the same rotational speed, while the outer rings remain stationary, firmly attached to the spindle assembly shell. The effect of gravity cannot be neglected in the study, gravity acceleration acting along the negative Y axis.

### 7.4.3.3 Cutting Forces

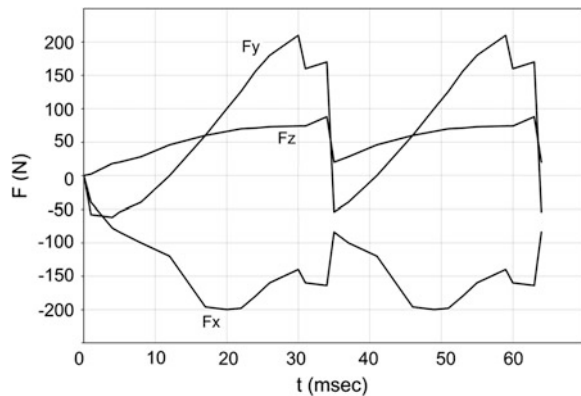
Typical cutting force variation in one full rotation of the spindle can be obtained using a calibrated theoretical model, e.g. see [18], or by experiments, using a 3-axis piezoelectric accelerometer for various types of milling and for various machining conditions. A typical case for peripheral milling with a tool with helical teeth rotating at  $\omega = 210$  rad/s is shown in Fig. 7.9 as digitized at 26 points. The cutting force is distributed along a certain length of the tool cutting edge corresponding to the axial engagement of the tool.

### 7.4.4 Contact Surfaces

The bearing surfaces that come into contact are defined, i.e. the internal ones of the outer rings and the external ones of the inner rings. Friction coefficient between them is then defined, with the value  $\mu = 0.002$ , as well as the contact overall behavior both at the beginning and during the solution process.

At each contact surface, the user can model different contact behavior. The surfaces in contact are considered not to detach, thus they are defined as “Bonded always”. When a pair of contact surfaces is created, ANSYS automatically inserts

**Fig. 7.9** Typical digitised cutting force variation with time



two types of FE, i.e. TARGE170 concerning the target surface and CONTA174 concerning the contact surface. These FE types introduce non-linearity to the problem solution. The target surface is discretized with a set of TARGE170 FEs and it is coupled with a contact surface defined by CONTA174 FEs through the usage of a common real constant set. These FE types are allowed to displace linearly and rotationally, and to take on loading forces and torques as well. CONTA174 FE type can be used to model contact and slip between target and deformed surfaces.

## 7.5 Spindle Variant Design

Based on the design principles discussed in Sect. 7.3, in order to conduct a detailed investigation, a number of different spindle assemblies must be defined, by assigning different values to the design variables. There are two main points that need to be addressed; firstly, how to select the values to be assigned to each design variable and secondly how to balance between the number of variants investigated and the required amount of time needed to perform the complete FEA for each variant.

The adopted approach follows Design of Experiments (DoE) philosophy [19]. DoE is a methodology for systematic experimental design, execution and analysis. One of the basic concepts of DoE is the use of orthogonal arrays (OAs) that are employed to perform fractional instead of full factorial experiments without loss of statistically significant information. OAs define the number of required experimental runs (i.e. the number of different factor combinations) as well as the value of each factor per individual run.

The selection of the appropriate OA for any design depends on the following criteria: (a) Number of factors that are examined in the experiment. (b) Number of different values (or levels) of each factor that are examined in the experiment. (c) Whether it is expected or not that interactions between factors exist. (d) Which factor interactions are thought as important and up to what order. Using these criteria and by comparing with the available OAs the resolution of the experiment can be determined, i.e. the lowest order of interaction that is confounded with a main factor. Normally, designs that result in resolutions III, IV and V are advised.

By conducting the experimental runs and analyzing the data, the most influencing factors and their values can be identified. It is then possible to either plan a new experimental procedure using only these factors and values as a baseline or to directly employ these factors for developing an analytical model in order to determine their optimum values.

**Table 7.2** Selected values of outer spindle diameter

Bearing location	A	A	A	B	B	B
Outer diameter (mm)	100	105	110	75	80	85

**Table 7.3** Selected values for number and distribution of bearings

Bearing configuration	No. of bearings	No. of bearings (location A)	No. of bearings (location B)
1	3	2	1
2	2	1	1
3	3	1	2

### 7.5.1 Shape Modelling

In this work, three values are chosen for each design variable; a centre value, which is equal to the one of the original model presented in [4] and two symmetrically positioned values around the centre. As far as the outer diameter is concerned, the selected values are based on dimensions of commercially available bearings, with 3 different values selected for each location, see Table 7.2.

Either two or three bearings are considered resulting in three possible configurations at locations A and B along the spindle assembly, see Table 7.3. Last, the three values dictating the distance between the bearings are 265, 325 and 385 mm.

If all possible combinations were to be considered, then a total of  $3^4 = 81$  different spindle assemblies should be investigated. This would be a very time consuming process taking into consideration the time needed to setup and execute each FEA run. The application of the DoE philosophy significantly reduces the number of assembly variants investigated and the associated time devoted. The OA that is used for this purpose is L18 that has the ability to incorporate one factor with two levels and up to seven factors with three levels each [19]. By placing the spindle assembly design parameters in the appropriate columns and eliminating the empty ones, Table 7.4 is produced with the final spindle assemblies.

To illustrate the effect that the different values of the design parameters have on the actual spindle assembly geometry, three of the variants corresponding to nos 1, 6 and 17 respectively are presented in Fig. 7.10.

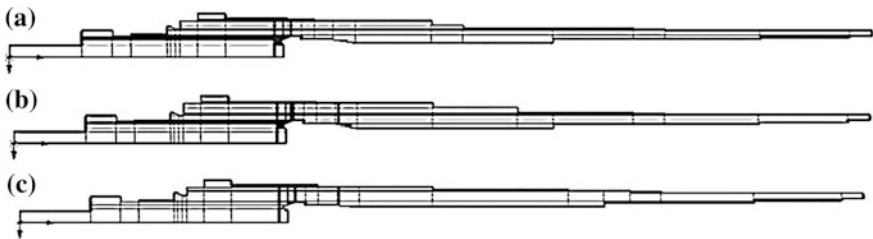
### 7.5.2 Modal Analysis

Modal analysis is performed using FE for each and every variant of the total 18 different design cases investigated in DoE. For each design case, 28 modes are obtained with frequencies varying from 20 to 8,500 Hz.

In the present study, modal frequencies up to 2,100 Hz are focused on due to an upper bound on spindle speed, see Tables 7.5 and 7.6. Note that 4–6 modes at the

**Table 7.4** Spindle assembly variants with regard to DoE (L18)

Variant	Outer diameter location B (mm)	Outer diameter location A (mm)	Bearing configuration	Distance (mm)
1	75	100	1	265
2	75	105	2	325
3	75	110	3	385
4	80	100	2	385
5	80	105	3	265
6	80	110	1	325
7	85	105	3	385
8	85	110	1	265
9	85	100	2	325
10	75	110	2	265
11	75	100	3	325
12	75	105	1	385
13	80	105	1	325
14	80	110	2	385
15	80	100	3	265
16	85	110	3	325
17	85	100	1	385
18	85	105	2	265



**Fig. 7.10** Spindle variants according to L18 OA: **a** No 1, **b** No 6, **c** No 17

most appear in frequencies within the operational limits of the machine for any case.

The first seven modes for Case 1 are depicted in Fig. 7.11. For all cases, the first mode is a torsional one (see Tables 7.5 and 7.6), and it appears at frequencies between 24 and 73.3 Hz. Modes 2 and 3 are bending modes in X and Z directions respectively for all cases too. Similarly, in all cases, 4th and 5th mode are bending modes at directions X and Z of the front part of the spindle-bearings assembly.

The only exception is in Case 1, for which these last two modes are ranked 5th and 6th instead. In most cases, 6th mode is torsional about Y axis, with the exception of Cases 3, 12 and 14, where this appears in the 8th position, and in Case 1, where it appears at the 4th position.

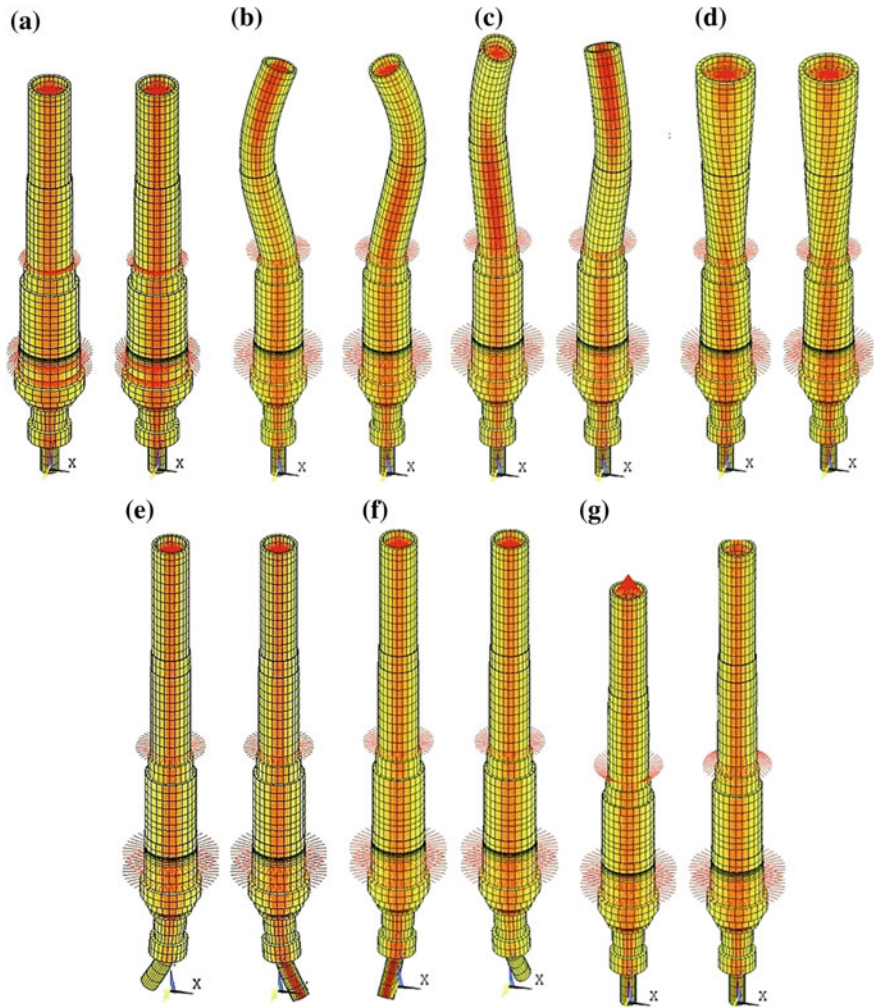
**Table 7.5** Mode frequencies (in Hz) for cases 1–9 of L18

	Case								
Modes	1	2	3	4	5	6			
1	71.8	60.1	50.0	44.6	49.7	30.8			
2	1144.4	1449.7	1494.1	1454.9	1189.9	1508.2			
3	1144.4	1449.7	1494.1	1454.9	1189.9	1508.2			
4	2023.5	1490.8	1805.1	1761.6	1480.8	1518.8			
5	2165.1	1490.8	1805.1	1761.6	1480.8	1518.8			
6	2165.1	2137.6	2230.0	2086.7	2026.1	2130.6			
7	2533.6	2305.3	2230.0	2149.2	2490.4	2678.8			
8	3124.2	2305.3	2307.5	2149.2	2718.3	2758.6			
9	3124.2	2597.9	2653.3	2435.5	2718.3	2758.6			
.....									
28	8076.9	8507.3	8537.1	8175.2	8110.6	8212.7			
	Case								
Modes	7	8	9	10	11	12			
1	65.5	44.5	55.2	40.9	70.1	73.3			
2	1478.0	1224.2	1470.6	1144.3	1472.4	1499.1			
3	1478.0	1224.2	1470.6	1144.3	1472.4	1499.1			
4	1882.0	1512.3	1524.8	1499.3	1556.8	1870.5			
5	1882.0	1512.3	1524.8	1499.3	1556.8	1870.5			
6	2085.3	2007.9	2052.8	2018.6	2097.3	2231.7			
7	2418.3	2543.9	2370.4	2584.4	2340.8	2231.7			
8	2445.9	3175.0	2401.9	2662.3	2340.8	2245.7			
9	2445.9	3175.0	2401.9	2662.3	2537.7	2685.5			

(continued)

Table 7.5 (continued)

	Case											
Modes	7	8	9	10	11	12						
.....												
28	8150.6	7845.3	7879.1	8132.5	8530.4	8237.2						
	Case											
Modes	13	14	15	16	17	18						
1	65.5	24.0	48.4	52.0	66.0	58.4						
2	1496.6	1494.6	1253.3	1497.9	1485.4	1211.3						
3	1496.6	1494.6	1253.3	1497.9	1485.4	1211.3						
4	1507.5	1799.4	1475.5	1660.4	1921.2	1490.2						
5	1507.5	1799.4	1475.5	1660.4	1921.2	1490.2						
6	2093.9	2122.8	1995.3	2091.9	2086.4	1999.7						
7	2585.3	2122.8	2421.5	2353.3	2301.6	2400.3						
8	2730.7	2234.7	2786.2	2353.3	2301.6	2757.9						
9	2730.7	2567.1	2786.2	2490.0	2433.9	2757.9						
.....												
28	8216.0	8246.6	8198.2	7895.2	8011.3	7845.3						



**Fig. 7.11** Assembly modes for case 1 **a** Torsional mode around Y axis. **b** Bending mode of back part in X direction. **c** Bending mode of back part in Z direction. **d** Torsional mode of back part about Y axis. **e** Bending mode of front part in X direction. **f** Bending mode of front part in Y direction. **g** Tension/compressive mode of back part in Y direction

Reviewing the modal results, 7th or 9th mode is a tension/compression mode (see Tables 7.5 and 7.6), which, however, appears at a frequency higher than 2,100 Hz in all the studied cases.



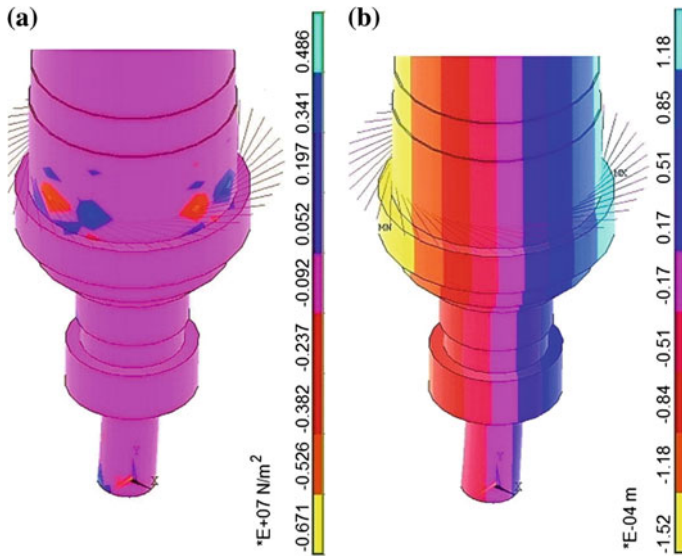


Fig. 7.12 Typical X components in case 14 for **a** stress, **b** displacement

### 7.5.3 Transient Dynamic Analysis

Investigation of the dynamic behavior of spindle-bearing assembly is conducted according to the model presented in Sect. 7.4. The period of the variation of cutting force applied on the periphery of the lower end of the assembly is 64 ms, see Fig. 7.9, leading to a time step of 1 ms, i.e. 64 time steps per revolution. A typical snapshot of the stress and displacement distribution obtained by FEA is shown in Fig. 7.12.

In general, stress is far too low to be considered as an assessment criterion, reaching values between 22 and 51 N/mm<sup>2</sup>. On the contrary, displacement does constitute a criterion for comparing different cases, in two ways: first, deflection at the tool tip gives some insight into the accuracy expected of the particular machining process for the particular spindle assembly configuration, and, second, maximum displacement that may appear anywhere in the spindle assembly, e.g. at the bearings interface or at the coupling area with the motor, should be minimal.

Based on FEA transient analysis, Table 7.6 presents the maximum displacement values observed at the tool tip in X, Y and Z directions for each of the 18 different design cases. The largest deflection appears in X and Z directions, values varying between 21–75  $\mu\text{m}$  and 11–23  $\mu\text{m}$ , and the smallest deflection appears in Y direction (axis of rotation), values varying between 3.7 and 5.2  $\mu\text{m}$ .

It must be noted that maximum deflection values in the three main directions do not appear concurrently at the same time-step, as the respective force components also exhibit their maxima at different time steps, see Fig. 7.9. Typical diagrams for

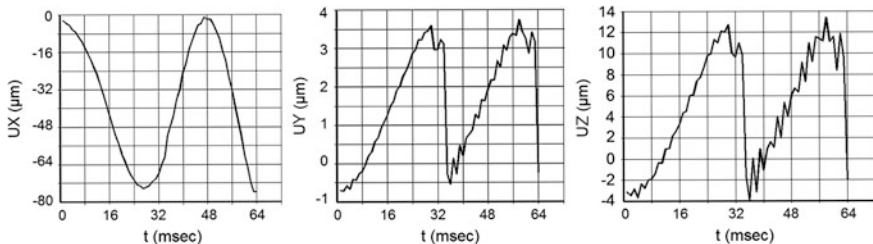
**Table 7.6** Maximum deflection of the tool tip in X, Y and Z directions and in total

Case	UX ( $\mu\text{m}$ )	UY ( $\mu\text{m}$ )	UZ ( $\mu\text{m}$ )	U( $\mu\text{m}$ )
1	24	3.5	11	27
2	22	3.7	14	26
3	26	3.7	14	30
4	36	5.2	23	43
5	29	4.6	18	34
6	58	3.7	14	60
7	23	4.6	18	30
8	29	3.8	14	32
9	24	3.8	14	28
10	34	3.8	14	37
11	27	3.8	14	31
12	23	3.8	14	27
13	23	3.8	14	27
14	75	3.8	14	76
15	33	3.8	14	36
16	24	3.8	14	28
17	23	3.8	14	27
18	21	3.8	14	26

the deflection as a function of time of the nodes where the cutting force is applied are shown in Fig. 7.13 regarding Case 14.

In Fig. 7.13, the response at the tool tip exhibits some periodicity that can be traced back to the periodicity of forces, see Fig. 7.8. It is not straightforward to estimate the influence of damping from these diagrams, but its existence is traceable. By qualitative comparison between Figs. 7.9 and 7.13, a time shift between the maximum deflection and maximum force can be observed especially in X axis. For example, the maximum force in this direction occurs at 20 and 49 ms while maximum deflection occurs at 26 and 64 ms respectively.

Table 7.7 presents maximum deflections and the corresponding time-step as they appear anywhere in the spindle assembly for all cases examined for the particular



**Fig. 7.13** Case 14: deflection variation in X, Y and Z directions at the tool tip time

**Table 7.7** Maximum displacement in X, Y and Z direction and total observed at any point of the assembly

Case	Time-step	UX ( $\mu\text{m}$ )	UY ( $\mu\text{m}$ )	UZ ( $\mu\text{m}$ )	U ( $\mu\text{m}$ )
1	50	56	2	56	79
2	23	43	3	43	60
3	51	59	3	59	84
4	53	78	4	78	110
5	51	63	3	63	89
6	58	207	4	207	293
7	51	36	3	36	51
8	53	75	3	75	106
9	51	46	3	46	65
10	53	95	3	95	135
11	51	56	3	56	79
12	50	45	2	45	64
13	53	47	3	47	66
14	27	268	3	268	379
15	53	83	3	83	118
16	51	51	3	51	72
17	53	47	3	47	66
18	23	39	3	39	56

rotation speed of 210 rad/s (=2,005 rpm). Case 14 is the most unfavourable one, followed by case 6, since deflection values are in the range of some tenths of a millimetre. Case 7 is clearly the most favourable one.

## 7.6 Spindle Functional Analysis

### 7.6.1 Functional Parameters

The behaviour of a given spindle design needs to be analysed for different functional parameters. The latter are those that are ultimately connected either with rotational speed of the spindle or with the cutting force that is applied to the tool tip. Note that functional parameters do not influence design parameters and especially the modes and their frequencies, which remain unaltered.

Rotation speed of the spindle as such is the obvious functional parameter that needs to be considered. If chip load (i.e. feed per revolution/per tooth in the case of milling) is kept the same, then the profile of the force is also affected but only undergoing scaling in time. This means effectively that the spindle will be excited at a different frequency, which might be closer to or farther from the previous or a new mode of vibration. This may cause a different response (deflection) of the tool tip

and of other parts of the spindle that are of interest, such as bearings interface, coupling interface etc. Transient FEA should reveal any such differences.

If for some reason rotation speed is kept the same but chip load is changed (e.g. through depth or width of cut or even a change in number of teeth of the cutting tool), then obviously the cutting force as a function of time also changes. In fact, a partly or totally different loading function needs to be taken into account and a new execution of transient FEA will give insight into the expected response.

The design case that is focused on next, as an example, is the worst case identified in Sect. 7.5, i.e. Case 14. However, any of the other cases would be equally eligible for investigation.

## **7.6.2 Transient Dynamic Analysis**

### **7.6.2.1 Rotational Speed Investigation**

As an example, two more rotational speed values of the spindle are examined in addition to 210 rad/s using transient analysis, i.e. half the original (105 rad/s) and twice the original (420 rad/s).

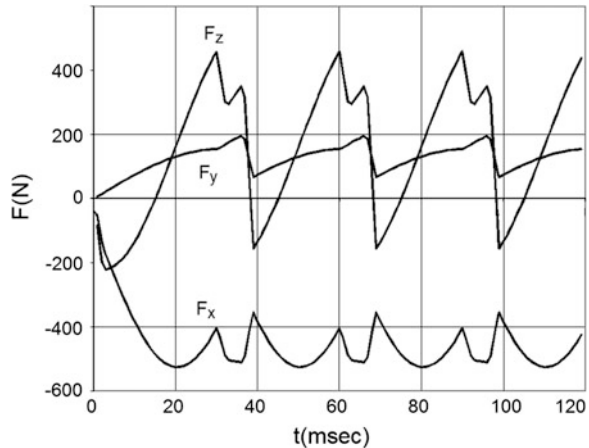
Results concerning maximum displacement of the nodes where the cutting force is applied are virtually identical for all three cases, coinciding within 4 % with the values documented for Case 14 in Table 7.6. Maximum displacement at any point of the spindle is again virtually the same (within 4 % tolerance) as for the original speed, see Case 14 in Table 7.7.

### **7.6.2.2 Cutting Force Investigation**

As an example, a different cutting force profile has been defined and applied, see Fig. 7.14, in place of the original one that shown in Fig. 7.8. The new force corresponds to doubled feed per tooth, at 0.05 mm and quadrupled depth of cut, at 2 mm, compared to the original one. This also makes a slight difference in tool engagement angle at 118.6 instead of 110°.

Maximum tool tip displacement obtained through transient analysis for the new cutting force profile is the same for all three rotational speeds (105, 210 and 420 rad/s) at 227, 8 and 28  $\mu\text{m}$  in X, Y and Z directions, i.e. 229  $\mu\text{m}$  in total. Maximum displacement at any point of the spindle is 1,144  $\mu\text{m}$  (817, 6 and 817  $\mu\text{m}$  respectively in the three main directions) and is virtually the same for all three rotational speeds examined). In all three cases, maximum calculated stresses are very small, namely below 97 N/mm<sup>2</sup>).

**Fig. 7.14** New cutting force profile



## 7.7 Spindle Performance Assessment

Performance specification/assessment of a machine tool spindle needs to be based on practical criteria, mainly regarding the final result on the machined surface quality. There are, of course, criteria relating to reliability and maintenance, but these are not considered in the current work.

Machining accuracy is defined by the displacement (vibration amplitude) of the tool tip with respect to the ideally followed cutting path due to machining forces. The lower the displacement, the better the attainable accuracy.

Frequency response function (FRF) gives, in general, a good idea about the expected behaviour since this constitutes a ‘multiplier’ of the exciting (machining force) and also defines the safe machining width against chattering. Moreover, in most cases, cutting force direction is not normal to the machined surface, thus it is the cross FRF between these directions that actually counts.

The complete picture should take into account not just the spindle, but the other parts of the machine tool, too, according to the well-known receptance coupling method, yet with inherent problems of noise sensitivity, inability to include all modes at the interfaces and numerical problems in inverting arrays in the presence of nonlinearities [18].

When a number of modes exist connected to different spindle or, generally, machine tool parts including cutting tool—tool holder assembly, any of those may influence machine performance through its own FRF. The degree of influence depends on the particular force pattern (including direction), which is associated with a different set of process parameter values.

In evaluating the performance of the spindle in forced vibrations in milling, the cutting force needs to be considered as a sum of 4–5 Fourier series harmonic terms. Thus, the spindle may be excited in a wide range of frequencies, noting that low static compliance of the structure generally results in a higher fundamental

frequency. Response will depend on how close to the natural frequencies of the spindle any of the harmonic exciting frequencies lies. Note that the frequencies at which chatter vibrations take place are very close to the natural frequencies of the machine (spindle), but actual chatter occurs when cutting width is large enough.

### ***7.7.1 Performance Factors***

Focus is put on the modal frequencies and on the nature of modes that occur. The significance of modal frequencies refers is that it becomes possible to identify the loading conditions, i.e. tooth passing frequency in the case of milling, for which near-resonance conditions might occur. The nature of modes is significant on a case-by-case reasoning, e.g. a bending mode should impact machining accuracy more than a torsional one.

Design parameters influence both these characteristics. Referring to the specific results presented in Sect. 7.5 the most important parameter appears to be the distance between bearing locations, as this influences the frequency at which the bending modes occur (2nd to 5th). When this distance acquires lower values, as in cases 1, 5, 8, 10, 15 and 18 modes 2 and 3 occur in the range 1,100–1,200 Hz by contrast to the other cases in which they occur between 1,450 and 1,500 Hz. Moreover, when this distance is maximum as in cases 3, 4, 7, 12, 14 and 17 modes 4 and 5 occur at a higher frequency range (1,750–1,900 Hz) compared to other cases (1,450–1,550 Hz).

The diameter of the spindle at the front bearing (A) seems to have an impact, too, because the lowest 5 frequencies at which the mode 1 occurs correspond to this parameter attaining its highest value (cases 4, 6, 8, 10 and 14).

In addition, the three highest frequencies at which mode 1 occurs correspond to the smallest diameter values at the locations of the bearings (cases 1, 11 and 12).

The other parameters do not seem to influence results in a clear way, at least within their designated limits. The respective frequencies are probably attributed to parameter interactions.

Displacement and deflection observed at crucial points of the spindle are the important factors calculated in transient analysis. In particular, it is necessary to focus on maximum displacement at the tool tip, pointing at the expected machining accuracy, and secondarily on the displacement variation with time there, pointing at ease or otherwise of possible compensation of the resulting machining error.

Regarding the influence of design parameters on functional behaviour of the spindle it is not possible to draw generally clear conclusions. Cases 4, 5, 6, 7, 10 and 14 share relatively large deflections. Four of these cases correspond to an intermediate diameter value at the front bearing.

In addition, a combination of large external diameter at the front with an intermediate diameter at the back bearing seems to be governing the largest deflections of the spindle (cases 14 and 6).

In executing transient analysis of Case 14, i.e. the worst case design variant, the rotational speeds that were tried yield significant differences in terms of maximum displacements at spindle regions other than those at the tool tip, i.e. when halving speed X and Z maximum displacement decreases by about 30 % and when doubling speed displacements increase by 50 %.

An increase in cutting force, by doubling it on average, causes a threefold increase in tool tip maximum displacement and an even large increase in other regions of the spindle.

### ***7.7.2 Performance Specifications***

Calculation of the tool tip displacement as well as displacement at other crucial parts of the spindle such as at the bearings and transmission interfaces, is recommended for comparing machine tool spindle performance and alternative designs. Displacement has to be as low as possible for: (a) the whole range of frequencies that are of interest, i.e. spindle speeds and number of tool teeth (b) all possible machining processes that can be executed on the machine tool (c) all possible cutting tools and tool holders in as far as they add new modes and associated dynamic characteristics including those at the interfaces (d) all workpiece materials to the extent that they influence the specific dynamic cutting force (e) the variety of cutting process parameters that influence chip area and width, i.e. cutting force.

This specification is practically impossible to cover exhaustively, thus an indirect specification may examine the following: (a) static compliance (stiffness), which needs to be low(high), fundamental natural frequency, which needs to be high (c) Number of modal frequencies in the frequency range of interest which need to be few and unequally distributed (d) Critical width of cut, which needs to be large in the frequency range of interest, as found by reference to the cross FRF real part magnitude.

The modal characteristics and the displacement at the tool tip and at other critical parts of the spindle as a response to cutting force may be calculated using FEA, as successfully demonstrated in this work. Due to the computational load of transient analysis with inherent nonlinearities etc., specific design variants and specific loading scenarios are only possible to investigate. However, in order to be able to investigate a range of design variants defined by DoE or other paradigms it is absolutely essential for the designer to be able to generate meshed models in an automatic straightforward manner, which was the novel aspect in this work.

Such flexibility in the design-analysis cycle enables various optimisation procedures, starting from Taguchi-based evaluation of a finite set of representative alternative spindles and reaching ultimately automation of the evaluation cycle, for instance in an evolutionary algorithm. This approach may be used not only in classic design of spindles but also in reconfiguring spindles according to their application on a particular machine tool.

## References

1. López de Lacalle LN, Lamikiz A, Sánchez JA, Salgado MA (2007) Toolpath selection based on the minimum deflection cutting forces in the programming of complex surfaces milling. *Int J Mach Tools Manuf* 47:388–400
2. Benardos P, Vosniakos G-C (2013) Off-line intelligent optimisation of feed and speed in sculptured surface machining using cutting force metamodels. *Proc Inst Mech Eng Part B J Eng Manuf* 228(6):878–892
3. Abele E, Altintas Y, Brecher C (2010) Machine tool spindle units. *CIRP Ann Manuf Technol* 59:781–802
4. Cao Y, Altintas Y (2007) Modeling of spindle-bearing and machine tool systems for virtual simulation of milling operations. *Int J Mach Tools Manuf* 47:1342–1350
5. Altintas Y, Cao Y (2005) Virtual design and optimization of machine tool spindles. In: *Proceedings of the general assembly of CIRP No 55, Antalya, Turkey, vol 54, issue 1*, pp 379–382
6. Law M, Altintas Y, Srikantha Phani A (2013) Rapid evaluation and optimization of machine tools with position-dependent stability. *Int J Mach Tools Manuf* 68:81–90
7. Zahedi A, Movahhedy MR (2012) Thermo-mechanical modeling of high speed spindles. *Scientia Iranica Trans B Mech Eng* 19(2):282–293
8. Cao H, Li B, He Z (2012) Chatter stability of milling with speed-varying dynamics of spindles. *Int J Mach Tools Manuf* 52:50–58
9. Rantatalo M, Aidanpaa J-O, Goransson B, Norman P (2007) Milling machine spindle analysis using FEM and non-contact spindle excitation and response measurement. *Int J Mach Tools Manuf* 47:1034–1045
10. Ertürk A, Budak E, Özgüven HN (2007) Selection of design and operational parameters in spindle-holder-tool assemblies for maximum chatter stability by using a new analytical model. *Int J Mach Tools Manuf* 47:1401–1409
11. Faasen RPH, van de Wouw N, Oosterling JAJ, Nijmeijer H (2003) Prediction of regenerative chatter by modelling and analysis of high-speed milling. *Int J Mach Tools Manuf* 43:1437–1446
12. Chang H-K, Kim J-H, Kim IH, Jang DY, Han DC (2007) In-process surface roughness prediction using displacement signals from spindle motion. *Int J Mach Tools Manuf* 47:1021–1026
13. Brecher C, Spachtholz G, Paepenmüller F (2007) Developments for high performance machine tool spindles. *CIRP Ann* 56:395–399
14. Maeda O, Cao Y, Altintas Y (2005) Expert spindle design system. *Int J Mach Tools Manuf* 45:537–548
15. Lin C-W, Tu JF (2007) Model-based design of motorized spindle systems to improve dynamic performance at high speeds. *J Manuf Process* 9(2):94–108
16. Haitao Z, Jianguo Y, Jinhua S (2007) Simulation of thermal behavior of a CNC machine tool spindle. *Int J Mach Tools Manuf* 47:1003–1010
17. Lee SH (2005) A CAD–CAE integration approach using feature-based multi-resolution and multi-abstraction modelling techniques. *Comput Aided Des* 37:941–955
18. Altintas Y (2012) *Manufacturing automation: metal cutting mechanics, machine tool vibrations, and CNC design, chapter 2: mechanics of metal cutting*, 2nd edn. Cambridge University Press, Cambridge
19. Montgomery DC (2012) *Design and analysis of experiments*, 8th edn. Wiley, New York



# Index

## A

Aeronautics, 134, 137, 139, 148  
Automotive, 134, 137, 148

## B

Blanks, 9, 29

## C

Casting defects, 21, 23  
Chip curling, 109, 110, 112, 113, 120, 123  
Chip formation, 154, 155, 159, 162, 164, 168, 198, 199, 202, 204  
Cohen's model, 160  
Contact surfaces, 211, 220  
Control friction, 192  
Cutting, 110–114, 116–125, 127, 129, 130, 153–156, 159, 164–166, 168, 169, 181, 183, 184, 198, 203  
Cutting forces, 50, 51, 56, 66, 87, 125–127, 210, 220  
Cutting geometry, 51, 55, 66  
Cutting specific coefficients, 58, 61, 64, 66, 71  
Cutting speed, 35, 36, 39, 40, 42, 47, 51, 58, 62, 66, 87, 94, 98  
Cutting tool, 34, 35, 41, 46

## D

Defence, 137, 139  
Degrees of Freedom (DoF), 218, 219  
Design framework, 209  
Design parameters, 209, 212, 214, 229, 232  
Diamond-coated tools, 34, 37

## E

Edge radius, 34, 39, 41, 42, 46, 47  
Experiments, 35, 37

## F

Failure, 8, 13, 20, 21  
FEA software, 213, 216  
Feedrate, 51, 54, 58, 61, 62, 65, 94  
Finite element analysis (FEA), 210–212, 215, 222  
Flexible integration, 209  
Fluid-like flow, 162  
Force, 34, 37, 41, 47  
Friction coefficient, 118–120  
Frictional heating, 154, 171, 187, 188, 190  
Frictional interactions, 153, 164, 187, 202  
Functional analysis, 229  
Functional modelling, 217

## G

Gas shields, 113, 114, 118, 122, 125  
Grinding process, 153, 197, 199, 203  
Grinding science, 153, 204

## H

High performance, 50

## I

Industrial applications, 113  
Inertia forces, 220

**L**

Langford model, 160  
 Large strains, 154, 160, 162  
 Liquid lubrication, 193  
 Loads, 211, 218, 219  
 Lubrication, 154, 192, 194–196, 200

**M**

Machinability, 140, 141, 148  
 Machine tool, 210, 211, 214, 231, 233  
 Machining, 134, 135, 137, 140–142, 144–146, 148  
 Machining interface, 153, 154, 164  
 Magnesium, 133, 134, 136–148  
 Magnesium alloys, 134, 136, 137, 139, 142, 147  
 Magnesium ignition, 141, 142  
 Material models, 217  
 Measurements, 36, 37, 47  
 Mechanics of cutting, 154, 198  
 Mechanistic models, 73  
 Medical, 134, 139, 148  
 Mesh types, 217  
 Metal-matrix composites (MMCs), 2, 136, 137, 139, 141, 147  
 Microscale, 154, 170  
 Milling, 113, 125, 127, 129, 130  
 Modal analysis, 210, 222

**O**

Optimisation framework, 209  
 Orthogonal cutting, 34, 37, 47, 117, 120

**P**

Parametric shape modelling, 213  
 PCD tools, 9, 12, 15, 21, 23  
 Performance factors, 232  
 Performance specifications, 233  
 Plastic behaviour, 154, 160  
 Ploughing, 153, 154, 169, 179, 180, 182–184, 198, 200, 201  
 Polycrystalline diamond (PCD), 2

**R**

Rotational speed, 210, 211, 220, 230, 232

**S**

Shape, 213, 214, 222  
 Shape modelling, 213, 214, 222  
 Shaw model, 161  
 Shear angle, 157, 158  
 Simulation, 34, 36, 44, 47  
 Sintered carbides, 9, 28  
 Sliding friction, 164, 179, 181, 182, 186, 200  
 Sliding interactions, 154, 164, 200, 204  
 Solid modelling, 216  
 Spindle performance, 210, 231, 233  
 Spindle variant, 221  
 Spindles, 210, 214  
 Sports, 133, 137, 139, 148  
 Static friction, 164, 171, 172, 174, 175, 177  
 Stick-slip, 164, 171, 177, 178

**T**

Temperature, 34, 36, 39–42, 44, 134, 135, 141, 143, 145, 147, 148  
 Thermal stability, 24, 27, 30  
 Thrust forces, 117–119  
 Tool life testing, 12  
 Tool material, 8, 12, 16  
 Tool tip radius, 64, 51, 53, 57, 61, 73, 83  
 Tool wear, 3, 12, 18, 21, 50, 59, 87, 92, 125, 126, 129, 131  
 Transient dynamic analysis, 209, 227, 230  
 Turning, 50, 58, 83, 94, 106

**U**

Uncut chip thicknesses, 39, 41  
 Usui model, 162

**V**

Validation, 51, 68, 73, 77, 83, 84, 102

**W**

Walker model, 161  
 Wear, 3, 5, 7, 10, 14–16, 20, 22, 26, 27  
 Workpieces, 36